The Synthesis and Characterisation of Metal Organic Frameworks using Functionalised and Flexible Linkers

Thesis submitted in accordance with the requirements of the University of Liverpool for the degree of Doctor in Philosophy by Jibreel Haddad

August 2017

Acknowledgements

First and foremost I would like to thank God, to whom I owe thanks for everything I have achieved, and without whom I would not be here.

I would like to thank all contributing academics at University of Liverpool for their help and support throughout my PhD with special thanks to Dr George Whitehead who successfully solved all structures that are reported and presented in this thesis. Thanks for all of his help, all of the knowledge that he passed on and all of his support, as well as, of course, his highly entertaining conversations in the office! Thanks to all other contributors to this work including (but not limited to) Dr Marco Zanella, Dr Andy Stephenson, Prof. Pete Myers, Dr Alexandros Katsoulidis, Martin Smith and all of the staff at DSTL, and finally, all academics at Diamond Light Source who helped during beamline visits.

On a personal note, I would like to give a huge thanks to everybody who helped make this experience enjoyable both in University and outside. Special thanks go to Zoe for her emotional support and constant giggles in the office and of course all of her impressive nutrition advice, thank you Zoe, and furthermore, thanks for the first of every month aka calendar day, which we looked forward to every month. Oliver for his constant laughter around the lab and in the office, Frisbee, cricket, basketball and bouldering, thanks for all the jokes buddy. Harry, who introduced himself by telling us that he liked goats, from there on, the jokes have been thoroughly welcomed and enjoyed. Thank you. Daniel, even though at times he could be extremely stubborn, he always offered sound advice in the lab and the kitchen, and was a fellow lover of Only Fools and Horses, thank you for the banter. Dave,

thank you for always being there to offer your support, advice and life experiences, from which, I learned to deal with a lot of stressful and discouraging situations. Thank you. A few other past and current members who I cannot forget to thank for all the good times we had together both in work and outside; Noemie, Tim, Rachel, Gethin and of course thanks to Tom for those hilarious situations he always used to find himself in, and for introducing us to the extraordinary game that is Piggy.

If anybody in the Rosseinsky group finds themselves reading this thesis in the future, I hope that the quote wall or its replacement is still going strong, and if you do not know what this is, ask an old member of the group, I'm sure they will explain.

I would like to further thank my Mum, Dad and the rest of my family for their constant support and words of advice throughout this experience. Thanks for putting up with me being a nightmare at times, I cannot thank them enough and I feel incredibly blessed to have them as my family.

Finally, I would like to thank the EPSRC for funding this research and Prof. Matthew Rosseinsky for providing some useful advice and support throughout.

Abbreviations

Al-PMOF	Aluminium – Porphyrin MOF
BDC	Benzene Dicarboxylate
BET	Brunner-Emmett-Teller Model
Bipy	2,2′-bipyridine
BPDC	Biphenyl Dicarboxylate
BTC	Benzene Tricarboxylate
BTTri	1,3,5-tris(1,2,3-triazol-5-yl)benzene
CN	Coordination Number
CPM	Crystalline Porous Material
BUT	Beijing University of Technology
COF	Covalent Organic Framework
CSA	N-(4-carboxyphenyl) succinamic acid
DEF	Diethylformamide
DMF	Dimethylformamide
DMA	Dimethylacetamide
DMAM	Dimethyl ammonium
Dobdc	2,5-dihydroxyterephthalic acid
DOT	2,5-dioxidoterephthalate
EB	Ethylbenzene
EtOH	Ethanol

FDC	2,5-Furandicarboxylic Acid
FL-MOF	Flexible Linker MOF
G13	Group 13
GC	Gas Chromatography
Gly-Ala	Glycylalanine
HPLC	High Performance Liquid Chromatography
IBU	Inorganic Building Unit
IRMOF	Isoreticular Metal Organic Framework
MA	Mucic Acid
MeCN	Acetonitrile
MeOH	Methanol
MIL	Materials of Institut Lavoisier
mX	Meta-Xylene
MOF	Metal Organic Framework.
NOTT	Nottingham
oX	Ortho-Xylene
PDG	N,N′-(1,4-Phenylenedicarbonyl) diglycine
PCN	Porous Coordination Network
PEI	polyethyleneimine
POST	Pohang University of Science and Technology
PSM	Post Synthetic Modification
pX	Para-Xylene
PXRD	Powder X-Ray Diffraction
RH	Relative Humidity

SBU	Secondary Building Unit
SCXRD	Single Crystal X-Ray Diffraction
SEM	Scanning Electron Microscope
TGA	Thermogravimetric Analysis
THF	Tetrahydrofuran
TIC	Toxic Industrial Chemical
UiO	Universitetet i Oslo
XRD	X-Ray Diffraction
ZnCar	Zinc:Carnosine

Abstract

Chapter 3

In this chapter, an aluminium based MOF using the 2,5-furandicarboxylic acid (FDC) linker was synthesised and shown to have a BET surface area of 1150 m^2 g^{-1}. The material demonstrates a higher affinity towards CO_2 than CH_4, with isosteric heats of adsorption of 27.5 kJ mol^{-1} and 18.6 kJ mol^{-1}, respectively. The MOF was assessed for separating binary mixtures of several gases including CO_2 / CH_4 and CO_2 / N_2, the selectivity factors were calculated to 6.5 and 21, respectively, which are comparable to reported similar MOFs. Attempts at xylene separations were less successful, with no baseline resolution between peaks, making it impossible to calculate a separation factor. Micro–breakthrough experiments were conducted to assess ammonia uptake under dry and humid flows, showing breakthrough after 70 minutes, which is an impressive five–fold improvement over a benchmark activated carbon.

Chapter 4

An indium based MOF, isostructural to Al: FDC described in chapter 3, was targeted. However, three different In: FDC structures were discovered, two of which are the only reported examples of MOFs to contain both co-ordination number (CN) 6 and 7 indium within the same structure. The third structure exhibits a unique feature in the form of a pseudo crown - ether formed around the furanic oxygens and hydroxy groups from the In(OH) chains, with a sodium in the centre, which is present from the synthesis. All three materials are shown to have no

porosity, for a number of reasons. The first material, which has an overall negative charge counterbalanced by the presence of dimethyl ammonium ions (DMAM), has a high density. The other two materials are made of interlocking 2–dimensional sheets, which undergo a structural collapse / change upon activation.

Chapter 5

Two new isostructural group 13 (G13) MOFs have been synthesised using indium and aluminium. Due to the flexibility of the N–(4–carboxyphenyl) succinamic acid (CSA) linker, the formation of a 3–dimensional framework was restricted, thus both structures consist of 2–dimensional sheets. It is for this reason that neither of the MOFs exhibit any porosity towards N_2, CO_2 or CH_4. An interesting difference between the two MOFs is that In: CSA undergoes a reversible structural change upon activation, which is not seen for the aluminium analogue.

Chapter 6

A further two new G13 MOFs were synthesised, using a flexible linker; N,N'-(1,4-Phenylenedicarbonyl) diglycine (PDG), with indium and aluminium. The structure of the Al:PDG material remains unknown due to a lack of single crystal data, and was found not to be isostructural to In:PDG (structure determined by SCXRD). The flexibility of the PDG linker inhibits the formation of a 3–dimensional framework, thus the final structure of In: PDG consists of 2–dimensional sheets. Both materials show no porosity towards CO_2, CH_4 and N_2, as seen with the flexible CSA materials detailed in chapter 5.

Chapter 7

A novel magnesium based MOF has been synthesised using a mucic acid (MA) linker, the structure was solved using SCXRD. The MOF possesses hydrophilic channels, which are inaccessible to N_2 at 77 K. The material, however, is shown to be porous to CO_2 with uptakes at 150 mbar of 0.38 and 1.90 mmol / g at 298 and 195 K, respectively. Furthermore this MOF undergoes a structural change to a Mg:MA chain when exposed to water overnight.

Contents

1.1 General Introduction....1
1.2 Organic Porous Materials....1
1.2.1 Activated Carbon....1
1.2.2 Covalent Organic Frameworks....2
1.3 Inorganic Porous Materials....3
1.3.1 Zeolites....3
1.4 Hybrid Porous Materials....4
1.4.1 Metal – organic Frameworks....4
1.5 Postsynthetic Modification (PSM)....7
1.6 Isoreticular Synthesis....8
1.7 MOFs with Flexible Linkers (FL–MOFs)....12
1.8 Applications of MOFs....16
1.8.1 Separations....16
1.8.1.1 CO_2 / CH_4....17
1.8.1.2 CO_2 / N_2 separations....19
1.8.1.3 Liquid Separations....21
1.8.1.4 Xylene Separations....21
1.8.2 Gas Storage....23
1.8.2.1 Hydrogen Storage....23
1.8.2.2 Methane Storage....25
1.8.2.3 Carbon Dioxide Storage....25
1.8.3 Catalysis....26
1.8.4 Sensing....27
1.8.5 Ammonia Uptake....29
1.9 Summary....31
1.10 Project Aims....32
1.11 References....33

Chapter 2 Synthetic and Experimental Techniques....38
2.1 General Overview....38
2.2 Solvo / Hydrothermal Synthesis....39
2.3 X-Ray Diffraction....40
2.3.1 Principles of a crystal structure....40
2.3.2 Principles of XRD....41
2.3.3 Single Crystal X-Ray Diffraction....42
2.3.4 Powder X-Ray Diffraction....43
2.3.5 Data Collection....44
2.4 Gas Sorption....44
2.4.1 Types of Adsorption....45

2.4.2 Adsorption Isotherms 45
2.4.3 Surface Area Calculations 47
2.4.4 Isosteric Heat of Adsorption 48
2.4.5 Sorption Measurements 49
2.5 Thermogravimetric Analysis 49
2.6 Elemental Microanalysis 50
2.7 Scanning Electron Microscopy 50
2.8 Gas Separation Experiments 51
2.9 Ammonia Breakthrough Experiments 53
2.10 Infra-Red Spectroscopy 54
2.11 Xylene Separation Experiments 54
2.12 References 56

Chapter 3 Al FDC MOF 57
3.1 Overview 57
3.1.1 FDC : A Renewable Linker 58
3.2 Synthesis 60
3.2.1 Exploring Synthetic Conditions 60
3.2.2 Optimised Synthesis for Al:FDC material 62
3.3 Characterisation 62
3.3.1 Structure 62
3.3.2 PXRD 67
3.3.3 TGA 69
3.3.4 Elemental Analysis 71
3.3.5 Surface Area Measurement 72
3.3.6 SEM 73
3.4 Heat of Adsorption of gases 74
3.4.1 CO_2 Adsorption Measurements 74
3.4.2 CH_4 Adsorption Measurements 77
3.5 High pressure gas sorption 80
3.5 Gas Separation Experiments 81
3.5.1 CO_2 / CH_4 Separation Experiments 82
3.5.2 CO_2 / N_2 separations 84
3.6 NH_3 breakthrough 86
3.6.1 Dry ammonia breakthrough 86
3.6.2 Humid ammonia breakthrough 89
3.7 Xylene separations 90
3.8 Conclusions 92
3.9 Future Work 93
3.10 References 93

Chapter 4 Indium: FDC 94
4.1 Overview 94
4.2 Synthesis 96
4.2.1 Synthesis of compound 1 97
4.2.2 Synthesis of compound 2 98
4.2.3 Synthesis of Compound 3 98
4.3 Characterisation of Compound 1 99
4.3.1 Structure 99
4.3.2 Structure of Activated Compound 1 102
4.3.3 PXRD 104
4.3.4 TGA 106
4.3.5 Elemental Analysis 107
4.4 Characterisation of compound 2 108
4.4.1 Structure 109
4.4.2 PXRD 113
4.5 Characterisation of compound 3 114
4.5.1 Structure 114
4.5.2 PXRD 120
4.5.3 TGA 122
4.5.4 Elemental Analysis 123
4.6 Conclusions 124
4.7 Future Work 125
4.8 References 126
Chapter 5 CSA Systems 128
5.1 Overview 128
5.2 CSA Systems 129
5.3 Synthesis 130
5.3.1 Optimised Synthesis of In:CSA 130
5.3.2 Optimised Synthesis of Al:CSA 131
5.3.3 Activation Procedure 132
5.3.4 Water Stability Tests 132
5.4 Characterisation of In:CSA 133
5.4.1 Structure 133
5.4.2 Structure of In: CSA post activation 138
5.4.3 PXRD 141
5.4.4 TGA 144
5.4.5 Elemental Analysis 145
5.4.6 SEM 146
5.4.7 Surface Area Measurement 147
5.5 CO_2 adsorption measurements 148
5.6 Water Stability 150
5.7 Characterisation of Al:CSA 151

5.7.2 TGA 153
5.7.3 Elemental Analysis 154
5.7.4 SEM 155
5.7.5 Surface Area Measurement 156
5.8 CO_2 Adsorption 156
5.9 Water Stability 159
5.10 On-going Exploratory Synthetic Work 160
5.10.1 Synthesis of Cu:CSA 160
5.10.2 Synthesis of Zn: CSA 161
5.10.3 Characterisation of Cu:CSA 162
5.10.4 Analysis of Zn:CSA 171
5.11 Conclusions 173
5.12 Future Work 174
5.13 References 175

Chapter 6 . PDG Systems 176
6.1 Synthesis 176
6.1.1 Synthesis of In: PDG 177
6.1.2 Synthesis of Al: PDG 177
6.1.3 Activation Procedure 178
6.1.4 Water Stability Tests 178
6.2 Characterisation of In:PDG 178
6.2.1 Structure 178
6.2.2 PXRD 182
6.2.3 TGA 183
6.2.4 Elemental Analysis 184
6.2.5 SEM 185
6.2.6 Surface Area Measurements 186
6.2.7 CO_2 Sorption Measurements 187
6.2.8 Water Stability 189
6.3 Characterisation of Al: PDG 190
6.3.1 PXRD 190
6.3.2 TGA 191
6.3.3 Elemental Analysis 192
6.3.4 SEM 193
6.3.5 BET 194
6.4 CO_2 Adsorption 195
6.5 Water Stability 197
6.6 Conclusions 198
6.7 Future Work 199
6.8 References 200

Chapter 7 Mg: Mucic Acid 201

7.1 Overview 201
7.2 Experimental 203
7.2.1 Synthesis of Mg: MA 203
7.3 Characterisation of Mg: MA 204
7.3.1 Structure 204
7.3.2 PXRD 210
7.3.3 TGA 213
7.3.4 Elemental Analysis 214
7.3.5 Surface Area Measurement 214
7.4 CO_2 Sorption Measurements 215
7.5 Water stability 217
7.6 Conclusions 218
7.7 Future Work 219
7.8 References 220
Chapter 8 Summary 221
Appendix I 223
Appendix II 225
Appendix III 237

Chapter 1 Introduction

1.1 General Introduction

Materials that contain pores (porous materials)[1] allow access to molecules and ions to the bulk of the material, not just the external surface.[2] Pores themselves can be defined as one of three distinct groups according to IUPAC;[3]

1) Micropores which are between 2 and 20 Å in diameter
2) Mesopores which are between 20 and 500 Å
3) Macropores are the largest with pore diameter of greater than 500 Å.

The presence of these pores mean that the materials can be used for a number of applications including, but not limited to, gas separation and storage, catalysis, ion exchange, drug delivery and as molecular sieves.

Defined by their general compositions, there are three types of porous materials; organic porous materials e.g. covalent organic frameworks (COFs), porous organic polymers and activated carbons, inorganic porous materials e.g. zeolites and hybrid porous materials e.g. metal organic frameworks (MOFs).

1.2 Organic Porous Materials

1.2.1 Activated Carbon

Produced from a number of natural sources with a high carbon concentration from wood and coal to coconut husk and nutshells, activated carbon is an amorphous material with generally high surface areas with measured values of up to 3,000 m^2 / g.[4] The production of said materials is done via one of two methods: chemical or thermal activation.

Chemical activation involves impregnating the raw material with chemicals such as $ZnCl_2$ and phosphoric acid. This then reduces the temperature required for the carbonisation (thermal activation) step from 600 – 1200 ^{o} C to 450 – 900 ^{o}C. [5]

The pore size and surface chemistry are dependent on the raw material, the activation procedure and can be modified to a degree by incorporating metal salts and amines into the final material. Hence there are several types of activated carbon that have a wide variety of applications in gas storage and separation, water purification and toxic gas uptake.[6]

1.2.2 Covalent Organic Frameworks

First discovered in 2005 with condensation reactions between phenyldiboronic acid and hexahydroxyphenylene,[7] COFs are normally synthesised relying on reversible covalent bonds, resulting in highly crystalline materials with mild to low stability. Rigid monomers can polymerise into either porous organic cages[8] or extended COFs.[7] The first COFs reported, COF–1 and COF–5, are made of 2–dimensional sheets which, through π–π stacking, form 3–dimensional structures with surface areas of 711 m^2 / g and 1590 m^2 / g respectively.[7] COFs are the most recently discovered crystalline porous material and adopt distinct 2D or 3D structures and their pore size is determined by the length of monomers used[9] with reported pore widths of 9 to 42 Å.[7, 10] The synthesis of fully covalent 3–dimensional structures is somewhat more difficult giving the far fewer reports of such structures. In 2007, COF–102, 103 and 105 and 108, fully covalent 3–dimensional frameworks were reported with surface areas of 3472, 4210 m^2 / g for COF-102 and 103 respectively.[11] BET surface areas of COF–105 and 108 were not reported. COF–102 has been evaluated for its ability to adsorb various gases, H_2, CH_4 and CO_2, and due to its large surface

area, it exhibited capacities of 72.4 mg / g, 187 mg / g and 1200 mg / g, respectively.[12]

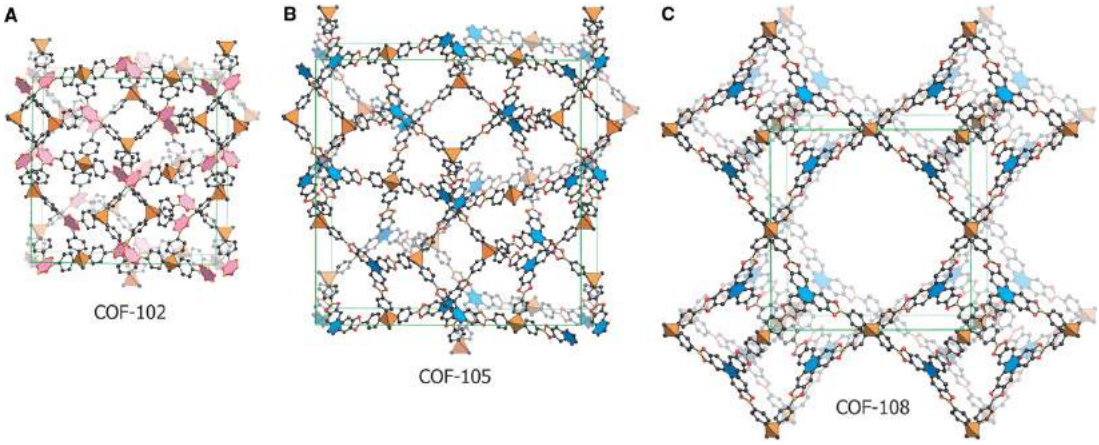

Figure 1.1. Structures of COF–102, COF–105 and COF–108 (COF–103 has an identical structure to COF–102). Hydrogen atoms are omitted for clarity. Carbon, boron, and oxygen atoms are represented as grey, orange, and red spheres, respectively. Figure from reference.[11]

1.3 Inorganic Porous Materials

1.3.1 Zeolites

Zeolites were the first porous materials to be discovered, named due to the observation of large amounts of steam given off under rapid heating of the stone (believed to be stillbite). The word zeolite itself comes from the Greek words for "to boil" and "stone".[13]

Zeolites are porous, crystalline aluminosilicates with the general formula $M_{x/y}^{n+}[(AlO_2)_x(SiO_2)_y]^{x-}$, M^{n+} is the exchangeable cation, which is counterbalanced by the remaining anionic framework.[14] They differ from each other by the ratio of alumina and silica groups, as well as the type of counter cation. The number of variables within these structures gives rise to their assorted properties and applications.[15, 16]

Although the first zeolite discovered was natural (and many of them are found in nature), synthetic zeolites were developed and synthesised on an industrial scale by Barrer in the 1930's and 40's.[15, 16] Since then, zeolites have been commercialized and used in various industrial applications such as water purification, heating and refrigeration and gas separation.[17-19]

1.4 Hybrid Porous Materials

1.4.1 Metal – organic Frameworks

Constructed from metal or metal – oxo clusters, bridged together via organic components, giving rise to the inorganic building unit (IBU) or secondary building unit (SBU), some examples of these are shown in Figure 1.2. These IBUs are then bridged to each other in various ways to form the final framework. Metal organic frameworks (MOFs) are highly crystalline materials and can be 2 or 3–dimensional frameworks. Although MOFs are generally associated with high porosity and pore volumes, not all reported materials and structures have this attribute, with some reporting immeasurable porosity.[20] The massive amount of possible organic linkers, metals and structural topologies give rise to a huge number of combinations, resulting in over 20,000 reported MOFs. The geometry of the IBU dictates the final overall topology of the framework. Since this component is dependent on so many different variables in the synthesis, from time and temperature of the reaction, to metal source and solvent mixture, it is almost impossible to predict the structure of the final material.[21] The study of metal organic frameworks and the number of reported materials has significantly increased recently, which improves our understanding of the formation and assembly of these complex structures.

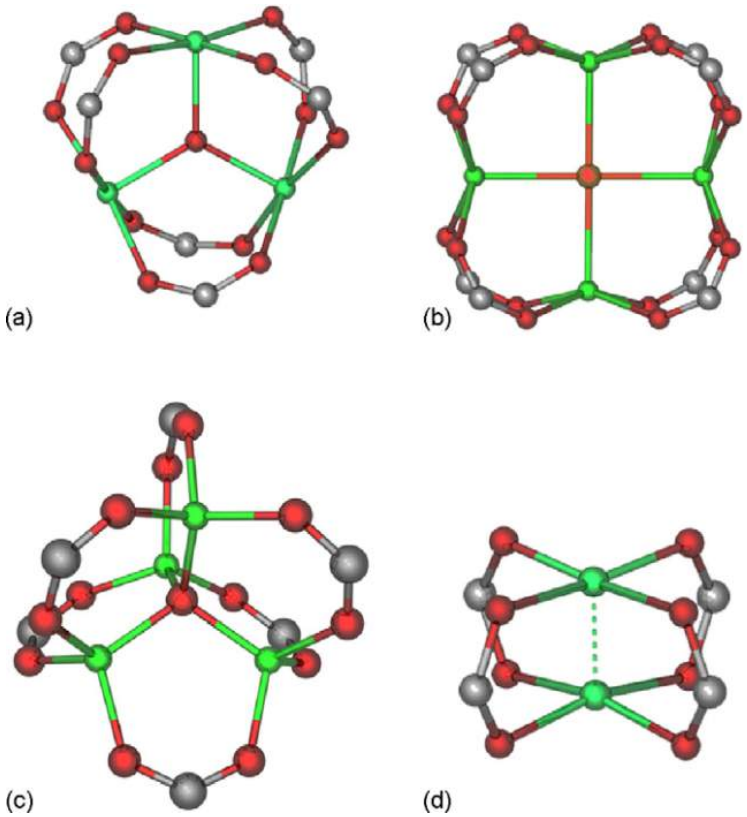

Figure 1.2 Examples of non–specific common MOF IBUs; Trigonal Planar (a), square planar (b), tetrahedral (c) and paddlewheel (d). Metal, carbon and oxygen atoms are represented by green, grey and red spheres respectively. Figure from reference.[21]

Research by the groups of Kitagawa and Yaghi resulted in the first reported permanently porous MOFs in the late 1990's.[14, 22] In 1997, MOFs with several divalent metals (Co, Zn and Ni) were synthesised using 4,4'–bipyridine as the organic linker. Although these materials had permanent porosity, shown by reversible isotherms, the voids were small due to the interpenetrated nature of the framework. Interpenetration is the phenomenon whereby the void space within the MOF is filled by another framework. MOF–2 was made in 1998, by the Yaghi group, from zinc nitrate tetrahydrate and BDC, with an inorganic building unit (IBU) of a zinc paddlewheel $[Zn_2(O_2CR)_4(H_2O)_2]$ with water bound on the axial positions.

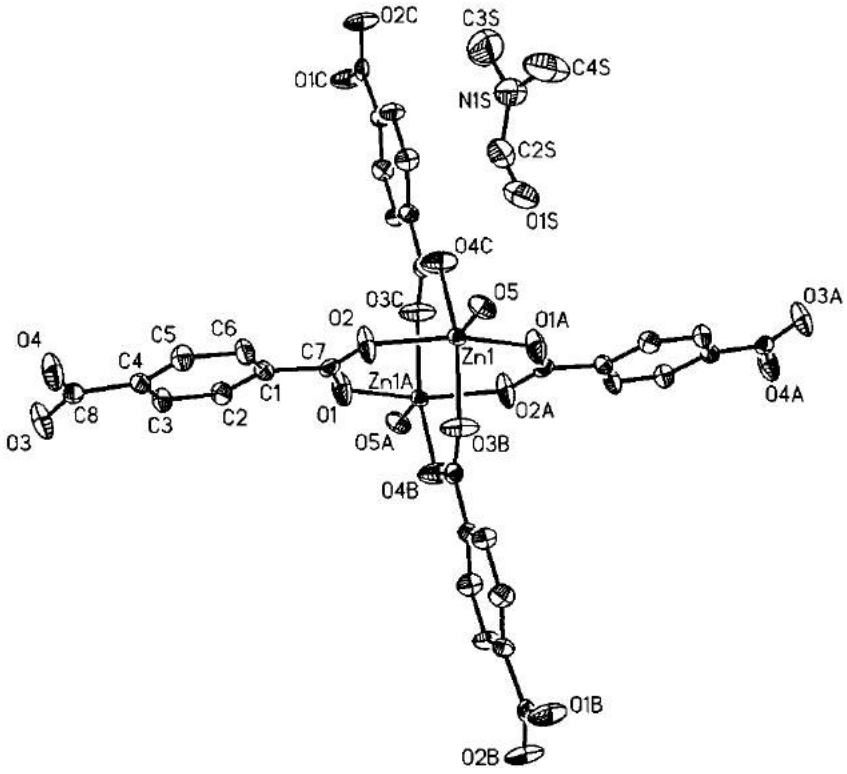

Figure 1.3. Crystal structure of MOF–2. Figure from reference[22].

The overall structure consisted of 2–dimensional sheets held together by hydrogen bonds formed between axially co – ordinated waters and carboxylate oxygens. The material retained its crystal structure after activation at 140 ^{o}C for 16 hours under vacuum of 5 x 10^{-5} Torr. The porosity was measured and the material displayed reversible N_2 and CO_2 isotherms.[22] This was the pioneering material that caused huge surge in the research into MOFs, allowing for the discovery of many different IBUs.[23, 24]

The organic component of a MOF (linker) must have at least two co – ordinating groups, the most common being carboxylic acid groups. There have, however, been many materials reported whereby other co – ordination groups are used e.g. peptides (ZnCar).

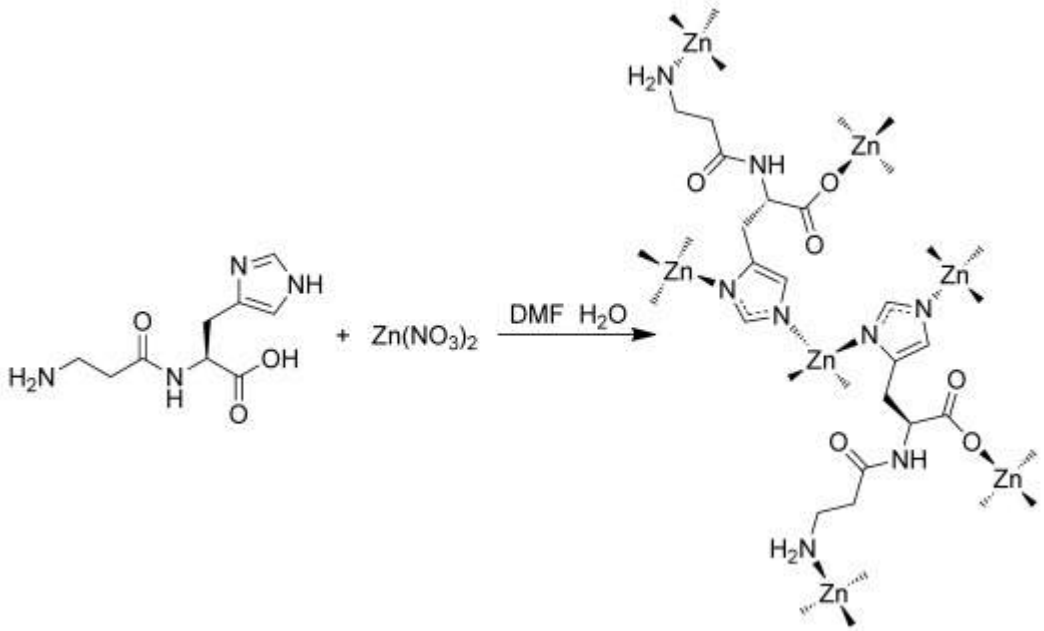

Figure 1.4. Formation pathway of ZnCar·DMF. Figure from reference.[25]

1.5 Postsynthetic Modification (PSM)

The ability to tune a MOF's pore chemistry and selectivity stems from the ability to modify and functionalise the linker to enhance their performance in a particular application. Linker molecules can be functionalised by one of several routes; post synthetic modification (PSM), which includes linker exchange, or isoreticular synthesis. This concept means that MOFs can be adapted and modified, giving them potential for use in a wide variety of applications; gas separation and storage, catalysis, biomedical applications.[26-30]

PSM is a process whereby the surface chemistry of the MOF is altered and usually involves one of two possible routes. The first route is when some or all of the linkers are exchanged for functionalised or longer analogues e.g. NH_2 – BDC (benzene dicarboxylate) for BDC or BPDC (Biphenyl dicarboxylate) for BDC. The second route involves functionalising the linker molecule itself, once the framework has been formed. This method is highly

useful when trying to incorporate highly acidic or basic groups into the framework.[7, 31-33]

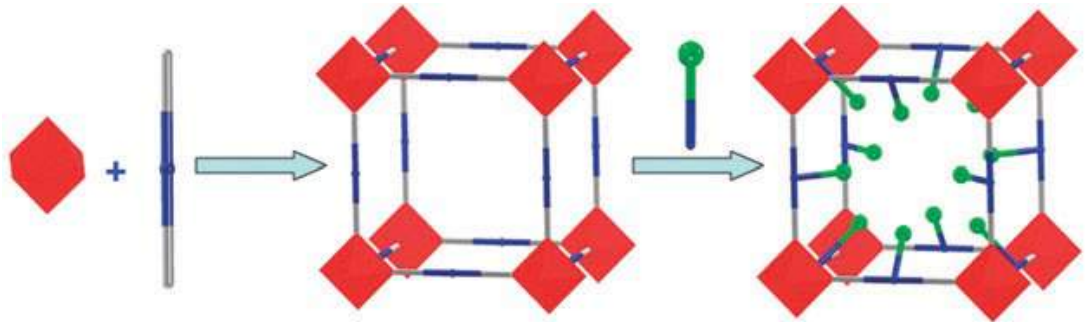

Figure 1.5. General schematic demonstrating the idea of PSM. Figure from reference.[34]

Once a linker's functionality is adjusted, this requires a change in reaction conditions and sometimes a MOF cannot be synthesised, this is when PSM would be employed.

1.6 Isoreticular Synthesis

The ability to replace one of the components in the synthesis with a similar component, causing the synthesis of a similar MOF is known as isoreticular synthesis.[35] This allows for the discovery of MOFs with the same overall structure, but with larger pores or pores that have potential for a specific application due to the new functionality. The most known examples of these are IRMOF series, developed by the Yaghi group, from the parent material MOF–5 (IRMOF–1).[35] MOF–5 was first reported in 1999 and is made of Zn_4O clusters which are bridged by BDC linkers, giving rise to a cubic structure and is known for its large capacity for hydrogen adsorption,[36, 37] and thermal stability.[38] Regardless of these desirable properties, the material has also been shown to be very unstable in water and is shown to decompose quickly even in humid air.[39] Since many real world applications for MOFs rely heavily on

the chemical and thermal stability of the materials, these are two very important features of interest to researchers. The large porosity and pore sizes, however, come with their problems since most of these materials rely on the trapped solvent molecules to retain their crystalline structure, once these are removed during the activation process, the structure collapses.

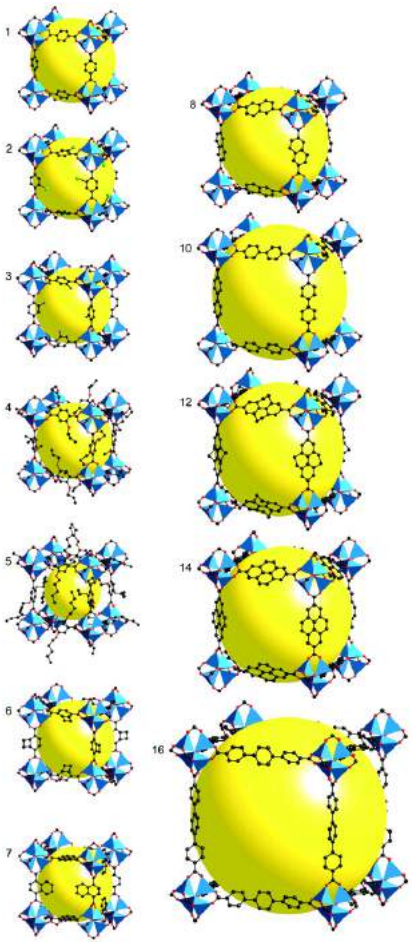

Figure 1.6. Structures of IRMOF–n, value of n labeled respectively. Zn (blue polyhedra), O (red spheres), C (black spheres), Br (green spheres), amino-groups (blue spheres). The large yellow spheres represent the largest van der Waals spheres that would fit in the cavities without touching the frameworks. All hydrogen atoms have been omitted. Figure from reference.[35]

UiO–66 are another family of materials known for their high chemical and thermal stability, as well as their isoreticular series. Based on $Zr_6O_4(OH)_4$

cluster IBUs (Figure 1.7) which are bridged to adjacent IBUs up to twelve times via BDC linkers.

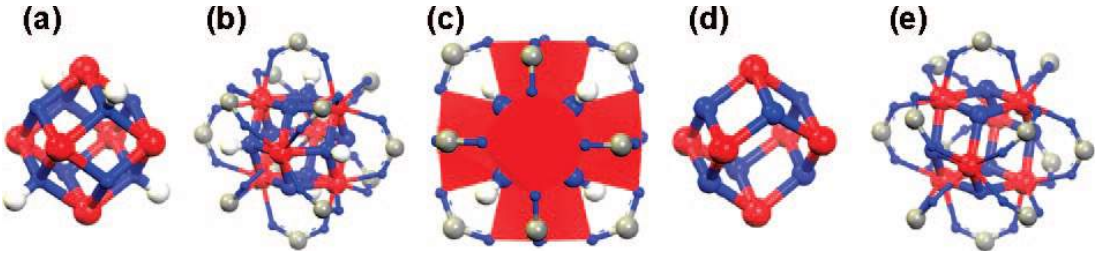

Figure 1.7. Structure of a hydroxylated cluster (a), a complete cluster (b), a complete cluster with ZrO octahedra (c), a dehydroxylated cluster (d) and a dehydrated cluster (e). Figure from reference.[40]

When the linker is replaced with its bi – and tri – phenyl equivalent, UiO–67 and UiO–68 are synthesised respectively,[40] giving rise to an isoreticular series of MOFs (Figure 1.8) as seen with MOF–5.

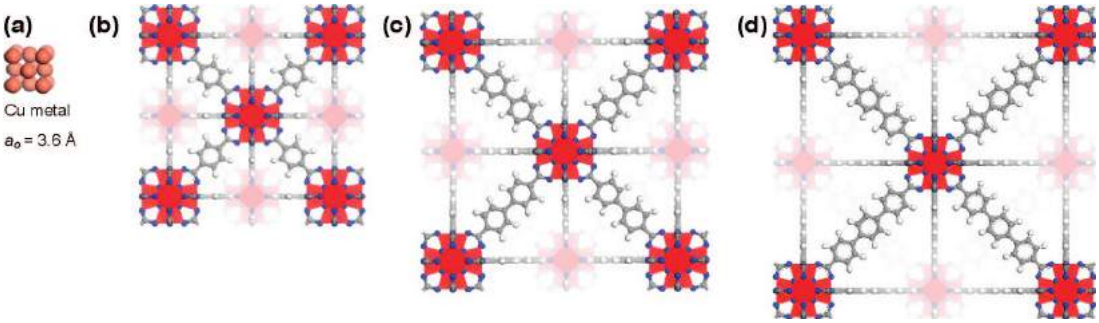

Figure 1.8. A series of isoreticular zirconium MOFs (b); UiO–66, (c) UiO–67 and (d) UiO–68, compared to the size of metallic copper (a). Zirconium (red polyhedra), oxygen (blue spheres), carbon (grey spheres), hydrogen (white spheres).[40]

The remarkably high chemical and thermal stability of this family of materials stems from the ability of the Zr_6 clusters to undergo a reversible rearrangement upon dehydroxylation or rehydration. As well, the strong Zr–O bonds provide these materials with superior stability to other MOFs, as

proven by UiO–66 being thermally stable up to 500 ^{o}C.[40, 41] As well as increasing the length of the linker, a wide variety of linkers with different functionalities (e.g. NH_2 –, OH – BDC) have been used which give rise to numerous different materials with a range of pore sizes and functionalities.[42]

A family of MOFs that exhibit high chemical and thermal stability were discovered and first reported by the research group of Ferey, the MIL–53 family.[43] MIL–53 is made up of infinite chains of $M(OH)_2(–COO)_4$ octahedra where M is a trivalent metal ion Fe^{3+}, Al^{3+}, Ga^{3+}, In^{3+}, Cr^{3+} or Sc^{3+} bridged together via BDC linkers.

MIL-53(Al) and MIL-53(Cr) exhibit particularly high chemical and thermal stability and the family is well known for their "breathing" behaviour upon the removal and uptake of guests, this phenomenon is shown in figure 1.9.[44, 45] This phenomenon is responsible for a change in cell volume of up to 40 % in the case of MIL–53(Al).[46]

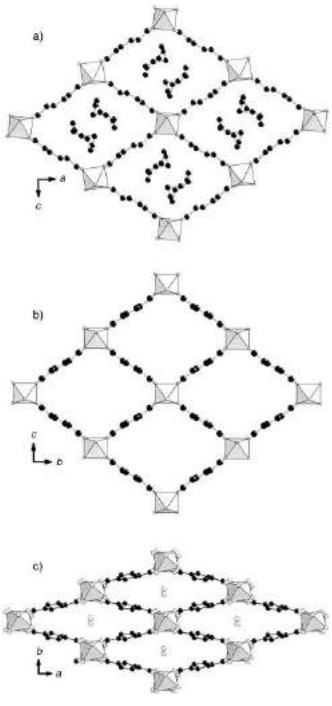

Figure 1.9. Channel structure of a) MIL–53(as-made) whereby the channels are occupied by BDC molecules, b) MIL–53(activated) with empty channels and c) MIL–53 whereby a water molecule is located in the channels. $Al(OH)_2O_4$ octahedra (grey octahedra), carbon (black) and oxygen (grey). Figure from reference.[47]

By replacing the Al(OH) IBU in MIL–53 with Cr_3O triangles, this gives rise to a new MIL–type MOF: MIL–101. This new IBU consists of corner or edge sharing $[Cr_3O(H_2O)_2(OH)]$ supertetrahedra that form the final structure with extremely large pores of 25 – 34 Å.[48, 49] As well as chromium, MIL–101 has been synthesised with Al and Fe. If the organic linker of this material is then replaced with trimesic acid, this gives rise to MIL–100, which has also been synthesised with Fe, Sc, Al, Mn and V.[50-52] These materials again show high thermal and chemical stability and have been tested for their application in gas storage and catalysis. [48, 49, 53]

1.7 MOFs with Flexible Linkers (FL–MOFs)

A flexible linker, here, is defined as one that has at least one sp^3 hybridised atom in their backbone. It should also be noted that there is a clear difference between flexible MOFs and FL – MOFs, being that the former responds to external stimuli such as seen in MIL–53. The latter contains a component that has some flexibility. Chiral MOFs can be quite useful for applications in enantioselective separation and asymmetric catalysis. In order to produce a chiral MOF, a chiral organic linker must be used, many of which are flexible; amino acids, peptides and sugar derivatives. It is for this reason that FL – MOFs have attracted a lot of attention recently.

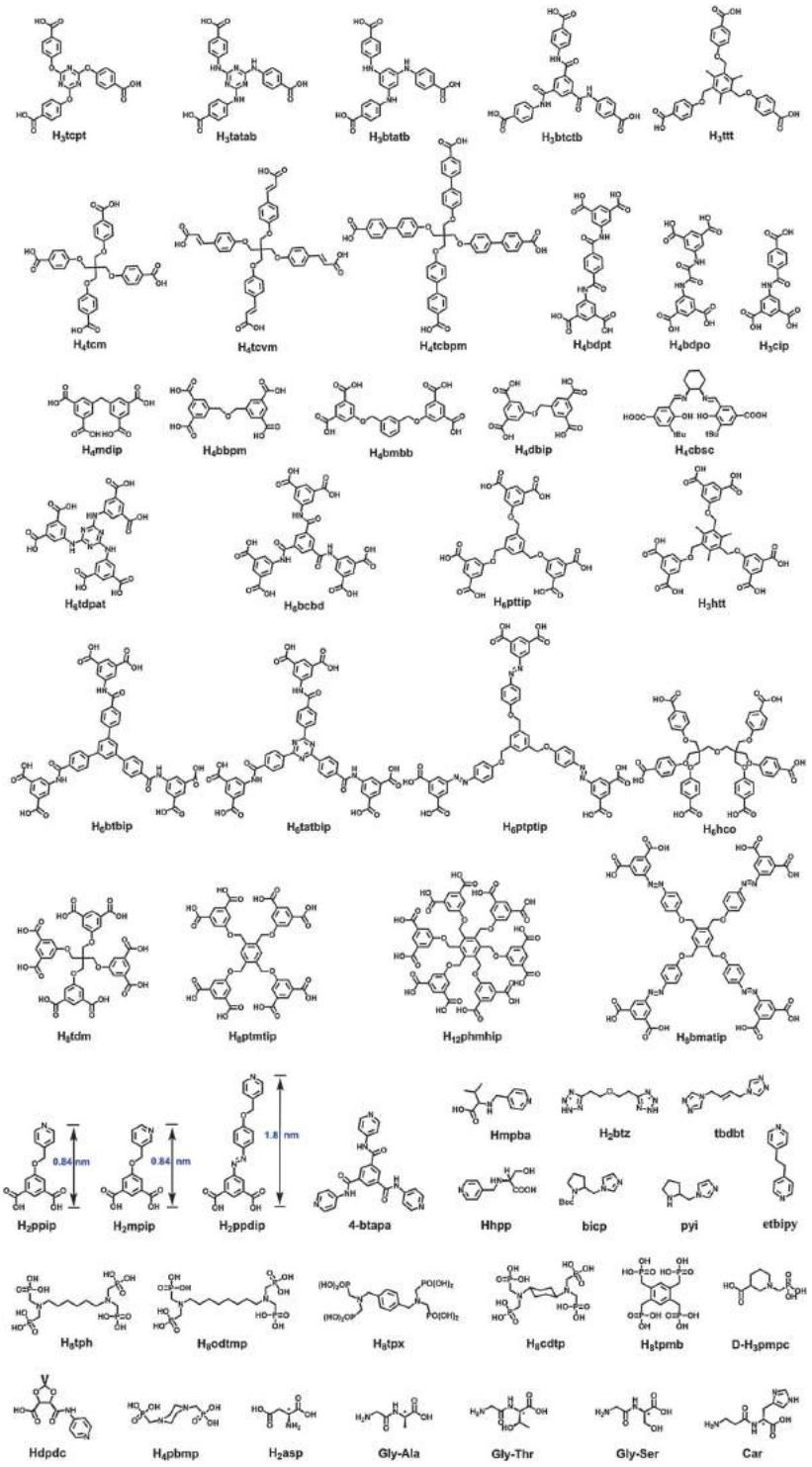

Figure 1.9. A selection of flexible linkers used in the synthesis of FL – MOFs. Figure from reference.[54]

In 2000, the first homochiral MOF capable of enantiomerically catalysing a chemical reaction was reported (POST–1). This zinc based MOF, in the

presence of a large excess of 1–phenyl–2–propanol with either enantiomer of the MOF, produces the corresponding ester.[55]

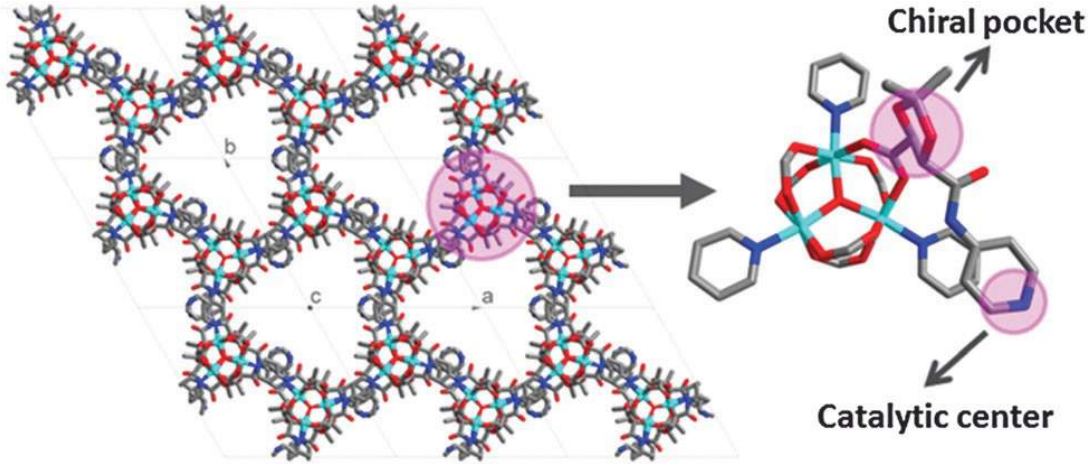

Figure 1.10. Triangular shaped chiral channels of POST–1 along the *c* – axis (left) and the IBU and co – ordination environment of POST–1 (right). Zinc, carbon, nitrogen and oxygen in turquoise, grey, blue and red, respectively. Figure from reference.[54]

In 2010, an adaptable peptide based MOF was reported with the ability to self-block the pores in the presence of no guests, and upon introduction of small, polar bond – containing molecules, gradually open. This MOF uses a dipeptide linker Gly–Ala (glycylalanine), shown in Figure 1.11 and is a fine example of how different co – ordination groups can be used in the formation of such materials.[56]

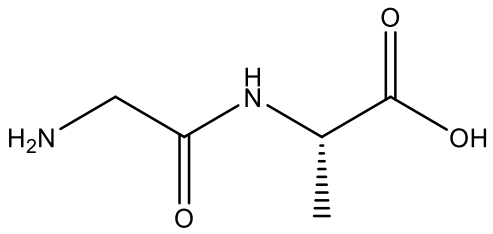

Figure 1.11. Glycylalanine.

Sugar – derived linkers (aldaric acids) have also been used in the synthesis of MOFs and complexes due their bioavailability. In 2003, saccharic acid (Figure 1.12) was used with zinc to make a chiral MOF with two types of parallel channels; one hydrophobic and one hydrophilic.[48]

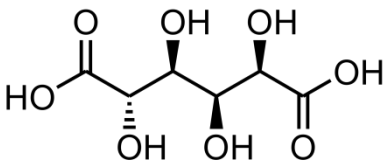

Figure 1.12. Saccharic acid

The chirality of the linker gives rise to the chessboard arrangement of hydrophobic and hydrophilic chains as shown in Figure 1.13.

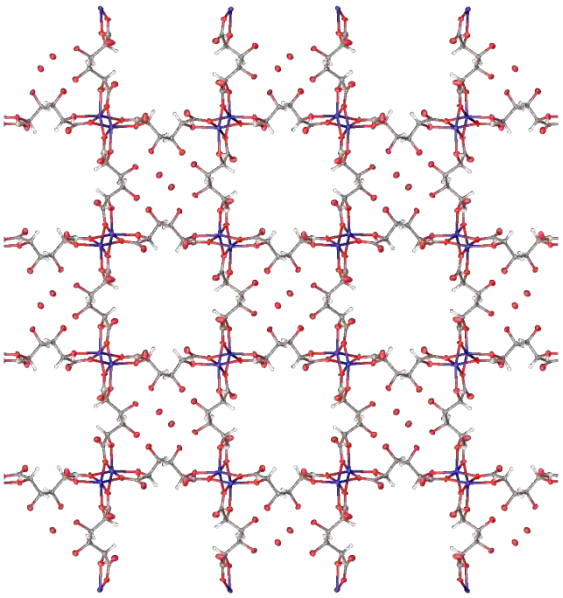

Figure 1.13. View of Zn(sac) showing the two different channels. Zinc, carbon, and oxygen are shown in blue, grey and red, respectively. Figure adapted from reference.[57]

This material showed the ability to incorporate I_2 into the hydrophobic channels while still retaining the water molecules in the hydrophilic ones. This provided the possibility of a MOF taking up two different species simultaneously.

The research into MOFs with flexible and chiral linkers emphasises how structurally diverse MOFs can be and demonstrates their capability to be used in a wide variety of applications. Research into FL–MOFs is ongoing because, as of yet, the successful design and structure prediction of such a MOF is almost impossible. Further research is necessary in order to fully understand the structural features and the relationship between the structure and the property. This will progress the field towards establishing a reliable strategy for the successful design and synthesis of a target FL–MOF.

1.8 Applications of MOFs

1.8.1 Separations

The separation of gaseous and liquid mixtures is an essential industrial process used to purify starting reagents and products. As well as separating gases such as CO_2 / CH_4 and CO_2 / N_2, separating isomers in racemic or random mixtures of xylenes for example is also highly important.

Distillation is probably the most commonly used method of separation but does have its drawbacks when separating mixtures of similar boiling point compounds, or those that are unstable at high temperatures.

Porous materials have been used to separate such mixtures, by passing the mixture through a column which is packed with the material. In order for the material to be successful for this application, it should have a higher affinity towards one of the components within the mixture according to its pore size and surface chemistry. This allows the material to separate a mixture based on steric, equilibrium or kinetic effects. MOFs are emerging in this area due to the ability to tune the pore size and surface chemistry to selectively adsorb compound X over Y allowing for complete separation.[58]

Zeolites tend to be used to separate mixtures based on steric effects, whereby the smaller molecules within the mixture can pass through the material, while the larger are trapped in the pores. This is the primary application of zeolites, however, when it comes to separating mixtures of small, yet similarly sized molecules, a small pore size distribution is required. MOFs can provide this and therefore have potential in the separation of mixtures such as N_2 and CO_2 and CH_4 and CO_2.

Other factors can cause a molecule to become trapped while the other(s) in the mixture pass through, if the pore walls have specific functionality, some molecules will interact via intermolecular interactions. This is known as the thermodynamic equilibrium effect. Incorporating basic sites into the MOF can increase the framework's affinity towards CO_2 over CH_4 thus allowing for great separation, as is evidenced by NH_2 – MIL-53.[59]

Other MOFs have been synthesized with two different pore environments, one small, and one large. This gives rise to separating a mixture of branched and non-branched isomers, whereby the branched isomers cannot pass through the smaller channels, but the non-branched can pass through both. An example of this is the separation of hexane isomers (hexane, 3–methylpentane and 2,2–dimethylbutane) using a mixed linker zinc based MOF.[60]

1.8.1.1 CO_2 / CH_4

CO_2 is the main, undesirable compound present in natural gas (CH_4), therefore separating a mixture of the two gases is very important due to the need for pure CH_4 for use in many industrial and domestic applications.

MOFs have been reported to have excellent capability of separating mixtures of CO_2 over CH_4 for the purification of natural gas. CO_2, unlike CH_4 has a quadrupole moment, which can be taken advantage of by introducing

complimentary functional groups into the pores. These functional groups attract the polar CO_2 molecule, and through strong host – guest interactions, it becomes trapped in the material, while CH_4 passes through.

An example of this modification was reported in 2009 where MIL–53(Al) was functionalised with an amino group.[59] Non–functionalised MIL–53(Al) shows an adsorption capacity of 40 % wt for CO_2, with the adsorbate forming strong interactions with the corner – sharing hydroxyl groups of the framework. This initial adsorption causes a contraction of the pores, which upon adsorption at higher pressures are reopened allowing for further adsorption. NH_2–MIL–53(Al) shows that upon breakthrough experiments using an equimolar CO_2/CH_4 mixture, CH_4 elutes very rapidly while CO_2 is retained for a longer time. The amino groups provided an extra source of interaction for the CO_2 molecules, increasing the zero – coverage adsorption enthalpy from 20.1 kJ / mol to 38.4 kJ / mol.

Research into the UiO family of MOFs for this application showed that the addition of polar functional groups onto the linker has a greater impact on the performance over pore size. This was evidenced by evaluating UiO–66 and UiO–67 which are the phenyl and biphenyl analogues of each other, respectively. The result showed that the interaction between the CO_2 molecule and the framework is a lot weaker for that of UiO–67 than UiO–66. Functionalising the linker with a thiophene group and a fluorenone group (Figure 1.14) had a huge impact on the strength of the guest–host interactions, increasing the isosteric heat of adsorption from 15.8 kJ / mol to 21.8 kJ / mol and 25.9 kJ / mol for the thiophenic functionalised and fluorenone functionalised materials respectively.[61]

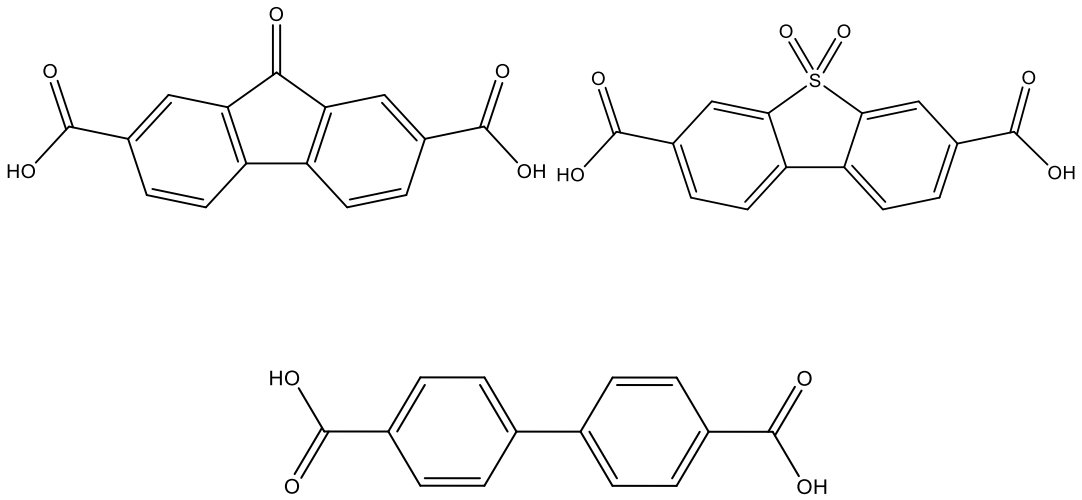

Figure 1.14. Functionalised linkers used for CO_2 separation experiments. (a) 9–fluorenone–2,7–dicarboxylic acid (BUT–10) (b) dibenzo[b,d]– thiophene–3,7–dicarboxylic acid 5,5–dioxide and (BUT–11) (c) 4,4′ – biphenyldicarboxylic acid (UiO–67).

The selectivity of CO_2 over CH_4 and N_2 were measured for all 3 of these materials and the results are shown in Table 1.1.

MOF	Separation factor$_{CO_2/CH_4}$	Separation factor$_{CO_2/N_2}$
BUT–10	5.1	18.6
BUT–11	9.0	31.5
UiO–67	2.7	9.4

Table 1.1. Measured selectivities for various UiO – based MOFs. Figure adapted from reference.[61]

1.8.1.2 CO_2 / N_2 separations

The removal of CO_2 from flue gases in power plants is of particular importance for the reduction of greenhouse gas emissions. Flue gases have a general composition of 1 : 1 : 6.5 O_2 : CO_2 : N_2 and so the removal of CO_2 from such mixtures is necessary to reduce the amount of greenhouse gas

emissions.[62, 63] As seen with CH_4, N_2 also has no potential for interaction with a framework in the same way that CO_2 has.

In 2008, the first example of a microporous MOF used in the separation of CO_2 from binary mixtures of CO_2 / N_2 and CO_2 / CH_4 was reported.[64] This zinc based, mixed linker MOF (MOF-508b) has pores of 4.0 Å x 4.0 Å, making them just large enough to accommodate all gas molecules of interest (kinetic diameters of 3.30 Å, 3.64 Å and 3.80 Å for CO_2, N_2 and CH_4 respectively.[64, 65] The selectivity of CO_2 over N_2 was calculated to be 3, providing the first evidence that MOFs have the potential to be used in such applications. More recently, a MOF was shown to exhibit an extraordinary selectivity of CO_2 over N_2; Ni–MOF–74, with a selectivity of 38.[66] This MOF makes use of vacant metal sites, combined with its large surface area (1200 m^2 / g) and hydroxy functionalised linkers to enhance its performance in this application.

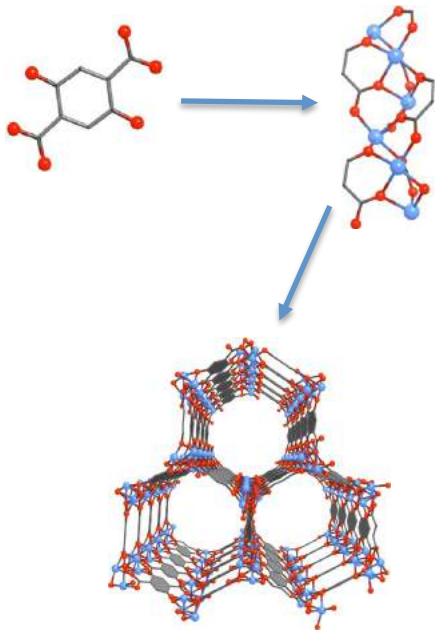

Figure 1.15. General schematic for the synthesis of M-MOF-74 (M = Co, Mg, Ni, Zn). Synthesis from 2,5-dioxidoterephthalate (DOT). Carbon, oxygen and metal represented by grey, red and blue respectively. Figure adapted from reference.[67]

The general consensus from research in this field is that the functionality within the framework plays a larger role than pores size, in the successful separation of binary gaseous mixtures.

1.8.1.3 Liquid Separations

Liquid separations rely on similar mechanisms to gas separations, size / shape exclusion as well as guest – host interactions. A fine example of this comes from the study of a zinc based MOF.[68] This MOF is made of 2-dimensional sheets with hydrogen bonding sites between the layers. The presence of such sites allows the material to adsorb protic solvents (H_2O, ethanol and methanol). It also has no ability to adsorb smaller gas molecules such as H_2, N_2 or MeCN. This work provided evidence that size exclusion as well as guest – host interactions play a role in the selective adsorption of liquids.

1.8.1.4 Xylene Separations

The separation of xylene mixtures is important due to xylenes themselves playing important roles in many industrial chemical syntheses. Since xylenes exist commercially in random mixtures of all three isomers, *ortho* – (oX), *para* – (pX) and *meta* – (mX) xylene) they need to be isolated as purely as possible to be used for their specific applications. oX can be oxidised to phthalic anhydride which is used in the synthesis of polyvinyl chloride, while mX can be used in the production of isophthalic acid. pX can be oxidised to terephthalic acid, which is the precursor for the synthesis of polyethylene terephthalate,[69] commonly known as polyester, and a number of MOFs mentioned in this thesis. This makes pX the most useful and therefore the most desirable isomer of xylene.

Research into selective separation of xylene isomers using chromatographic separation is being carried out. Separating pX and mX however is the most crucial step and is also the most expensive.

There are two main ways of separating xylene isomers due to them existing in the liquid phase. Vapourising them and separating the resultant vapours, achieved by gas chromatography (GC), or separation in liquid phase, achieved by liquid chromatography (HPLC).

MIL-101 has been reported to successfully separate three xylene isomers using GC with baseline resolution within two minutes. pX eluted first, followed by mX, then EB (ethylbenzene) and finally, oX.[70] Due to all xylene isomers having boiling points of around 140 ^{o}C,[71] separating them in the gas phase can be expensive and time consuming for industry, therefore, liquid phase xylene separations has been of great interest to researchers.

Zeolite Y has been shown to separate xylene isomers with a separation factor of 4.0, meaning that the material selectively adsorbs four times more pX than mX from the mixture.[72] The vast majority of MOFs tested for this application have been based on trivalent metals, this is due to their high chemical stability.

In 2008, MIL-53(Al) successfully separated oX, showing that the framework had a higher affinity towards oX than pX, mX and EB, with oX eluting last.[73] The material, however, could not successfully separate other isomers from the mixtures but showed some promise and provided evidence that MOFs have potential for this industrial application.

In 2011, MIL-101(Cr) separated mixtures of these three isomers, this material showed the same trend as seen in MIL-53, with oX eluting last. Baseline separation was achieved between pX and mX, with pX eluting first, with separation between mX and pX decreasing as temperature increases. This selectivity was a result of host – guest interactions, pore – filling effects and polarity of the framework.[70]

An example of a material which separated four aromatic C8 isomers via shape exclusion in the gas phase is MIL–47, whereby pX and mX eluted first, followed by EB then oX.[74] The linear pX molecule has the ability to pass through channel of the MOF causing immediate elution, mX, which has some steric hindrance relative to pX also elutes rapidly due to its ability to orient itself to reduce these steric effects. EB has even more steric hindrance, however, the molecule can align the ethyl group to allow for slower elution than seen for mX and pX, with the largest isomer oX eluting last.[74]

More recently, MIL–53(Fe) was tested as a stationary phase for reverse phase HPLC separation of xylene isomers.[75] The material displayed a wide range of retention mechanisms from guest–host interactions including hydrogen bonding and π–π stacking, to size exclusion, allowing for successful separation of all three xylene isomers along with other aromatic positional isomers.

1.8.2 Gas Storage

Storage of gases such as hydrogen, and methane, are incredibly important as they have important uses in industry, as well as greenhouse gases such carbon dioxide. Research into MOFs for the storage of different gases has proved that, via guest – host and even guest – guest interactions, these materials have great potential in this area. Introducing functionality into the framework through vacant metal sites or functional organic linkers can also enhance the performance of MOFs.

1.8.2.1 Hydrogen Storage

Hydrogen has been identified as an environmentally friendly and renewable alternative to hydrocarbons as a fuel source, with a very high energy density by weight.[76] In order to transport hydrogen in sufficient quantities to be of

any use, it must first be liquefied which is a very expensive process, as the volumetric density under ambient conditions is very low. Porous materials have the potential to overcome this issue[77] with the ability to reversibly adsorb hydrogen onto their surface, storing it in in a density similar to that of liquid hydrogen. As well as these features, other key attributes that the material must have in order to be a suitable candidate for this application include low cost and stable enough to be recycled. The U.S. Department of Energy (DOE) introduced a target hydrogen storage of 1.8 kg / kg (5.5 wt%) at 40–60 ^{o}C by 2020.

Studies into MOFs for this application lead to the discovery that host – guest interactions play a more important role in the storage of hydrogen over pore size. An example was given using the NOTT family of MOFs whereby the length of the linker was extended such that the surface area was increased by 1300 m^2 / g yet the uptake of hydrogen decreased.[78] This indicated that the pore size has to be large enough to accommodate the guest, but small enough to encourage the hydrogen to interact with the pore wall in order to obtain significant uptake capacities. Another attribute which enhanced a material's ability to adsorb hydrogen is the incorporation of vacant metal sites, which provide a site of interaction between the host and the guest, an example of this comes from Mg–MOF–74.[79-81]

As mentioned earlier, MOF–5, along with other zinc based MOFs IRMOF–6 and 8 were studied for their hydrogen storage.[36] MOF–5, remains one of the best known materials for hydrogen storage with an uptake of 10.0 wt% at 77 K and 100 bar, despite the vast number of materials tested since.[76, 82, 83] Some of the tested materials at 77 K (MOF–200 and NU–100) out-performed MOF–5 by adsorbing 14.0 wt% and 14.09% at 80 bar and 70 bar respectively.[84 85]

1.8.2.2 Methane Storage

Methane is the primary component in natural gas and due to it being typically stored under pressures of 207 bar, which requires multi – stage compression is very costly.[76] Therefore, being able to adsorb the gas onto porous materials at lower pressures is highly desirable.[86] The correlation between functionality and methane uptake remains unclear and requires further study.[87]

PCN–14 demonstrated that smaller pores are often important for methane uptake, exhibiting an uptake of 15 wt% at 298 K and 35 bar. MOFs with vacant metal sites such as MOF–74 have been found to have remarkable methane capacities with Ni–MOF–74 reaching 13.7 wt% under the same conditions.

1.8.2.3 Carbon Dioxide Storage

Carbon dioxide emissions are responsible for approximately 60 % of global warming effects, making the removal of such gas from the flue gases of power plants highly important.[88] CO_2 is at relatively low partial pressure (0.15 bar) in these streams, which means that the sorbent of choice must have a high affinity and selectivity towards carbon dioxide at this low pressure.[89]

One of the highest uptakes of CO_2 at 0.15 bar is that of Mg–MOF–74, which not only has an uptake capacity of 20.6 wt%, but also exhibits high selectivity over methane and nitrogen.[88, 90] MIL–100(Cr) displays one of the highest reported heats of adsorption for carbon dioxide of 62 kJ / mol meaning that the host-guest interactions are of the strongest reported for all MOFs. The highest reported uptake capacity of carbon dioxide on a MOF is that seen for MOF–200 and MOF–210, the latter of which has the highest reported BET surface area of 6240 m^2 / g. Both of these materials adsorb 73.9 wt% CO_2 at 298 K and a higher pressure of 50 bar.[84, 91, 92]

1.8.3 Catalysis

MOFs have the ability to contain a variety of different catalytically active sites within their structure, from vacant metal sites to the incorporation of organic functional sites. Alongside these, impregnating the pores of the MOF with catalysts or nanoparticles, can also provide MOFs with the platform to perform well as heterogeneous catalysts.[93] These key factors, coupled with large internal pore volumes and surface areas make for promising materials in this application.

A manganese based MOF with open metal sites was evaluated for its application in catalysing the cyanosilylation reactions of carbonyl organic substrates. The cyanosilylation of aldehydes is now the typical reaction used to evaluate the Lewis acidity of the vacant metal sites in MOFs. This study also looked into how the pore size affected the process by using biphenyl ketones and aldehydes. The results showed a much lower yield for the larger reagents, indicating that size selectivity also plays a role in such a process.[81]

Catalytic activity at the organic linkers is a feasible route when using linkers with active functional groups. The earliest report of such a material was a Mn^{3+} and Zn^{2+} based porphyrincarboxylate MOFs, which catalysed the epoxidation of olefins[94] and acyl transfer to pyridylcarbinols,[95] respectively. In these instances, it is likely that the metal – loading of the porphyrin linker provides the active site rather than the linker itself. An example whereby the linker itself is catalytically active is IRMOF-3, which uses an amino functionalised terephthalate linker and acts as a successful catalyst for the Knoevenagel condensations benzaldehyde with ethyl cyanoacetate.[35]

Asymmetric catalysis has also been successful using a manganese based MOF with an enantiomerically pure chiral salen linker, which catalyses the asymmetric epoxidation of chromene derivatives.[96]

Furthermore, impregnating the pores of the MOF with metal nanoparticles, which have been used for catalysis, as such, a number of MOFs that have had nanoparticles inserted into the pores. Gold is one of the most attractive elements in the research into catalysis since gold nanoparticles were loaded onto a metal oxide support and used to catalyse a CO oxidation at – 70 ^{o}C. Since MOFs have can be tuned to perform specific catalysis, loading these nanoparticles onto a MOF would combine the best of both materials. In 2008, a simple, yet effective method of loading gold nanoparticles onto various MOFs was reported and the outcome of the catalysis experiments revealed that the loaded MOFs exhibited noticeably high catalytic activity in the liquid phase. The materials also showed product selectivity according to the functionality on the MOF support. More examples include palladium nanoparticles that were incorporated into MOF-5 and was successful in catalysing Suzuki and Sonogashira couplings. Gold nanoparticles have been inserted into MIL-101 and used for the 1–phenyl ethanol oxidation, as well as platinum, silver and nickel nanoparticles have also been inserted into MOFs and used for various catalytic processes.

1.8.4 Sensing

As discussed previously, MOFs can be tuned to enhance their performance in a specific application, increasing their potential to be used as sensors. Sensors rely on detectable changes to the system, which can be mechanical, or as a result of a chemical or physical stimulus.

In 2010, an indium based MOF with a fluorescent pyrene based linker was synthesised, which showed that upon the uptake of water and other solvents, such as dioxane, onto the framework, the emission intensity was quenched.[97] It is well known that, due to quenching, the hydration states of

lanthanide MOFs have a substantial effect on the luminescent properties of the material. This phenomenon was reduced when DMF, a polar, aprotic solvent was incorporated into the framework, as this increased the structural order of the framework, separating the linkers further. This material showed that MOFs have the ability to be used for the detection of various solvents.

As well as tuning the linker to the specific property, incorporating a metal which has luminescence properties e.g. lanthanides, will also enhance the performance. Lanthanide complexes exhibit unique co-ordination chemistry and have long excited-state lifetimes, which is why they have attracted substantial attention as potential sensory materials.

In 2004, MIL–78 was synthesised with the formula $Y_{1-x}Eu_x$(1,3,5–BTC) where $x \approx 0.024$. This is a highly luminescent Eu-doped yttrium framework and the same structure is formed when yttrium is replaced with rare-earth elements (Tb and Dy) which emit red, green and blue under UV radiation, respectively (Figure 1.16). [98]

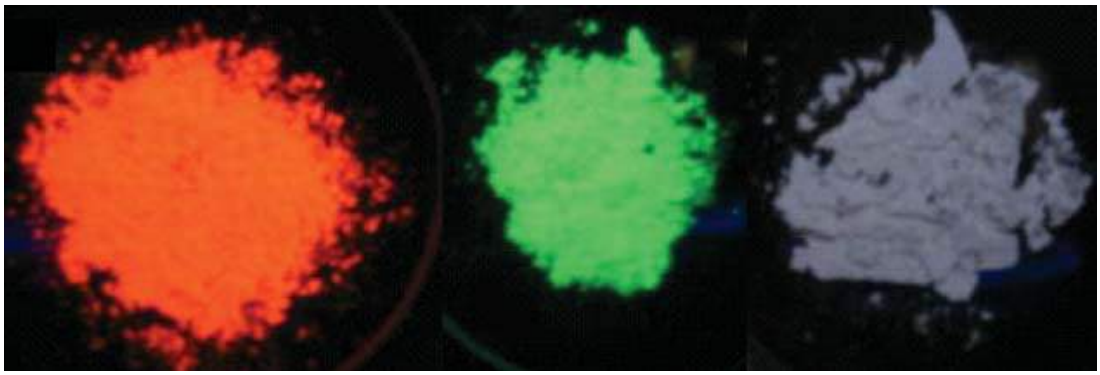

Figure 1.16. Picture of MIL-78 under UV radiation when doped with Eu (red), Tb (green) and Dy (blue). Figure from reference.[98]

In 2006, a Tb: mucic acid framework was synthesised and tested for its luminescent properties for reversible selective anion monitoring.[99] The material was made of 2-dimensional sheets which, through hydrogen bonding of inter-sheet water molecules, formed a 3-dimensional overall

framework. The luminescence spectrum of the material was measured before and after the addition of aqueous sodium salts of I^-, Br^-, Cl^-, F^-, CN^- and CO_3^{2-} whereby the largest enhancement of the luminescence intensity was observed for the CO_3^{2-} anion. This research indicated that MOFs have potential to be used in the detection of the presence of various anions.

1.8.5 Ammonia Uptake

Ammonia is one of the most significantly produced chemicals in the world and has many uses from production of fertiliser, commercial cleaning products and pharmaceuticals to explosives.[100, 101] Classified as a high hazard toxic industrial chemical (TIC), it can be lethal with long and short-term exposure limits of 25 ppm and 35 ppm respectively.[101, 102] The uptake of ammonia, therefore, is extremely important. Current technology for this application employ filters containing activated carbon, which has been modified to incorporate metal salts such as silver and zinc. This has been shown to be a successful method in the uptake of TICs,[100, 103-106] however, MOFs have the potential to outperform activated carbon due to the ability to tune the surface chemistry to favour such a process. The inability to control the pore size or functionality within activated carbons poses a significant problem.

The study of MOFs for this application began in 2008, when a number of MOFs were tested as sorbents for ammonia and other TICs including sulphur dioxide, benzene and carbon monoxide. The results were compared with those for BPL activated carbon and they showed that the MOFs outperformed the benchmark material.[104] The study demonstrated that the MOF with the added amino functionality (IRMOF–3), performed better than its non – functionalised analogue (MOF–5), indicating that the extra amino

group provided preferential hydrogen bonding site for the ammonia. Another feature which improved the uptake capacity of the materials was the presence of vacant metal sites in MOF–74 and MOF–199 (Cu–BTC) which act as Lewis acid sites, providing reactivity towards ammonia which is Lewis basic.

M-MOF-74 (M = Co / Mg / Ni / Zn) was tested under dry and humid conditions and all materials were successful in the uptake of ammonia, with Co and Mg analogues performing substantially better than the others. As well as this, the results showed that octane was also readily adsorbed onto the material, the uptakes of which were consistent with the surface areas of the materials.[67] This shows that although functionality does play a major role in this application, surface are also has an impact on the performance.

MOF–199 was also tested under humid flow of ammonia (80 % RH).[28] It showed superior performance under humid conditions to dry conditions by an increased capacity of 2.3 mmol / g. According to the analysis of the material afterwards however, the ammonia reacted with the framework directly to form copper hydroxide with an ammonium BTC salt under humid conditions and a copper – diamine complex under dry conditions. This, of course, had a detrimental impact on the framework, which was known from a study whereby upon exposure to ammonia, MOF-199 decomposed.[107]

A more recent demonstration of this type of study was in 2015 when Al–PMOF was tested for ammonia uptake. The porphyrin linker of material was loaded with hydrochloric and formic acid and both were tested under dry and humid conditions. It was reported that upon loading the material with these acids, improved the performance towards ammonia uptake. It was hypothesized that once the material was loaded with the acids, the basic ammonia has a higher reactivity towards the framework, as seen in previous examples whereby vacant metal sites have the same affect.[27]

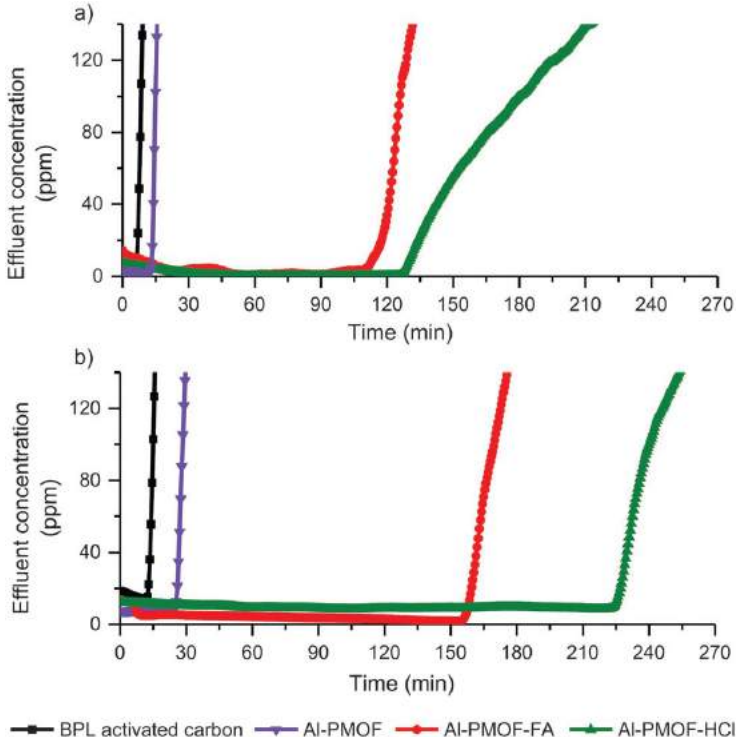

Figure 1.17. Ammonia breakthrough measurements at 0 % relative humidity and (b) 80 % relative humidity. Figure from reference.[27]

With regards to ammonia uptake, like with other gases, guest – host interactions play a substantial role in enhancing the performance of the material for this application.

1.9 Summary

Recent research into MOFs has provided evidence that functionalised linkers, as well as vacant metal sites can provide the material with enhanced performance in particular applications. Structural diversity of this family of porous materials is then increased with FL-MOFs and MOFs with chiral linkers, offering a whole new range of potential applications from asymmetric catalysis to enantioselective separations.

1.10 Project Aims

The overall aim of this work was to synthesise a variety of porous 3-dimensional frameworks using functionalised linkers and flexible linkers.

It is known from previous works, as described in this chapter, that functional linkers can enhance the performance of materials in different applications such as gas storage and separations. The aim of the research in chapter 3 was to use 2,5-furandicarboxylic acid (FDC), a functionalised and biogenic substitute for BDC, to synthesise a 3-dimensional porous material with enhanced gas adsorption and separation capabilities.

In chapter 4, the aim was to synthesise a single crystal of an indium analogue of the MOF synthesised in chapter 3. Due to the difficulty of solving the crystal structure of a MOF from PXRD data, a single crystal of an analogous material would ease this process.

The research presented in chapters 5, 6 and 7 aims to use three different functionalised linkers; N-(4-carboxyphenyl) succinamic acid (CSA), N,N'-(1,4-phenylenedicarbonyl) diglycine (PDG) and mucic acid (MA), respectively, to synthesise a series of new FL-MOFs and test whether they can perform better than reported materials in the uptake of N_2, CO_2 and CH_4.

1.11 References

1. K. Ishizaki, S. Komarneni and M. Nanko, in *Porous Materials*, Springer US, 1998, 10.
2. M. E. Davis, *Nature*, 2002, **417**, 813.
3. D. H. Everett, *Pure Appl. Chem.*, 1972, **31**, 577.
4. E. C. Dillon, J. H. Wilton, J. C. Barlow and A. William, *Annals of Emergency Medicine*, 1989, **18**, 547.
5. H. Marsh and F. Rodriguez-Reinoso, *Activated Carbon*, Elsevier Science Ltd, Oxford, 2006.
6. j. A. Menendez-Diaz and I. Martin-Gullon, *Activated Carbon Surfaces in Environmental Remediation*, Elsevier, 2006.
7. A. P. Cote, A. I. Benin, N. W. Ockwig, M. O'Keeffe, A. J. Matzger and O. M. Yaghi, *Science*, 2005, **310**, 1166.
8. T. Tozawa, J. T. Jones, S. I. Swamy, S. Jiang, D. J. Adams, S. Shakespeare, R. Clowes, D. Bradshaw, T. Hasell, S. Y. Chong, C. Tang, S. Thompson, J. Parker, A. Trewin, J. Bacsa, A. M. Slawin, A. Steiner and A. I. Cooper, *Nat. Mater.*, 2009, **8**, 973.
9. S. Y. Ding and W. Wang, *Chem. Soc. Rev.*, 2013, **42**, 548.
10. E. L. Spitler, B. T. Koo, J. L. Novotney, J. W. Colson, F. J. Uribe - Romo, G. D. Gutierrez, P. Clancy and W. R. Ditchel, *J. Am. Chem. Soc.*, 2011, **133**, 19416.
11. H. M. El-Kaderi, J. R. Hunt, J. Mendoza-Cortes, A. Cote, R. E. Taylor, M. O'Keeffe and O. M. Yaghi, *Science*, 2007, **316**, 268.
12. H. Furukawa and O. M. Yaghi, *J. Am. Chem. Soc*, 2009, **131**, 8875.
13. A. F. Cronstedt, *Kongl Vetenskaps Akademiens Handlingar Stockholm*, 1756, **17**, 120.
14. M. Kondo, T. Yoshitomi, H. Matsuzaka, S. Kitagawa and K. Seki, *Angew. Chem. Int. Edit.*, 1997, **36**, 1725.
15. S. M. Auerbach, K. A. Carrado and P. K. Dutta, *Handbook of Zeolite Science and Technology*, CRC Press, 2003.
16. E. M. Flanigen, *Studies in Surface Science and Catalysis*, Elsevier, 2001.
17. E. M. Flanigen, *Pure Appl. Chem.*, 1980, **52**, 2191.
18. M. Schoonover and M. Cohn, *Top. Fatal.*, 2000, **13**, 367.
19. A. Galarneau, F. Di Renzo, F. Fajula and J. Vedrine, *Zeolites and Porous Materials at the dawn of the 21st century*, Elsevier, 2001.
20. Y. He, J. Shang, Q. Zhao, Q. Gu, K. Xie, G. Li, R. Singh, P. Xiao and P. Webley, *Polyhedron*, 2016, **120,** 30.
21. R. J. Kuppler, D. J. Timmons, Q. R. Fang, J. R. Li, T. A. Makal, M. D. Young, D. Yuan, D. Zhao, W. Zhuang and H. C. Zhou, *Coordin. Chem. Rev.*, 2009, **253**, 3042.

22. H. Li, M. Eddaoudi, T. L. Groy and O. M. Yaghi, *J. Am. Chem. Soc.*, 1998, **120**, 8571.
23. M. Eddaoudi and J. F. Eubank, *Metal-Organic Frameworks*, John Wiley & Sons, 2010.
24. D. J. Tranchemontagne, J. L. Mendoza-Cortes, M. O'Keeffe and O. M. Yaghi, *Chem. Soc. Rev*, 2009, **38**, 1257.
25. A. Katsoulidis, K. S. Park, D. Antypov, C. Marti-Gastaldo, G. J. Miller, J. E. Warren, C. Robertson, F. Blanc, G. Darling, N. G. Berry, J. A. Purton, D. J. Adams and M. J. Rosseinsky, *Angew. Chem. Int. Ed.*, 2014, **53**, 193.
26. E. Stavitski, E. A. Pidko, S. Couck, T. Remy, E. J. Hensen, B. M. Weckhuysen, J. Denayer, J. Gascon and F. Kapteijn, *Langmuir*, 2011, **27**, 3970.
27. O. T. Wilcox, A. Fateeva, A. P. Katsoulidis, M. W. Smith, C. A. Stone and M. J. Rosseinsky, *Chem. Commun.*, 2015, **51**, 14989.
28. G. W. Peterson, G. W. Wagner, A. Balboa, J. Mahle, T. Sewell and C. J. Karwacki, *J. Phys. Chem*, 2009, **113**, 13906.
29. L. Bromberg, X. Su and T. A. Hatton, *Chem. Mater.*, 2013, **25**, 1636.
30. J. Song, Z. Luo, D. K. Britt, H. Furukawa, O. M. Yaghi, K. I. Hardcastle and C. L. Hill, *J. Am. Chem. Soc.*, 2011, **133**, 16839.
31. S. Marx, W. Kliest, J. Huang, M. Maciejewski and A. Baiker, *Dalton Trans.*, 2010, **39**, 3795.
32. N. C. Burtch, H. Jasuya and K. S. Walton, *Chem. Rev.*, 2014, **114**, 10575.
33. X. Qian, B. Yadian, R. Wu, Y. Long, K. Zhou, B. Zhu and Y. Huang, *Int. J. Hydrogen Energy*, 2013, **38**, 16710.
34. Z. Wang and S. M. Cohen, *Chem. Soc. Rev*, 2009, **38**, 1315.
35. M. Eddaoudi, J. Kim, N. Rosi, D. Vodak, J. Wachter, M. O'Keeffe and O. M. Yaghi, *Science*, 2002, **295**, 469.
36. N. Rosi, J. Eckert, M. Eddaoudi, D. Vodak, J. Kim, M. O'Keeffe and O. M. Yaghi, *Science*, 2003, **300**, 1127.
37. C. Rowsell, A. R. Millward, K. S. Park and O. M. Yaghi, *J. Am. Chem. Soc.*, 2004, **126**, 5666.
38. H. Li, M. Eddaoudi, M. O'Keeffe and O. M. Yaghi, *Nature*, 1999, **402**, 276.
39. H. Li, W. Shi, K. Zhao, H. Li, Y. Bing and P. Cheng, *Inorg. Chem.*, 2012, **51**, 9200.
40. J. H. Cavka, S. Jakobsen, U. Olsbye, N. Guillou, C. Lamberti, S. Bordiga and K. P. Lillerud, *J. Am. Chem. Soc*, 2008, **130**, 13850.
41. M. Kandiah, M. H. Nilsen, S. Usseglio, S. Jakobsen, U. Olsbye, M. Tilset, C. Larabi, E. A. Quadrelli, F. Bonino, K. P. Lillerud and 2010, **22**, 6632.
42. M. Kim and S. M. Cohen, *CrystEngComm.*, 2012, **14**, 4096.

43. T. Loiseau, C. Serre, C. Huguenard, G. Fink, F. Taulelle, M. Henry, T. Bataille and G. Ferey, *Chem. Eur. J*, 2004, **10**, 1373.
44. T. Loiseau, C. Serre, C. Huguenard, G. Fink, F. Taulelle, M. Henry, T. Bataille and G. Ferey, *Chem. Eur. J.*, 2004, **10**, 1371.
45. C. serre, F. Millange, C. Thouvenot, M. Nogues, G. Marsolier, D. Louer and G. Ferey, *J. Am. Chem. Soc.*, 2002, **124**, 13519.
46. A. Boutin, F. Coudert, M. Springuel-Huet, V. Neimark, G. Ferey and A. H. Fuchs, *J. Phy. Chem. C*, 2010, **114**, 22237.
47. T. Loiseau, C. Serre, C. Huguenard, G. Fink, F. Taulelle, M. Henry, B. T and G. Ferey, *Chem. Eur. J*, **10**, 1373.
48. M. Latroche, S. Surble, C. Serre, C. Mellot-Draznieks, P. Llewellyn, J. H. Lee, S. J. Chang, S. H. Jhung and G. Ferey, *Angew. Chem. Int. Edit.*, 2006, **45**, 8227.
49. P. Llewellyn, S. Bourrelly, C. Serre, A. Vimont, M. Daturi, L. Hamon, G. De weireld, J. S. Chang, D. Hong, Y. Kyu Hwang, S. Hwa Jhung and G. Ferey, *Langmuir*, 2008, **24**, 7245.
50. M. Lammert, S. Bernt, F. Vermoortele, D. De Vos and N. stock, *Inorg. Chem*, 2013, **52**, 8521.
51. L. Mitchell, P. Williamson, B. Ehrlichova, A. Anderson, V. Seymour, S. Ashbrook, N. Acerbi, L. Daniels, R. Walton, M. Clarke and P. Wright, *Chemistry - Eur. J*, 2014, **20**, 17185.
52. P. Llewellyn, G. Maurin and J. Rouquerol, *Adsorption by Powders and Porous Solids (Second Edition)*, Academic Press, Oxford, 2014.
53. S. Bhattacharjee, C. Chen and W. Ahn, *RSC Adv.*, 2014, **4**, 52500.
54. Z. J. Lin, J. Lu, M. Hong and R. Cao, *Chem. Soc. Rev.*, 2014, **43**, 5867.
55. J. S. Seo, D. Whang, H. Lee, S. I. Jun, J. Oh, Y. J. Jeon and K. Kim, *Nature*, 2000, **404**, 982.
56. J. Rabone, Y. Yue, S. Chong, K. Stylianou, J. Bacsa, D. Bradshaw, G. Darling, N. Berry, Y. Zhimyak, A. Ganin, P. Wiper, J. Claridge and Rosseinsky, *Science*, 2010, **329**, 1053.
57. B. F. Abrahams, M. Moylan, S. D. Orchard and R. Robson, *Angew. Chem. Int. Ed.*, 2003, **42**, 1848.
58. Z. Zhang, Z. Yao, S. Xiang and B. Chen, *Energy Environ., Sci*, 2014, **7**, 2868.
59. S. Couck, J. F. M. Denayer, G. V. Baron, T. Rémy, J. Gascon and F. Kapteijn, *J. Am. Chem. Soc.*, 2009, **131**, 6326.
60. P. S. Barcia, F. Zapata, J. A. Silva, A. E. rodrigues and B. Chen, *J. Phy. Chem. B.*, 2007, **111**, 6101.
61. B. Wang, H. Huang, X. Lv, Y. Xie, M. Li and J. Li, *Inorg. Chem.*, 2014, **53**, 9254.
62. A. Demessence, D. M. D'Alessandro, M. L. Foo and J. R. Long, *J. Am. Chem. Soc*, 2009, **131**, 12792.

63. J. D. Figueroa, T. Fout, S. Plasynski, H. McIlvried and R. D. Srivastava, *Int. J. Greenh. Gas Con.*, 2008, **2**, 9.
64. L. Bastin, P. S. Barcia, E. J. Hurtado, J. A. C. Silva, A. E. Rodrigues and B. Chen, *J. Phys. Chem. C*, 2008, **112**, 1575.
65. D. W. Beck, *Zeolite Molecular Sieves*, Wiley & Sons, New York, 1974.
66. J. Liu, J. Tian, P. K. Thallapally and P. McGrail, *J. Phys. Chem. C*, 2012, **116**, 9575.
67. T. G. Glover, G. W. Peterson, B. J. Schindler, D. Britt and O. M. Yaghi, *Chem. Eng. Sci.*, 2011, **66**, 163.
68. M. Sadakiyo, T. Yamada and H. Kitagawa, *J. Am. Chem. Soc.*, 2011, **133**, 11050.
69. M. Minceva and A. E. Rodrigues, *AlChE J.*, 2007, **53**, 138.
70. Z. Y. Gu and X. P. Yan, *Angew. Chem. Int. Edit.*, 2010, **49**, 1477.
71. W. M. Haynes, *CRC Handbook of Chemistry and Physics. 95th Edition*, CRC Press LLC, Boca Raton, 2014-2015.
72. M. Guisnet and J. Gilson, *Zeolites for Cleaner Technologies*, Imperial College Press, London, 2002.
73. L. Alaerts, M. Maes, L. Giebeler, P. A. Jacobs, J. A. Martens, J. Denayer, C. Kirschhock and D. De Vos, *J. Am. Chem. Soc.*, 2008, **130**, 14710.
74. V. Finsy, H. Verelst, L. alaerts, D. De Vos, P. A. Jacobs, G. V. Baron and J. Denayer, *J. Am. Chem. Soc.*, 2008, **130**, 7110.
75. Z. Yan, W. Zhang, J. Gao, Y. Lin, J. li, Z. Lin and L. Zhang, *RSD Adv.*, 2015, **5**, 40094.
76. K. M. Radha, L. Jian, A. F. Carlos, K. N. Satish, T. Praveen and P. McGrail, *Industrial Catalysis and Separations*, Apple Academic Press, 2014.
77. L. Wang, A. J. Lacawiec and R. T. Yang, *RSC Adv.*, 2013, **3**, 23935.
78. X. Lin, J. Jia, Z. X, M. Thomas, A. J. Blake, G. Walker, N. Champness, P. Hubberstey and M. Schroder, *Angew. Chem. Int. Edit.*, 2006, **45**, 7358.
79. M. Dinca and J. R. Long, *J. Am. Chem. Soc.*, 2005, **127**.
80. M. Dinca, A. F. Yu and J. R. Long, *J. Am. Chem. Soc.*, 2006, **128**, 8904.
81. M. Dinca, A. Dailly, J. Liu, C. Brown, D. Neumann and J. R. Long, *J. Am. Chem. Soc.*, 2006, **128**, 16876.
82. H. W. Langmi, J. Ren, B. North, M. Mathe and D. Bessarabov, *Electrochim. Acta*, 2014, **128**, 368.
83. S. S. Kaye, A. Dailly, O. M. Yaghi and J. R. Long, *J. Am. Chem. Soc.*, 2007, **129**, 14176.
84. H. Furukawa, Y. Go, N. Aratani, S. Choi, E. Choi, A. Yazaydin, R. Q. Snurr, M. O'Keeffe, J. Kim and O. M. Yaghi, *Science*, 2010, **329**, 424.
85. O. Farha, I. Yazaydin, I. Eryazici, C. Malliakas, B. Hauser, M. Kanatzidis, S. Nguyen, R. Q. Snurr and J. T. Hupp, *Nat. Chem.*, 2010, **2**, 944.

86. T. Duren, L. Sarkisov, O. M. Yaghi and R. Q. Snurr, *Langmuir*, 2004, **20**, 2683.
87. Y. He, W. Zhou, G. Qian and B. Chen, *Chem. Soc. Rev.*, 2014, **43**, 5657.
88. R. Saboumi, H. Kazemian and S. Rohani, *Environ. Sci. Pollut. Res.*, 2014, **21**, 5427.
89. J. Liu, P. K. Thallapally, B. P. McGrail, D. R. Brown and J. Liu, *Chem. Soc. Rev.*, 2012, **41**, 2308.
90. D. K. Britt, H. Furukawa, B. Wang, T. G. Glover and O. M. Yaghi, *Proc. Natl. Acad. Sci. U.S.A.*, 2009, **106**, 20637.
91. A. Yazaydin, R. Q. Snurr, T. Park, K. Koh, J. Liu, M. D. LeVan, A. I. Benin, P. Jakubczak, M. Lanuza, D. B. Galloway, J. J. Low and R. R. Willis, *J. Am. Chem. Soc.*, 2009, **131**, 18198.
92. A. R. Millward and O. M. Yaghi, *J . Am. Chem. Soc.*, 2005, **127**, 17998.
93. J. Liu, L. Chen, H. Cui, J. Zhang, L. Zhang and C.-Y. Su, *Chem. Soc. Rev.*, 2014, **43**, 6011.
94. K. Suslick, P. Bhyrappa, J. Chou, M. Kosal, S. Nakagaki, D. Smithenry and S. Wilson, *Acc. Chem. Res.*, 2005, **38**, 283.
95. A. M. Shultz, O. Farha, J. T. Hupp and S. Nguyen, *J. Am. Chem. Soc.*, 2009, **131**, 4204.
96. G. Morris, S. Nguyen and J. Hupp, *J. Mol. Catal. A: Chem*, 2001, **174**, 15-20.
97. K. C. stylianou, R. Heck, S. Y. Chong, J. Bacsa, J. T. Jones, Y. Khimyak, D. Bradshaw and M. Rosseinsky, *J. Am. Chem. Soc.*, 2010, **132**, 4119.
98. C. Serre, F. Millange, C. Thouvenot, N. Gardant, F. Pellé and G. Ferey, *J. Mater. Chem.*, 2004, **14**, 1540.
99. K. L. Wong, G. L. Law, Y. Y. Yang and W. T. Wong, *Adv. Mater.*, 2006, **18**, 1051.
100. J. B. DeCoste and G. W. Peterson, *Chem. Rev.*, 2014, **114**, 5695.
101. F. Hincal and P. Erkekoglu, *J. Pharm. Sci.*, 2006, **31**, 220.
102. *EH40/2005 Workplace exposure limits: Containing the list of workplace exposure limits for use with the Control of Substances Hazardous to Health Regulations 2002 Environmental Hygiene guidance Note EH40 (second edition)*, http://www.hse.gov.uk/pUbns/priced/eh40.pdf. Accessed April 2017.
103. G. W. Peterson, C. J. Karwacki, W. B. Feaver and J. A. Rossin, *Ind. Eng. Chem. Res.*, 2008, **47**, 185.
104. D. Britt, D. J. Tranchemontagne and O. M. Yaghi, *Proc. Natl. Acad. Sci. U.S.A.*, 2008, **105**, 11623.
105. C. J. Karwacki, G. W. Peterson and T. Bandosz, *J. Phys. Chem. C*, 2007, **111**, 12705.
106. G. Odell Wood, *Carbon*, 1991, **30**, 593.
107. K. Schlichte, T. Kratzke and S. Kaskel, *Microporous Mesoporous Mater.*, 2004, **73**, 81.

Chapter 2 Synthetic and Experimental Techniques

In this chapter, all experimental procedures, characterisation and analytical techniques used for all work carried out in this thesis will be discussed. Synthesis of specific MOFs discussed in this thesis can be found in their respective chapters.

2.1 General Overview

It is essential for MOFs to be synthesised in a phase pure manner in order to fully understand their structure – function relationships. The synthesis of a MOF is dependent on a large number of variables including but not limited to reaction time, temperature, heating/cooling ramp rates, reagent concentration, solvent systems, metal salt and linker: metal molar ratio. Only when the exact reaction conditions have been identified will the desired, phase pure product form. With so many variables, it is necessary to use exploratory synthesis methods, employing a high throughput procedure in order to pin point the perfect synthesis conditions. Examples of such high – throughput exploratory synthetic approach are described in each chapter.

In order to ascertain whether the material is phase pure, a number analytical and characterisation techniques are employed; PXRD, TGA, SCXRD, and elemental microanalysis. Not all materials in this thesis were subjected to SCXRD since no single crystals were obtained, however, where beneficial, most techniques were utilised to characterise the products.

Once a phase pure material has been synthesised, potential applications are then investigated. Gas adsorption measurements are carried out, primarily using N_2 to determine the BET surface area of the material. This is the initial

measurement carried out in order to determine whether the material will have a valid application relative to its porosity. Some of the materials in this thesis were subjected to extensive gas adsorption measurements, using CO_2 and CH_4, to determine isosteric heat of adsorption (Q_{st}) for the materials. Since not all MOFs are in fact porous, it is not critical to have a high BET surface area, the structure of the MOF (determined by SCXRD and / or PXRD) may present other interesting features which could give it an application in a completely different field i.e. ionic conductors.

In this thesis, one material was tested for xylene separation experiments using HPLC, as well as NH_3 uptake and breakthrough experiments, these techniques will be discussed in this chapter.

2.2 Solvo / Hydrothermal Synthesis

Solvothermal and hydrothermal methods are the main routes of synthesis of MOFs. Although there have been reports of some MOFs being synthesised at room temperature,[1] in general, higher temperatures are required. As the name suggests, both systems require the use of a solvent, under hydrothermal conditions the solvent of choice is water, whereas the solvent(s) used for solvothermal conditions have a wider scope. Solvothermal reactions are carried out in sealed reaction vessels, which can be heated to high temperatures (as high as 250 ^{o}C if required). The ability for said reactors to reach such high temperatures allows for reactions to be carried out at temperatures higher than that of the boiling points of the solvents in the solvent system. The benefit of heating a system up beyond the boiling point of the solvents is that this causes a build-up of pressure within the vessel, this increase in pressure, along with the high temperature, increases the solubility of the starting reagents. However, using such a high temperature does have its disadvantage; a simple glass vial with a Teflon

sealed cap is insufficient in dealing with such high pressures. In these instances it is necessary to use solvothermal autoclave reactors. Starting reagents are loaded into a Teflon liner which has been conditioned to fit a specific stainless steel autoclave.

2.3 X-Ray Diffraction

2.3.1 Principles of a crystal structure

When atoms of a material are arranged in a highly ordered fashion, the material is described as crystalline. The structure of the material is made up of a repeating unit known as the asymmetric unit, which is defined as the part of the crystallographic unit cell that can be used to generate the complete unit cell, using the symmetry of the space group. Lattice parameters; three edges (*a*, *b*, *c*) and three angles (α, β, γ) provide information about the size and shape of the unit cell, which differ between materials. There are seven possible crystal systems depending on the relationship between lattice parameters shown in Table 2.1.[2]

There are four different lattice types within each of these crystal systems that a lattice can be categorised into depending on where lattice points fall within the unit cell; Primitive (*P*) only has lattice points in the corners of the unit cell, Face centred (*F*) has a lattice point on each corner and each face of the unit cell, Body centred (*I*) has a lattice point on each corner and one in the centre of the unit cell, and Base centred (*A*, *B* or *C*) has a lattice point on each corner and one on two parallel faces of the unit cell. Lattice types and crystal systems form the basis of determining the space group of a crystal structure, however, other symmetry operations need to be taken into account, some simple (mirror planes) and some more complex (glide planes, screw axis). In total there are 230 space groups which fully describe a crystal structure based on their symmetry.[2]

Table 2.1. Seven possible crystal systems.

Crystal System	Unit Cell Dimensions	Minimum Symmetry Elements
Triclinic	$a \neq b \neq c$	None
	$\alpha \neq \beta \neq \gamma$	
Monoclinic	$a \neq b \neq c$	One C_2 axis or mirror plane
	$\alpha = \gamma = 90^o \neq \beta$	
Cubic	$a = b = c$	Four C_3 axis
	$\alpha = \beta = \gamma = 90^o$	
Orthorhombic	$a \neq b \neq c$	Three C_2 axis or mirror planes
	$\alpha = \gamma = \beta = 90^o$	
Hexagonal	a = b ≠ c	One C_6 axis
	$\alpha = \beta = 90^o$, $\gamma = 120^o$	
Trigonal	$a = b = c$	Once C_3 axis
	$\alpha = \beta = \gamma \neq 90^o$	
Tetragonal	$a = b \neq c$	One C_4 axis
	$\alpha = \beta = \gamma = 90^o$	

2.3.2 Principles of XRD

When X-Rays are "fired" at a sample in real space, it is the electrons within the atom that produce elastic scattering of the X-rays, meaning that the energy and wavelength of the radiation remains constant. From this, an electron density map can be generated whereby each atom has a unique map. For example, an aluminium atom will have 13 electrons, whereas a carbon atom will have 6, therefore they will be easily distinguishable from their electron density maps.

In this work, a combination of single crystal X-ray diffraction (SCXRD) and powder X-ray diffraction (PXRD) was used to determine the structure of the materials. PXRD was mainly used to determine phase purity of the bulk material and to identify any structural changes after different treatments. All structures in this thesis, unless otherwise stated, were solved by Dr George F. S. Whitehead, a crystallographer in our research group.

2.3.3 Single Crystal X-Ray Diffraction

Single crystal XRD (SCXRD) is a very powerful tool for determining the crystal structure of a material. Crystal structures solved by SCXRD in this thesis were solved using OLEX2 and SHELX software, which employ a direct method.

The diffraction patterns observed by the detector represent reciprocal space images of the crystal structure, the lattice of which can be described using Miller indices (h, k, l). These Miller indices relate to the x, y, z (*a*, *b*, *c*) coordinates of the atoms within the single crystal in real space. Each diffraction point (reflection) has a unique Miller index, which allows the reciprocal 3D structure to be generated. All data collected is then processed in order to obtain the magnitude of the structure factors for each spot.

When a diffraction measurement is carried out, only the amplitude of the structure factor, is measured.[3] The structure factor is a mathematical description of how a material scatters incident radiation, in this case, X-ray radiation, which can be considered as vector quantities since they have both amplitude (magnitude) and a phase (direction).[4] Since only the amplitude is measured during a diffraction measurement, a lot of information associated with the phase of the structure factor is lost. Direct methods make use of the

relationship between the magnitude and the phase of the structure factor in order to determine the phase directly from the observed amplitudes.

In order to employ this method, a main assumption must be made; atoms are found as peaks in the density map, which are typically separated by 1–2 Å due to chemical bonding. This means that a requirement for the successful solution of a structure via this method is that the data must be measured to atomic resolution.

SCXRD data collections for In: FDC compounds 1-3, In,Cu: CSA, In: PDG and Co: MA were all carried out on a Rigaku Saturn 247+ instrument with Cu K_α radiation.

SCXRD Data collection for Mg: MA was collected at Diamond Light Source under synchrotron radiation. The principle remains the same for synchrotron radiation, with the added advantage of intense and tuneable radiation enabling the successful solving of weakly scattering structures such as Mg: MA.

2.3.4 Powder X-Ray Diffraction

PXRD operates using the same principles as SCXRD, however, instead of the sample consisting of one crystal, it is made of multiple smaller crystallites. This prohibits the generation of a 3-dimensional diffraction pattern, as such only 2-dimensional patterns are obtained. In SCXRD, all spots in the pattern are produced from a single crystal, spots at the same 2θ value of a PXRD pattern are produced from multiple crystallites. This produces concentric rings in the diffraction pattern, which can be translated into a 2-dimensional graph, or pattern. This pattern can then be indexed to a known unit cell to determine phase purity of the bulk of the material. It is possible to determine a crystal structure of MOF using PXRD data, however it is a taxing and

challenging job involving a Rietveld refinement. In this thesis, the structure of Al: FDC was determined by Dr George F. S. Whitehead using a Rietveld refinement on the PXRD data obtained from a synchrotron radiation source. This was done using Jana software, using the unit cell from the CAU-10 as the parent material. The Rietveld refinement takes into account all relevant instrumental and structural parameters, which are refined by fitting a calculated and sensible model to the experimental data.

2.3.5 Data Collection

During high-throughput exploratory synthesis, PXRD patterns were collected using a Panalytical X'Pert Pro diffractometer using Cu Kα radiation.

All PXRD patterns presented in this thesis (unless otherwise stated) were collected on a Bruker D8 Advance instrument using Cu Kα.

2.4 Gas Sorption

Analysing the porous properties of the newly synthesised material is necessary in order to determine a potential application. Gas sorption experiments are the most common techniques used to determine such properties in porous materials such as MOFs. As well as the surface area of the material, this type of experiment can provide additional information regarding the surface of the material; pore volume, pore size, pore size distribution and can provide insights into the interactions between the surface and the sorbate. Carrying out sorption measurements using different gases with different chemical and physical properties, allows for a more complete investigation into the porous characteristics of the material.

It should be noted here that the reported BET surface area values should not be regarded as a realistic value of a material, but should be used as an apparent value in order to compare porous materials.[5]

2.4.1 Types of Adsorption

There are two ways in which the sorbate can interact with the surface; reversibly through weak Van der Waals interactions, namely physisorption, and strongly through binding to active sites on the surface, namely chemisorption. Physisorption can result in multilayer adsorption and the pores of the material can be completely filled due to weak interactions with already adsorbed molecules. These weak interactions cause the process to be fully reversible. Chemisorption exhibits different behaviour, as a result of the direct interaction between the surface and the sorbate, chemisorption is limited to monolayer adsorption.[6]

2.4.2 Adsorption Isotherms

Sorption isotherms take on one of six different shapes (Figure 2.1), each of which has specific characteristics, which offer information about the surface of the material.

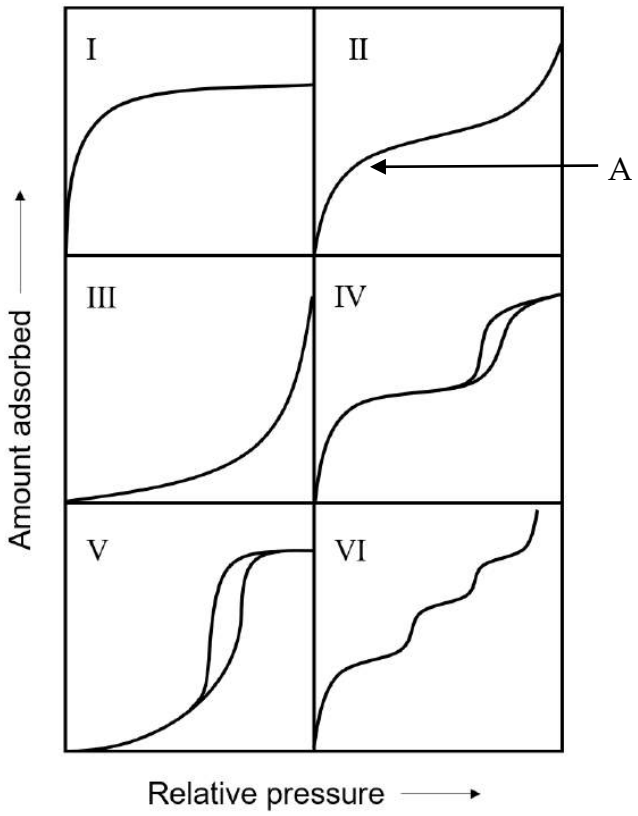

Figure 2.1. Types of adsorption isotherm. Figure used with expressed permission from the author.

Type I isotherm (Langmuir Isotherm) is characteristic of microporous materials (pore diameter < 2nm). The characteristic feature of this isotherm is the plateau which occurs from low relative pressure to high relative pressure, signifying that once the monolayer is saturated, no more molecules can be adsorbed. The adsorbed amount at this plateau can be used to calculate the pore volume of the material, for this calculation it is necessary to assume that the adsorbed molecules are in the liquid phase. To calculate the pore volume, the adsorbed amount is multiplied by the gas-liquid density ratio (for N_2 at 77K, this is 0.0015).

Type II isotherms do not show a saturation limit that is seen in type I. This type of isotherm is usually seen for non – porous or macroporous materials pore diameter > 50nm). An initial monolayer is formed up to point A, after which, unrestricted adsorption occurs causing successive multilayer adsorption.

Type III isotherms are relatively uncommon and are associated with weak adsorbate – adsorbent interactions relative to that of adsorbate – adsorbate interactions.

Type IV isotherms are typical for mesoporous materials (pore diameters > 2nm and < 50nm). This type of material undergoes multilayer adsorption, followed by capillary condensation, giving rise to the hysteresis loop.

Type V isotherms are related to type II isotherms and generally seen for micro – or meso – porous materials.

Type VI isotherms exhibit characteristic stepwise adsorption, typical for non – porous materials, each layer is formed uniformly before the next layer starts to form. The height of each step indicates the capacity for each layer.[6]

2.4.3 Surface Area Calculations

From the adsorption isotherms, the surface area of the material can be calculated using the Brunauer-Emmett-Teller (BET) method, BET equation (Equation 2.1). This model is an extension of the Langmuir method from monolayer to multilayer adsorption, and works under the assumption that the adsorbed monolayers of guest are in dynamic equilibrium with the measurement vapour, i.e. adsorption and desorption rates are similar.

$$\frac{\mathbf{1}}{\boldsymbol{v}\left[\left(\frac{\boldsymbol{p_0}}{\boldsymbol{p}}\right)-\mathbf{1}\right]} = \frac{\boldsymbol{c}-\mathbf{1}}{\boldsymbol{v_m c}}\frac{\boldsymbol{p}}{\boldsymbol{p_0}} + \frac{\mathbf{1}}{\boldsymbol{v_m c}}$$

Equation 2.1. BET equation where p is the equilibrium pressure, p_0 is the saturation pressure, v is the volume of gas adsorbed at equilibrium, v_m is the volume of gas adsorbed in a monolayer, c is a constant.

A plot of $\frac{1}{v\left[\left(\frac{p_0}{p}\right)-1\right]}$ against $\frac{p}{p_0}$ gives a straight line at low pressures, with the gradient; $\frac{c-1}{v_m c}$ and intercept; $\frac{1}{v_m c}$. A value for v_m can then be calculated using Equation 2.2.

$$v_m = \frac{1}{A+I}$$

Equation 2.2. Where $\boldsymbol{A}$ is the gradient and $\boldsymbol{I}$ is the intercept

The BET surface area can then finally be calculated using Equation 2.3.[7]

$$S = \frac{v_m N a}{Vm}$$

Equation 2.3. Where $\boldsymbol{v_m}$ is the monolayer volume, $\boldsymbol{N}$ is Avagadro's number, $\boldsymbol{a}$ is cross sectional area of one adsorbate molecule, $\boldsymbol{V}$ is the molar volume of gas, $\boldsymbol{m}$ is the adsorbent mass.

2.4.4 Isosteric Heat of Adsorption

The strength of the adsorbate-adsorbent interactions can be quantified as the isosteric heat of adsorption (Q_{st}). Before this can be calculated, isotherms of the same process must be measured at several different temperatures, in this thesis, temperatures used for such calculations were 273 K, 283 K and 293 K. Plots of lnP against amount adsorbed per gram (for the different temperatures), can be fitted to the virial equation (Equation 2.4),[8] thus determining values for the virial coefficients a_i and b_i. Once these values are known, they can be used in Equation 2.5 to calculate the isosteric heat of

adsorption, a final plot of Q_{st} against amount adsorbed per gram, can be used to determine Q_{st} at zero coverage i.e. the initial heat of adsorption.

$$ln\ p = \frac{1}{T}\sum_{i=0}^{n1} a_i v^i + \sum_{i=0}^{n2} b_i v^i + ln\ v$$

Equation 2.4. Virial equation where $\boldsymbol{P}$ is pressure (Torr), $\boldsymbol{v}$ is the amount of gas adsorbed (mmol/g), $\boldsymbol{T}$ is temperature (K), $\boldsymbol{a_i}$ and $\boldsymbol{b_i}$ are virial coefficients.

$$\boldsymbol{Q_{st} = -R\sum_{i=0}^{n1} a_i v^i}$$

Equation 2.5. Where R is the gas constant

2.4.5 Sorption Measurements

In this thesis, gas sorption measurements were carried out on various different instruments; a Micromeritics Tristar II instrument was used for general N_2 isotherms and a Micromeritics 3Flex instrument was used to measure CO_2 and CH_4 adsorption isotherms for Q_{st} calculations. In a typical measurement, a sample of 70 – 80 mg was degassed at 155 ^oC under dynamic vacuum overnight before each measurement.

High pressure isotherms were measured on a Hiden Intelligent Gravimetric Analysis (IGA). A typical experiment here used 35 mg of activated sample which was re-activated at 100 ^oC overnight under dynamic vacuum again.

2.5 Thermogravimetric Analysis

Thermogravimetric analysis (TGA) is a precise technique which measures the mass of a sample as a function of temperature. In a typical case, the heating of the sample results in a change (decrease) in mass, which can be attributed to several effects. In porous materials, including some of those presented in

this thesis, the initial mass loss is due to the removal of adsorbed solvent molecules, from either the synthesis or the washing procedure. As well, some materials (particularly hydrophilic materials) adsorb moisture from the atmosphere which can be seen on a TGA measurement. Thermal stability (or decomposition temperature) of the material is also measured using TGA, typically, a large mass loss at relatively high temperatures indicates the combustion of the organic content leaving behind the inorganic residue in the form of the metal oxide. Using the information provided from this measurement, an activation temperature can be decided, also, the metal content of the material can be calculated.

Measurements in this thesis were carried out on a TA instruments Q500 Thermogravimetric Analyzer and a TA instruments Q600 Thermogravimetric Analyzer. A typical measurement saw 5 – 10 mg of sample being heated to 800 – 1200 ^{o}C (varied from sample to sample) at 10 ^{o}C / min under a 50 mL / min flow of air.

2.6 Elemental Microanalysis

This technique is employed to determine the relative amounts of carbon, hydrogen and nitrogen in a sample. Elemental analysis used in this thesis was performed at the University of Liverpool, using a Thermo EA1112 Flash CHNS-O Analyzer. Typically 2 – 3 mg of sample is combusted in an oxygen environment, giving CO_2, H_2 and H_2O and NO_x, which are separated via a GC column.[9]

2.7 Scanning Electron Microscopy

Scanning electron microscopy (SEM) provides high resolution images of a sample surface at high magnification. This allows for the details of the

surface as well as the topology of the sample to be studied in greater detail than by using an optical microscope.

A focused beam of electrons is scanned across the surface causing an excitation, thereby producing two types of electrons, which are detected; secondary electrons (produced by ionisation) or back scattered electrons (produced by elastic scattering). These detected electrons are used to then generate the image.[10]

SEM images were obtained by Dr Marco Zanella and Harry Sansom using a Hitachi S-4800 scanning electron microscope. A typical sample preparation involved loading a small amount of sample onto an adhesive carbon tab attached to an aluminium SEM holder. A sputter coater was then used to coat the sample (and the holder) with a thin layer (5 – 10 nm) of gold.

2.8 Gas Separation Experiments

These measurements were carried out by Dr Andrew Stephenson using a Hiden Analytical dynamic sorption analyser. Activated Al: FDC was packed into an adsorption bed and was re-activated at 100 ^{o}C overnight under a helium purge flow. This was to ensure all adsorbed atmospheric water was removed and the sample mass was measured immediately after unloading the sample; 2.307 g and 2.080 g for the CO_2 / N_2 and CO_2 / CH_4 separations respectively. The separations were carried out using 85:15 and 20:80 mixtures of N_2:CO_2 and CO_2:CH_4, respectively at flow rates of 3 mL / min at 1 bar. In order to calculate the selectivity of one gas over another, the area above the breakthrough curve (which was normalised to 1) was calculated. This was then used in Equation 2.6 to calculate the equilibrium adsorption capacity.[11]

$$q = \frac{C_o V t_s}{22.4W}$$

Equation 2.6. Where q is the equilibrium adsorption capacity of gas (mmol / g), t_s is the stoichiometric time (min) C_0 is the feed gas concentration, V is the volumetric feed flow rate (cm^3 / min) and W is the mass of the activated adsorbent (g).

Selectivity was then calculated using Equation 2.7.

$$S_{AB} = \left({}^{X_A}/_{X_B}\right) * \left({}^{Y_B}/_{Y_A}\right)$$

Equation 2.7. Selectivity equation where X is the mole fraction of gas in the adsorbed phase, Y is the mole fraction of gas in bulk phase. X_A and X_B can be calculated using Equation 2.8 and Equation 2.9 respectively. Y_B / Y_A is the fractional composition of the adsorbates.

$$X_A = \frac{q_A}{q_A + q_B}$$

Equation 2.8. where q_A is calculated from **Equation 2.6** for gas A.

$$X_B = \frac{q_B}{q_A + q_B}$$

Equation 2.9. where q_B is calculated from **Equation 2.6** for gas B.

A number of experimental parameters were adjusted in order to obtain the best possible data. Unfortunately, the best obtained data (presented in chapter 3) shows that CO_2 breaks through almost immediately, as seen with N_2 and CH_4.

2.9 Ammonia Breakthrough Experiments

Breakthrough experiments were carried out using a custom micro – breakthrough rig at Defence Science and Technology Laboratory, Porton Down by M. W. Smith. Ammonia breakthrough testing was carried out using a small scale breakthrough apparatus as used previously for work in this research group.[12]

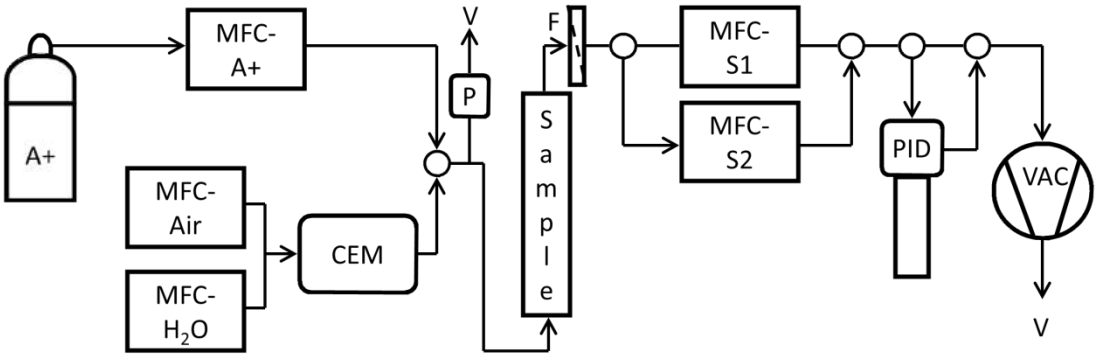

A+	Agent gas
MFC	Mass flow controller
MFC S1	Low sample flow mass flow controller
MFC S2	High sample flow mass flow controller
CEM	Controlled evaporator mixer
P	Relative humidity and temperature probe
F	PTFE dust filter
VAC	Diaphragm vacuum pump
PID	Photo-ionisation detector
V	Vent to fume cupboard
O	Tube junction

Figure 2.2. Schematic of the micro-breakthrough apparatus

The challenge concentration was generated by mixing ammonia (from a lecture bottle) into a stream of either dry (<10% RH) or humid (70-80% RH) air. The flow of air was 2 L / min, and that of ammonia 1 ml / min, resulting in a test concentration of 500 ppm. For each test, 20±1 mg of adsorbent was weighed and loosely packed into a 4 mm internal diameter tube between cotton wool plugs. Clean (dry or humid) air was drawn through the sample for 20 minutes at 30 ml / min, before switching to 500 ppm ammonia (dry or humid) at the same flow rate. The effluent was monitored using a PhoCheck Tiger photoionisation detector.

The amount of ammonia adsorbed at breakthrough was calculated using the concentration of flow (mol / m^3), the flow rate and the breakthrough time, the uptake of ammonia can be calculated in moles.

At saturation, the amount of ammonia adsorbed can be calculated by integrating underneath the breakthrough curve, using OriginPro 2015 graphical software,[13] in the area between breakthrough and saturation, which could then be used to calculate the amount of ammonia adsorbed at saturation.

2.10 Infra-Red Spectroscopy

FTIR spectroscopy of the Al: FDC material was carried out before and after the ammonia breakthrough experiments by M. W. Smith, using a Perkin Elmer spectrometer with a Specac Quest ATR diamond accessory, at Defence Science and Technology Laboratory, Porton Down.

2.11 Xylene Separation Experiments

Xylene separation experiments were carried out by Dr. Michael E. Briggs. A 100 x 2.1 mm column was packed with activated Al: FDC (ca 20 g) material by the research group of Professor Peter Myers. HPLC pulse separation

experiments of were carried out on a Thermo Scientific Dionex UltiMate 3000, using a diode array detector set at 254 nm. Solutions of *ortho-*, *meta-*, and *para-* xylene were prepared in methanol (0.25 mg / mL). Pulse measurements were carried out at 30 °C under a flow rate of 0.1 mL / min with 1 μL injections.

In order to accurately quantify the data obtained by such measurements, baseline separation is required. Baseline separation occurs when the resolution between peaks is 1.5 or greater, this is calculated using Equation 2.10.[14]

$$R_s = \frac{2(t_2 - t_1)}{W_1 + W_2}$$

Equation 2.10. Calculation of resolution between two bands (R_s) where t_2 and t_1 are retention times of the first and second adjacent bands and W_1 and W_2 are baseline bandwidths of the respective bands.

A number of parameters have an overall effect on the resolution of the bands. Examples of such parameters are choice of mobile phase, temperature of measurement, column dimensions and flow rate. The results presented in this thesis represent the best data set obtained for these measurements after a number of parameters were altered.

2.12 References

1. D. J. Tranchemontagne, J. R. Hunt and O. M. Yaghi, *Tetrahedron*, 2008, **64**, 8553.
2. C. Hammond, *Introduction to crystallography (revised edition)*, Oxford University Press, New York, 1992.
3. H. Hauptman, *Science*, 1986, **233**, 178.
4. A. J. Blake, W. Clegg, J. M. Cole, J. S. O. Evans, P. Main, S. Parsons and D. J. Watkin, *Crystal Structure Analysis Principles and Practice (second edition)*, Oxford University Press Inc., New York, 2009.
5. G. Pickett, *J. Am. Chem. Soc.*, 1945, **67**, 1958.
6. K. S. Sing, D. H. Everett, R. A. Haul, L. Moscou, R. A. Pierotti, J. Rouqierol and T. Siemieniewska, *Pure Appl. Chem.*, 1985, **57**, 1365.
7. S. Brunauer, P. H. Emmett and E. Teller, *J. Am. Chem. Soc.*, 1938, **60**, 309.
8. L. Czepirski and J. JagieŁŁo, *Chem. Eng. Sci.*, 1989, **44**, 797.
9. R. Levens, *More Modern Chemical Techniques*, RSC Publishing, 2001.
10. W. Zhou, R. Apkarian, Z. Wang and D. Joy, *Sanning Microscopy for Nanotechnology*, Springer, New York, 2007.
11. T. Tozawa, J. T. Jones, S. I. Swamy, S. Jiang, D. J. Adams, S. Shakespeare, R. Clowes, D. Bradshaw, T. Hasell, S. Y. Chong, C. Tang, S. Thompson, J. Parker, A. Trewin, J. Bacsa, A. M. Slawin, A. Steiner and A. I. Cooper, *Nat. Mater.*, 2009, **8**, 973.
12. O. T. Wilcox, A. Fateeva, A. P. Katsoulidis, M. W. Smith, C. A. Stone and M. J. Rosseinsky, *Chem. Commun.*, 2015, **51**, 14989.
13. OriginPro., *Journal*, 1991-2015.
14. L. R. Snyder, J. J. Kirkland and J. L. Glajch, *Practical HPLC Method Development*, John Wiley & Sons inc., Canada, 1997.

Chapter 3 Al FDC MOF

3.1 Overview

A large number of MOFs have been reported using divalent metal ions, reported MOFs with trivalent group XIII (G13) elements however, are far fewer.[1-3] This is strange since G13 MOFs, especially aluminium, have been studied and reported to have high thermal and chemical stability, making them ideal candidates for future applications.[4] The use of aluminium is especially desirable due to its low toxicity and high availability with high purity and low cost.

Aluminium MOFs have been of great interest to industry due to their aforementioned attributes, as evidenced by the large number of patents filed by BASF.[5] As well as this, academic groups such as Ferey et al have conducted some revolutionary research into aluminium MOFs.[6]

There are a number of common inorganic building units (IBUs) amongst G13 MOFs, while very few different unique IBUs have been reported for aluminium MOFs. All reported aluminium IBUs consist of octahedrally co – ordinated aluminium ions, which are then connected to each other. There has only been one reported case of a MOF containing isolated aluminium octahedra, CAU-4.[7] The majority of IBUs found for aluminium MOFs are chains of $Al(OH)_2(COO)_4$ octahedra, both *trans* and *cis* – corner sharing. Here, *trans* and *cis* – refer to the relative positions of the co – ordinated hydroxy groups. There is significant correlation between using water as the solvent in the synthesis, and the formation of the chain IBU. When other solvents are used for the synthesis, more complex IBUs have been reported in the form of ring shaped IBUs.

The first Aluminium MOF, MIL-53, was reported in 2004,[8] causing a subsequent study of aluminium MOFs, many of the syntheses used water as the solvent, at

reaction temperatures of 220 °C for three days. From here, other solvents and mixtures such as DMF and alcohols were used, leading to the discovery of the more complex IBUs mentioned earlier. Since then, milder reaction conditions and substantially shorter reaction times have been used to synthesise Al – MOFs.

The change in shape of the linker causes a change in IBU, which, as a result, changes the final topology of the framework. The change in shape comes from the change in angle between the two co – ordinating group, for example, reducing the angle from 180 ° as in terephthalic acid (BDC) used in MIL-53 to 120 ° as in isophthalic acid used in CAU-10, the IBU changes from *trans* – corner – sharing octahedra to *cis* – corner – sharing octahedra.[1] CAU-10 also undergoes a phase transition upon removal of guest molecules despite being much more rigid than MIL-53. Furthermore, once the angle is reduced further, to 60 ° as in phthalic acid used in CAU-15, the IBU no longer consists of corner – sharing octahedra, but instead is made up from edge – sharing octahedra.[9]

3.1.1 FDC : A Renewable Linker

2,5 – Furandicarboxylic acid (FDC) has been identified by the US Department of Energy as a priority chemical for establishing the "green" chemistry industry of the future.[10]

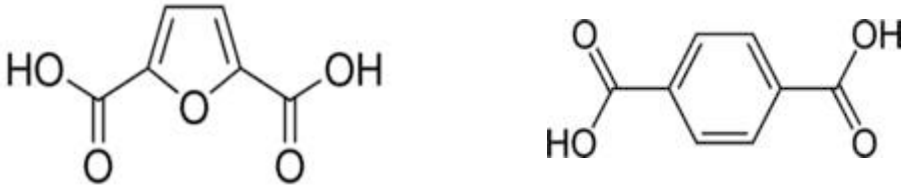

Figure 3.1. FDC (left) and BDC (right).

Due to the similarities between FDC and BDC, it has also been named as an important renewable building block, which can replace BDC in polymer

synthesis, specifically polyester and other current polymers containing an aromatic portion.[10] Recently, DuPont announced that they would be using FDC in the production of PTFE, while in 2016, BASF and Avantium announced that they were to set up a plant to produce FDC based on fructose.

Recently, a MOF using aluminium with this FDC linker was reported as MIL-160 and studied for its application in chillers. Although the paper reports the use of this material for a specific application, the bulk purity was not mentioned in the article. The structure of the material was reported in this article, refined using a simulated model based on the structure of CAU-10 (shown in Figure 3.2), however, the structure was shown to be very similar to that presented in this thesis, however, it was refined to a lower symmetry space group ($I4_1md$) than that presented here ($I4_1/amd$). These slight structural differences between the two were difficult to deduce. This paper was published after majority of the work had been done for this chapter already.[11]

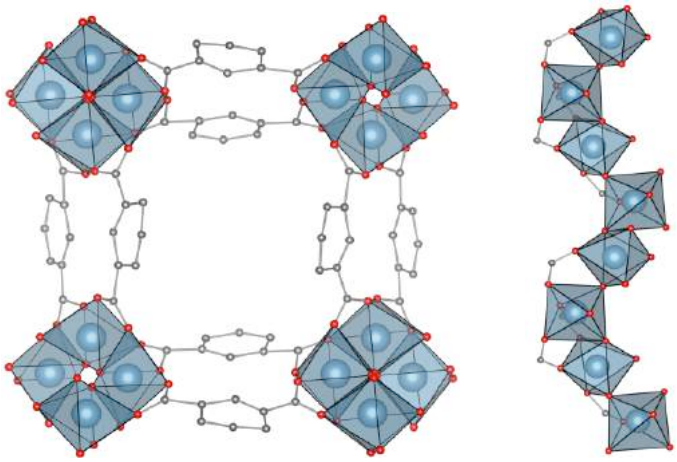

Figure 3.2. Structure of CAU-10, square shaped channels shown (left) along the crystallographic *c* - axis and helical chains (right) shown along the crystallographic *b* – axis. Carbon, oxygen and aluminium represented by grey, red and blue spheres respectively. Hydrogen atoms have been omitted for clarity. Figure adapted from reference.[1]

Here, Al: FDC has been synthesised, fully characterised and the purity has been measured. The structure, has been solved and refined to the space group

*I*4$_1$/*amd*, using PXRD data collected at Diamond Light Source synchrotron facility, by Dr George Whitehead. The material has been tested for some potential applications from gas separations, ammonia uptake, and separation of xylene isomers.

3.2 Synthesis

3.2.1 Exploring Synthetic Conditions

$Al(NO_3)_3.9H_2O$ and 2,5-furandicarboxylic acid (FDC) were purchased from Sigma-Aldrich in 97% and 98% purity respectively. *N*,*N*-dimethylformamide (DMF), was purchased from Fischer Scientific in 99.8% purity. All reagents and solvents were used without any further purification.

Synthesising a phase pure, crystalline, porous MOF is not particularly straightforward. There are many factors that can affect the final product; reaction temperature and time, metal: linker molar ratio, concentration of starting reagents, solvents used, metal salt, and the addition of a modulator. A high throughput approach must be adopted in order to ensure that all factors and their effects are investigated, thus allowing for a final, optimised synthetic protocol for the desired material. An example of such approach can be found in appendix I.

The synthetic protocol for MIL-53(Al) was selected as a starting point for this material since the desired product would have the MIL type topology of Al(OH) chains. $Al(NO_3)_3.9H_2O$ (0.375 g, 3.5 mmol), FDC (0.265 g, 1.7 mmol) and deionised water (5 mL) were charged into a 21 mL Teflon-lined stainless steel Parr bomb, and reacted at 220 ^oC for 72 hours. The metal to linker molar ratio was altered (0.1:1, 0.5:1, 0.75:1, 1:1, 1.25:1, 1.5:1, 1.75:1 2:1) in parallel reactions to investigate its effect on the product, however, all reactions yielded amorphous gels as opposed to crystalline powders. It was clear that another solvent was

necessary to aid the reaction, DMF was chosen due to its ability to dissolve the FDC linker. It was clear that carrying out exploratory syntheses using this type of reaction vessel would quickly become highly inefficient, therefore, 40 mL glass vials with Teflon screw-top lids were tested as potential reaction vessels. The same reactions as before were carried out in both 40 mL glass vials and Parr vessels in order to provide evidence that reactions in these glass vials yield the same product as seen in the high pressure vessels. Here, DMF was used as the solvent instead of deionised water. The products were washed with DMF and $CHCl_3$ and left to dry in air before being analysed by PXRD on (CMD instrument). All products were amorphous, therefore, since the Parr vessels gave no better products, all future reactions were carried out in the glass vials. Reaction temperatures and times were also investigated, using 220, 150 and 120 ^oC and 72, 48, 24 hours were investigated along with the influence of a modulator (2-furoic acid and HCl), which were added in varying amounts. The addition of the modulator had no effect on the crystallinity or purity and was therefore unnecessary. The next set of reactions were ran at 150 and 120 ^oC for 24 and 48 hours the molar ratios were such that the linker was always in excess, since it was necessary to ensure all Al was reacted and incorporated into the material. The DMF/H_2O ratio was altered between reaction sets but the overall volume remained constant at 5 mL. The products were washed with DMF, THF and ethanol and left to dry in air. The best product in terms of yield, crystallinity, purity and surface area came from the reaction of 0.6 mmol $Al(NO_3)_3.9H_2O$, 1 mmol FDC, 3 mL H_2O and 2 mL DMF, at 120 ^oC for 24 hours.

3.2.2 Optimised Synthesis for Al:FDC material

A 1M stock solution of $Al(NO_3)_3.9H_2O$ in H_2O and a 0.7M stock solution of 2,5-furandicarboxylic acid in DMF were prepared. To a 40 mL Teflon capped glass

vial, FDC solution (1.43 mL, 1 mmol), $Al(NO_3)_3$ solution (0.6 mL, 0.6 mmol) H_2O (2.40 mL), DMF (0.57 mL) were added. The reaction mixture was heated up to 100 ^oC, at a rate of 2.5 ^oC / min for 12 hours before cooling to room temperature at 0.2 ^oC / min. The white solid was filtered and washed with DMF (4 x 20 mL), THF (3 x 20 mL) and Ethanol (3 x 20 mL), and left to pump dry. Once dry, 140 mg of the solid was obtained as a white powder. The material was activated at 155 ^oC, in accordance with the TGA analysis, under vacuum (10^{-2} mbar) overnight to remove guest solvent molecules. A final yield of approximately 95 mg was obtained (formula $[Al(OH)C_6H_2O_5]$).

3.3 Characterisation

3.3.1 Structure

The structure of Al:FDC was solved by Dr George Whitehead using Jana software using PXRD data. Starting with the lattice parameters of CAU-10 and then using a Rietveld refinement on PXRD data obtained from a completely desolvated sample, the final structure was able to be successfully determined. Al: FDC crystallises in the tetragonal space group $I4_1/amd$, with lattice parameters a = 21.0627(12) Å, c = 10.5018(16)Å and V = 4659.0(8) $Å^3$. Data collection and refinement parameters are presented in Appendix II.

The IBU of this material is one which is commonly seen in aluminium MOFs and is shown figure 3.3, infinite chains of *cis*-connected, corner sharing $AlO_4(OH)_2$ octahedra. Here, *cis* refers to the relative positions of the co – ordinated hydroxy groups. As discussed earlier, due to the smaller angle between carboxylate groups, *cis* – corner – sharing octahedra were expected in this material.

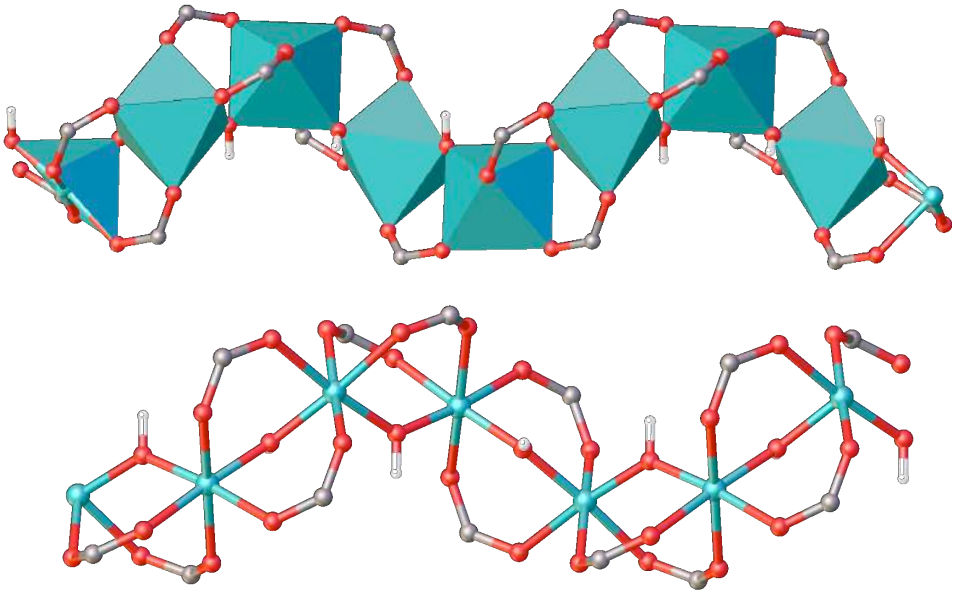

Figure 3.3 Al(OH) chains in Al: FDC. Al (turquoise), carbon (grey), oxygen (red), hydrogen (white).

This connection motif gives rise to a four – fold screw axis, or helix, along the unique axis of the structure. The framework is then finalised by the connection of each of these helical chains to four adjacent chains via bridging μ_4 - FDC linker molecules. The view along crystallographic *a* and *b* – axes are identical.

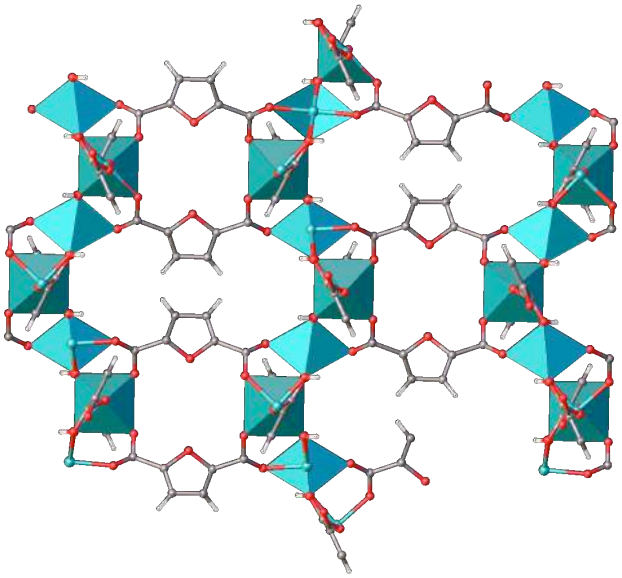

Figure 3.4 Al:FDC viewed along crystallographic *a* and *b* – axes. Al (turquoise), carbon (grey), oxygen (red), hydrogen (white).

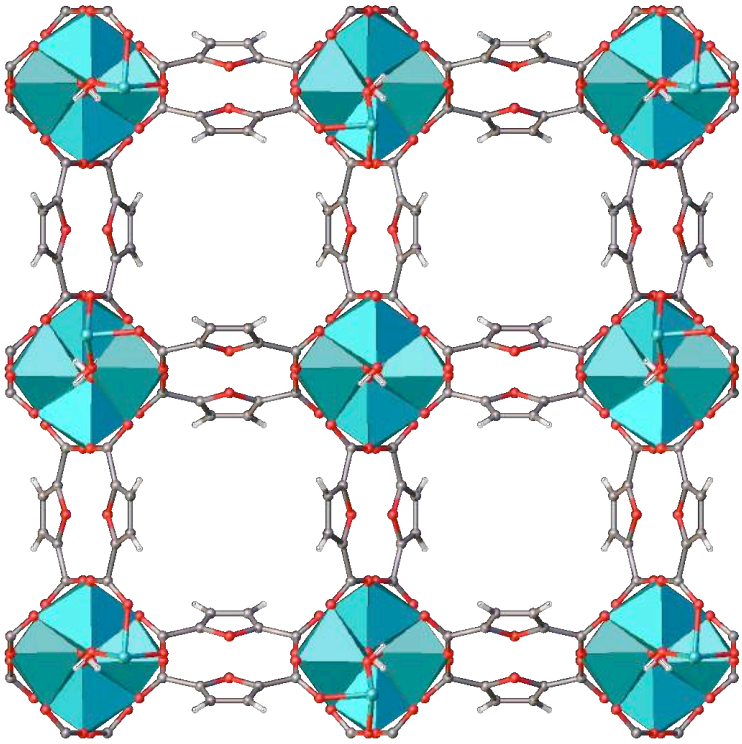

Figure 3.5 Al: FDC viewed along crystallographic *c* – axis. Al (turquoise), carbon (grey), oxygen (red), hydrogen (white).

The non – linearity and asymmetry of the FDC linker is balanced by its adjacent bridging linker, whereby the furanic rings point in opposite directions shown in figure 3.5. The symmetry of the structure is maintained throughout due to this motif being rotated about 90° along the infinite Al(OH) chains. The opposing facing furanic rings gives rise to an interesting feature which, to the best of our knowledge has not yet been reported; 16 – membered pseudo crown ethers, shown in figure 3.4. These run down the Al(OH) chains and due to the aforementioned 90 ° rotation, two of these pseudo crown ethers lie parallel with the plane of the Al(OH) chains while two lie orthogonal to the plane.

There is some porosity along all three crystallographic axes, majority comes from the large channels running along the crystallographic *c* – axis, where the furanic oxygen atoms are pointing away from the centre of the channel (**Figure 3.5**).

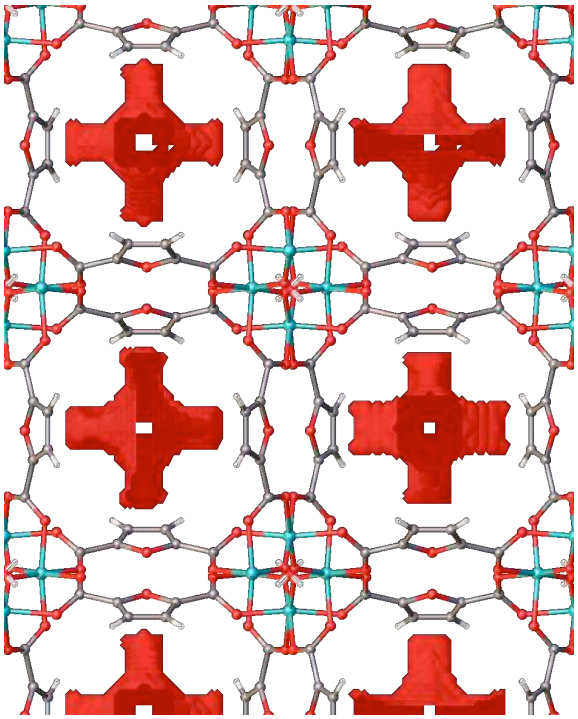

Figure 3.6. Voids (red masses) of Al: FDC running along the crystallographic *c* – axis. Al (turquoise), carbon (grey), oxygen (red), hydrogen (white).

Figure 3.6 shows the voids of this material along the crystallographic *c* – axis calculated using a nitrogen sized probe. The largest sphere that can penetrate this channel has a diameter of 4.40 Å, making it large enough to accommodate a number of common gas molecules from helium and water (kinetic diameters of 2.60 Å and 2.65 Å respectively), to H_2S (3.60 Å) and potentially propane which has a kinetic diameter of 4.30 Å. This shows some early promise for this material and its use in future applications in gas storage.

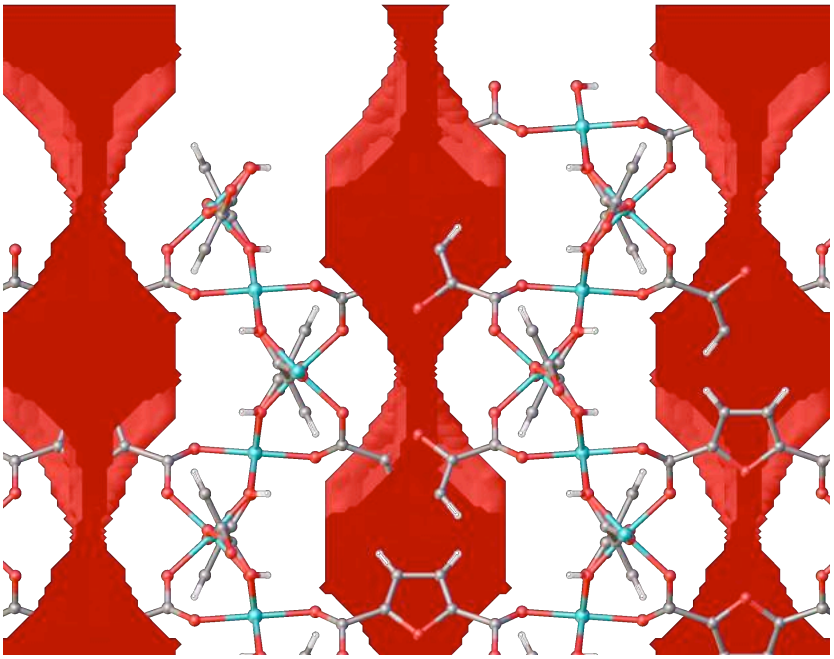

Figure 3.7 voids (red masses) of Al: FDC running along the crystallographic *c* – axis viewed along the crystallographic *a* and *b* - axes .Al (turquoise), carbon (grey), oxygen (red), hydrogen (white).

The channels that run along the crystallographic *a* and *b* – axes, shown in Figure 3.7, are identical and have limited accessibility, both can be penetrated by spheres with a radius of 1.00 Å, making them too small to accommodate most gas molecules.

The total solvent accessible volume per unit cell is 1710.9 $Å^3$, which equates to 36.7 % of the structure. Using this data, the theoretical pore volume was calculated to be 0.32 $cm^3\ g^{-1}$. The largest spherical void of this material was found to have a radius of 2.20 Å, showing that this material has great potential for the uptake of many gases.

3.3.2 PXRD

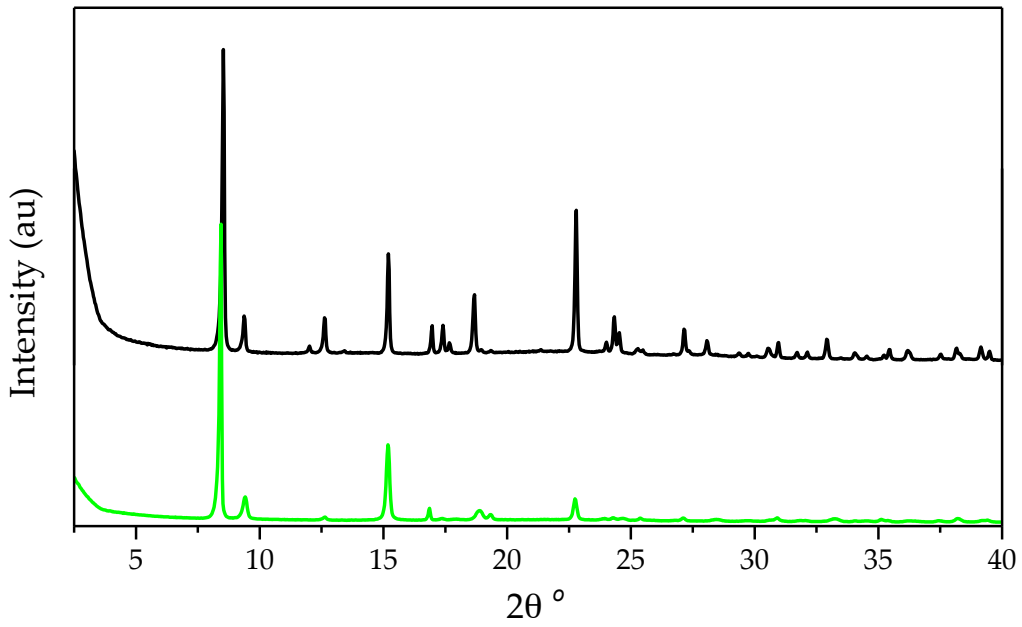

Figure 3.8. PXRD of Al: FDC, as-made (black) and activated (green).

The PXRD data, displayed in figure 3.8, shows a highly crystalline material, with many sharp peaks, which, after activation, remains to be the case. This shows that the structure remains intact and shows no signs of a phase change as seen in MIL-53. This is surprising since this MOF has a similar shaped linker to that of CAU-10 which does undergo a phase change upon activation.[1] This implies that this MOF is a lot more rigid than its benzene counterpart and no "breathing" effect is observed upon uptake and removal of gases.

Figure 3.8, does however, shows that some peaks do lose a lot of their intensity after activation, which could be due to the removal of ordered guest molecules within the structure. This was problematic when trying to solve the structure from the PXRD data as it was not possible to accurately model water molecules to get a good fit. Therefore, a PXRD pattern of the fully desolvated material was required. A sample of the material was activated under the same, established procedure, and packed into a 0.7 mm borosilicate capillary under an inert atmosphere and sealed, ensuring no exposure to air. The data for this sample

was collected at the synchrotron facility in Didcot and it was this data (Figure 3.9) that was used by Dr George Whitehead to solve the structure using JANA software.

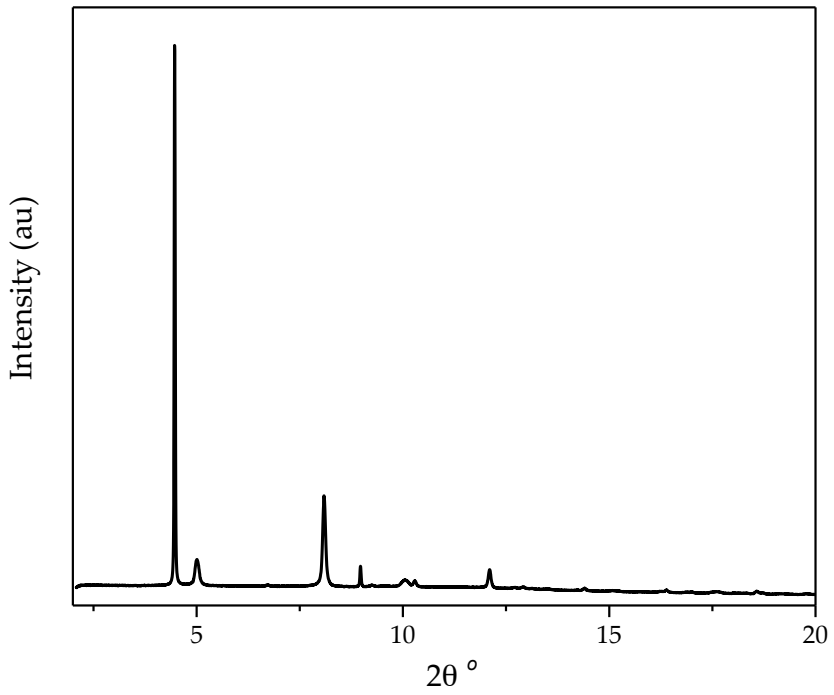

Figure 3.9. PXRD of Al: FDC obtained from the synchrotron at Diamond Light Source.

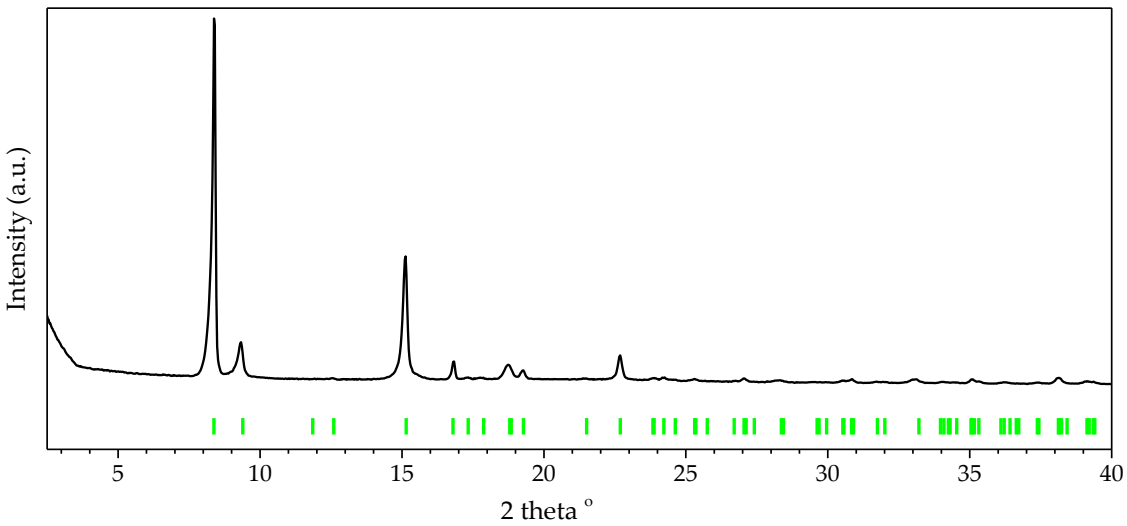

Figure 3.10. PXRD of a completely desolvated sample of Al: FDC, indexed to the unit cell. Calculated peaks indicated by green tick marks.

3.3.3 TGA

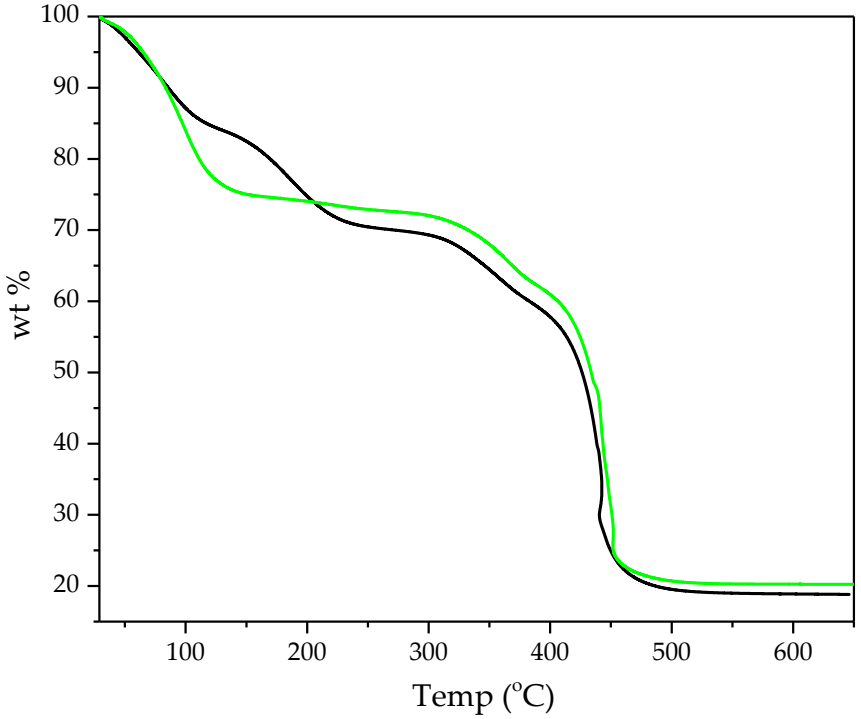

Figure 3.11. TGA trace of Al: FDC, as-made (black) and activated (green).

The TGA trace of the as-made material (Figure 3.11) shows a total of three distinct mass losses. The first of which (ca 23 % up to 100 °C) can be attributed to the removal of relatively low boiling point solvents used during the synthesis and washing procedure of the material. The second mass loss (ca 15 % from 130 °C to 230 °C) is due to the removal of DMF, which has been trapped inside the pores or adsorbed onto the surface of the MOF during the synthesis and washing procedures. The third and final mass loss occurs at ca 300 °C and is caused by the decomposition of the material, all of the organic content combusts, leaving behind Al_2O_3 residue.

From this measurement, an activation temperature of 210 °C was chosen to ensure full removal of trapped solvent. This temperature however, had a

detrimental effect on the crystallinity of the material, therefore different activation temperatures were investigated. The difficulty here is maintaining the crystallinity of the product while still removing all guest solvent molecules. The finalised activation protocol involved heating the material under vacuum (10^{-2} mbar) overnight at 155 ^{o}C.

The TGA trace of the activated material (Figure 3.11) shows only two distinct mass losses proving that all the unwanted DMF has been removed from the material during the activation procedure. There is an initial mass loss, which is due to the removal of the moisture that has been adsorbed onto the material from the atmosphere. This is not unusual since a number of aluminium MOFs exhibit the same phenomenon. It has been reported that the water hydrogen bonds to the hydroxy chains in the material, giving rise to the material's hygroscopicity.[12] The final residue of Al_2O_3 equates to 20 % of the original mass, and therefore 27 % of the dry mass (taken from the first plateau). 52.94 % of the alumina residue is due to Al, therefore it can be calculated that Al makes up 14.29% of the dry material. According to the formula $Al(OH)(C_6H_2O_5)$, aluminium makes up 13.62% which shows that the material has the expected formula and there is very little alumina formed during the synthesis. To ensure that the TGA data was correct, further analysis was completed.

3.3.4 Elemental Analysis

CHN analysis confirmed that the activation procedure was successful as indicated by the 0 % nitrogen content (Table 3.1). Based on the formula $Al(OH)(C_6H_2O_5)$, carbon has an expected content of 36.36 % and 1.52 % for Carbon and Hydrogen respectively. The measured values of 32.32 % and 2.88 % for Carbon and Hydrogen respectively indicate an uptake of atmospheric water which is confirmed by the TGA trace. If 1.5 water molecules are added into the

formula, the theoretical contents of carbon and hydrogen stand at 32.02 % and 2.69 % respectively, which agree with the measured values.

$Al(OH)(C_6H_2O_5).\ 1.5H_2O$		
Element	Expected %	Measured %
C	32.02	32.32
H	2.69	2.88
N	0.00	0.00

Table 3.1. Elemental analysis of an activated sample of Al: FDC.

1.5 water molecules per Aluminium equates to 12 % of the material implying that the initially adsorbed water molecules then provide another binding site for extra molecules to bind to. The discrepancy between the TGA and elemental analysis regarding the amount of adsorbed water stems from the time difference between the two analyses. According to the TGA of the activated material, a mass loss of approximately 25 % due to adsorbed water equates to the formula $Al(OH)(C_6H_2O_5).\ 3H_2O$.

All of the data collected thus far, points to a phase pure material with the dry formula [$Al(OH)(C_6H_2O_5)$]. Due to the material's ability to uptake water from the atmosphere, it is of great importance that it undergoes a light activation by heating it to 100 ^oC under dynamic vacuum, to ensure the removal of these guests, before any further measurements.

3.3.5 Surface Area Measurement

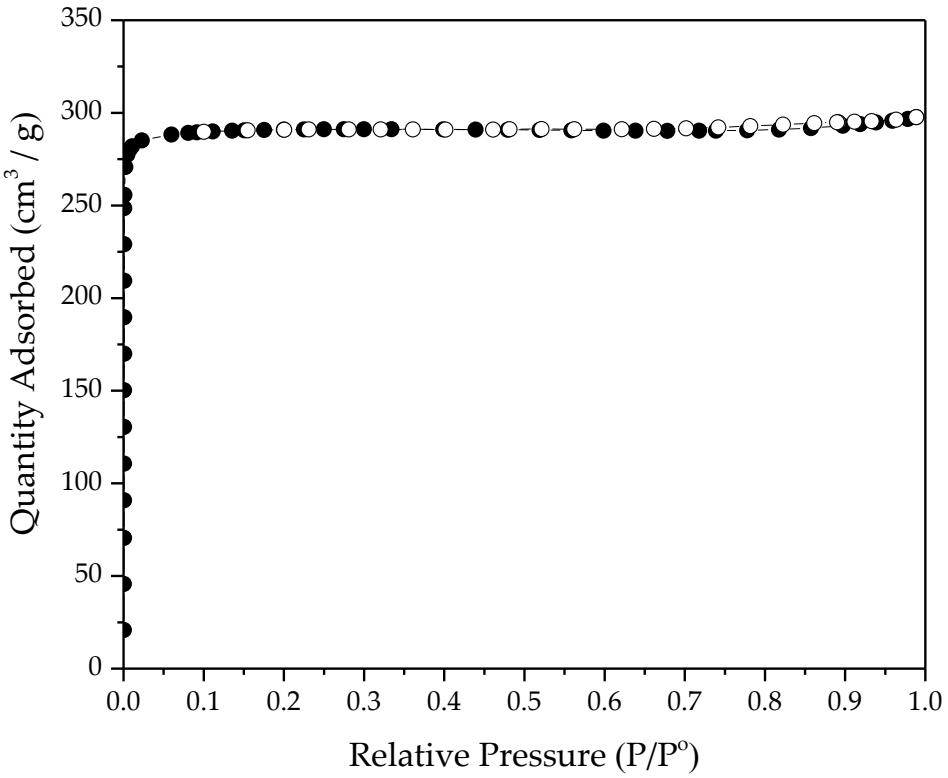

Figure 3.12. N_2 adsorption isotherm on Al: FDC at 77.3 K.

The N_2 adsorption isotherm for this material, shown in Figure 3.12, follows the trend of a type I, which is characteristic of microporous materials. The BET model was applied between the relative pressure range of 0.0015 and 0.1 to calculate the surface area of 1150(30) $m^2\ g^{-1}$. The pore volume was calculated from the adsorption isotherm to be 0.44(13) $cm^3\ g^{-1}$, which is in agreement with the theoretical pore volume (0.33 $cm^3\ g^{-1}$), calculated from the crystal structure.

This data exceeds that which was reported for CAU-10, which has a reported BET area of 635 m^2 / g,[8] showing that Al: FDC has comparable attributes.

3.3.6 SEM

SEM images (Figure 3.13) show a single, uniform crystallite morphology throughout the material, cuboidal blocks, which stack together to form very structured clusters. The lack of amorphous content (which would be indicated by the presence of fluffy matter), further proves that there is very little or no amorphous alumina formed during the synthesis.

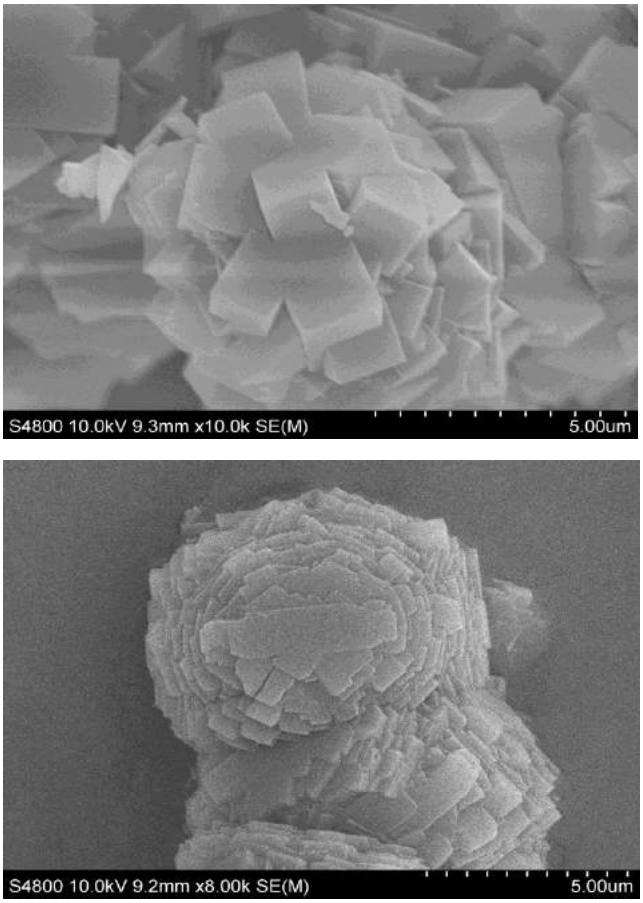

Figure 3.13. SEM images of an activated sample of Al: FDC

3.4 Heat of Adsorption of gases

When a MOF has a higher affinity towards one gas over another, it makes them a probable candidate for separating a mixture of the two. A method for determining a material's affinity for a specific gas, is to measure the gas

adsorption isotherm. The ability to uptake CO_2 and ultimately separate it from gaseous mixtures is highly useful in reducing the amount of greenhouse gases released into the atmosphere. Currently, amine scrubbers are the common material used for this application, however, the activation of such materials can be difficult.

3.4.1 CO_2 Adsorption Measurements

The adsorption measurements for CO_2 were carried out at 273 K, 283 K and 293 K, the data is presented in Figure 3.14.

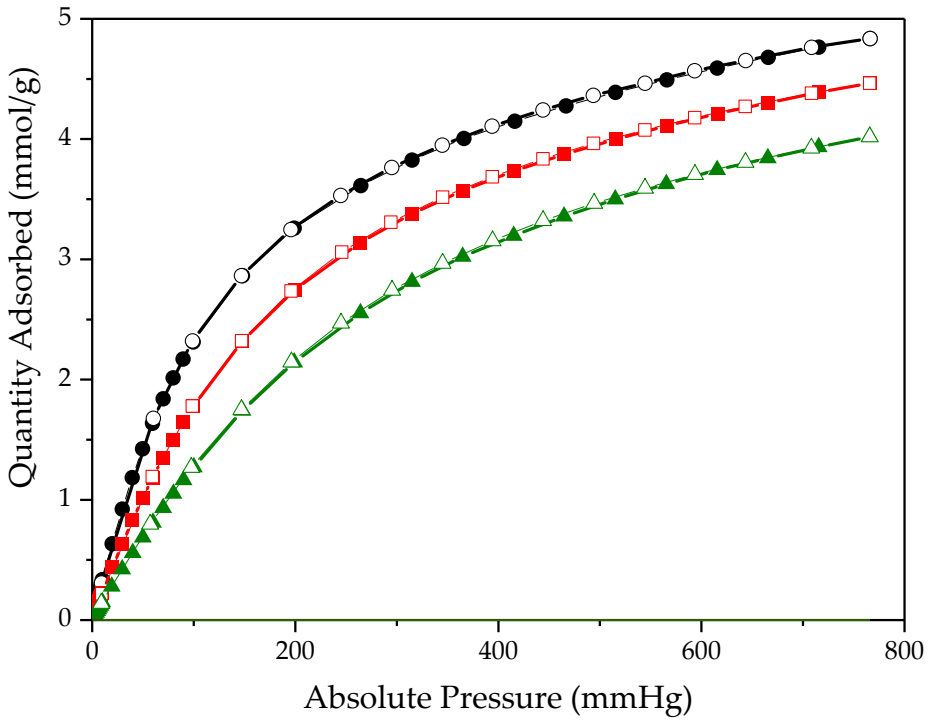

Figure 3.14. CO_2 adsorption isotherms of Al: FDC at 273 K (black), 283 K (red) and 293 K (green). Adsorption branches are represented by solid symbols and desorption branches represented by hollow symbols.

From the isotherm measured at 293 K, the ability of Al: FDC to adsorb CO_2 can be evaluated and compared with other MOFs. According to a recent article, the ideal CO_2 adsorbents should have high CO_2 uptake and selectivity at a

temperature near 40°C and at a pressure of 0.15 bar.[13] For Al: FDC, the closest temperature to 40°C that was measured was 293 K, based on this, the quantity adsorbed at 0.15 bar (approximately 112 mmHg) equates to 1.37 mmol / g.

Many MOFs have a reported uptake of between 1 and 4 mmol / g within the temperature range of 290 – 300K, with a large number of materials reporting uptakes of less than 1 mmol / g.[13] Some MOFs, however, have reported huge uptakes of CO_2 of almost 6 mmol / g at 298-303 K.[13]

There are two highly common functional sites exhibited by materials with high CO_2 uptake; open metal sites and Lewis basic sites. Open metal sites form in MOFs when terminally coordinated solvent molecules are removed. These open metal sites can behave as Lewis acidic sites, causing strong polarisation of gas adsorbents, therefore increasing the capability of CO_2 capture. The MOF series with the highest reported CO_2 adsorption capacity is the M-MOF-74 series where M = Mg, Ni, Co and Zn, particularly Mg-MOF-74, with an uptake of 5.87 mmol / g at 0.15 bar and 303 K.[14] This MOF makes use of a high concentration of open metal sites which face into the pores, resulting in its exceptionally high uptake of CO_2.

PEI-MIL-101-100, makes use of Lewis basic sites to enhance its capability. MIL-101 was loaded with different wt% of polyethyleneimine (PEI), which binds to the open metal sites of the chromium cluster IBU. This provides the MOF with enhanced basicity, resulting in a CO_2 uptake of 4.02 $mmol^{-1}$ g^{-1} at 0.15 bar and 298 K.[13]

Al: FDC has a comparable uptake of CO_2 to many reported materials under these conditions, but with PSM of the linker, introducing extra functionality, e.g. hydroxyl groups, could enhance its capability, which is some potential future works to be carried out on this material.

From the isotherms at sequential temperatures, the isosteric heat of adsorption at zero coverage can be calculated for CO_2 onto the material.

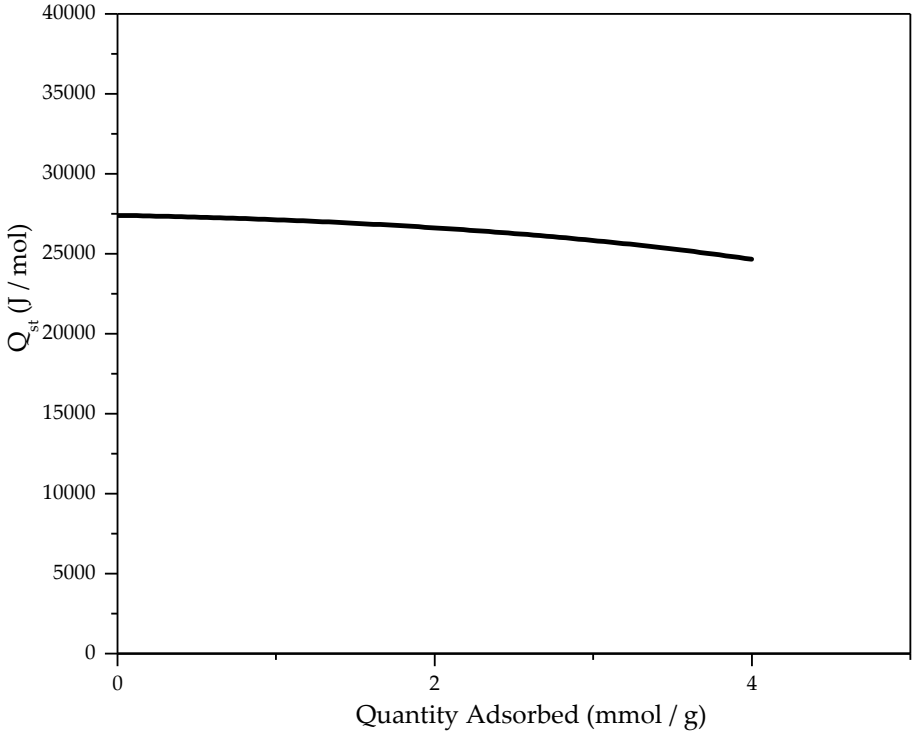

Figure 3.15. Heat of adsorption for CO_2 onto Al: FDC

Figure 3.15 shows that the isosteric heat of adsorption at zero coverage (quantity adsorbed = 0) for CO_2 onto the material is 27.5 kJ / mol. Al: FDC displays a comparable value to many other reported MOFs though, which fall within the range of 20 – 30 kJ / mol, while many others exhibit values of almost double.[15] These large values can be attributed to the use of PSM as discussed before, for example, ethylenediamine functionalised CuBTTri (BTTri refers to 1,3,5-tris(1,2,3-triazol-5-yl)benzene) exhibits a Q_{st} of 90 kJ / mol, while the parent material has a Q_{st} of 21 kJ / mol.[16]

3.4.2 CH_4 Adsorption Measurements

Natural gas, primarily consisting of methane, has many uses such as fuel for vehicles, heating, electricity generation and as a chemical feedstock in the

manufacture of plastics. In order for the gas to be used effectively, it must be transported from source. The major problem with transporting such gas is due to its low density, meaning it is not easy to store or transport by vehicle. The current method of storing and transporting methane involves liquefaction, which can be quite a long and difficult process, which includes keeping the temperature sufficiently low so as to prevent any loss due to boiling. A potential solution to circumnavigate this problem involves the sorption of methane onto porous materials, the most common sorbent used right now is activated carbon which serves as the benchmark for methane adsorption. Methane sorption isotherms onto Al: FDC were ran at three different temperatures (273 K, 283 K and 293 K) in order to calculate the isosteric heat of adsorption. The data for these experiments are shown in Figure 3.16.

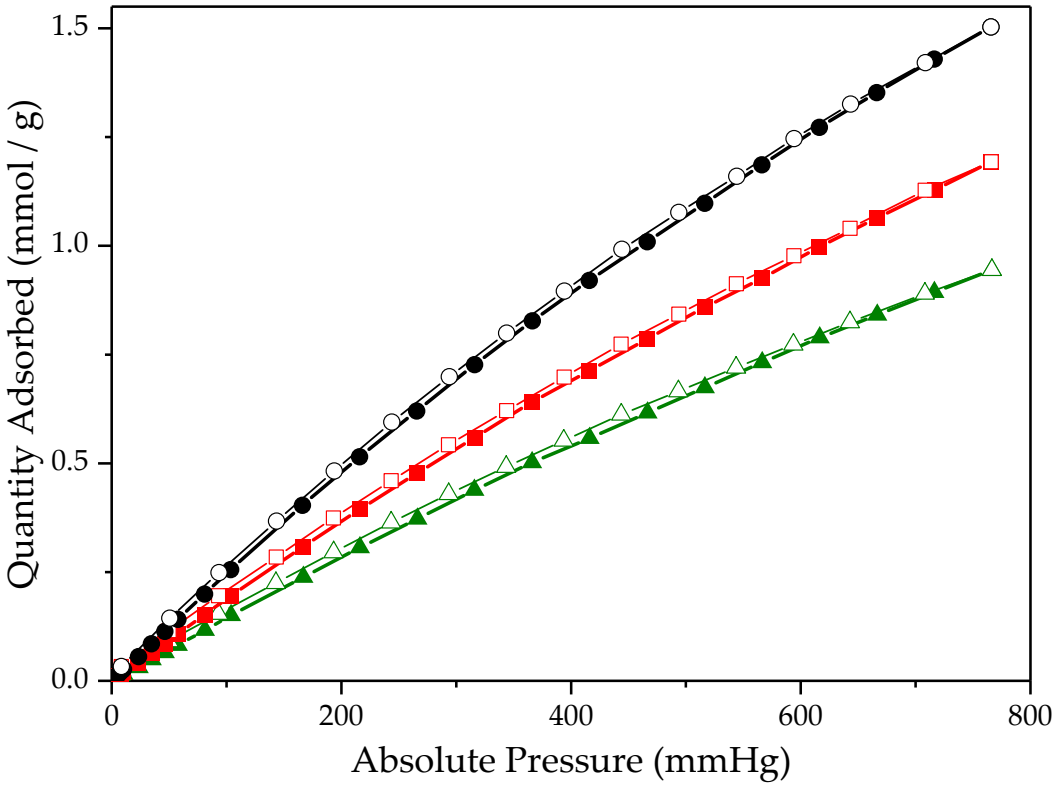

Figure 3.16. CH_4 adsorption isotherms onto Al: FDC at 273 K (black), 283 (red) and 293 (green). Adsorption branches are represented by solid symbols and desorption branches are represented by hollow symbols.

Compared with the CO_2 sorption isotherms, it is immediately noticeable that the quantity adsorbed is significantly lower for CH_4. This is to be expected for multiple reasons. The kinetic diameter of methane is 380 pm compared with that of carbon dioxide which is 330 pm, combined with the linear nature of carbon dioxide means that it is easily adsorbed into the pores of the material. Carbon dioxide acts as a Lewis acid, using the carbon atom as an electron pair acceptor. As discussed earlier, Al:FDC material has ordered Lewis basic sites running throughout, in the form of the Al(OH) chains, which encourage the carbon dioxide molecule to interact with the material.

Methane on the other hand has no such interaction with the material and therefore Al:FDC has less of an affinity towards methane over carbon dioxide.

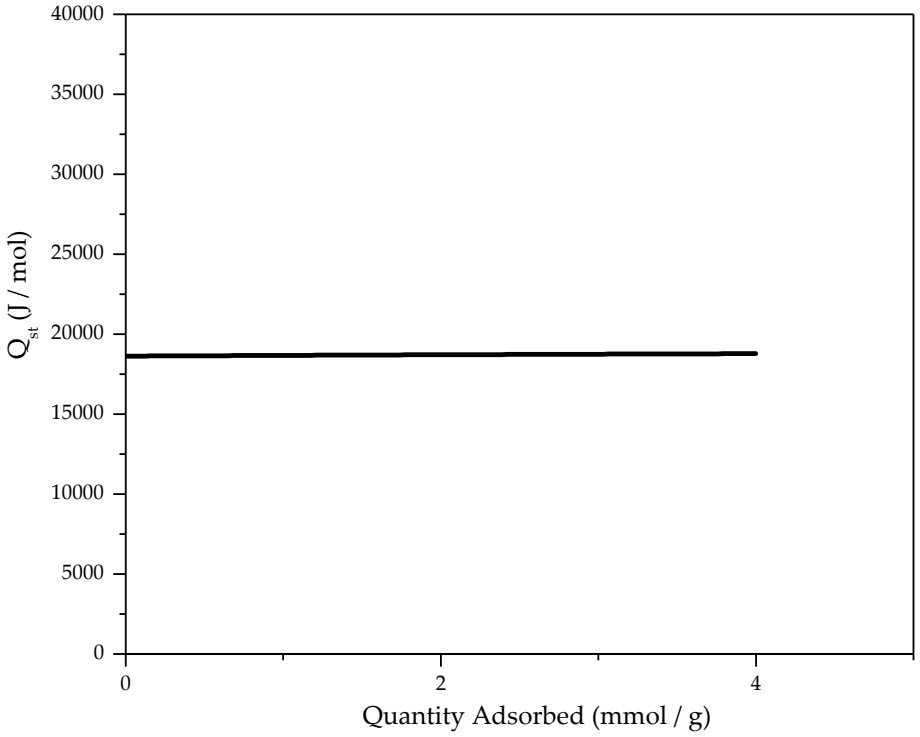

Figure 3.17. Heat of adsorption for CH_4 onto Al: FDC

The isosteric heat of adsorption at zero coverage can be calculated for methane onto the material using the virial fit. A value of 18.6 kJ / mol was calculated

from Figure 3.17, which is comparable to that of MIL-53 which reported 18.3 kJ / mol.[17] The range of reported heats of adsorption varies from 21 kJ / mol for Ni_2dobdc (dobdc refers to 2,5-dihydroxyterephthalic acid) to 12 kJ / mol for MOF-5.[18]

As with CO_2, in order for the material to be useful for this application, the isosteric heat of adsorption must be large enough to influence a high affinity for the gas, but low enough for regeneration of the material i.e. removal of the gas upon requirement. It was reported that the ideal heat of adsorption for the storage of methane is 18.8 kJ / mol,[19] meaning that Al: FDC is a very promising candidate for such an application.

3.5 High pressure gas sorption

High pressure sorption measurements were carried out on a Hiden analytical Intelligent Gravimetric Analyser at 25 ^oC. Since the material readily adsorbs water from the atmosphere, which can inhibit the adsorption of other gases, an extra activation step was required before this measurement was carried out. Approximately 33 mg of material was loaded into the instrument and activated at 100 ^oC overnight under vacuum overnight.

The data for these measurements is shown in Figure 3.18. It can be seen that they agree further with previous results, in which it can be seen that Al: FDC has a higher affinity towards CO_2 than CH_4. Approximately 97 cm^3 / g and 151 cm^3 / g of CH_4 and CO_2 respectively were adsorbed.

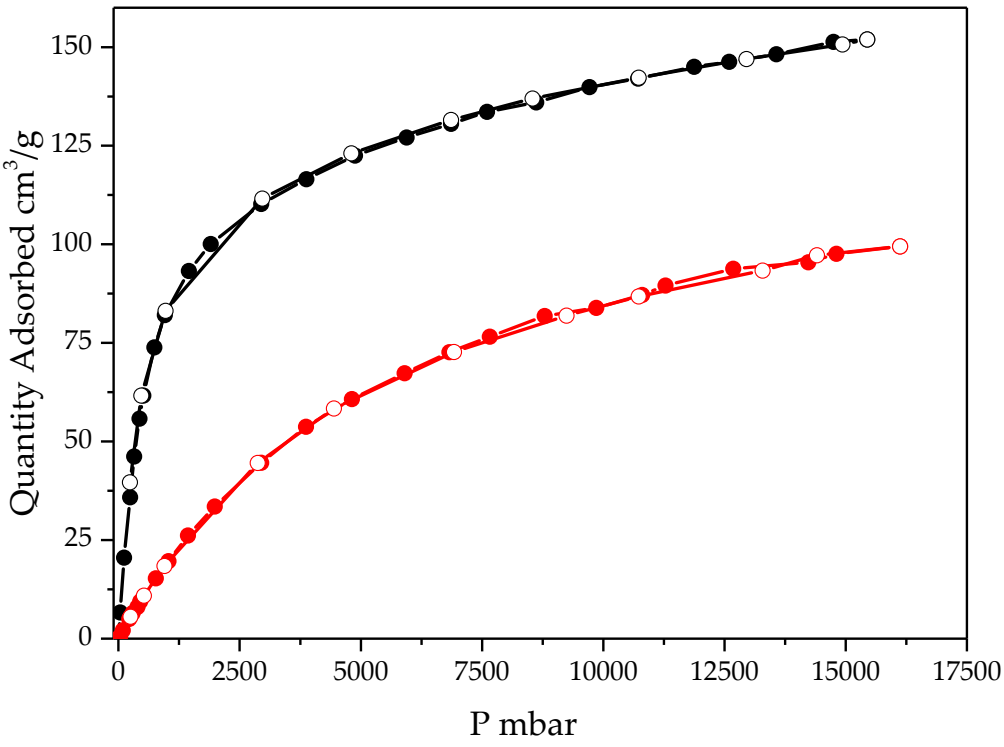

Figure 3.18. High pressure CO_2 (black) and CH_4 (red) isotherms onto Al: FDC.

Since all results of previous measurements show that Al: FDC has a higher affinity for CO_2 over CH_4, with comparable isosteric heats of adsorption, it was hypothesised that it could separate a binary mixture of the gases.

3.5 Gas Separation Experiments

CO_2 is the main, undesirable compound present in natural gas, therefore separating a mixture of the two gases is very important due to the need for pure CH_4 for use in many industrial and domestic applications. MOFs have shown some promise in this field, with some out – performing the usual industrial adsorbents such as activated carbons and zeolites.

3.5.1 CO_2 / CH_4 Separation Experiments

Separation experiments were ran using the setup described in chapter 2, by Dr Andrew Stephenson in Professor Andy Cooper's research group.

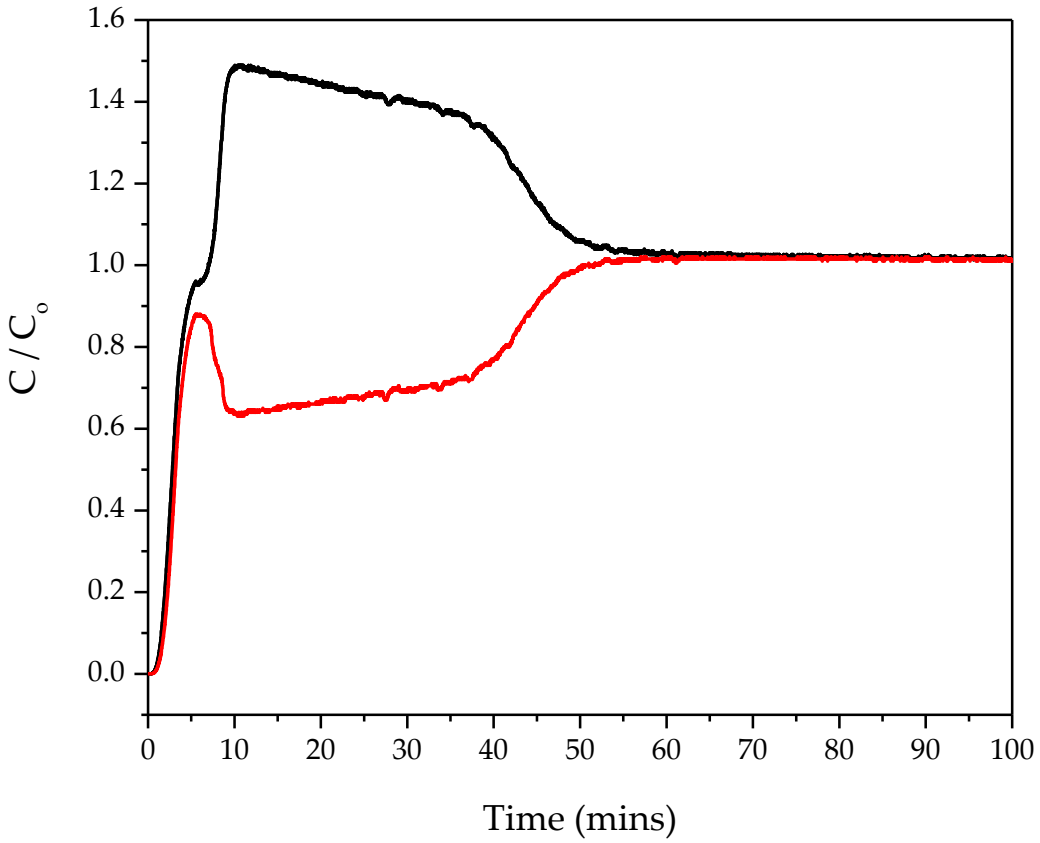

Figure 3.19. Breakthrough measurements of CO_2 (red) and CH_4 (black).

The results of the breakthrough experiments (Figure 3.19) are interesting as initially, it can be seen that both CO_2 and CH_4 breakthrough together up to c.a. 5 minutes. After this, there is a steep increase in CH_4 detection while the CO_2 decreases, this was the expected result since the adsorption isotherms discussed earlier show that Al: FDC has a higher affinity towards CO_2 over CH_4. The reason for this initial breakthrough of CO_2 is unknown, although if this data is compared with the adsorption isotherms shown in the previous section, at 293 K, the adsorption of CO_2 is slow. Since the material was activated prior to both of these measurements, the slow adsorption is not due to competition between water and CO_2, and even when the rate of gas flow is reduced by half, the curve remains the same, implying that this is not due to a kinetic effect.

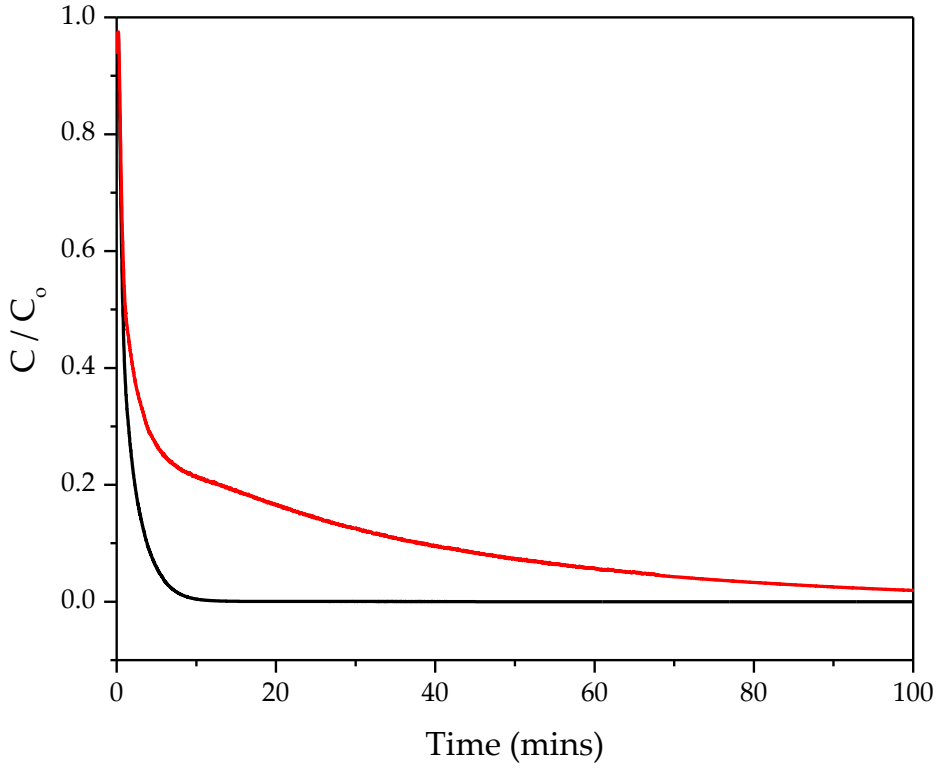

Figure 3.20. Desorption profiles of CO_2 (red) and CH_4 (black).

The slow desorption seen by CO_2 compared with CH_4 (shown in Figure 3.20), is also expected due to the material having a higher affinity towards CO_2. CO_2 has a quadrupole moment which allows for strong host – guest interactions with the hydroxy groups along the Al(OH) chains.

The selectivity was calculated, using the equations described in chapter 2, to be 6.5 which is comparable to that of MIL-53 (Al), having a selectivity of 7.[20] When MIL-53 is functionalised with an amino group however, the selectivity is almost infinite, with no CH_4 being adsorbed onto the material.[21] Both of these materials show a distinct difference in breakthrough between the two gases, unlike Al: FDC.

3.5.2 CO_2 / N_2 separations

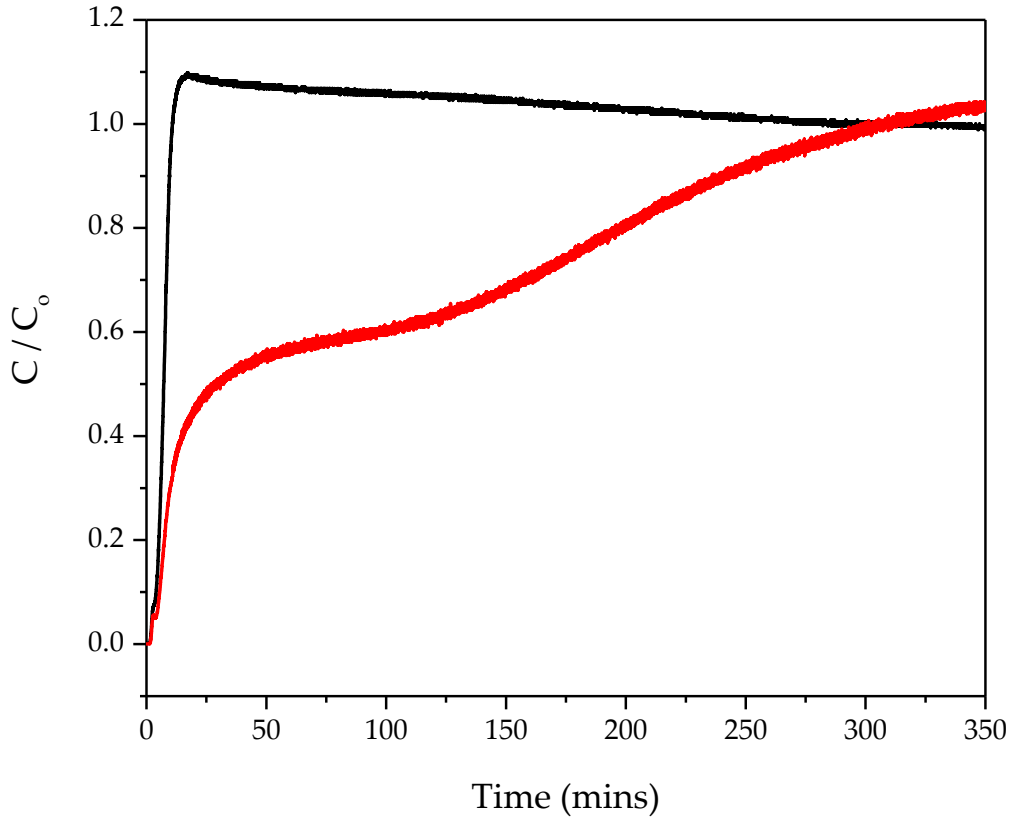

Figure 3.21. Breakthrough curves of CO_2 (red) and N_2 (black).

These measurements show a similar trend seen for the CO_2 / CH_4 separation experiments whereby CO_2 breaks through initially, although here it is much slower for CO_2. Due to nitrogen having no intermolecular interactions with the pore compared to CO_2, this gives rise to the rapid breakthrough of nitrogen.

The selectivity of CO_2 over nitrogen was calculated to be 21, which is a very respectable value when compared to reported values, Ni-MOF-74 for example has an extraordinary selectivity of 38.[22] This MOF uses 2,5 – dihydroxy terephthalic acid as the linker and has a surface area of 1200 m^2 / g and a pore

volume of 0.47 cm^3 / g. As mentioned earlier, this MOF has vacant metal sites which enhances its CO_2 uptake capacity.

While MOF-508b has a selectivity of 3.[23] MOF-508b is a mixed linker, zinc based MOF using BDC and Bipy (2,2'-bipyridine). The CO_2 was proposed to have the ability to interact with the MOF whereas CH_4 and N_2 have no such ability, in the same way as Al: FDC. The reason for the lower selectivity in MOF-508b stems from the smaller pore volume and surface area of 0.27 cm^3 / g, 946 m^2 / g respectively.[24]

The desorption profile of nitrogen and carbon dioxide (figure 3.22) shows that the nitrogen is desorbed relatively quickly compared to the CO_2 which implies that Al: FDC has the capacity to successfully separate a binary mixture of these two gases.

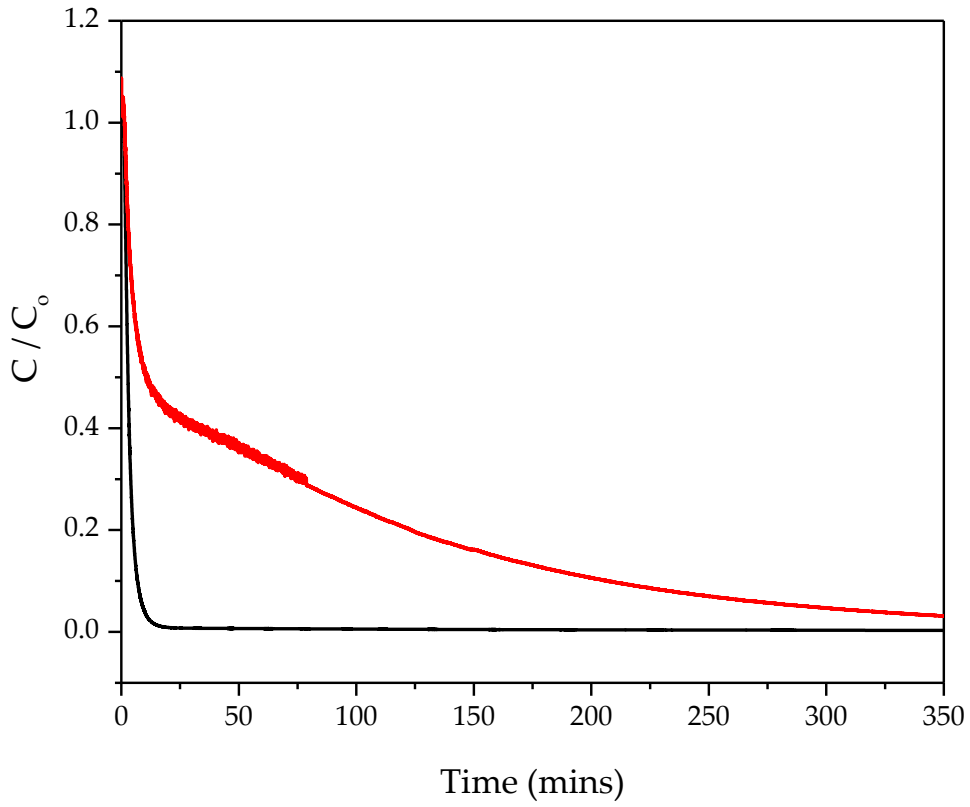

Figure 3.22. Desorption profiles of CO_2 (red) and N_2 (black).

3.6 NH_3 breakthrough

3.6.1 Dry ammonia breakthrough

This material has been shown to have a high affinity towards water, evidenced by the adsorption of water from the atmosphere once it is exposed to air shown in Figure 3.11, as well as the reported water isotherms by Serre et al.[12] It was for this reason that it was hypothesised that Al:FDC would be a suitable candidate for the uptake of ammonia, since it has a similar chemistry to that of water. Ammonia has a kinetic diameter of 2.60 Å, and as this material can accommodate molecules of up to 4.40 Å in diameter according to the crystal structure, ammonia should be adsorbed readily. Before any in-depth measurements were taken, the material had to be assessed for its potential as a sorbent of ammonia and the data is presented in figure 3.23.

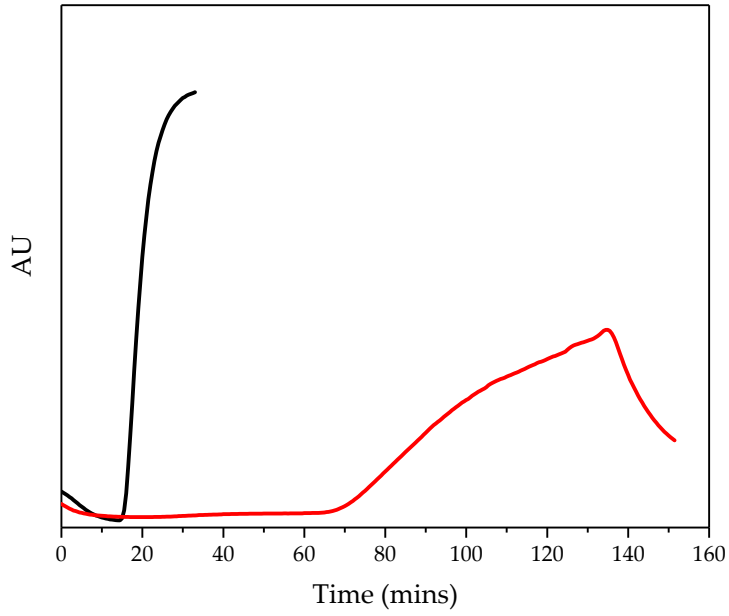

Figure 3.23. Ammonia breakthrough curves in dry conditions of benchmark activated carbon (black) and Al: FDC (red)

The initial result i.e. in dry conditions (<10% RH) flow of ammonia, can be seen in Figure 3.23. Ammonia is only detected after 70 mins when Al: FDC is used as

the sorbent compared with the benchmark activated carbon, which breaks through after only 15 minutes. This implies that Al: FDC has a much higher affinity towards ammonia over activated carbon due to the presence of the hydroxy groups, providing a source of interaction for the ammonia molecules.

Another significant difference seen between the two adsorbents is the gradient of the breakthrough curves, activated carbon has a much steeper gradient indicating faster diffusion of ammonia through the material. The result for Al: FDC implies that the host – guest interactions are stronger, probably due to the interaction with the hydroxy groups, causing a slower diffusion rate.

From the initial test in a dry flow of ammonia, it can be said that Al: FDC has potential as an adsorbent for ammonia, therefore further tests were necessary to see what conditions it can work under.

PXRD data was collected on the sample after these breakthrough experiments were run and the result is presented in Figure 3.24.

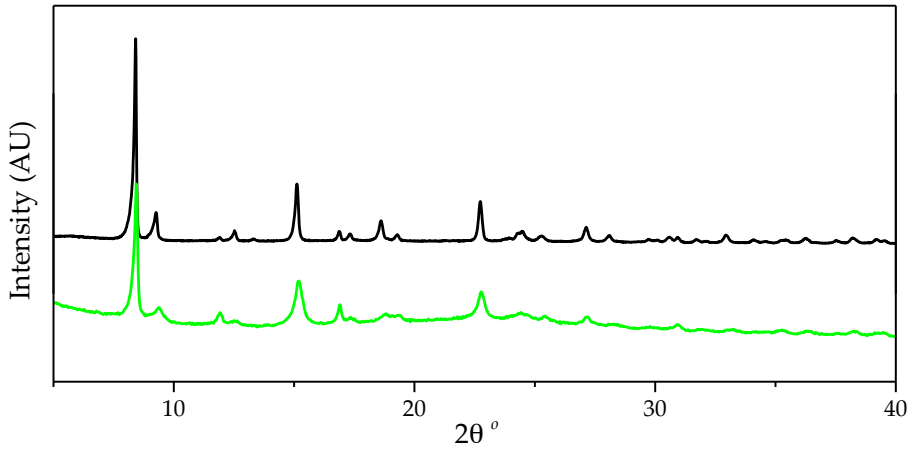

Figure 3.24. PXRD of activated (black) and post ammonia testing (green) Al: FDC

The PXRD data shows that structure itself remains intact, however, there is a loss of crystallinity. The slight change in relative peak intensities implies a change in the unit cell contents, which could be attributed to the adsorption of

NH_3 onto the material. This is possible since it is evident from the IR data (Figure 3.25) that there is some amine functionality present after these measurements.

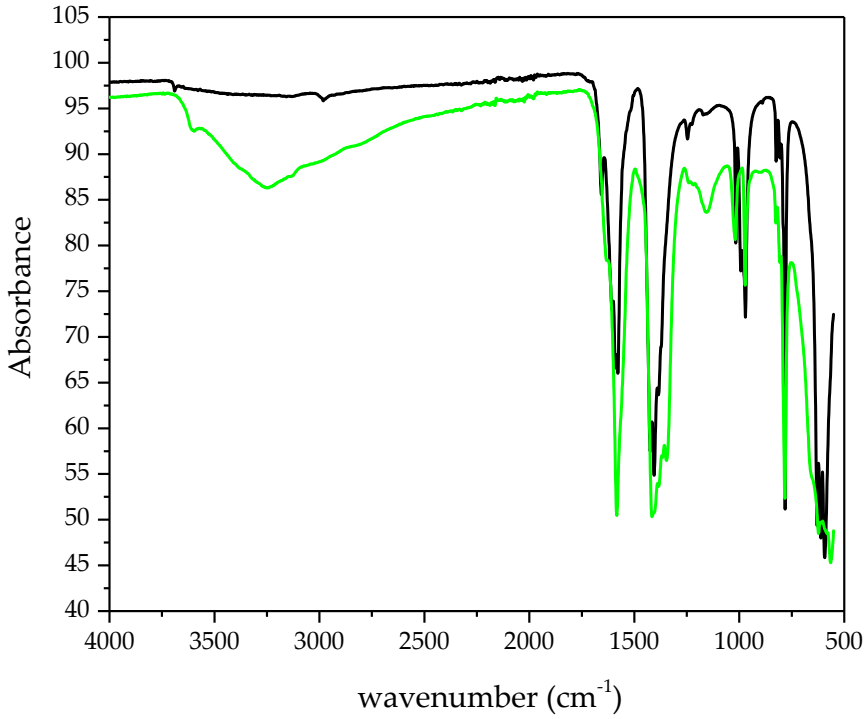

Figure 3.25. IR data of Al: FDC before (black) and post breakthrough measurements (green).

FTIR measurements were taken of the sample before and after the breakthrough measurement to see if there are any significant structural changes.

From the IR spectra presented in Figure 3.25, it can be seen that there are some significant differences before and after ammonia breakthrough. Mainly, the appearance of a medium strength broad band at 3500 – 3250 cm^{-1} after the breakthrough measurement. This band is most likely to come from an N-H stretch, which indicates that there is some ammonia trapped inside the pores of the material. In order to fully support this, future work should involve a TGA of the material after the breakthrough experiments.

3.6.2 Humid ammonia breakthrough

Humid ammonia breakthrough experiments were performed on Al: FDC in 80 % relative humidity (RH) and the results are presented in Figure 3.26.

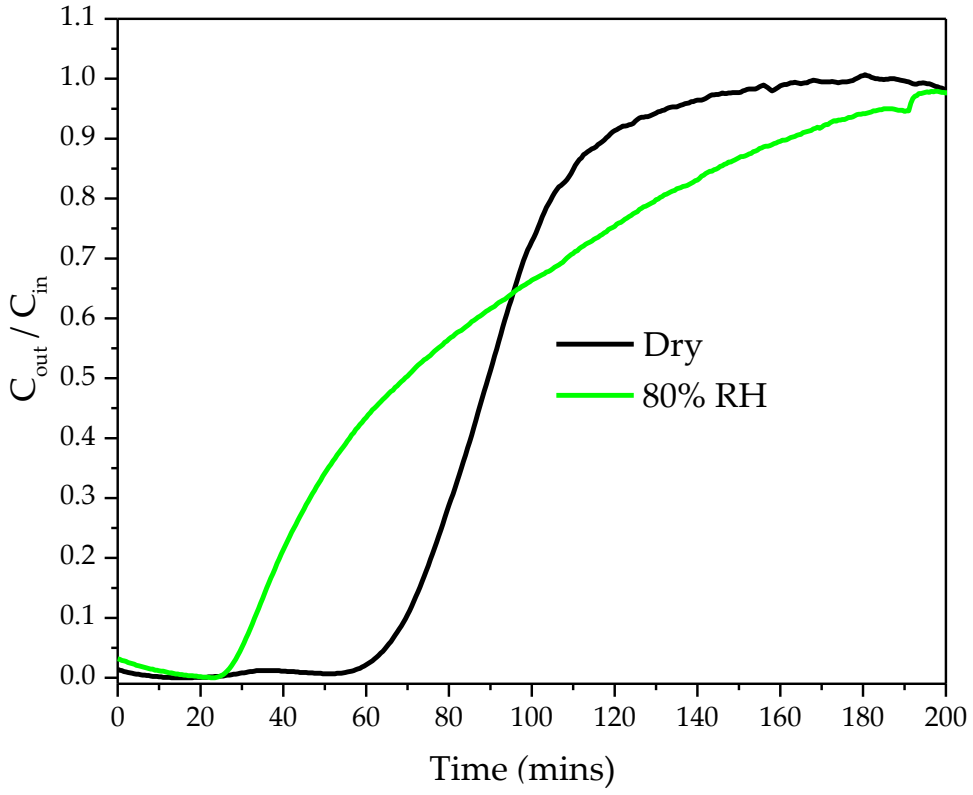

Figure 3.26. Ammonia breakthrough measurements of Al: FDC under dry (black) and humid conditions (green).

The breakthrough time measured is significantly reduced under humid flow from 65 mins to 30 mins. This is expected since the ammonia has to compete with water for the binding sites, and as is known for this material, it is highly hygroscopic. The results indicate that, initially, water adsorbs onto majority of the binding sites, leaving few for ammonia, which causes it to diffuse relatively quicker through the material. The less steep curve to saturation for the humid experiment implies that eventually, ammonia molecules start to interact with the framework, causing a slower diffusion.

The amount of ammonia adsorbed at breakthrough in dry conditions was calculated to be 0.040 mmol, which equates to an ammonia: OH ratio of approximately 0.39: 1. Under humid conditions the amount of ammonia adsorbed at breakthrough was calculated to be 0.018 mmol, equating to a ratio of 0.18:1 ammonia: OH.

3.7 Xylene separations

The separation experiments were carried out in liquid phase at room temperature, since room temperature separations are a lot more desirable than heating to 220 ^{o}C. The experiments were ran by Dr Michael Briggs in Prof. Andrew Cooper's research group, and the column was packed by Prof. Peter Myers' research group. Experimental conditions such as mobile phase, temperature, flow rate and injection volume were altered in order to improve the data for these experiments. The results presented here, represent the best obtained data.

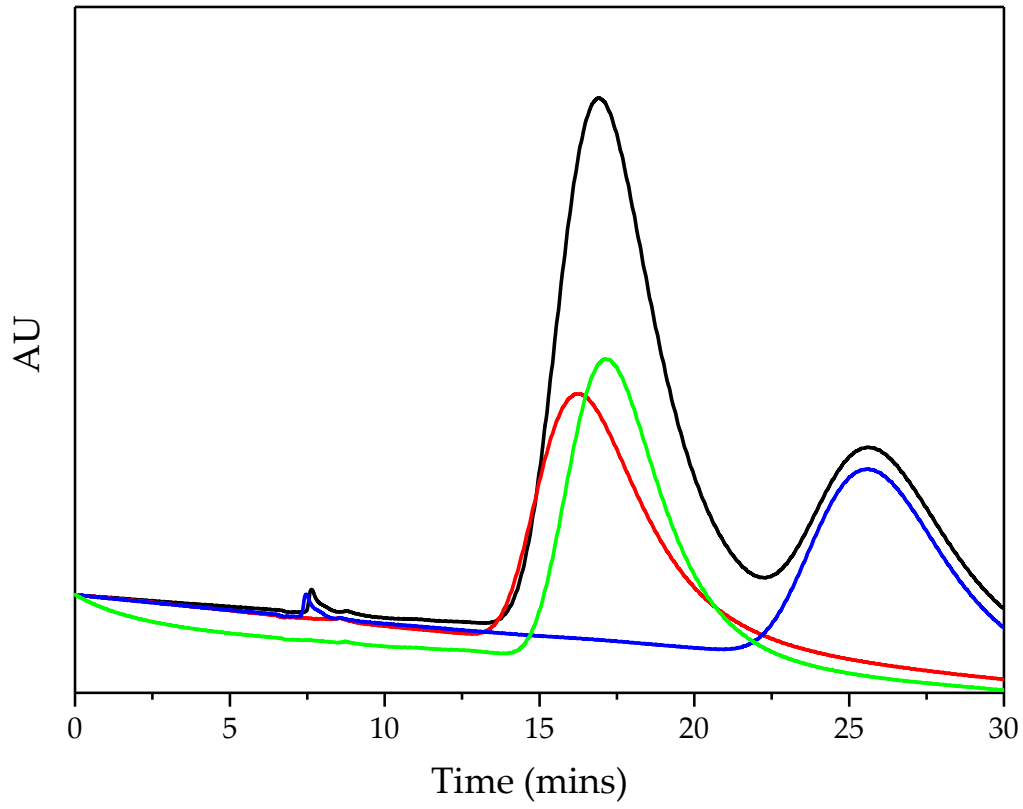

Figure 3.27. HPLC chromatographs of oX (red), mX (blue), pX (green) and a mixture of the three isomers (black).

The data for these experiments shown in Figure 3.27 shows that mX is separated out from the other two isomers last, however, the results show no baseline separation between the isomers. The resolution of the two peaks was calculated to be 0.66, which is lower than the threshold for baseline separation (1.5). Therefore quantification calculations were not possible for this data.

As mentioned earlier, MIL-53(Fe) has reported some good baseline separations and separation factors between xylene isomers, with the ability to successfully separate mX from pX.

3.8 Conclusions

Al: FDC, which was recently published under the name MIL-160, has been synthesised and fully characterised via a variety of different analytical techniques. The bulk purity of the material was measured and was determined to be phase pure, with the formula $Al(OH)(C_6H_2O_5)\cdot XH_2O$. The final structure of Al: FDC was solved by Dr George Whitehead via Rietveld refinement on PXRD data of a completely desolvated sample of material. The structure of Al: FDC consists of *cis* – corner sharing octahedra, which is the same IBU as many aluminium based MOFs and retains the crystallinity upon activation and after many of the application testing.

The gas sorption measurements of CO_2 and CH_4 suggest that the material has a higher affinity towards CO_2 over CH_4 with respective isosteric heats of adsorption of 27.5 and 18.6 KJ mol^{-1}, which is comparable to many reported materials. This was supported further by the separation experiments, which show that the selectivity of CO_2 over CH_4 to be 6.5. The data does however, show some interesting features whereby both gases show initial breakthrough, which is not due to a kinetic effect as this feature remains when the flow rates are adjusted.

Ammonia breakthrough experiments were carried out on the material, under dry and humid conditions, which proved to be successful, as evidenced by the long breakthrough time exhibited by the material compared with the benchmark activated carbon.

The xylene separation experiments were not completely successful, with no baseline separation seen between any of the isomers as seen with other porous materials. From the results, a separation factor could not be calculated but when the size of the xylene isomers are compared with the pore sizes in the MOF,

uptake of xylene onto the material was unexpected. The data, however, shows that the material has potential to separate a mixture of xylene isomers, and by changing the experiment parameters baseline separation could be achieved.

3.9 Future Work

The behaviour of how this material reacts to external stimuli could be investigated using in – situ PXRD with gas loading to detect any changes in lattice parameters as gases are adsorbed.

So far, xylene separations proved to be unsuccessful, however, by modifying experimental parameters such as flow rates, mobile phase, injection rate and temperatures, baseline separation could potentially be obtained for all three isomers and possibly ethylbenzene.

3.10 References

1. H. Reinsch, M. A. Van Der Veen, B. Gil, B. Marszalek, T. Verbiest, D. De Vos and N. Stock, *Chem. Mater.*, 2013, **25**, 17.
2. N. Stock and S. Biswas, *Chem. Rev.*, 2012, **112**, 933.
3. T. Devic and C. Serre, *Chem. Soc. Rev.*, 2014, **43**, 6097.
4. A. U. Czaja, N. Trukhan and U. Muller, *Chem. Soc. Rev.*, 2009, **38**, 1284.
5. N. Stock and S. Biswas, *Chem. Rev.*, 2012, **112**, 933.
6. T. Loiseau, C. Serre, C. Huguenard, G. Fink, F. Taulelle, M. Henry, T. Bataille and G. Ferey, *Chem. Eur. J.*, 2004, **10**, 1371.
7. H. Reinsch, M. Kruger, J. Wack, J. Senker, F. Salles, G. Maurin and N. Stock, *Microporous Mesoporous Mater.*, 2012, **157**, 50.
8. T. Loiseau, C. Serre, C. Huguenard, G. Fink, F. Taulelle, M. Henry, T. Bataille and G. Ferey, *Chem. Eur. J*, 2004, **10**, 1373.
9. H. Reinsch, D. De Vos and N. Stock, *Z. Anorg. Allg. Chem.*, 2013, **639**, 2785.
10. J. J. Bozell and G. R. Petersen, *Green Chemistry*, 2010, **12**, 539.
11. A. Cadiau, J. S. Lee., D. D. Borges, P. Fabry, T. Devic, M. T. Wharmby, C. Martineau, D. Foucher, F. Taulelle, C-H. Jun, Y. K. Hwang, N. Stock, M. F. De Lange, F. Kapteijn, J. Gascon, G. Maurin, J-S. Chang and C. Serre, *Adv. Mater*, 2015, **27**, 4775.

12. A. Cadiau, J. S. Lee, D. Damasceno Borges, P. Fabry, T. Devic, M. T. Wharmby, C. Martineau, D. Foucher, F. Taulelle, C. H. Jun, Y. K. Hwang, N. Stock, M. F. De Lange, F. Kapteijn, J. Gascon, G. Maurin, J. S. Chang and C. Serre, *Adv. Mater.*, 2015, **27**, 4775.
13. Z. Zhang, Z. Yao, S. Xiang and B. Chen, *Energy Environ., Sci*, 2014, **7**, 2868.
14. J. A. Mason, K. Sumida, Z. R. Herm, R. Krishna and J. R. Long, *Energy Environ. Sci.*, 2011, **4**, 3030.
15. J. A. Mason, M. Veenstra and J. R. Long, *Chem. Sci.,*, 2014, **5**, 32-51.
16. A. Demessence, D. M. D'Alessandro, M. L. Foo and J. R. Long, *J. Am. Chem. Soc.*, 2009, **131**, 8784.
17. T. Loiseau, C. Mellot-Drazneiks, H. Muguerra, G. Ferey, M. Haouas and F. Taulelle, *C. R. Chimie*, 2005, **8**, 765.
18. J. A. Mason, M. Veenstra and J. R. Long, *Chemical Science*, 2014, **5**, 32.
19. S. K. Bhatia and A. L. Myers, *Langmuir*, 2006, **22**, 1688.
20. V. Finsy, L. Ma, L. Alaerts, D. E. De Vos, G. V. Baron and J. F. M. Denayer, *Microporous Mesoporous Mater*, 2009, **120**, 221.
21. S. Couck, J. F. M. Denayer, G. V. Baron, T. Rémy, J. Gascon and F. Kapteijn, *J. Am. Chem. Soc.*, 2009, **131**, 6326.
22. J. Liu, J. Tian, P. K. Thallapally and P. McGrail, *J. Phys. Chem. C*, 2012, **116**, 9575.
23. L. Bastin, P. S. Barcia, E. J. Hurtado, J. A. C. Silva, A. E. Rodrigues and B. Chen, *J. Phys. Chem. C*, 2008, **112**, 1575.
24. B. Chen, C. Liang, J. Yang, D. S. Contreras, Y. L. Clancy, E. B. Lobkovsky, O. M. Yaghi and S. Dai, *Angew. Chem. Int. Ed.*, 2006, **45**, 1390.

Chapter 4 Indium: FDC

4.1 Overview

Indium is known to adopt a co-ordination number (CN) of greater than six due to its significantly larger ionic radius of 0.940 Å compared to 0.675 Å for Al^{3+}.[1,2] This means that it has a much smaller charge density, which, in turn increases the lability, and ultimately the ligand exchange rate of $In(L_6)$ complexes.[3, 4] The higher ligand exchange rate of In^{3+} complexes means that larger crystals, which are suitable for SCXRD are often obtained during the synthesis. Given this fact, and the fact that indium is known to produce isoreticular MOFs to its aluminium analogue, it was hypothesised that a single crystal of In: FDC could be synthesised and the outcome would help confirm the structure for Al: FDC.

The fact that In^{3+} has a significantly larger ionic radius than aluminium is also in line with the fact that In^{3+} has a lower bond strength with the oxygen donor atoms than Al^{3+}.[5] This also accounts for its ability to adopt CN > 6 as mentioned earlier. When comparing the structures of two different MOFs for both metals, MIL-53 and MIL-96, the M – O bond distances average at 1.881 Å [6, 7] and 2.130 Å [8, 9] for aluminium and indium respectively. Given this, and the larger co – ordination sphere of In^{3+}, it prefers to adopt CNs between 6 and 8, while there are few reported MOFs containing CN = 7, many structures are based on eight co – ordinate In^{3+}. Almost all of these reported materials contain $[In(CO_2)_4]^-$ IBUs, in which the indium is dodecahedrally co – ordinated.

Most indium MOFs are based on six co – ordinate In^{3+}, majority of which are isoreticular to their aluminium analogues, forming the same chain – like IBU. The most prevalent example is MIL – 53 (In) has been reported showing its

ability to adopt isostructural materials to its aluminium counterpart.

Although this IBU is very common for G13 MOFs, indium MOFs also form cluster IBUs of $[M_3(\mu_3\text{- O})(-CO)_6]^+$ and $[In(-CO_2)_4]^-$, as shown in Figure 4.1 on the right and left respectively. The chain IBU is shown in the middle diagram of the figure.[2]

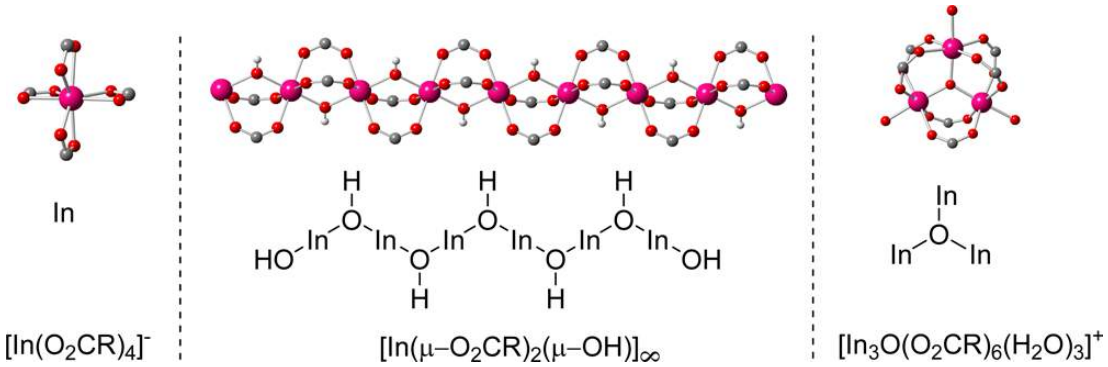

Figure 4.1. Common reported indium IBUs figure from reference.[2]

The latter of these two mentioned IBUs is formed when four carboxylates act as chelating groups as seen in ATF-1.[10] This gives rise to an InO_8 dodecahedron as mentioned earlier, which resembles a distorted tetrahedral node.

Indium MOFs are the only G13 MOFs with reported examples that contain both two different metal ions with two distinct IBUs, and there has been one interesting indium MOF reported (CPM – 5) which contains only indium ions but two distinct IBUs: $[In(-CO_2)_4]^-$ and $[In_3(\mu_3 - O)(-CO_2)_6]^+$.[11] The overall structure has a very unique cage – within – cage motif. However, there has been no reported indium MOF that contains both seven and a six co – ordinate In^{3+} ions with two distinct IBUs.

In 2005, three In: FDC materials with three different structures were reported.[12] This research showed that subtle differences in reaction conditions i.e. In: FDC ratio can cause the formation of a different IBU and

therefore a different overall structure. In all instances, $In(NO_3)_3$ was used with FDC, however they use a mixture of additives; 2-(2-aminoethylamino)ethanol, nitric acid and dimethylacetamide, with methanol as the solvent. Increasing the concentration of indium in the reaction mixture such that it was in excess, causes the formation of the $[In(O_2CR)_4]^-$ over the triangular $[In_3O(O_2CR)_6(H_2O)_3]^+$. The third structure uses a completely different mixture of additives; 3-amino-5-mercapto-1,2,4-triazole, trimethylurea with water was the solvent, giving rise to the neutral framework based on the In(OH) chain IBU. One thing consistent among all reaction conditions was the reaction time, all reactions were carried out for 3 days at 120 ^oC (compounds 1 and 2) and 80 ^oC (compound 3).

In this chapter, although the aim of synthesising an isoreticular material to Al: FDC was unsuccessful, herein, the first two reported indium MOFs with two different IBUs and indium CN = 6 and 7 are presented.

4.2 Synthesis

A high throughput approach, as in chapter 3, was employed in order to explore the effect of different reaction conditions on the final products. A large number of experiments were carried out, investigating reaction conditions such as In: FDC ratios, solvent mixtures, additives, reaction temperatures and times. Initial reactions began using the same reaction time, temperature and solvent ratios as used for Al: FDC. Even though the first set of reactions yielded a new In: FDC structure, further investigations into reaction conditions was needed to see if an isostructural material to Al: FDC could be synthesised. Volumes of reaction mixtures were varied from 5 – 20 mL and the nature of these solvent mixtures were changed from pure water, through to pure DMF, introducing different amounts of NaOH. Reaction

times and temperatures were also investigated, ranging from 80 ^{o}C – 130 ^{o}C and from 12 hours to 48 hours.

Eventually, it was seen that, as seen in previous publications, changing conditions has a drastic effect on the product, evidenced by the three different structures of In: FDC reported herein. One of the three previously mentioned structures was synthesised by introducing trimethylurea into the mixture.

$In(NO_3)_3 \cdot xH_2O$ and FDC were purchased from Sigma Aldrich in 99 % and 98 % purity. NaOH, DMF, THF were purchased from Fisher Scientific and all reagents were used without any further purification. Materials that required activation were all activated under the same conditions; 155 ^{o}C, under vacuum (10^{-2} mbar) overnight.

4.2.1 Synthesis of compound 1

A 0.7M stock solution of FDC in DMF was made up. To a 40 mL Teflon capped glass vial, $In(NO_3)_3.XH_2O$ (245 mg), H_2O (3 mL), DMF (0.57 mL) and FDC solution (1.43 mL, 1 mmol), were added. The reaction mixture was heated to 100^{o}C at 2.5 ^{o}C / min and left for 12 hours before allowing to cool to room temperature at 0.2 ^{o}C / min. A small aliquot of the product was removed for single crystal X-ray analysis while the rest of the white powder was washed with DMF (4 x 20 mL), THF (3 x 20 mL) and ethanol (3 x 20 mL) and left to pump dry. Once dried, the remaining 79 mg of white powder was analysed by PXRD and TGA. Analysis of this material showed that c.a. 7 % of the mass was attributed to adsorbed solvent molecules and the formula of the final product was found to be $In_3(OH)_3(FDC)_4(DMAM)_2$ after the removal

of the DMF molecules. DMAM here refers to the dimethyl ammonium counter cation.

4.2.2 Synthesis of compound 2

A 1M NaOH stock solution was made up with H_2O, then $In(NO_3).XH_2O$ (932 mg), FDC (390 mg, 2.5 mmol), H_2O (4.5 mL), NaOH (2.5 mL, 2.5 mmol) were added to a 40 mL Teflon capped glass vial. The reaction mixture was heated to 100°C at a rate of 2.5 °C / min and left for 24 hours before allowing to cool to room temperature at 0.2 °C / min. After soaking the product in DMF to dissolve any unreacted linker, a small sample was removed for SCXRD leaving 54 mg of material to be analysed using PXRD. The formula of compound 2 was determined to be $In_7(OH)_5(C_6H_2O_5)_8(H_2O)_5$.

4.2.3 Synthesis of Compound 3

A 0.18 mg mL^{-1} and a 1M Stock solution of $In(NO_3)_3.\mathbf{X}H_2O$ and NaOH, respectively were made up with water. FDC (424 mg, 2.72 mmol), $In(NO)_3$ solution (2 mL), NaOH (5.44 mL, 5.44 mmol), H_2O (7.56 mL), were all added to a 40 mL Teflon lined glass vial. The mixture was heated to 110°C at 2.5 °C / min and left for 24 hours before cooling to room temperature at 0.2 °C / min. This yielded needle – shaped crystals. A small portion of the product was removed for SCXRD, leaving 204 mg of sample. Analysis of this material show that c.a. 15 % of the mass of the final product is attributed to adsorbed guest molecules and the final dry formula was found to be $In_3(OH)_2(FDC)_3(NO_3)_2Na(H_2O)_5$.

4.3 Characterisation of Compound 1

4.3.1 Structure

Compound 1 crystallises in primitive orthorhombic P*bca* with lattice parameters a = 17.7313(2) Å b = 20.5132(4) Å c = 21.2291(3) Å with a unit cell volume of 7721.6(2) Å^3. Data collection and refinement parameters can be found in Appendix II.

The asymmetric unit and IBU of compound 1·DMF shown in Figure 4.2 and Figure 4.3 respectively are both different to that of Al: FDC already showing that the two materials are not isostructural. The asymmetric unit of this material is highly uncommon, with each indium ion having a μ_1 carboxylate group co – ordinated to it as part of a μ_2 – bridging FDC linker, two bridging hydroxy groups and the octahedra completed by three bridging μ_2 carboxylates.

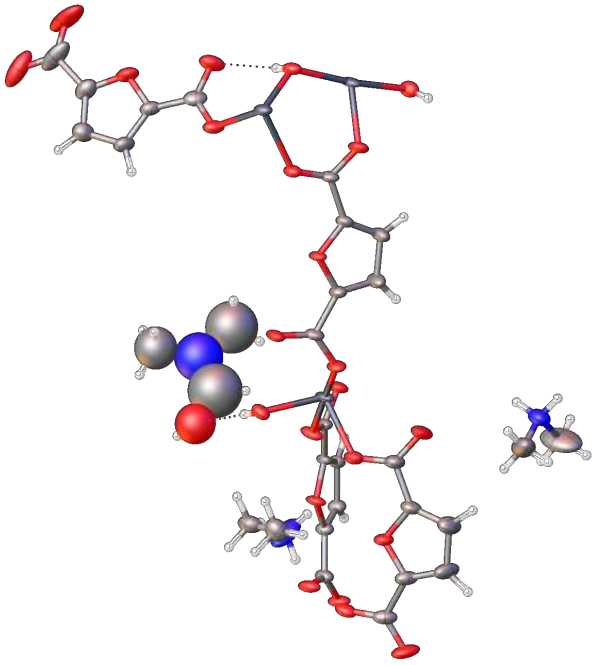

Figure 4.2 The asymmetric unit of compound 1, indium (dark grey), carbon (pale grey), oxygen (red), nitrogen (blue), hydrogen (white).

The IBU of compound 1 is typical for many G13 MOFs, infinite chains of trans - corner sharing $In(OH)_2O_4$ octahedra, which are bridged to four adjacent chains via FDC linkers. Here, *trans* – refers to the positions of the bridging hydroxy groups. A DMF molecule is hydrogen bonded to a hydroxy bridge (O…O separation of 2.8974 Å) and the presence of two dimethylammonium (DMAM) cations are required to counterbalance the overall anionic framework.

The *trans* – corner – sharing octahedra, however, are unexpected with this linker because, as discussed earlier, linkers with angles of 120 ° between the two co – ordinating groups, tend to form *cis* – chains, which enables all carboxylate oxygen atoms to co – ordinate to their respective ions.

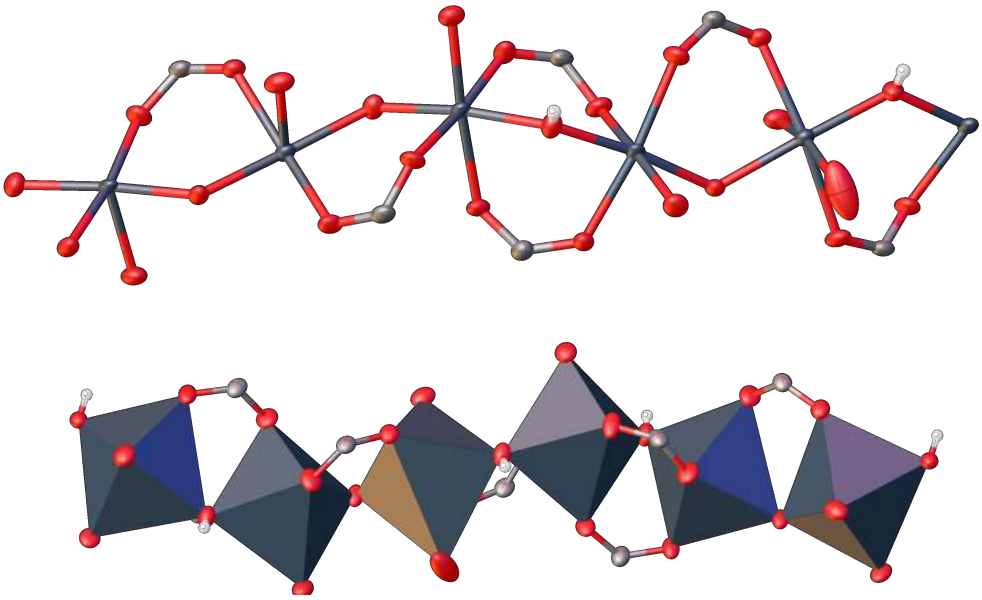

Figure 4.3 Chains of *trans* – corner – sharing In(OH), polyhedra are shown to display the corner sharing octahedra. Indium (dark grey), carbon (pale grey), oxygen (red), hydrogen (white).

The angles between the carboxylate groups in FDC is 137 °, which is slightly larger, but as seen in Al: FDC, *cis* – chains would be expected to be more

favourable. As well as the In(OH) chains, chains of In(μ_1 – COO), shown in Figure 4.4, form along the crystallographic *a* – axis.

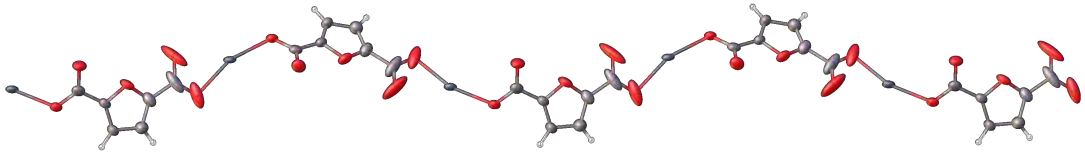

Figure 4.4 μ_2 – FDC bridges forming In(FDC) chains along crystallographic *a* – axis. Indium (dark grey), carbon (pale grey), oxygen (red), hydrogen (white).

Additionally, every third indium ion in the In(OH) chains is part of two of these In(μ_1 – COO) chains, running in perpendicular planes. Therefore, every third indium ion in an In(OH) chain, is co – ordinated by two μ_1 – carboxylate groups, two hydroxy groups and two bridging μ_2 – carboxylates. This is shown in the figure below whereby all DMAM ions and DMF molecules have been omitted for clarity.

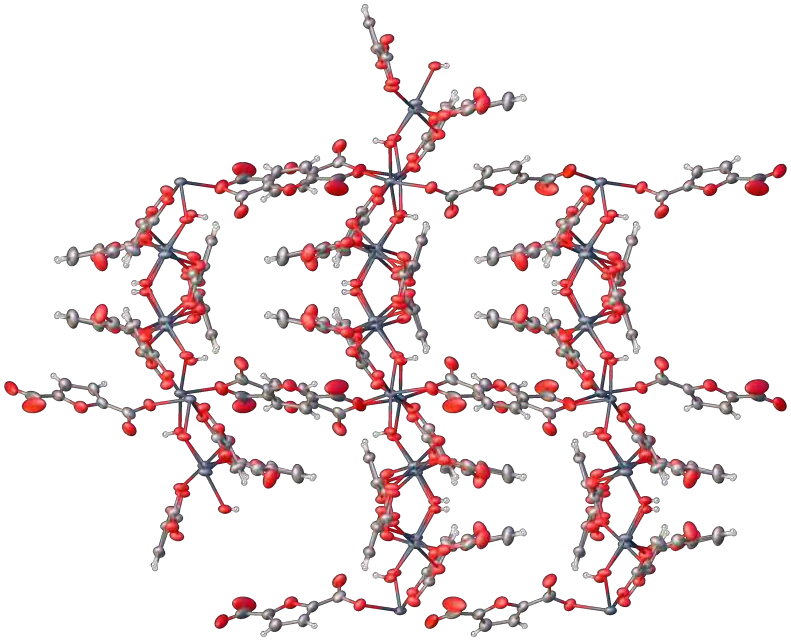

Figure 4.4. View along the crystallographic *a* – axis, DMAM and DMF molecules have been omitted for clarity Indium (dark grey), carbon (pale grey), oxygen (red), hydrogen (white).

The dimethylammonium (DMAM) cations are present to counter balance the overall negative charge across the material, while the DMF is present from the synthesis and is hydrogen bonded to a bridging hydroxy group, shown in Figure 4.5. The figure is presented in ball and stick format for clarity due to the large DMF ellipsoids obscuring the view. The structure showing anisotropic displacement can be found in Appendix III. This gives an overall formula of $In_3(OH)_3(FDC)_4(DMAM)_2 \cdot DMF$. This is highly unusual, as the only anionic indium framework has only ever been reported with the dodecahedral IBU, not the octahedral as seen in compound 1.

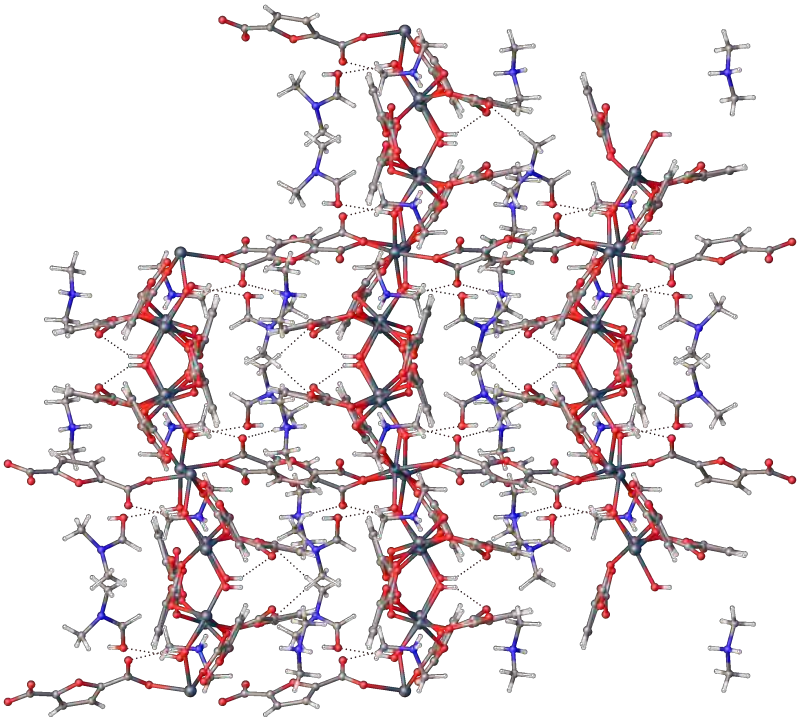

Figure 4.5. View along the crystallographic *a* – axis. Indium (dark grey), carbon (pale grey), oxygen (red), hydrogen (white).

4.3.2 Structure of Activated Compound 1

Due to the presence of the DMF and DMAM in the structure, in-situ SCXRD was ran at 500 K. This was to get a clearer view of the structure itself without

these molecules present. The crystal structure itself remains the same at 500 K, showing its thermal stability.

Upon activation and removal of the DMF molecules, the material remains in primitive orthorhombic P*bca* with a slight change of lattice parameters as displayed in Table 4.1.

Table 4.1. Lattice parameters of *as*-made and activated compound 1.

	***a* (Å)**	***b* (Å)**	***c* (Å)**	**V (Å^3)**
***As*-made**	17.7313(2)	20.5132(4)	21.2291(3)	7721.6(2)
Activated	17.7886(9)	20.9776(17)	21.4309(12)	8004.8(9)

There is a slight expansion in lattice parameters after activation, and according to the crystal structure, all DMF molecules are removed (**Figure 4.6**).

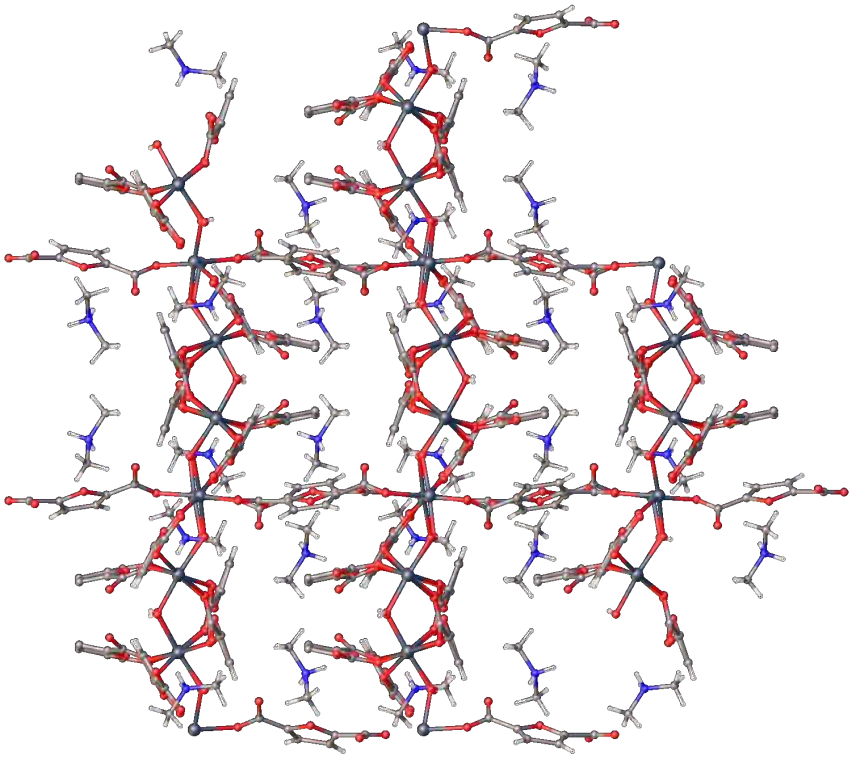

Figure 4.6. Structure of activated compound 1, view along crystallographic *a* – axis. Indium (dark grey), carbon (pale grey), oxygen (red), hydrogen (white).

It is clear from Figure 4.6 that the DMF molecules are removed and the DMAM ions remain. It is presented in ball and stick view for clarity, however, a figure showing anisotropic displacement parameters can be found in Appendix III. Due to the presence of these counter ions, compound 1 shows very slight porosity with a total solvent accessible volume of 686.7 $Å^3$ / unit cell, which equates to 8.60 %. The issue, however, stems from the largest penetrable sphere having a radius of 0.60 Å, which is far too small to allow any gases in. The voids were calculated using a probe size of 1.82 Å radius, consistent with that of nitrogen molecule, and are shown in Figure 4.7.

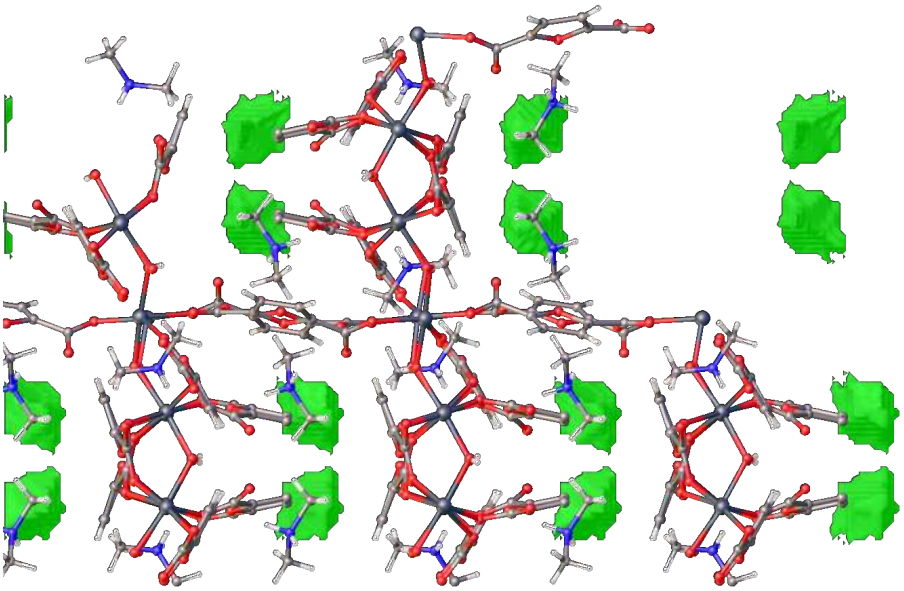

Figure 4.7. Surface map of activated compound 1 when viewed along the crystallographic *a* – axis Indium (dark grey), carbon (pale grey), oxygen (red), hydrogen (white). Voids represented by green surface maps.

4.3.3 PXRD

Although this material is not the desired product and showed no evidence of any potential porosity, it could still have some applications in the field of proton conduction as various other dense In: FDC compounds have and

have exhibited relatively high proton conductivity.[12] Bulk analysis was carried out to see if any impurities were present, the PXRD data is presented in Figure 4.8.

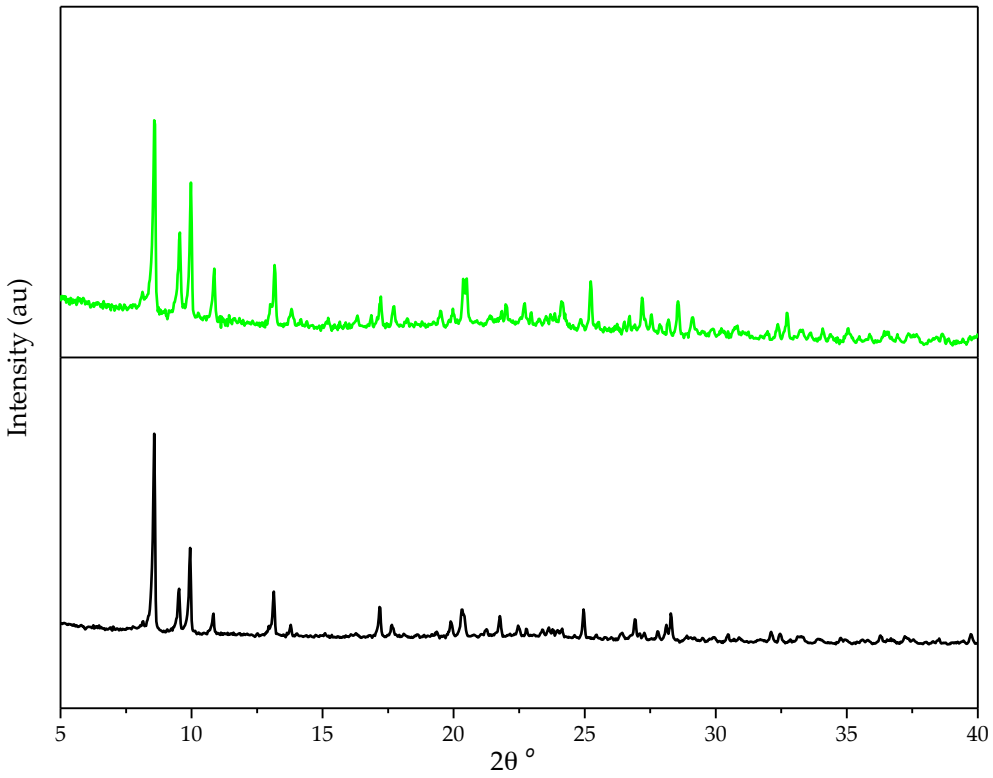

Figure 4.8. PXRD of compound 1. As-made (black), activated at 155 °C overnight under vacuum (green).

The PXRD pattern of the activated material can be fully indexed to the unit cell obtained from the single crystal data as shown Figure 4.9, indicating no crystalline impurities are present.

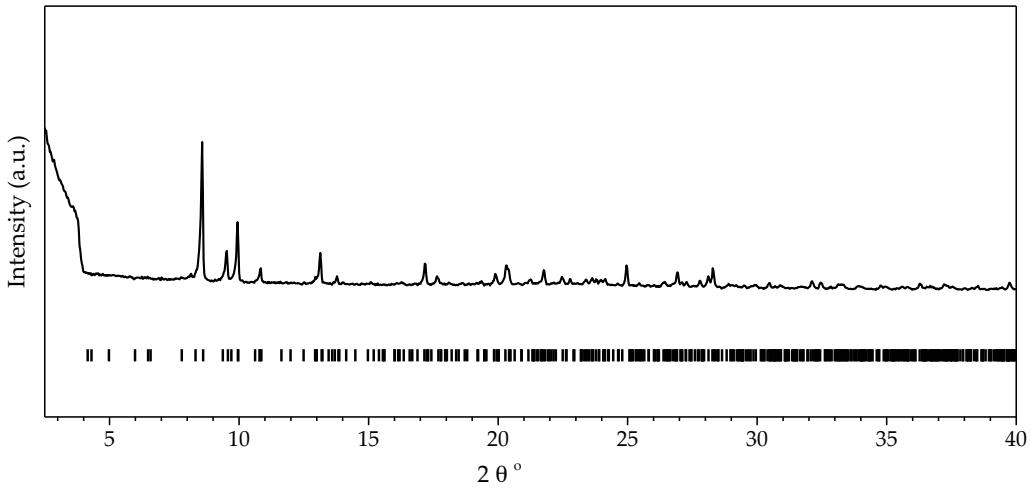

Figure 4.9 PXRD of activated compound 1 indexed against the unit cell generated from the single crystal, with calculated peaks (black ticks).

4.3.4 TGA

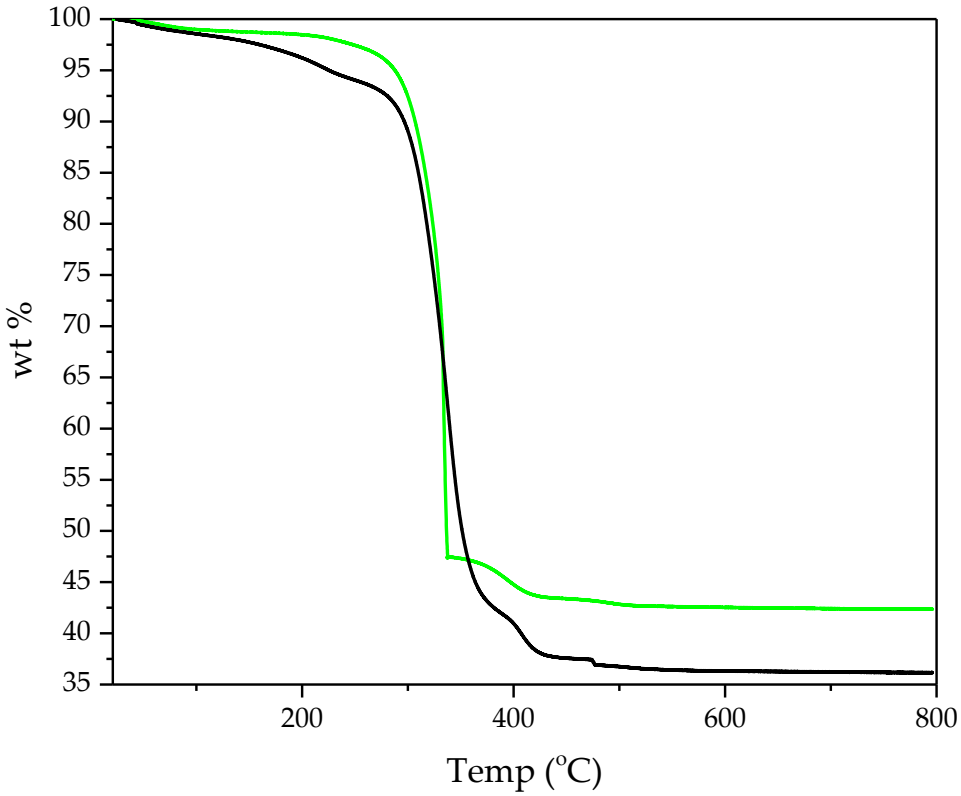

Figure 4.10. TGA trace of as-made (black) and activated (green) compound 1.

The TGA trace of the as-made material shows that up to 250 °C, there is a slight mass loss of 6.40 %, which is attributed to the removal of guest solvents from within the material.

The SCXRD data shows that for every three indium ions, one DMF molecule is Hydrogen bonded to a hydroxy group, which is calculated to make up 6.21 % of the material. The TGA trace shows two small mass losses, the initial loss of ca 2 % can be attributed to loss of the low boiling point solvents used during the washing procedure. This leaves a mass loss of c.a. 4.4 % due to the removal of the DMF from the synthesis, implying that approximately one third of the DMF molecules have been exchanged by the other solvents during the washing procedure.

Based on the dry formula: $In_3(OH)_3(C_6H_2O_5)_4(NH_2(CH_3)_2)_2$, which is known from the crystal structure, the expected indium content is 31.20 %. The indium content of the activated material was calculated, from the TGA to be 35.55 % using the residual In_2O_3, which indicates a small amount of indium impurity in the material. Since there was no yellow powder present in the product, the impurity was not likely to be indium oxide but could be some other amorphous inorganic phase.

4.3.5 Elemental Analysis

$In_3(OH)_3(FDC)_4(DMAM)_2 \cdot H_2O$		
Element	Expected %	Measured %
C	29.97	27.82
H	2.61	2.56
N	2.50	1.93

Table 4.2. CHN data of activated compound 1

The CHN data gives good agreement with the TGA data, which indicates that a slight excess of inorganic impurity was formed during the synthesis. According to the TGA data, there is a small amount of water adsorbed onto the material which equates to approximately one water molecule per three indium ions.

Although this material has a very interesting structure, the aim of this investigation, which was to synthesise a porous, isoreticular indium analogue of Al: FDC was not achieved. Therefore, no further investigations into this material were carried out.

4.4 Characterisation of compound 2

This is the first indium material to be reported that contains both six and seven co – ordinate indiums to be reported, this was confirmed by a CCDC database search. There has only been one reported MOF to contain two different indium environments; Bu *et al.*, reported a very interesting indium MOF (CPM-5) containing two types of IBU, an eight co – ordinate $[In(-CO_2)_4]^-$ and a six co – ordinate $[In_3O(-CO_2)_6]^+$.[11] The only other reported indium materials that have two distinct IBUs contain a second type of metal ion e.g. Cu^{2+}, Ru^{3+} and Co^{2+}.[13, 14, 15] Furthermore, a co-ordination number of seven for an indium MOF is extremely rare and has only been reported once for In-MOF-1.[16] The formula of compound 2, deduced from the crystal structure, was determined to be $In_7(OH)_5(C_6H_2O_5)_8(H_2O)_5$.

4.4.1 Structure

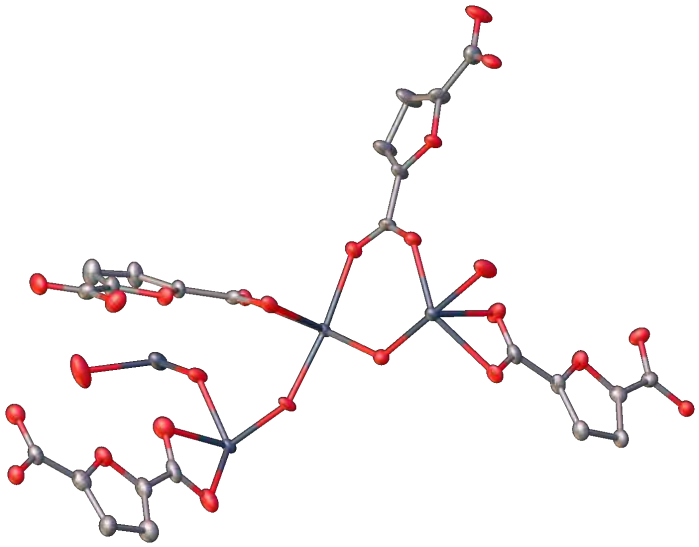

Figure 4.11. Asymmetric unit of compound 2. Indium (dark grey), carbon (pale grey), oxygen (red).

Compound 2 is made up of interlocking 2–dimensional sheets and crystallises in triclinic space group $P\bar{1}$, with lattice parameters a = 9.6981(2) Å, b = 14.1055(5) Å, c = 16.5294(6) Å, α = 69.109(3) °, β = 87.572(3) °, γ = 81.457(3) °, V = 2088.94(12) Å^3. Data collection and refinement parameters can be found in Appendix II. Two distinct SBUs make up each sheet of compound 2 and are shown in Figure 4.12. Type I consists of infinite chains of In(FDC). There are three of these chains running along the same direction (Figure 4.12 i, ii and iii). Type II consists of finite indium hydroxide chains, made up of seven indium ions and capped by a water molecule at each end.

All indium ions in the In(FDC) chains are 7 – co – ordinate and all have two μ_2 – carboxylate groups co - ordinated (Figure 4.12).

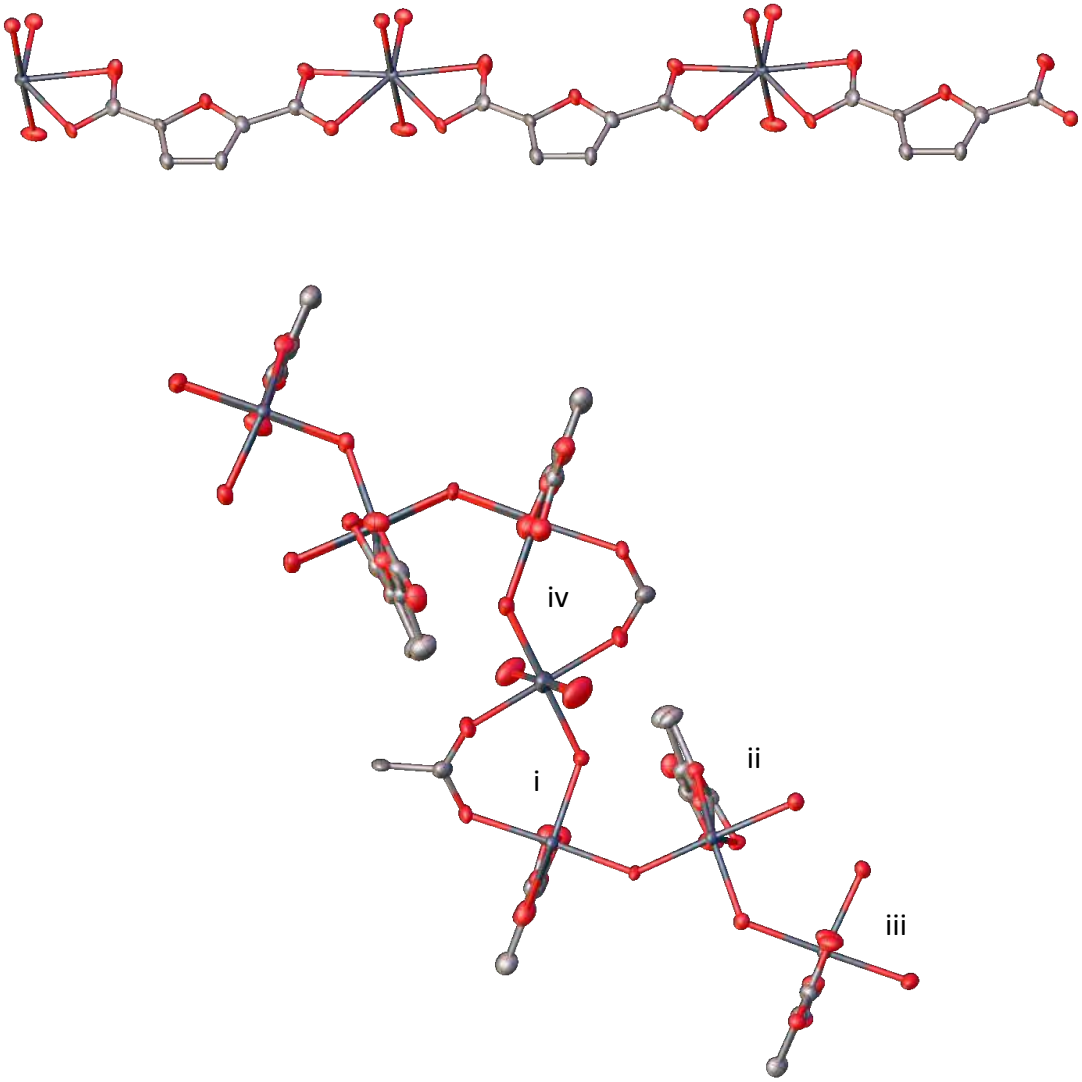

Figure 4.12. IBU type I (top) shows infinite In(FDC) chain and type II (bottom) shows finite In(OH). Indium (dark grey), carbon (pale grey), oxygen (red).

Figure 4.12 shows that the In(OH) chains consist of seven indium ions in total, six of which are part of the In(FDC) chains which run perpendicular to the In(OH) chains. The seventh being the central six co – ordinate indium ion which is not part of any In(FDC) chain.

In the centre of the finite In(OH) chain, is a six – co – ordinate indium ion (iv in Figure 4.12); $[In(OH)_2(H_2O)_2(\mu_1 - CO_2)_2]$. This octahedron is bridged to identical In(FDC) chains on either side via carboxylate groups and hydroxy groups, thus forming the finite In(OH) chains. Since the In(OH) chains are identical on either side of the central octahedron, for convenience, only one side will be described.

The first infinite In(FDC) chain (i), which is connected to the central octahedron is further bridged only via a hydroxy group to the chain (ii), which is then further bridged to the final In(FDC) chain (iii), via a hydroxy group and a bridging carboxylate group. This is the ultimate indium ion in the In(OH) chain and is capped by a water molecule, as mentioned earlier, this motif is repeated on the other side of the central indium octahedron.

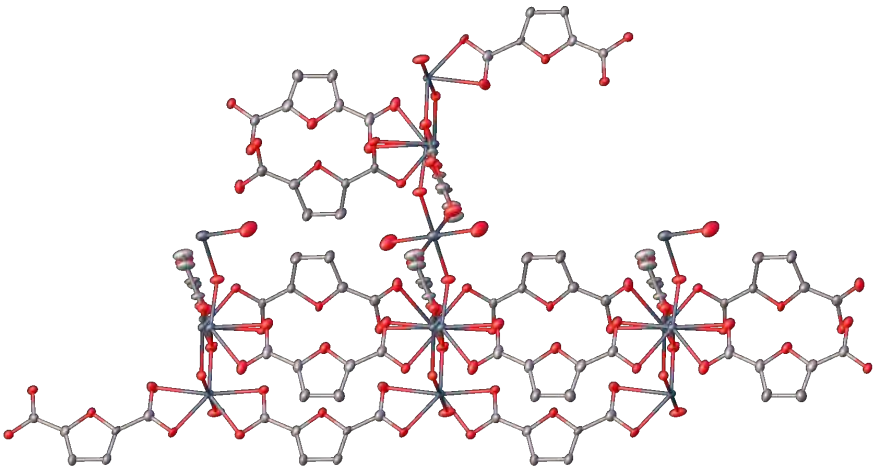

Figure 4.13. Compound 2 along the crystallographic *b* – axis. Indium (dark grey), carbon (pale grey), oxygen (red).

Viewing compound 2 along the crystallographic *b* – axis (Figure 4.13) shows the In(FDC) chains running perpendicular to the In(OH) chains.

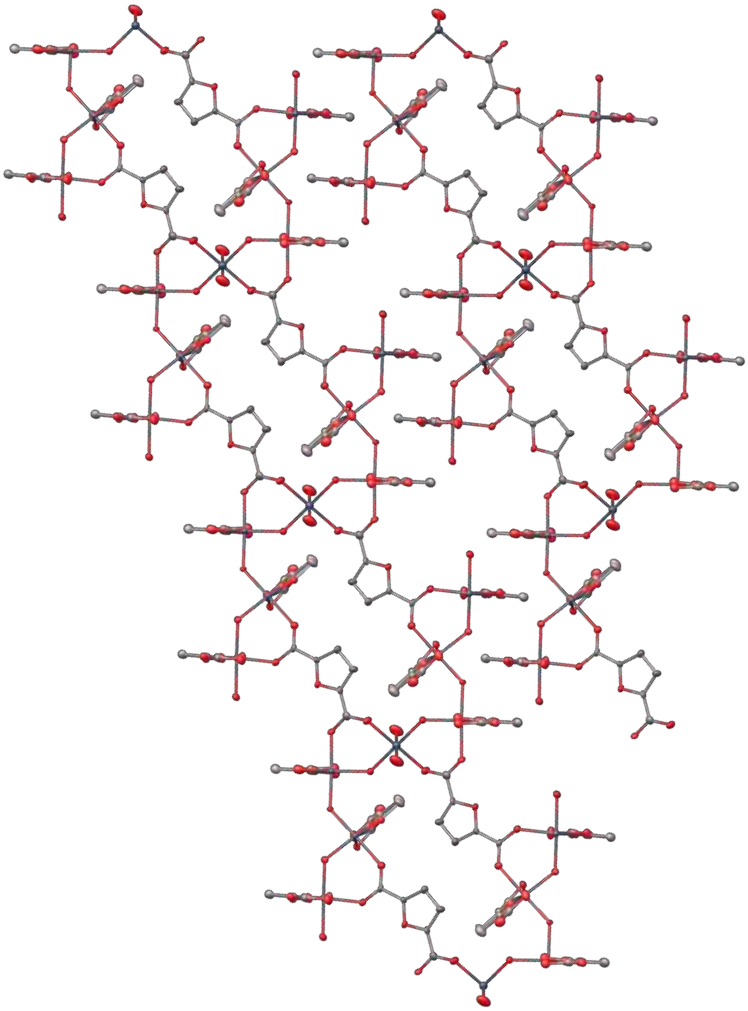

Figure 4.14. Overall structure of compound 2 along the crystallographic *a* – axis. Indium (dark grey), carbon (pale grey), oxygen (red), hydrogen (white).

Figure 4.14 demonstrates the interlocking of the 2-dimensional sheets and the full connectivity of the compound, which have no intermolecular forces between them.

4.4.2 PXRD

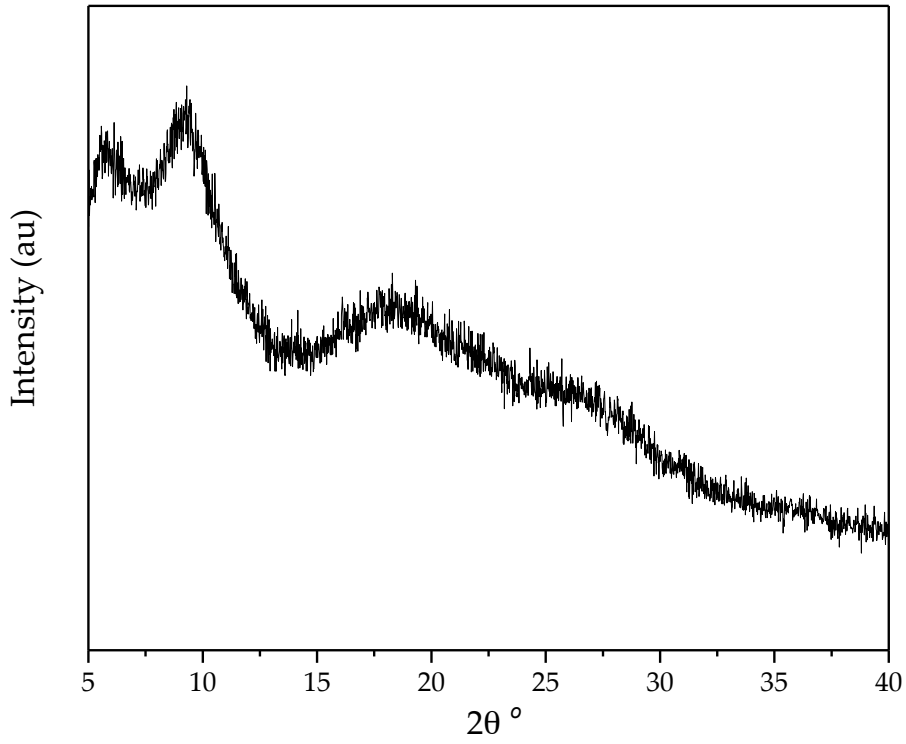

Figure 4.15. PXRD pattern of as-made compound 2.

The PXRD pattern shows that upon removal from solution and drying in air, the compound loses its crystallinity. This is probably due to the lack of intermolecular forces between the layers, and once the solvents are removed, the layers collapse, having a detrimental impact on the crystallinity.

Although the crystal structure of this material is interesting and is the first of its kind to be reported, once again, the objective of this investigation was not achieved. Due to its lack of crystallinity after washing and drying, along with the evident lack of porosity according to the crystal structure, no further investigation into this compound was carried out.

4.5 Characterisation of compound 3

4.5.1 Structure

Compound 3 crystallises in the triclinic $P\bar{1}$, with lattice parameters a = 10.0982(6) Å, b = 13.3547(8) Å, c = 15.3753(6) Å, α = 99.278(4) °, β = 95.128(4) °, γ = 110.047(5) °, V = 1898.84(19) Å^3. This compound has a similar structure to that of compound **2**, with the interlocking of 2–dimensional sheets and the presence of two different inorganic building units; infinite In(FDC) chains and finite In(OH) chains consisting of three indium ions. There are also two different indium environments present; seven co–ordinate $InO_5(OH)(H_2O)$ and six co–ordinate $InO_2(OH)_2(H_2O)_2$. Data collection and refinement parameters are presented in Appendix II.

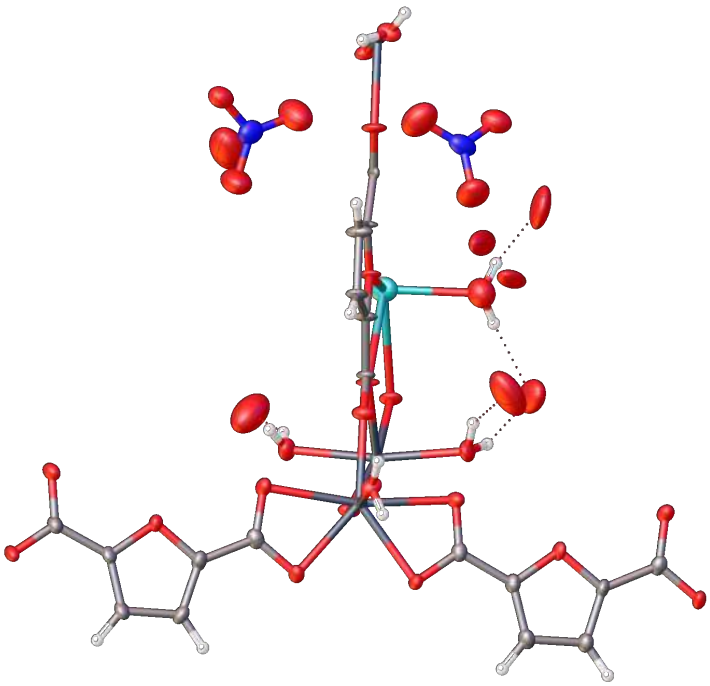

Figure 4.16. Asymmetric unit of compound 3. Indium (dark grey), sodium (turquoise), carbon (pale grey), oxygen (red), nitrogen (blue), hydrogen (white).

Figure 4.16 shows one of two parts, which make up the overall structure of this compound in a 37.45 : 62.55 occupancy split.

The figure shows several water molecules hydrogen bonded (O…O separations of 2.8087 Å, 2.7875 Å, 2.7691 Å, 2.8769 Å), to various sites within the structure. For clarity purposes, these molecules have been omitted from the figures presented in this chapter.

In the same fashion as compound 2, infinite In(FDC) chains make up the backbone of structure 3 and run in the same direction, as shown in Figure 4.17.

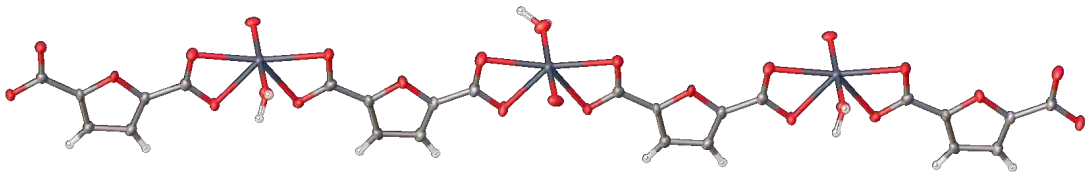

Figure 4.17. In(FDC) chains in compound 3. Indium (dark grey), carbon (pale grey), oxygen (red), hydrogen (white).

As well as these chains, there are finite indium hydroxide chains, linking two adjacent In(FDC) chains displayed in Figure 4.18. These finite chains consist of three indium ions, (two seven co–ordinate and a six co–ordinate) and are ultimately capped by co–ordinated water molecules.

Two μ_4–FDC linkers bridge between two of these indium hydroxide chains, each μ_2-carboxylate group co–ordinates to a six and seven co–ordinate indium.

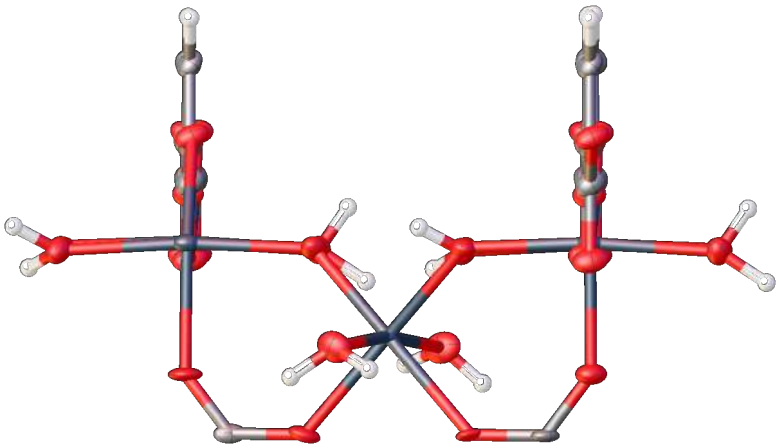

Figure 4.18. Finite In(OH) chains. Indium (dark grey), carbon (pale grey), oxygen (red), hydrogen (white).

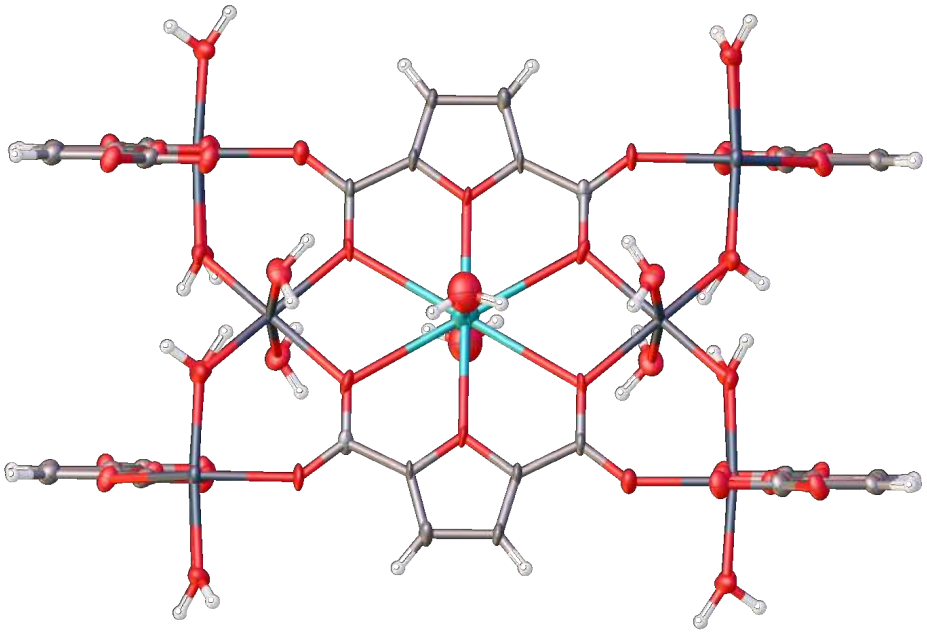

Figure 4.19. μ_4 – FDC linkers bridge between two In(OH) chains. Indium (dark grey), sodium (turquoise), carbon (pale grey), oxygen (red), hydrogen (white).

The orientation of inter–chain bridging linkers alternates such that the furanic oxygen atoms point towards each other, essentially forming a 16-membered pseudo crown–ether, bridging the two In(FDC) chains.

With a diameter of 5.091(19) Å between the two furanic oxygen atoms, the pseudo crown–ether is large enough to host a sodium ion which has a diameter of 2.32 Å. The overall charge on the framework incorporating the sodium ion, is 2^+, which is counterbalanced by the presence of two nitrate anions, one of which is hydrogen bonded to a water that is capping the In(OH) chains. This implies that the framework itself, with no sodium is cationic, with a nitrate countercation, and during the synthesis, the framework uptakes a salt.

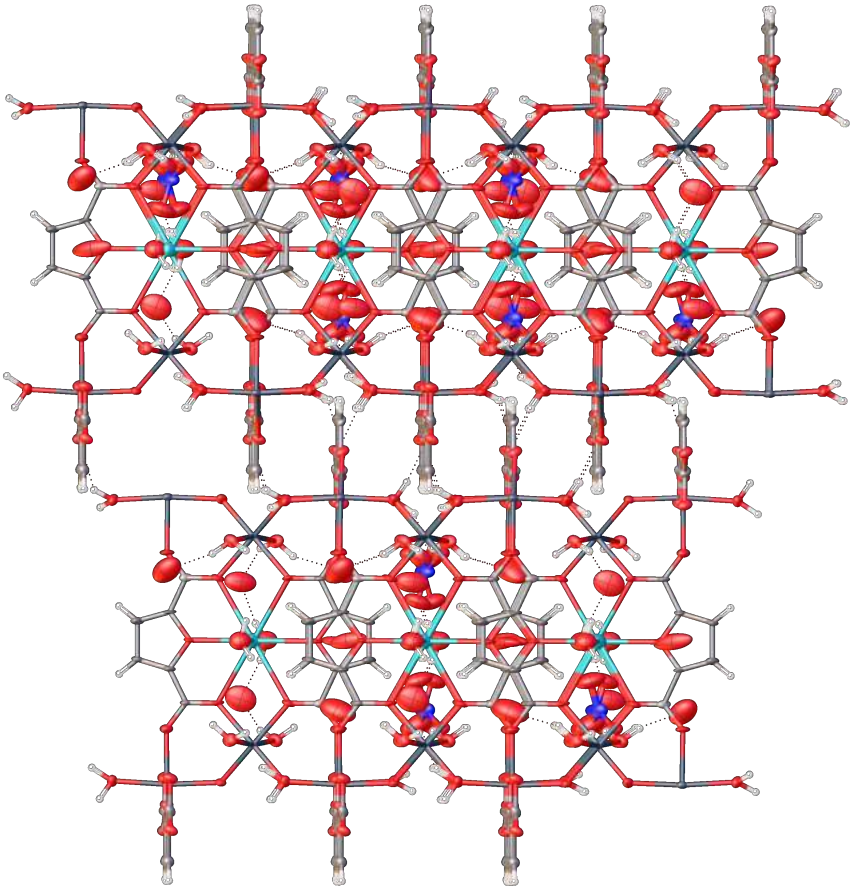

Figure 4.20. Interlocking of two sheets, indium (dark grey), carbon (pale grey), oxygen (red), hydrogen (white).

Figure 4.20 shows the interlocking of 2–dimensional sheets, between which, hydrogen bonds form co–ordinated water molecules, to co - ordinated carboxylate oxygen atoms. The overall formula which was deduced from SCXRD data is $In_3(OH)_2(C_6H_2O_5)_3(NO_3)_2Na(H_2O)_5$ with the nitrates counter balancing the overall positive charge on the framework.

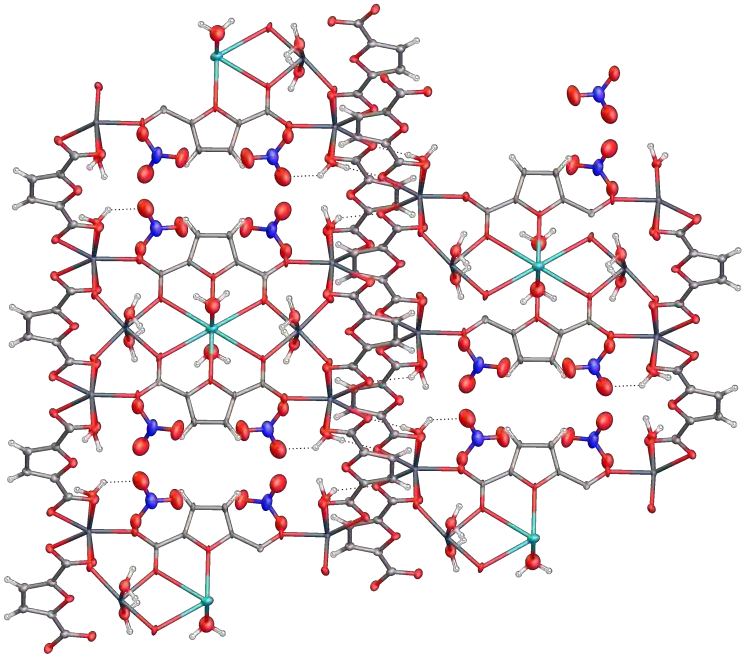

Figure 4.21. View of compound 3 along the crystallographic *a* - axis Indium (dark grey), carbon (pale grey), oxygen (red), hydrogen (white).

The material is extremely dense, as evidenced by the total solvent accessible volume, calculated using a probe size consistent with that of a nitrogen molecule, of 0.0 $Å^3$ / unit cell, which equates to 0.0 %. The largest sphere that can penetrate any direction has a radius of 0.20 Å with the largest spherical void having a radius of 1.60 Å.

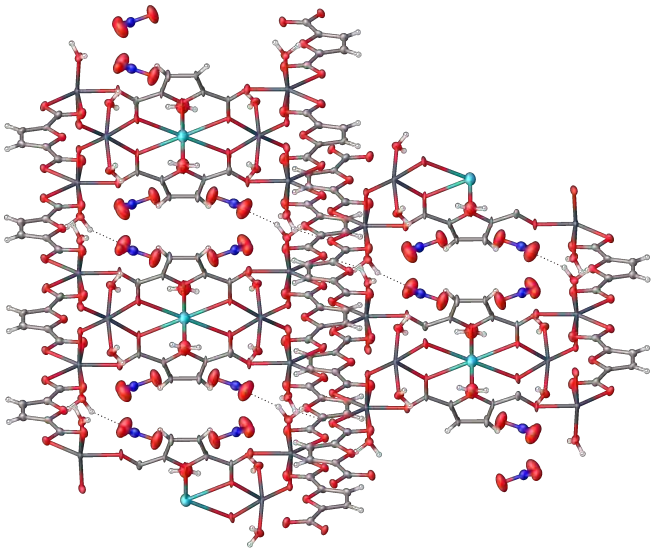

Figure 4.22. View of compound 3 along the crystallographic *b* - axis Indium (dark grey), carbon (pale grey), oxygen (red), hydrogen (white).

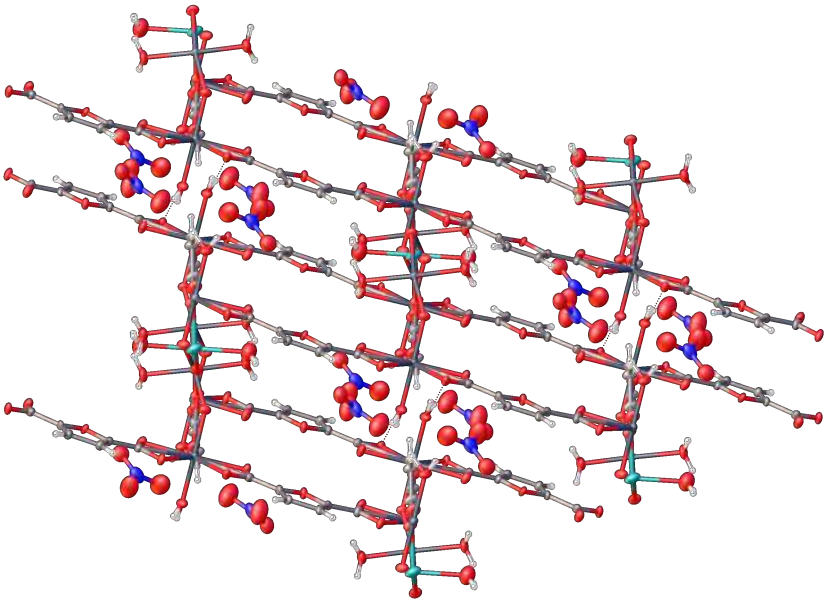

Figure 4.23. View of compound 3 along the crystallographic *c* - axis Indium (dark grey), carbon (pale grey), oxygen (red), hydrogen (white).

Although this is the case, due to the nature of the density and the incorporation of the sodium and nitrate ions into the structure, this compound, or type of compound, could have a potential use in the uptake of other salts from polluted water, by displacing the sodium ion, in the same

way that some zeolites undergo cation exchange. Although the only evidence of this potential application comes from the uptake of a salt during the synthesis, this provides some potential future work to be investigated for this material.

Compound 3 is the first example of a cationic In: FDC framework to be reported that does not consist of indium triangles as shown in Figure 4.1. The formation of the pseudo crown – ether (shown in **Figure 4.19**) is a remarkable discovery and could be used for its applications in water treatment. This route of investigation could prove to be very interesting and useful for future work to be carried out on this material.

4.5.2 PXRD

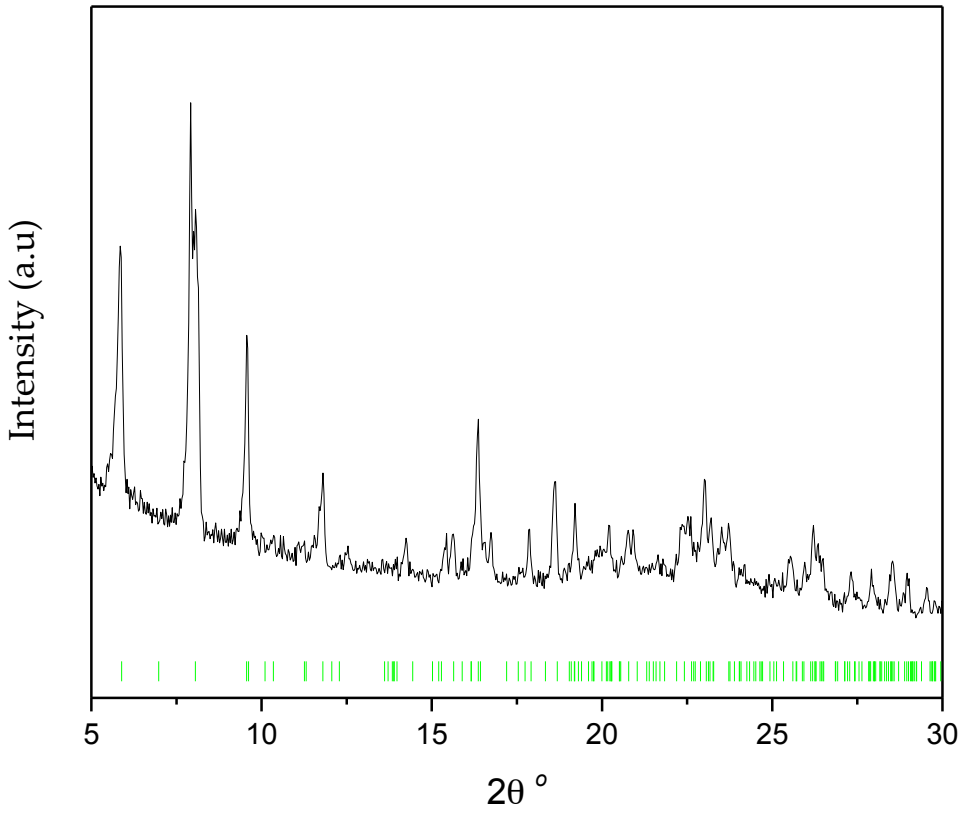

Figure 4.24. PXRD of as-made material indexed to the unit cell of the single crystals with calculated peaks shown by green tick points.

The PXRD pattern shows that majority of the peaks can be indexed to space group $P\bar{1}$ with lattice parameters a = 9.943(9) Å, b = 13.77(2) Å, c = 15.457(1) Å, α = 100.29(8) °, β = 95.62(7) °, γ = 109.37(1) °, V = 1936.6(8) Å^3. The unindexed peaks (14° 2θ) and others do not match any known compounds.

The sample was activated under the conditions described earlier in order to remove the water molecules shown in **Figure 4.16**, and the PXRD pattern of the activated material is shown in Figure 4.25.

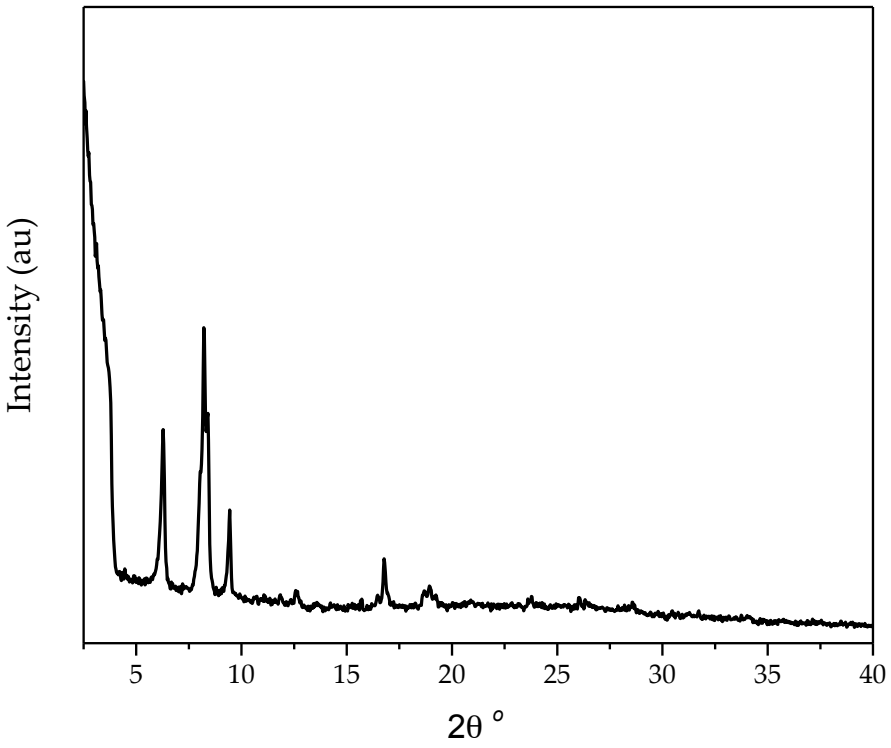

Figure 4.25. PXRD of activated compound 3.

The activation procedure, although successful according to the TGA (Figure 4.26), it also results in a severe loss of crystallinity with many peaks disappearing (Figure 4.25). This is not entirely unexpected given that the structure is made up of interlocking sheets, however, there are some

hydrogen bonds formed between two layers, which is why the material remains crystalline once dried. Although once exposed to heat as in the activation procedure, these hydrogen bonds are broken, allowing the structure to partially collapse.

4.5.3 TGA

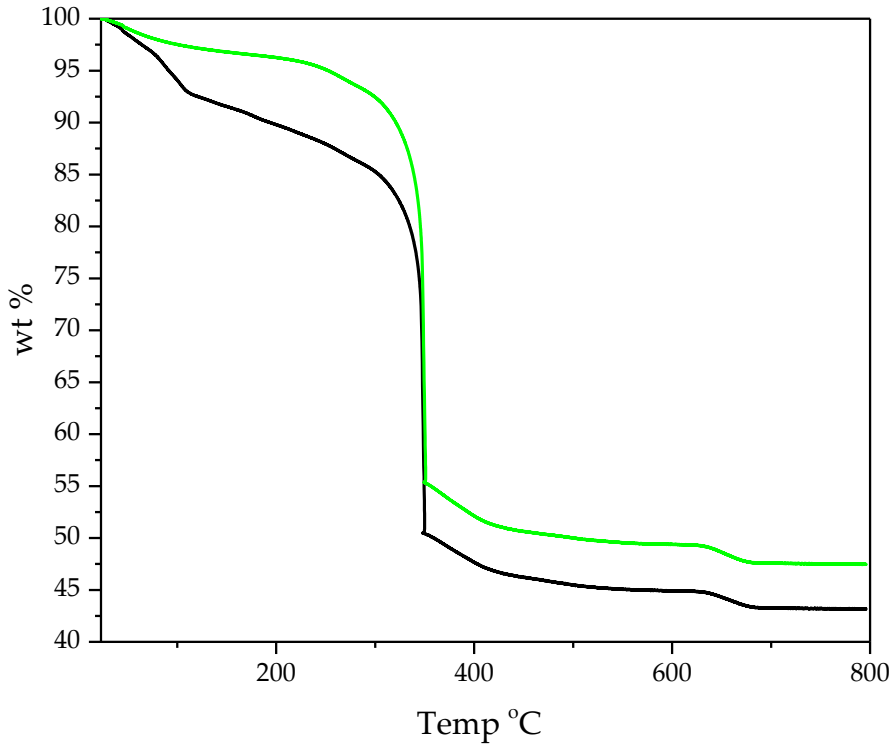

Figure 4.26. TGA trace of as-made (black) and activated (green) compound 3.

The TGA trace of the as-made material shows that there is approximately 15 wt % solvent present. This data shows that activation at 155 °C was necessary to remove all guest solvents, and according to the TGA trace of the activated material, the process was proven successful.

4.5.4 Elemental Analysis

$In_3(OH)_2(C_6H_2O_5)_3(NO_3)_2Na(H_2O)_5$		
Element	Expected %	Measured %
C	20.06	24.19
H	1.68	1.52
N	2.60	0.14

Table 4.3. Elemental analysis of activated compound 3.

The elemental analysis of the activated sample shows poor agreement with the formula composition, however, from the PXRD, it is known that compound 3 partially collapses upon activation. The significant lack of nitrogen measured by CHN indicates that majority of the nitrate ions are removed during the activation. As these are counter ions used to balance the positive charge on the framework, this further indicates a structural change / collapse whereby the positive charge is alleviated. This was highly unexpected and in order to fully understand how this compound changes under activation and to see how the removal of nitrate ions is compensated i.e. how the charge balance is fixed, in-situ SCXRD activation would need to be carried out, which would provide some interesting information about its behaviour.

This third In: FDC material has yet another interesting structure with some interesting and potentially useful properties, however, due to the lack of porosity, along with the inability to activate the material without structural collapse, there were no further investigations into this material.

4.6 Conclusions

The initial aim of the investigations into In: FDC materials was to obtain a material that was isostructural to Al: FDC in order to help solve the crystal structure. A secondary aim was based on indium's ability to adopt many different co – ordination geometries and IBUs; to synthesise a porous In: FDC material with a new structure.

From this perspective, none of the aims were achieved, however, some new and interesting chemistry of indium frameworks has been discovered in the form of three new In: FDC compounds, an anionic (compound 1), a neutral (compound 2) and a cationic framework (compound 3). Introducing NaOH into the reaction mixture results in the formation of structures formed of interlocking sheets, unlike compound 1 which is a fully 3-dimensional framework. Furthermore, changing the concentration of the reagents within the mixture causes the formation of a cationic framework, with the sodium ion incorporated into the structure itself.

When compared with the synthesis of previously reported In: FDC materials, it is clear that the different reaction conditions used are responsible for the formation of three completely different structures.

This is supported by the formation of the three new structures reported in this chapter. In general, lower reaction temperatures and shorter times can be used to synthesise these three new frameworks when compared with reported 3 day reactions. It is also clear that the use of DMF in the synthesis gives rise to the anionic compound 1, and upon use of a mineral base (NaOH), with no DMF, affords the formation of neutral compound 2 and cationic framework 3.

Compound 1 is the first reported example of an anionic framework with an octahedral IBU. As mentioned previously, an anionic In: FDC framework has only ever been reported with a dodecahedral IBU.

The reported synthesis mentioned previously involves the addition of nitric acid, therefore here, the impact of the addition of basic reagents was investigated. Evidence suggests that the presence of a base in the reaction mixture is the key to forming compounds 2 and 3 which contain both CN = 6 and CN = 7 indiums. When the concentration of the base is increased to a large excess, this causes a huge change in the structural outcome, causing the sodium ion to become incorporated into the framework itself. This also provides the material with a bit more stability in air.

Compound 2 is a neutral framework, consisting of CN = 6 and CN = 7 indium ions, which fails to retain its crystallinity after it is washed and dried in air.

Compound 3 has a very similar backbone to compound 2, with finite In(OH) chains and infinite In(FDC) chains, however, this compound is cationic with nitrate ions present to counter this charge.

4.7 Future Work

Although thus far, there have been no porous MOFs reported with In: FDC, it is clear that there are a number of different structures that this system can form.

Compound 1 could be tested for its application in proton conduction as there have been dense In: FDC materials reported to have some potential in this field. The anionic framework reported, displayed a conductivity of 6.7×10^{-6} S / cm, which increases with temperature compared with the neutral framework which showed none.[12] Not only this, but cation exchange could

be a promising route for this structure in the same way that zeolites work for their application in water treatment.

Compound 2 unfortunately, shows no potential benefit for any future work as it collapses once washed and dried, and the synthesis of this compound was found to be un-reproducible.

Compound 3, could have potential for an application in the uptake of metal salts from polluted bodies of water via exchange mechanisms. This is, however, speculation and there is no evidence to suggest that this material can undergo such an exchange, but preliminary tests could give an idea. Future work would include identifying a successful activation procedure to remove any guest solvents molecules.

4.8 References

1. R. D. Shannon, *Acta Crystallogr. Sect. A*, 1976, **32**, 751.
2. J. J. Mihaly, M. Zeller and D. T. Genna, *Cryst. Growth Des.*, 2016, **16**, 1550.
3. D. T. Richens, *Chem. Rev.*, 2005, **105**, 1961.
4. H. Taube, *Chem. Rev.*, 1952, **50**, 69.
5. R. E. Hester and R. A. Plane, *Inorg. Chem.*, 1964, **3,** 768.
6. T. Loiseau, C. Serre, C. Huguenard, G. Fink, F. Taulelle, M. Henry, T. Bataille and G. Ferey, *Chem. Eur. J.*, 2004, **10**, 1371.
7. T. Loiseau, L. Lecroq, C. Volkringer, J. Marrot, G. Férey, M. Haouas, F. Taulelle, S. Bourrelly, P. L. Llewellyn and M. Latroche, *J. Am. Chem. Soc.*, 2006, **128**, 10223.
8. C. Volkringer and T. Loiseau, *Mater. Res. Bull.*, 2006, **41**, 948 - 954.
9. E. V. Anokhina, M. Vougo-Zanda, X. Wang and A. J. Jacobson, *J. Am. Chem. Soc.*, 2005, **127**, 15000.
10. J. Zhang, S. Chen, T. Wu, P. Feng and X. Bu, *J. Am. Chem. Soc*, 2008, **130**, 12882.
11. S. T. Zheng, J. T. Bu, Y. Li, T. Wu, F. Zuo, P. Feng and X. Bu, *J. Am. Chem. Soc*, 2010, **132**, 17062.
12. F. Bu, Q. Lin, Q. G. Zhai, X. Bu and P. Feng, *Dalt. Trans*, 2015, **44**, 16671.

13. J. Qian, F. Jiang, K. Su, J. Pan, Z. Xue, L. Liang, P. P. Bag and M. Hong, *Chem. Commun.*, 2014, **50**, 15224.
14. S. Zhang, L. Han, L. Li, J. Cheng, D. Yuan and J. Luo, *Cryst. Growth. Des*, 2013, **13**, 5466.
15. A. Kong, Q. Lin, C. Mao, X. Bu and P. Feng, *Chem. Commun.*, 2014, **50**, 15619.
16. J. Xia, J. Zheng, J. Xu, L. Wang, L. Yang, Z. Su and Y. Fan, *Inorg. Chim. Acta.*, 2013, **411**, 35.

Chapter 5 CSA Systems

5.1 Overview

MOFs with flexible linkers (FL – MOFs) are of particular interest from a research perspective due to the unlocking of further potential applications of MOFs. A flexible linker, here, is defined as one with at least one sp^3 hybrid atom, in this case, carbon. The ability to incorporate flexible linkers into these frameworks means that chiral organic molecules such as amino acids and peptides, many of which are flexible, can be used to form MOFs with chiral centres. This means that the new MOFs can be used in such applications as enantioselective separations. It is for this reason that FL-MOFs have attracted a lot of attention.[1]

The ability of the flexible linker itself to adopt many different conformations poses a problem for the construction of such materials. As mentioned earlier, the synthesis of MOFs in general is highly dependent on several reaction conditions from time and temperature, to metal source and solvent mixtures, but for FL – MOFs, the reactions can be even more sensitive.[2] The amount of energy put into the reaction and the presence of different additives etc. can have an impact on the conformation that the linker adopts. This then has an overall effect on the self – assembly process leading to the formation of a framework or not.

The difficulties associated with FL – MOFs extend further than just the synthesis, the activation procedure for such materials poses many problems. FL – MOFs have potential to collapse after the removal of the guest solvents because the linker itself cannot hold and support the structure.

With all the complications and difficulties associated with FL – MOFs why is the research interest in them so strong? The ability of flexible linkers to adopt many conformations means that predicting their final structure is even more difficult, which is an exciting prospect for MOF chemists. This, coupled with different metals having different binding preferences significantly increases the number of possible structures. The best way to develop knowledge and concepts around this area of MOFs is to investigate new systems and their behaviours under different conditions.

In this chapter, this structural diversity is highlighted by the synthesis of several different structures using flexible linkers. A selection of flexible linkers is investigated, each with different functionalities and flexibilities.

5.2 CSA Systems

N-(4-carboxyphenyl) succinamic acid (CSA), shown in Figure 5.1 was chosen due to it having a flexible aliphatic chain at one end, with a rigid aromatic ring at the other. This, along with the in – built functionality of the amide group, provides the potential for some interesting new structures.

,

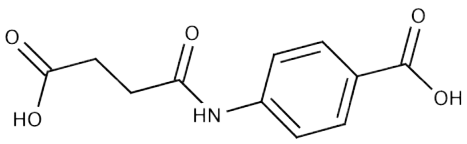

Figure 5.1. CSA linker

This linker, or any other amide containing linker, has never been used with trivalent metals to form a MOF due to the presence of Lewis acidic

metal ions in the reaction mixture, promoting the hydrolysis of the amide bond. Herein, the first examples of MOFs using amide containing linkers and trivalent metals are presented.

5.3 Synthesis

$Al(NO_3)_3.9H_2O$ and $Zn(NO_3)_2.6H_2O$ were purchased from Sigma Aldrich in 97 % and 98 % purity, N-(4-carboxyphenyl) succinamic acid (CSA), $In(NO_3)_3.xH_2O$, $InCl_3$ and $Cu(NO_3)_2.3H_2O$ were purchased from Alfa Aesar in 99 %, 99.99 %. 99.99 % and 98% purity respectively. DMF (dimethylformamide) was purchased from Fisher. All reagents were used without any further purification.

The initial stage of investigating a new material involves exploratory synthesis whereby synthesis conditions such as molar ratios, solvent mixtures, reaction temperatures and times are investigated in order to obtain a crystalline structure. Due to the hydration level of $In(NO_3)_3.XH_2O$ being not known, and TGA data was unclear and proved difficult to distinguish an accurate level, the exact molar ratios between the two reagents was unknown, the ratios were adjusted based on the mass of the indium source. Initial reaction conditions used for this investigation were based on those used to synthesise the three different In: FDC materials presented in chapter 4. From here, solvent ratios and mixtures were adjusted, using DMF, H_2O, EtOH and MeOH in varying ratios and volumes from 5 mL in total to 25 mL. From previous experiments (In: FDC), it was known that times and temperatures of the reactions can have a serious effect on the final outcome, therefore these were adjusted from 12 hours to 4 days and from 70 ^oC to 150 ^oC.

5.3.1 Optimised Synthesis of In:CSA

A 110 mg mL^{-1} aqueous stock solution of $In(NO_3)_3 \cdot XH_2O$ was made up. CSA (237.2 mg, 1 mmol) was weighed into a 40 mL Teflon capped glass vial, to this, $In(NO_3)_3$ solution (2 mL), DMF (2 mL) and H_2O (1 mL) were added. The reaction mixture was heated to 100 ^oC at a rate of 2.5 ^oC / min, and left for 12 hours before being cooled to room temperature at 0.2 ^oC / min. A small aliquot of the product was removed for SCXRD analysis, while the rest was washed with DMF (4 x 20 mL), EtOH (3 x 20 mL) and THF (3 x 20 mL) and left to filter dry, giving a yield of 86.5 mg. The formula of the material was determined from SCXRD to be $In(OH)(C_{11}H_9O_5N) \cdot H_2O$, however, there is one water molecule per indium ion throughout the structure. The final white powder was activated under the conditions described previously and analysed to be phase pure using TGA, PXRD, elemental analysis and SEM, the data is shown in this chapter.

5.3.2 Optimised Synthesis of Al:CSA

A 1M aqueous stock solution of $Al(NO_3)_3.9H_2O$ was made up. CSA (237.21 mg, 1 mmol) was weighed out into a 40 mL Teflon capped glass vial, to this, $Al(NO_3)_3$ solution (0.60 mL, 0.6 mmol), DMF (2 mL) and H_2O (2.40 mL) were added. The reaction mixture was heated to 100^oC at a rate of 2.5^oC per minute, and left for 12 hours before being cooled to room temperature at 0.2^oC per minute. The resultant white powder was filtered and washed with DMF (4 x 20 mL), THF (3 x 20mL) and ethanol (3 x 20mL) and left to pump dry, this yielded 122 mg of a white powder. 104 mg of the material was activated at 155^oC under vacuum (10^{-2} mbar)

overnight leaving a final yield of 95 mg (65% yield). The final composition was analysed to be [Al(OH)($C_{11}H_9O_5N$)], however, once exposed to air, the material adsorbs water which can be seen in the TGA and elemental analysis.

5.3.3 Activation Procedure

In order to establish the best activation procedure, which is one whereby all guest molecules are removed and the structure of the material remains in tact, various different conditions must be tried. In this instance, the activation procedure used in chapter 3 for the Al: FDC material proved to be successful, evidenced by data presented later in this chapter, and so no change or exploration was necessary. As-made material (70 – 90 mg) was activated at 155 ^{o}C, under vacuum (10 $^{-2}$ mbar) overnight.

5.3.4 Water Stability Tests

As-made material (30 – 40 mg) and H_2O (15 mL) were loaded into a 40 mL Teflon capped glass vial with a magnetic stirrer bar, which was placed on a stirrer plate at room temperature overnight.

5.4 Characterisation of In:CSA

5.4.1 Structure

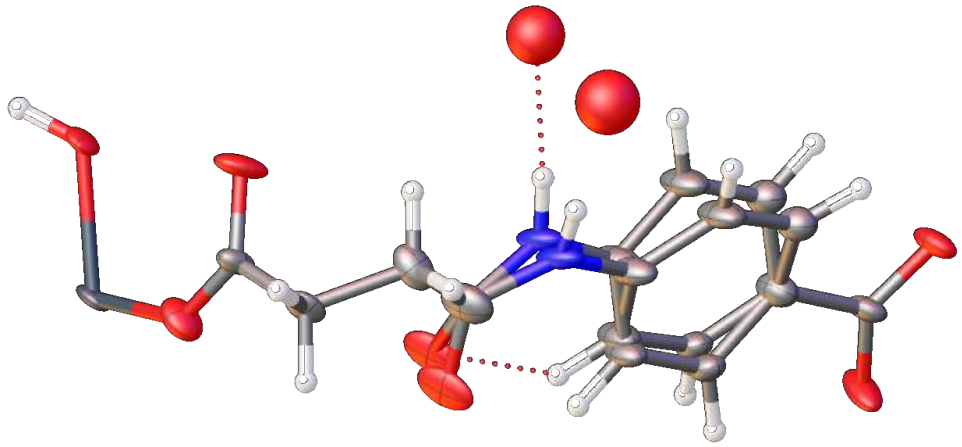

Figure 5.2. Asymmetric unit of In: CSA. Indium (dark grey), oxygen (red), carbon (grey), nitrogen (blue), hydrogen (white).

The structure of this material was solved from SCXRD by Dr George Whitehead using OLEX2 and Shelx software. The *as* – made material crystallises in the monoclinic space group $P2_1/c$ with lattice parameters a = 8.0483(3) Å , b = 7.2282(3) Å, c = 24.2472(18) Å, β = 93.708(8)°, V = 1407.62(18) Å^3. Data collection and refinement parameters can be found in Appendix II.

The asymmetric unit of this structure, shown in Figure 5.2, consists of a single CSA linker and a hydroxide group, co – ordinated to an indium, with a single water molecule hydrogen bonded (O…N bond length of 2.866 Å) to the amide hydrogen atom. In: CSA crystallises in the monoclinic space group $P2_1/c$ with the indium hydroxide chains running parallel to the crystallographic b – axis (unique axis) shown in Figure **5.3**.

The asymmetric unit demonstrates the ability of a flexible linker to adopt different conformations. It can be seen that the phenyl and amide groups of the CSA linker changes between two conformations in a 62:38

occupancy split. With each of the conformations, a water molecule is hydrogen bonded to the amide group, which is therefore disordered throughout the structure as the conformation switches between the two.

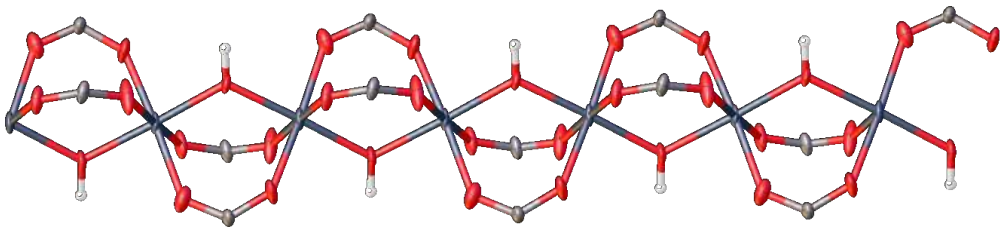

Figure 5.3. SBU of In: CSA. Indium (dark grey), oxygen (red), carbon (grey), nitrogen (blue), hydrogen (white).

The inorganic building unit of In:CSA is typical for many Al, Ga, In MOFs.[3, 4] Indium hydroxide chains, made up of corner sharing $InO_4(OH)_2$ octahedra are further bridged by dicarboxylate CSA linkers. Here, *trans* – refers to the relative positions of the co – ordinated hydroxy groups. Each In-OH-In pair are bridged additionally by two μ_2 carboxylates from two CSA linkers, one of which is from the flexible aliphatic end, the other from the rigid, phenyl end. The remaining carboxylates then bridge to a single adjacent indium hydroxide chain, completing the 2–dimensional sheet structure as shown in Figure 5.4.

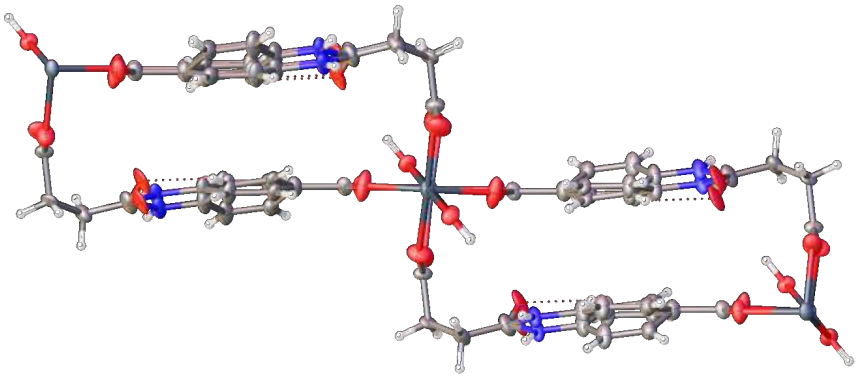

Figure 5.4. Connectivity of the CSA linker forming 2-dimensional sheets. Indium (dark grey), oxygen (red), carbon (grey), nitrogen (blue), hydrogen (white).

The flexible, aliphatic tail of the linker allows it to adopt an L – shaped conformation, which causes the sheets to cap themselves, prohibiting the growth any further into an extended 3 – dimensional framework. Each CSA linker contains one amide group, which do not align with amide groups of adjacent linkers, this is evidenced in Figure 5.4, meaning that hydrogen bonding between the layers is not possible. Weak Van der Waal's attractions is therefore the dominant intermolecular interaction which force the layers to pack tightly in a step – wise motif along the crystallographic *a* – axis. Each CSA linker has a water molecule hydrogen bonded between the amide proton and the adjacent hydroxyl group. These sit within the cylindrical voids, which run perpendicular to the planes of the 2 – dimensional sheets as shown in Figure 5.5.

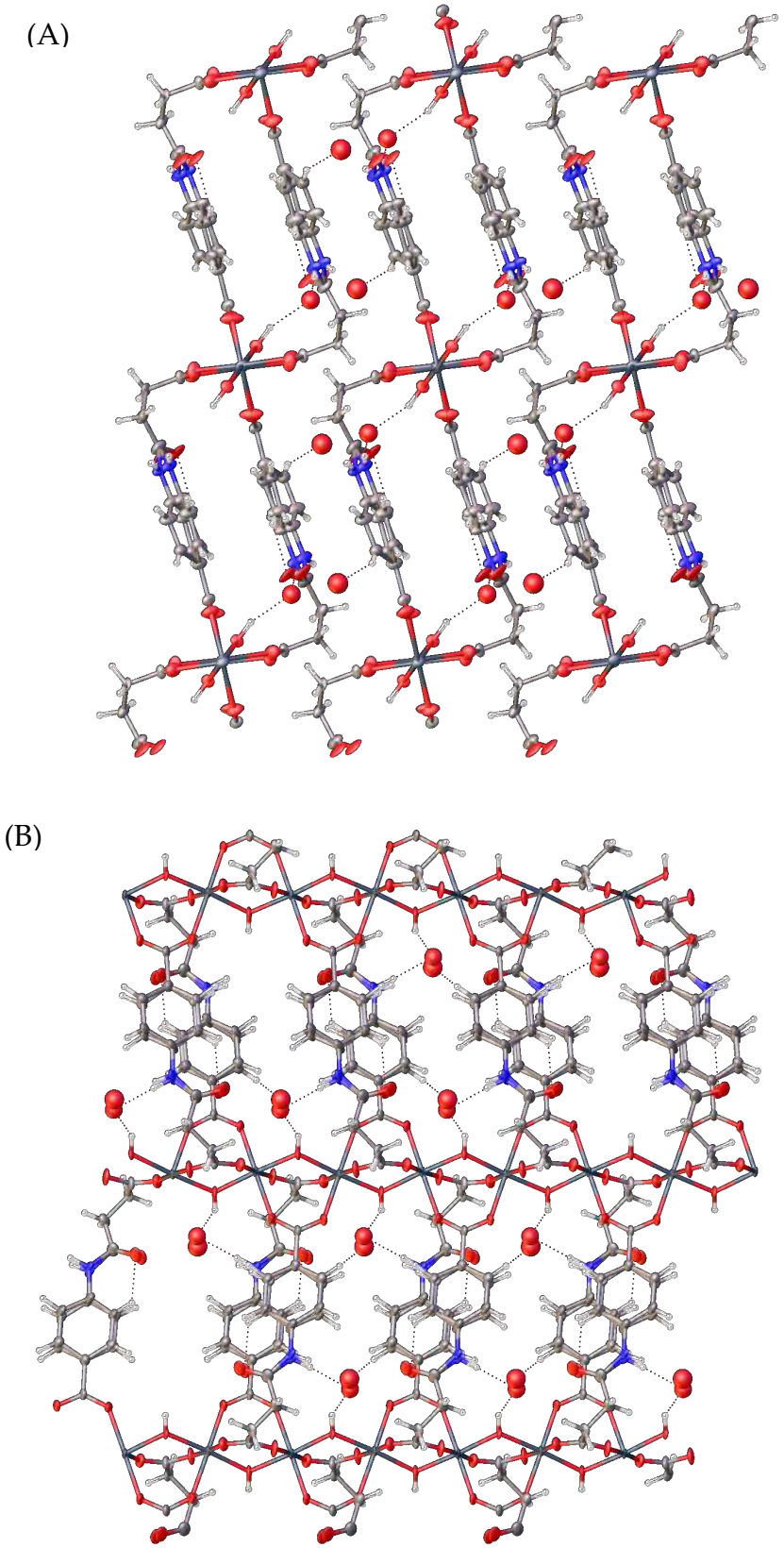

Figure 5.5. 2-Dimensional sheets of In: CSA viewed along the crystallographic *b* – axis (A) and *a* – axis (B). Indium (dark grey), oxygen (red), carbon (grey), nitrogen (blue), hydrogen (white).

The dashed bond lines in Figure 5.5 represent hydrogen bonds, which form between the framework and inter-layer water molecules. As well as these intermolecular interactions occurring between layers, there are two phenyl groups of adjacent CSA linkers, which are almost aligned (displacement of 1.369(7) Å), with a plane – plane distance of 3.834(3) Å, providing evidence of weak $\pi - \pi$ stacking within each sheet.

The total solvent accessible volume of In: CSA is 0.0 % for both parts (referring to both orientations of the phenyl group), which was calculated using probes of 1.8 Å and 1.65 Å radius, consistent with that of nitrogen and carbon dioxide respectively. The largest penetrable sphere for the whole structure is 0.80 Å radius, with a largest spherical void of 1.40 Å diameter, therefore it is hypothesised that the material is non – porous to both nitrogen and carbon dioxide, which was supported by data in Figure 5.14 and Figure 5.15 respectively. Water, with a kinetic diameter of 2.65 Å, is seen in the voids which run along the crystallographic *a* - axis, these voids are shown in Figure 5.6.

Figure 5.6 displays the whereabouts of the voids, evidenced by the presence of a water molecule, which run along the crystallographic *a* – axis. These voids have a largest penetrable sphere of 0.80 Å radius, which feed into the largest spherical void of 1.40 Å. When compared with Figure 5.5, the voids line up perfectly where the water molecules sit, which implies that the material has the ability to swell slightly, in order to allow the water in to sit in the larger pocket.

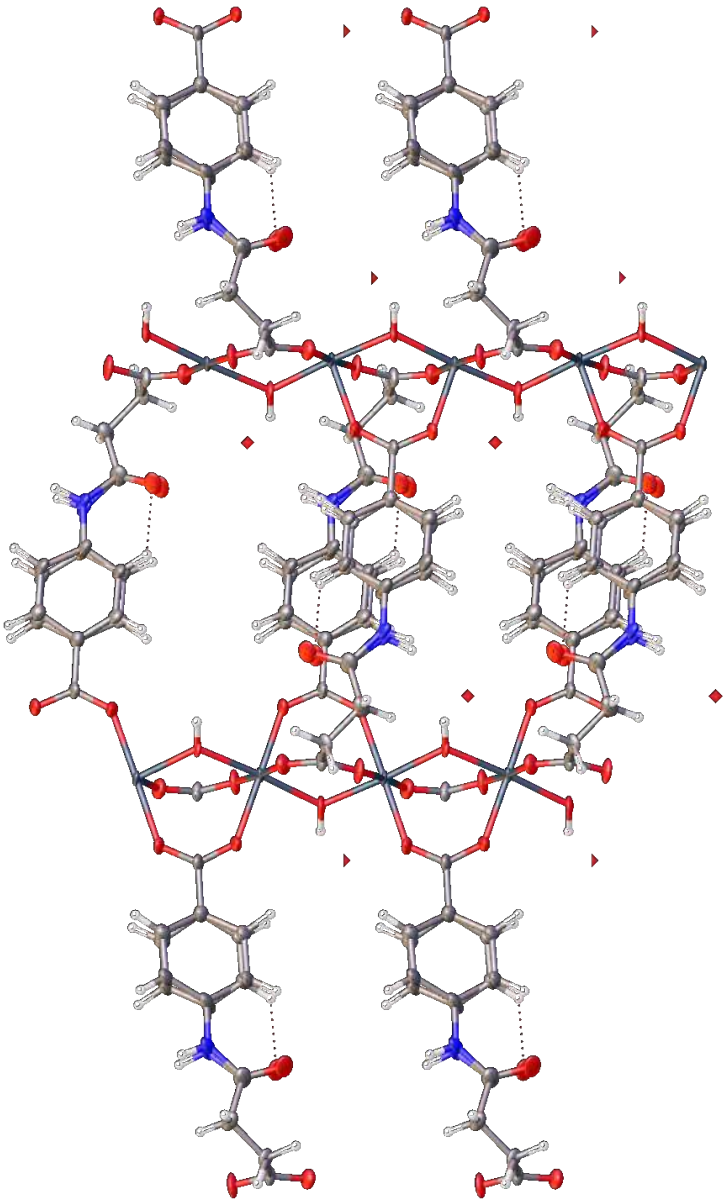

Figure 5.6. In:CSA view along the crystallographic *a* – axis, indium (dark grey), carbon (grey), nitrogen (blue), oxygen (red), hydrogen (white), void space (red squares / triangles).

5.4.2 Structure of In: CSA post activation

A single crystal was taken from the activated sample. The chemical composition of the material remains the same after activation. There is a slight change in the lattice parameters upon activation a = 7.9601(7) Å, b = 7.2502(6) Å, c = 23.809(3) Å, β = 90.729(9)°, V = 1374.0(2) Å^3. The

asymmetric unit and SBU are the same as for the as–made material, however, the overall structure have a difference; the CSA linker adopts one orientation throughout in the activated sample, and the water molecules are hydrogen bonded to an amide hydrogen and the amide oxygen of an adjacent linker in the as-made material. It is clear from Figure 5.7, that the water molecule in the "activated" material is hydrogen bonded to the amide oxygen (O…O separation of 2.9981 Å). This implies that the new hydrogen bonding mode of the water molecules effectively locks the linker molecules into a preferred orientation, which is further enhanced by $\pi - \pi$ stacking of facing phenyl rings. Data collection and refinement parameters can be found in Appendix II.

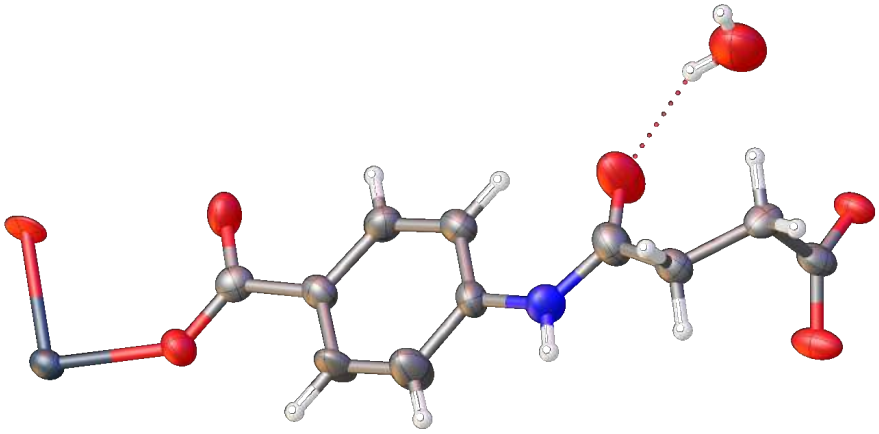

Figure 5.7. Asymmetric unit of the activated single crystal of In: CSA. Indium (purple), carbon (grey), oxygen (red) and hydrogen (white).

The presence of this water molecule means that this structure cannot be defined as "activated", and indicates that between the activation and data collection, water has been adsorbed from the atmosphere, which is supported by TGA data shown in Figure 5.12. In order to determine the structure of a completely desolvated sample, high temperature SCXRD

must be carried out and is proposed as future work for this line of research.

The overall connectivity of the structure remains identical after activation, and the largest spherical void remains at 1.40 Å diameter. The largest penetrable sphere along the crystallographic *a* – axis is 0.80 Å radius.

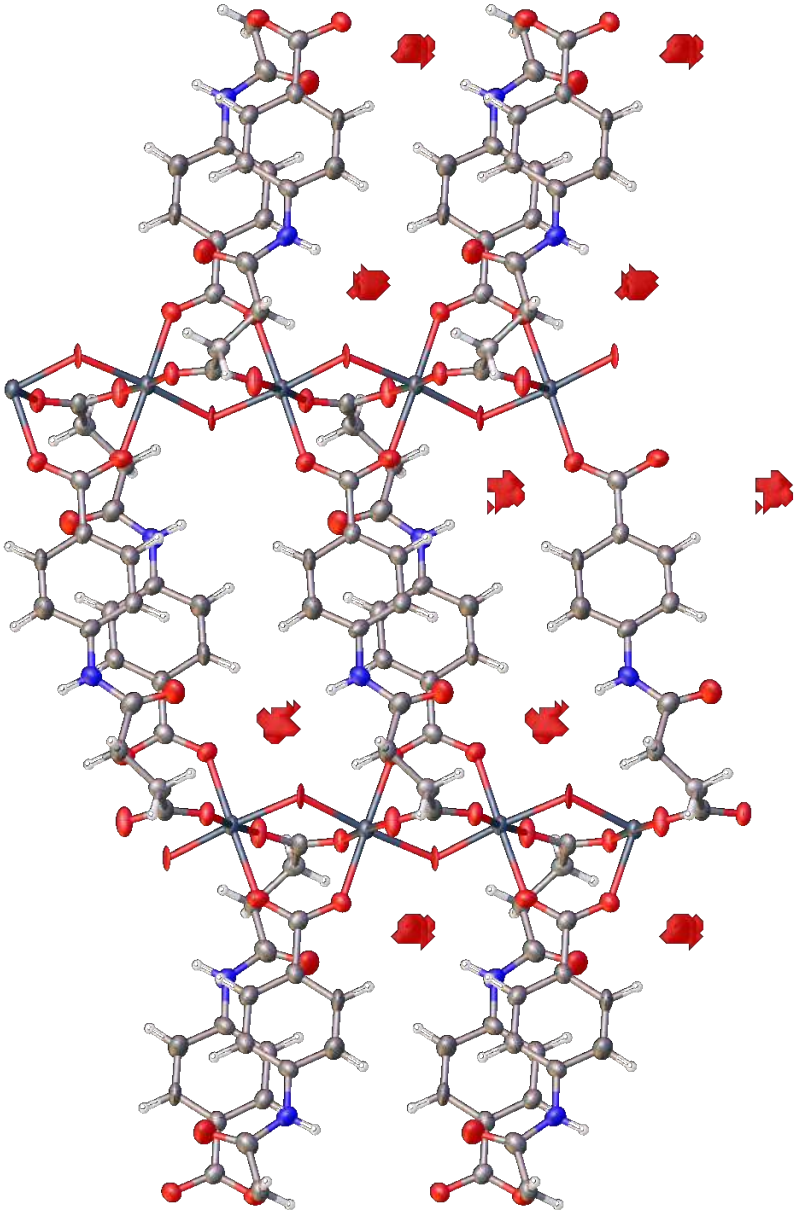

Figure 5.8. Voids (red masses) of activated In: CSA along the crystallographic *a* – axis. Indium (purple), carbon (grey), oxygen (red) and hydrogen (white).

The presence of the water in the activated material, again implies that it has the ability to swell in order to accommodate the molecule into the largest spherical void, which are shown in Figure 5.8.

5.4.3 PXRD

All peaks of the as-made material can be indexed to the unit cell obtained from the single crystal data as shown in Figure 5.9 indicating majority of the bulk material is phase pure.

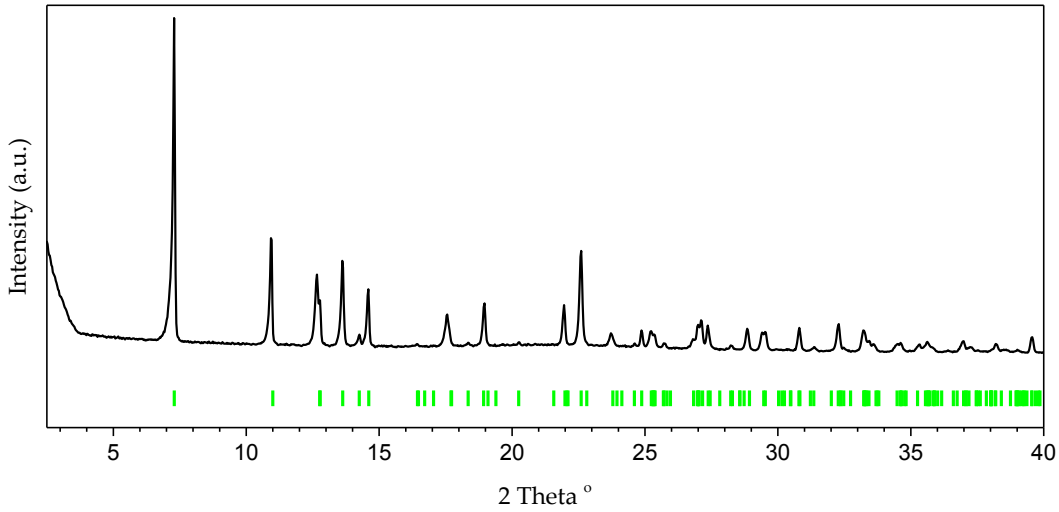

Figure 5.9. PXRD of as-made In: CSA indexed agains the unit cell from the single crystal data. Green tick marks indicate calculated peaks.

The experimentally obtained pattern from the activated sample, however, cannot fully index to the obtained unit cell (Figure 5.10), showing that a phase change has occurred, which requires further investigation.

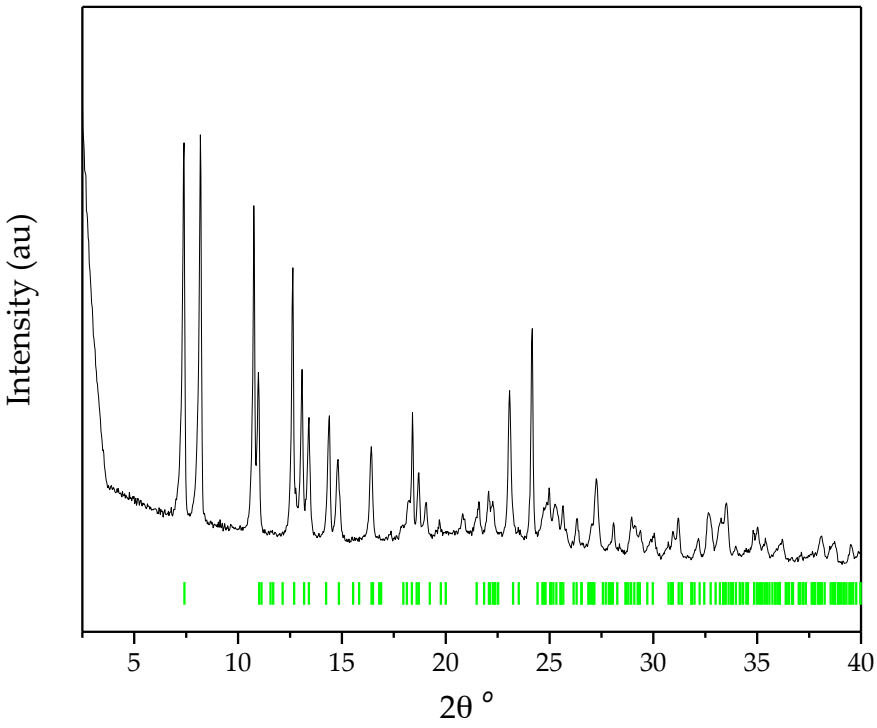

Figure 5.10. PXRD of activated In: CSA indexed to the unit cell of the activated single crystal. Green tick marks represent calculated peaks.

It was hypothesised that the activated material has taken up less atmospheric water between activation and running a PXRD measurement. For this reason, a PXRD pattern was measured of a completely desolvated sample and the data is presented in Figure 5.11. For this, the material was activated under normal procedure and loaded into a capillary in a helium dry box to avoid adsorption of atmospheric water.

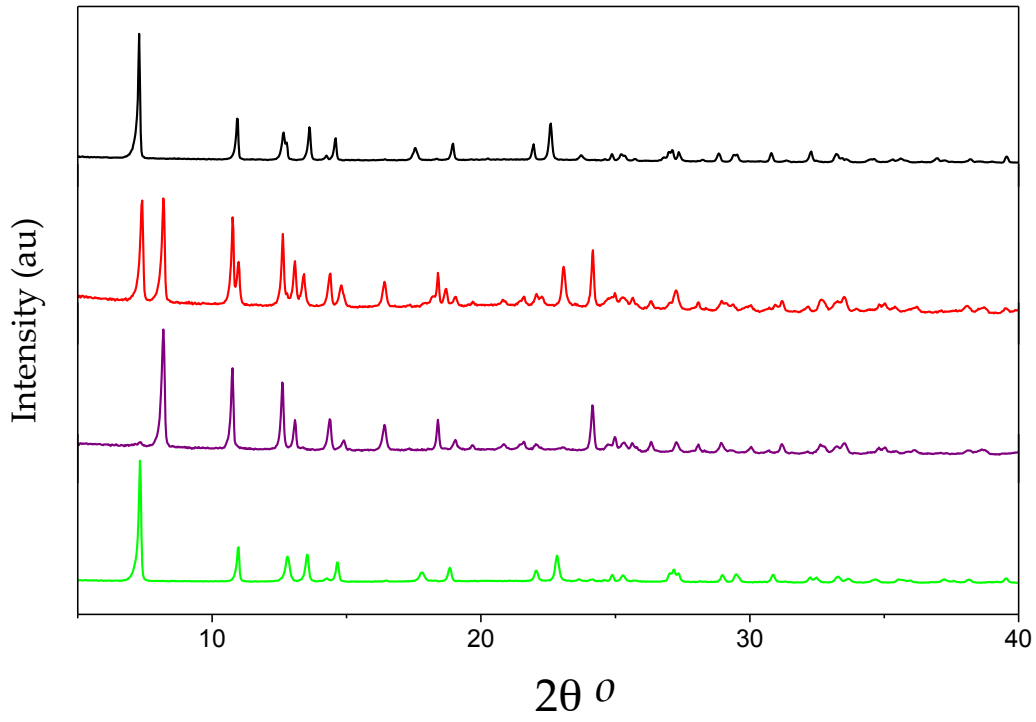

Figure 5.11. PXRD patterns of In: CSA, as-made (black), original activated (red), completely desolvated (purple), after exposure to air for one week (green).

It is immediately clear from that a reversible structural change occurs upon complete desolvation of this material as evidenced by the change of PXRD pattern after activation and its gradual return to the *as*-made structure upon re-exposure to air. This confirms the hypothesis that it is the activation process, and therefore the removal and uptake of guest solvent molecules, that causes a structural change to the material, the nature of which remains unclear. This would explain why this structural change is not evident in the SCXRD data from the activated crystal. High temperature, in – situ SCXRD data would need to be collected on this material in order to observe this change properly.

5.4.4 TGA

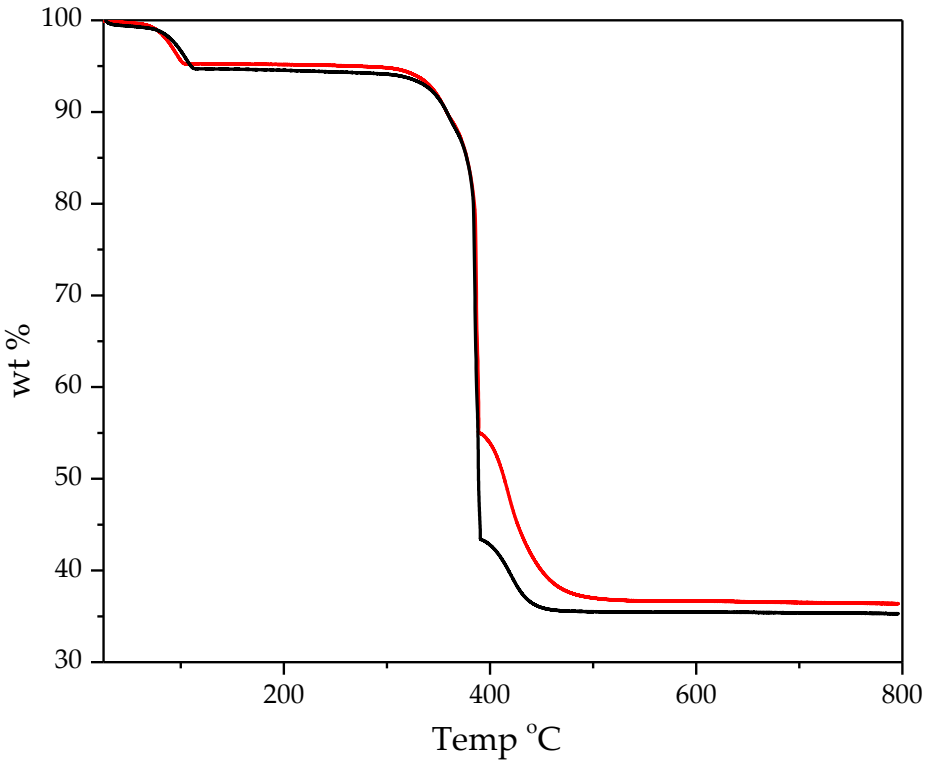

Figure 5.12. TGA trace of as-made (black) and activated (red) In: CSA**.**

The TGA traces of both the as – made and activated materials show no mass loss due to removal of guest DMF molecules, proving that all measured nitrogen content during the elemental analysis is from the linker. There is an initial mass loss seen in both traces up to 105 °C of ca 5 %, which can be attributed to the removal of adsorbed atmospheric water. From the SCXRD data, it is known that his material uptakes water from the atmosphere upon exposure to air, explaining this initial mass loss observed for the activated sample also.

The In_2O_3 residue from the activated sample makes up 36.52 % of the measured sample, of which 82.71 % is indium, therefore the indium

content of the dry material was calculated to be 31.74 %. Based on the dry formula [In(OH)(CSA)], which is known from the crystal structure, the theoretical indium content is 31.28 % implying that the bulk of the material is pure, with the same composition as the single crystal and the same as the as-made material.

5.4.5 Elemental Analysis

Elemental analysis was carried out on an activated sample and since this material adsorbs water from the atmosphere, this needed to be taken into account when fitting the elemental analysis data. From the crystal structure, it is known that one water molecule is hydrogen bonded per CSA linker.

$In(OH)(C_{11}H_9O_5N)(H_2O)$		
Element	Expected %	Measured %
C	34.31	33.96
H	3.14	3.07
N	3.64	3.54

Table 5.1. Elemental analysis of activated In: CSA

When one water molecule is added per formula unit, there is good agreement with the experimental and theoretical CHN data. One water molecule equates to 4.70 % of the composition, proving that the bulk of the material matches the composition of the single crystal and is pure. The presence of this water molecule is known from the single crystal data presented earlier.

5.4.6 SEM

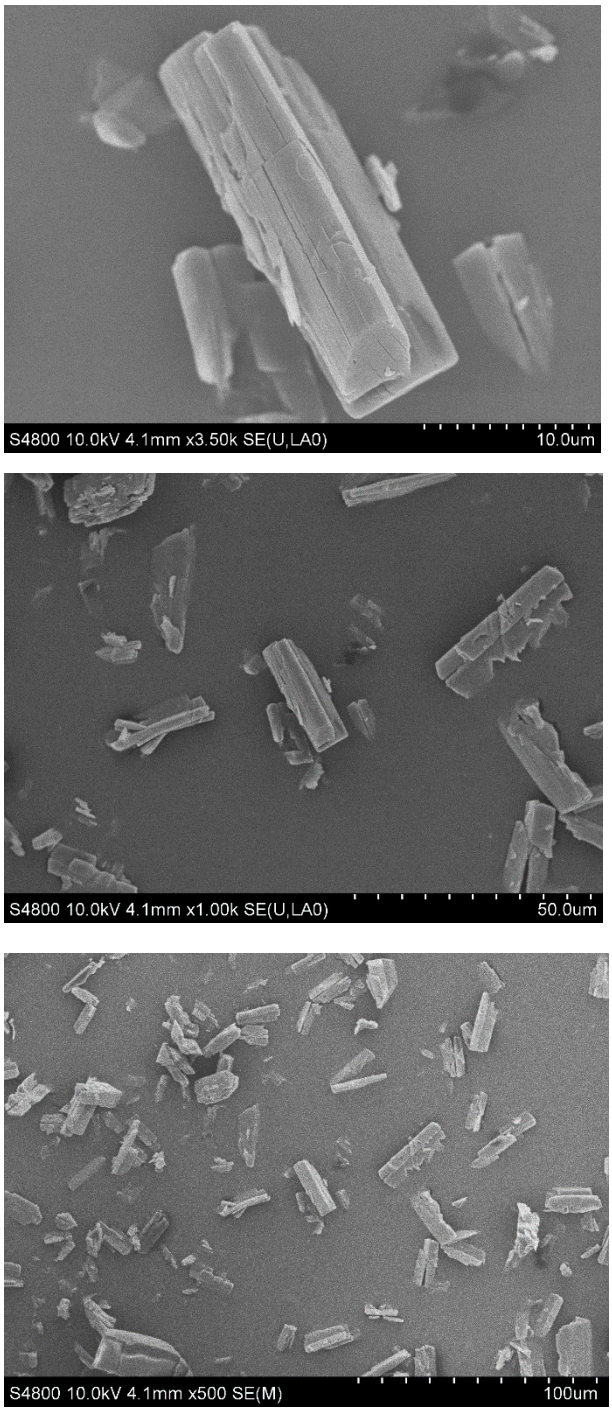

Figure 5.13. SEM images of an activated sample of In: CSA.

The SEM images of the activated material show a uniform rectangular block morphology suggesting a homogeneous bulk material.

5.4.7 Surface Area Measurement

Although from the SCXRD data, the material is made of 2–dimensional sheets, with no solvent accessible pore volume, the presence of water molecules within the structure implies that it can swell in order to accommodate guest molecules into its largest spherical void. The N_2 adsorption isotherm was run at 77.3 K and is presented in Figure 5.14.

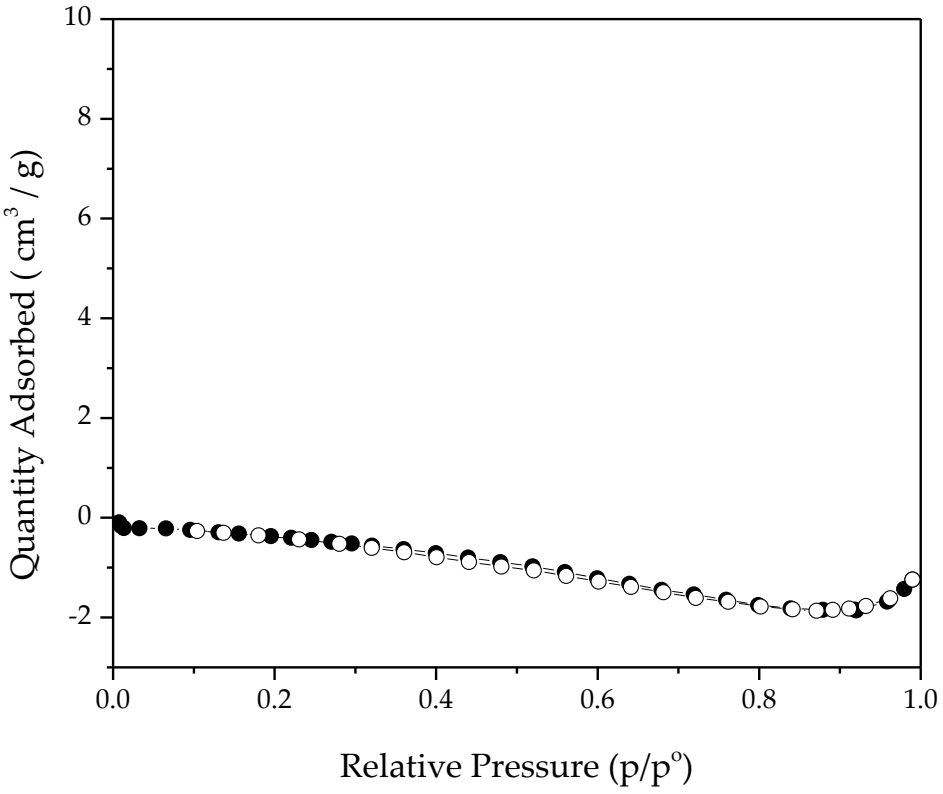

Figure 5.14. N_2 adsorption isotherm of In: CSA, solid points represent the adsorption branch and hollow points represent the desorption branch.

This is clear proof that there is no porosity towards nitrogen. The lack of measured porosity was expected since the solvent accessible pore volume

was calculated to be 0.0 $Å^3$ when using a probe of 1.82 Å radius, which is equivalent of N_2.

5.5 CO_2 adsorption measurements

CO_2 adsorption isotherms were measured on this material at 195 K, 273 K and 298 K to test whether it has the capability of adsorbing other gases, the results are presented in Figure 5.15. Although the calculations indicate that his material has no solvent accessible volume for molecules of this size, due to the presence of the amide group and the ability for CO_2 to interact with this, it could enhance the uptake ability of the material.

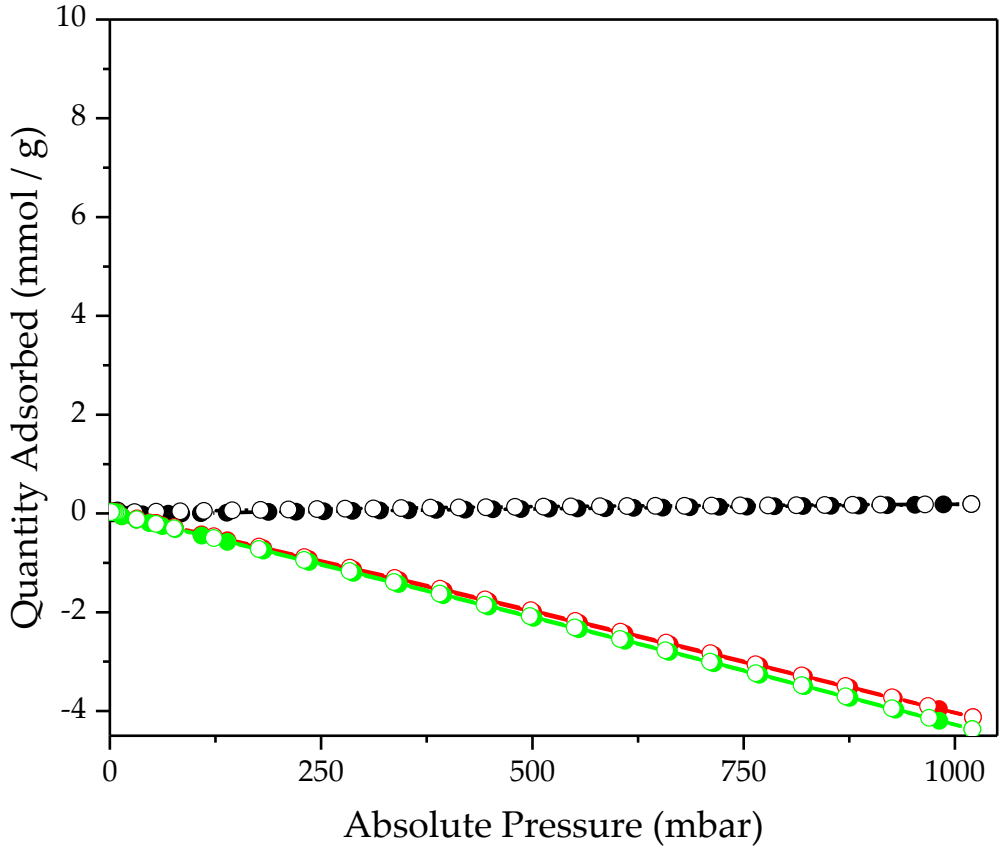

Figure 5.15. CO_2 adsorption isotherms onto In: CSA at 298 K (green), 273 K (red) and 195 K (black). Solid points represent the adsorption branch, while hollow points represent the desorption branch.

The CO_2 adsorption isotherms show a clear lack of porosity towards carbon dioxide, meaning that this functionality of the linker has no impact on this process.

The PXRD pattern after measuring the CO_2 isotherms, shown in Figure 5.16, show that the material adopts the same activated structure as shown earlier.

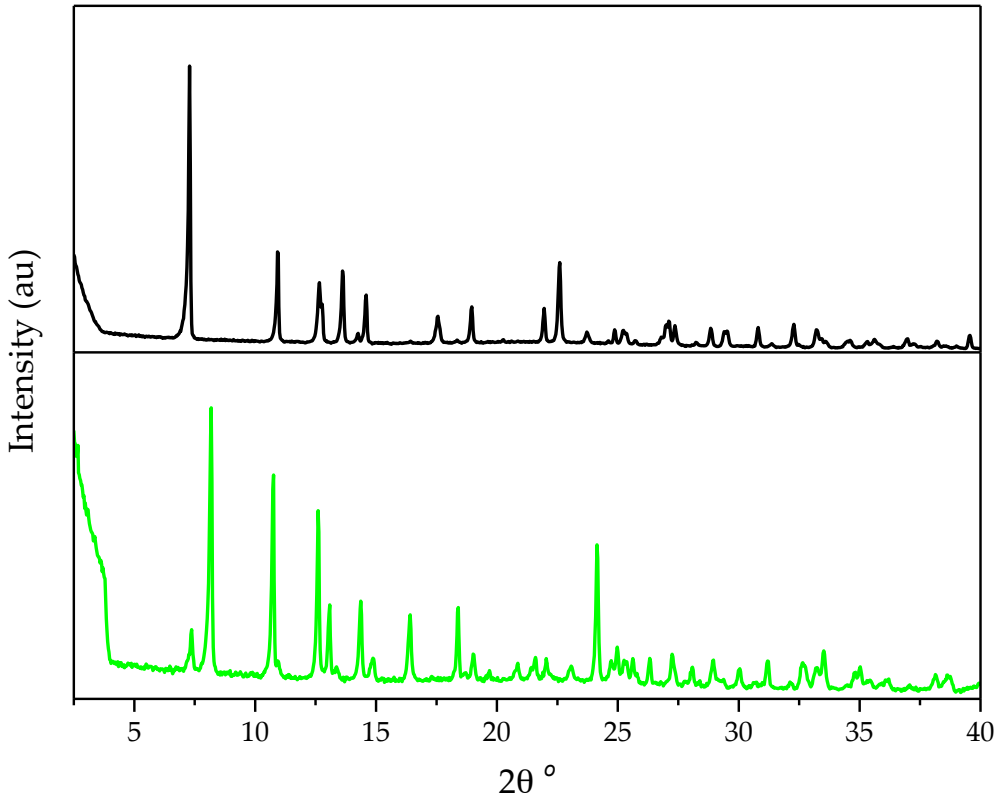

Figure 5.16. PXRD pattern of as-made (black) and post CO_2 isotherm measurement (green).

According to the PXRD patterns above, it is clear that there is no structural collapse, showing that the lack of porosity towards CO_2 stems solely from the lack of solvent accessible pore volume.

5.6 Water Stability

The PXRD pattern of the material after the water stability test was measured and the data is presented in Figure 5.17.

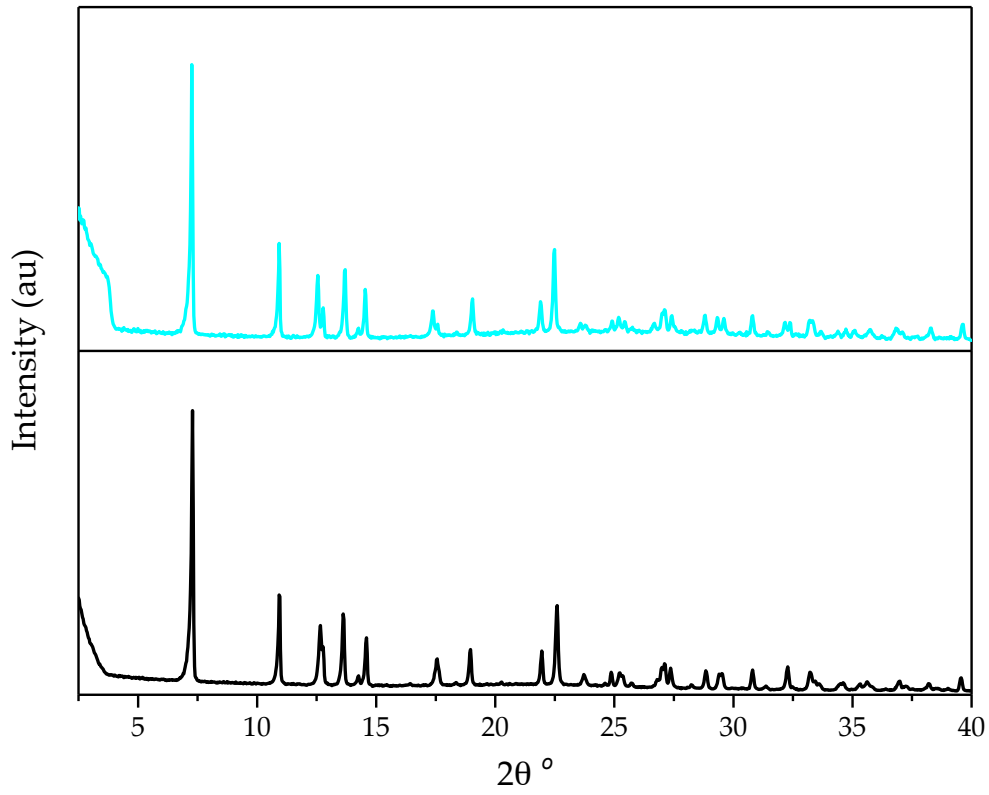

Figure 5.17. PXRD pattern of as-made (black) and after stirring in water overnight (cyan) In: CSA.

The result shows that the material remains intact after this treatment, confirming that it is structurally stable in water, evidenced by the same PXRD pattern both before and after water treatment, which is a key attribute in G13 MOFs, which include thermal and water stability.[5-7]

5.7 Characterisation of Al:CSA

5.7.1 PXRD

Since no single crystals were obtained in any of these syntheses, SCXRD was not possible and so the structure of the material was hypothesised to be isostructural to that of In: CSA, since the SBU formed in that material is highly common for aluminium MOFs also. This is evident with the number of reported aluminium MOFs with this SBU.

The PXRD patterns shown in Figure 5.18 show that Al: CSA remains the same, with no loss of crystallinity after activation.

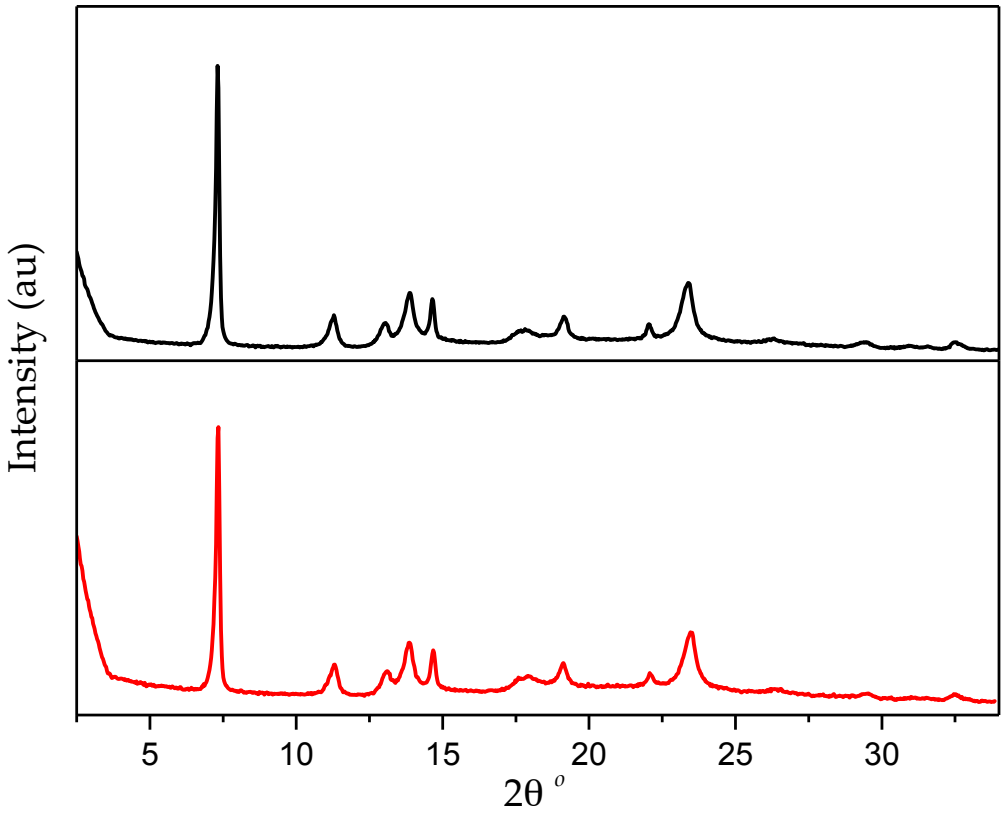

Figure 5.18. PXRD of as-made (black) and activated (red) Al: CSA.

All peaks of the PXRD pattern collected from the activated sample can be indexed to the same unit cell as for the In: CSA material (Figure 5.19), showing that the materials are isostructural, with a slight change in lattice parameters. It is unclear though, why Al: CSA does not undergo the same structural change upon activation that is seen for In: CSA.

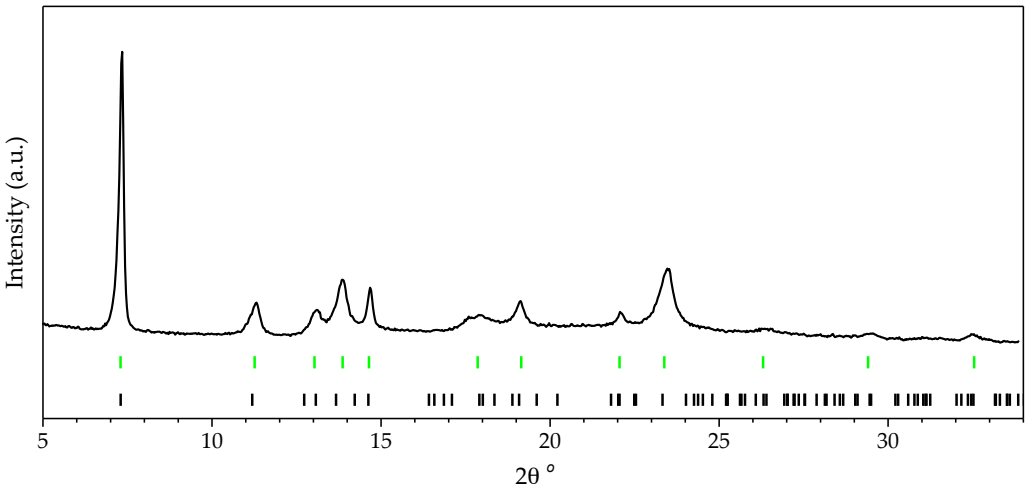

Figure 5.19. PXRD of activated Al: CSA indexed to the unit cell of In: CSA, allowed peaks (black tick marks), observed peaks (green tick points).

The lattice parameters for Al: CSA were obtained from a Pawley fit, using the lattice parameters from In: CSA. There is a slight change in lattice parameters from In: CSA to Al: CSA as shown in Table 5.2. This change in parameters explains the slight shift in some peak positions of the PXRD between the two materials and was expected due to the different sized metal ions.

	***a* (Å)**	***b* (Å)**	***c* (Å)**	**β (°)**	**V (Å³)**
In:CSA	7.9601(7)	7.2502(6)	23.809(3)	90.729(9)	1374.0(2)
Al:CSA	7.8586(6)	7.4662(1)	24.1935(1)	93.708(2)	1416.570

Table 5.2. Lattice parameters of activated In:CSA and Al:CSA.

5.7.2 TGA

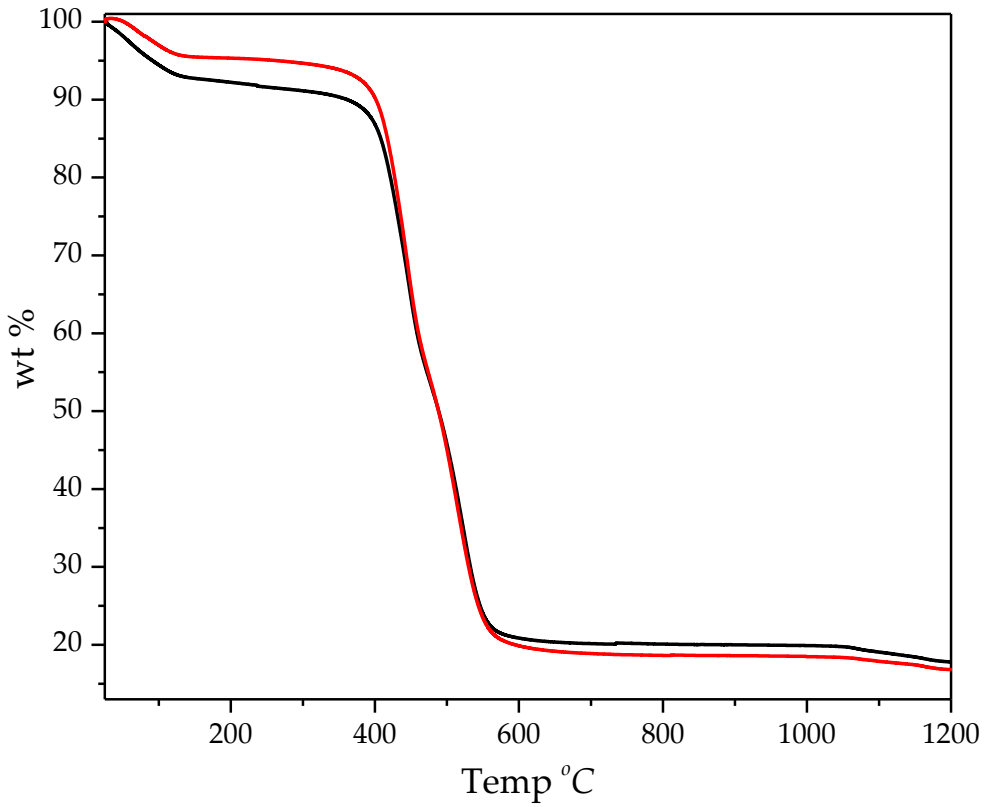

Figure 5.20. TGA traces of as-made (black) and activated (red) Al: CSA.

Comparing the TGA traces of both the *as* – made and activated samples show that the activation is successful. The activated trace shows a small initial mass loss of ca 6% which can be attributed to adsorbed atmospheric water, however, there is no mass loss due to guest DMF, proving that all DMF has been removed and any measured nitrogen content during the elemental analysis is due to the amide group in the CSA linker. The Al_2O_3 residue makes up 16.85 % of the activated sample, of which 52.94 % is aluminium, from this, the aluminium content of the dry material was calculated to be 9.35 %. Since this material is assumed to be isostructural to that of In:CSA, the formula is $Al(OH)(C_{11}H_9O_5N)$,

based on this, the theoretical aluminium content is 9.66 % which is in agreement with the TGA data.

5.7.3 Elemental Analysis

From the TGA data, it is clear that some water is adsorbed onto the material, therefore this had to be taken into account when analysing the elemental analysis data. If one water molecule is added to the formula unit, the data is in good agreement.

$Al(OH)(C_{11}H_9O_5N)(H_2O)$		
Element	Expected %	Measured %
C	44.46	44.09
H	4.07	3.84
N	4.71	4.81

Table 5.3. Elemental analysis of activated Al: CSA.

Also, this water makes up ca 6 % of the molecular weight of the material, which is in agreement with the TGA data presented earlier, which is further proof that Al: CSA and In: CSA have the same formula. It is clear from the elemental analysis that there is the correct amount of nitrogen in the material, corresponding to the proposed formula, meaning that there is no hydrolysis of the amide bond during the formation of the framework.

5.7.4 SEM

SEM images of activated Al: CSA, show a single morphology, spheres of *ca* 3 μm made from a collection of rods. It is clear that there is a homogeneous phase present which is in agreement with all analytical data.

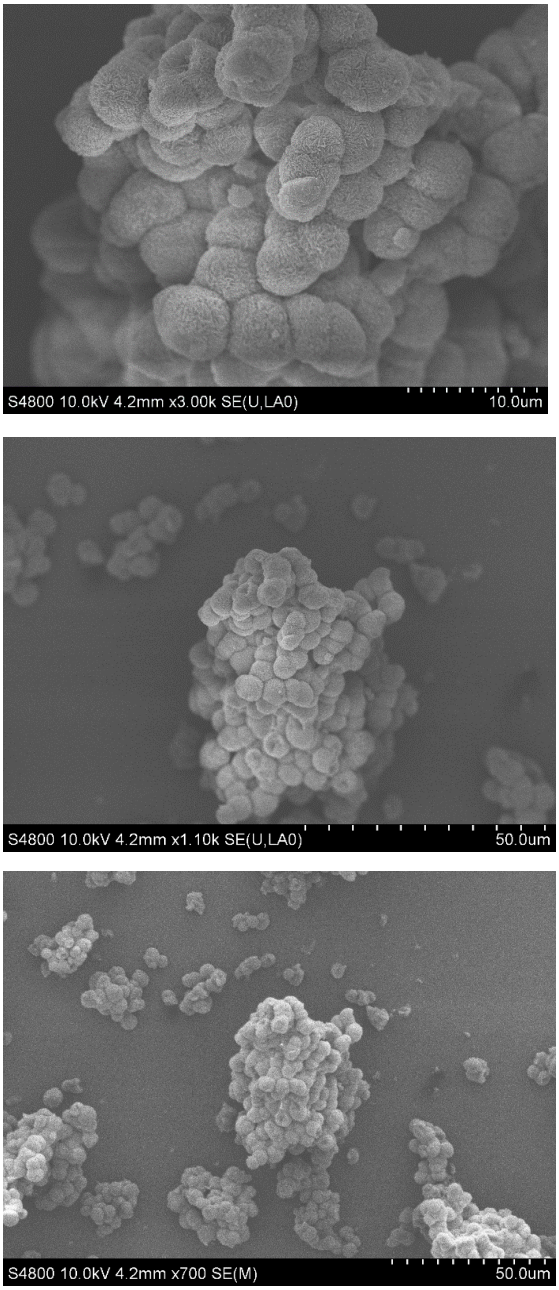

Figure 5.21. SEM images of activated Al: CSA.

5.7.5 Surface Area Measurement

Since PXRD data points towards this material being isostructural with its indium analogue, and the all analytical data points towards them having the same formula, no porosity towards nitrogen was expected. The data of this measurement is shown below.

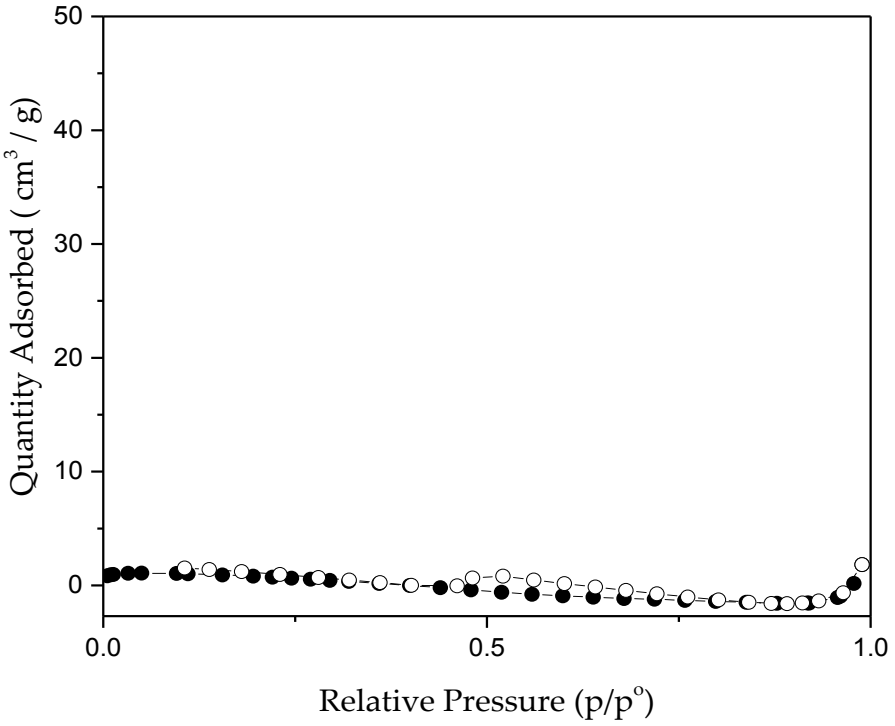

Figure 5.22. N_2 adsorption isotherm of Al: CSA.

As predicted, the material shows no porosity towards nitrogen, providing more evidence that it is isostructural to its indium analogue.

5.8 CO_2 Adsorption

For the same reasons discussed for In: CSA, CO_2 adsorption isotherms were measured on Al: CSA and the results are presented in Figure 5.23.

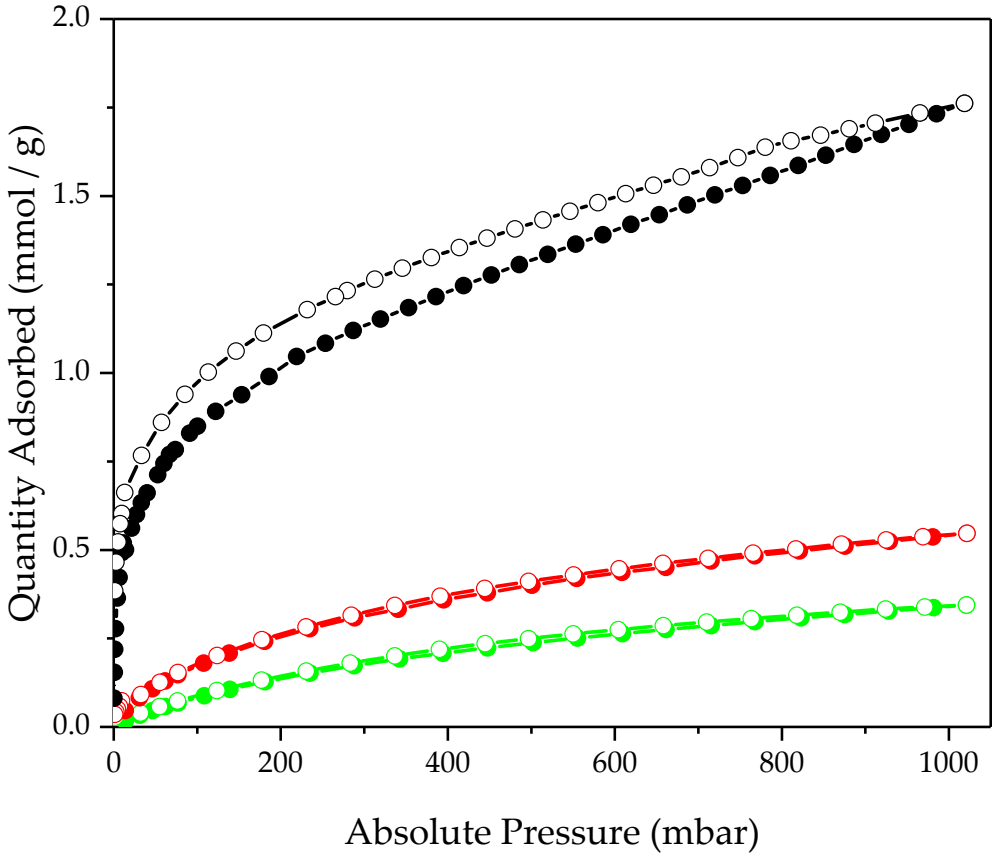

Figure 5.23. CO_2 adsorption isotherms of Al: CSA at 298 K (green), 273 K (red), 195 K (black).

The adsorption isotherms show that Al: CSA adsorbs CO_2, unlike its indium analogue. The reason for this is unknown but it could be due to a slight increase in the unit cell volume of Al: CSA over In: CSA. It could also be due to the evident lack of structural change observed upon activation for Al: CSA. As discussed previously, for the material to be a suitable candidate for CO_2 uptake, it must exhibit a high CO_2 adsorption at 0.15 bar at 40 ^oC.[8] The results show that the highest uptake of CO_2 onto Al: CSA occurs at 195 K and at 0.15 bar, the quantity adsorbed is 0.9 mmol / g which is not in agreement with the calculations performed on the crystal structure of the indium analogue. Also, when compared to literature materials such as Mg – MOF-74, which shows adsorption of

5.86 mmol g^{-1},[5] falls towards the lower end of the reported values. Due to this material being made up of 2-dimensional sheets, any adsorption of a gas is unexpected, especially since its indium analogue shows no adsorption.

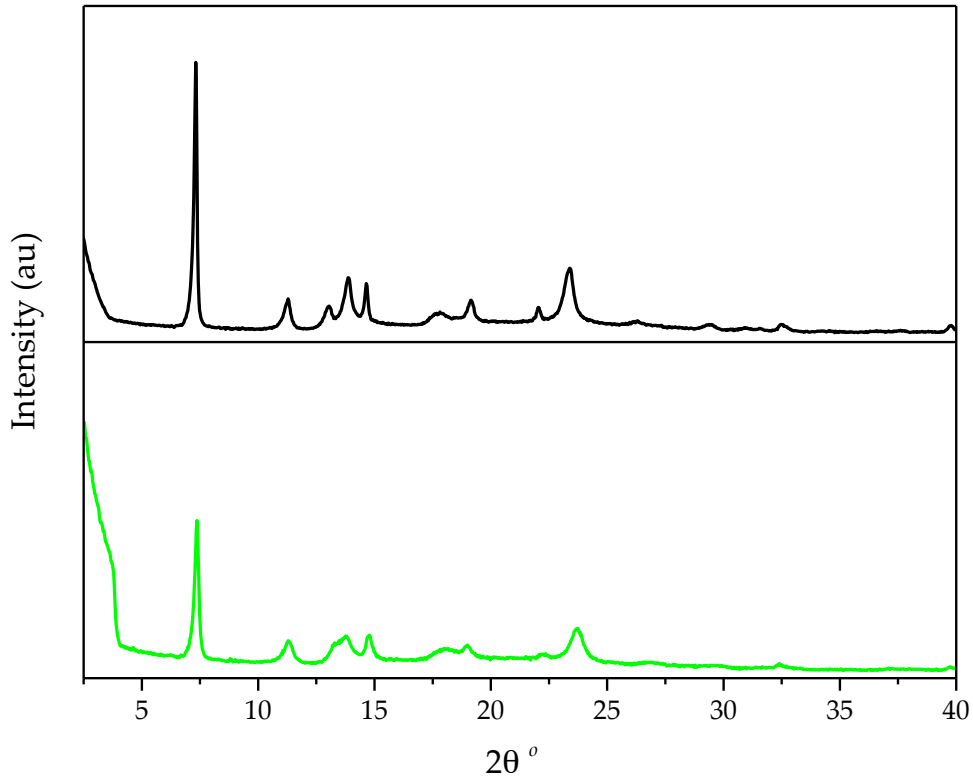

Figure 5.24. PXRD patterns of as-made (black) and post CO_2 adsorption measurement (green).

According to the PXRD pattern in figure 5.24, after the CO_2 sorption measurements, there is a slight loss of crystallinity, evidenced by broadening of some peaks. The reason for this is unknown, however, it is not a result of the activation procedure, since after activation, the PXRD pattern remains the same as shown in Figure 5.18.

5.9 Water Stability

This material was tested for its water stability using the same method described for In: CSA, the result is shown in figure 5.25.

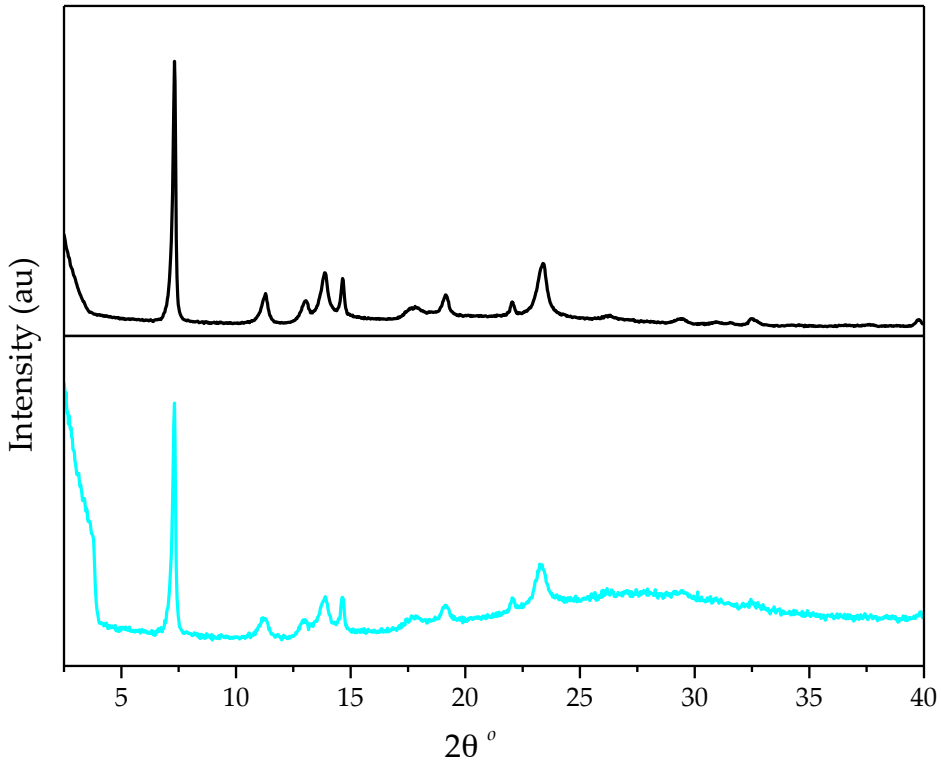

Figure 5.25. PXRD patterns of as-made (black) and post stirring in water (cyan) Al: CSA.

The data shows that the material retains its crystal structure after stirring in water overnight, showing that Al: CSA is equally as thermodynamically stable in water as its indium analogue. The large amorphous hump seen between 20 and 35° 2θ is attributed to the water present in the capillary during the measurement.

5.10 On-going Exploratory Synthetic Work

While working with G13 metals with this linker proved to be interesting, investigations into how this linker behaves with divalent metals were carried out. Exploratory synthesis into Cu: CSA and Zn: CSA remains on-going but the conditions presented in this chapter represent those that, so far, have given the best result in terms of purity and crystallinity.

For the Cu: CSA system, a number of reactions were carried out using different solvent mixtures, reaction temperatures, reaction times and molar ratios. A single crystal of this material was eventually obtained using the conditions presented in the next section of this chapter. Once the crystal structure of this material was determined by SCXRD, the next stage was to obtain a phase pure bulk material, which was not achieved, regardless of a high throughput exploratory synthesis approach. Metal:Linker molar ratios were adjusted from 0.1:1 through to 1:0.1, reaction temperatures and times tried ranged from 70 ^{o}C to 120 ^{o}C and from 12 hours through to 3 days. Solvent mixtures attempted ranged from pure H_2O to pure DMF and dimethylacetamide, and different volumes of EtOH were introduced. All attempts at synthesising a phase pure Cu: CSA material with the same composition as the single crystal, failed.

5.10.1 Synthesis of Cu:CSA

CSA (122.4 mg, 0.516 mmol) was weighed into a 40 mL Teflon capped glass vial, to this, $Cu(NO_3)_2{\cdot}3H_2O$ (39.14 mg, 0.162 mmol), Dimethylacetamide (DMA) (4.5 mL), H_2O (1mL), HBF_4 (0.2 mL 50% v/v) were added. The reaction mixture was then heated to 70 ^{o}C at a rate of 2.5 ^{o}C / min for 48 hours before cooling down to room temperature at 0.2 ^{o}C /

min. It was then re-heated at 2.5°C / min to 100 °C for a further 48 hours before cooling back to room temperature at 0.2 °C / min.

The same exploratory approach was adopted for the synthesis of Zn: CSA and involved a high throughput method of investigating how different reaction conditions effects the product. In this instance, dissimilar to that of the Cu: CSA system, no single crystal was obtained for Zn: CSA and therefore the optimisation of the reaction conditions in order to obtain a single crystal, remains on-going. Without this information, it was not possible to determine the structure of the material and therefore the formula of the material remains unknown. The synthesis presented in this chapter represents the most crystalline product, but it would be inaccurate to comment on the purity due to the lack of knowledge of the product formula.

5.10.2 Synthesis of Zn: CSA

A 0.7 M stock solution of $Zn(NO_3)_2 \cdot 6H_2O$ in DMF was prepared. CSA (0.100 g, 0.42 mmol), $Zn(NO_3)_2$ stock solution (0.29 mL, 0.42 mmol), DMF (9.71 mL), trimethylamine (100 μL) were loaded into a 40 mL Teflon capped glass vial. The mixture was heated to 140 °C at a 2.5 °C / min for 24 hours before being cooled back to room temperature at 0.2 °C / min. The product was washed with DMF (3 x 20 mL), ethanol (3 x 20 mL) and THF (3 x 20 mL) and left to vacuum dry. This gave a yield of 128 mg, of which, 93 mg was activated according to the previous procedure before being analysed in comparison with the remaining as-made material. The structure and formula were not resolved due to a lack of crystal structure and therefore no knowledge of a phase pure product.

5.10.3 Characterisation of Cu:CSA

5.10.3.1 Structure

As mentioned earlier, a single crystal of Cu: CSA was obtained and therefore the structure was determined by Dr George Whitehead by SCXRD.

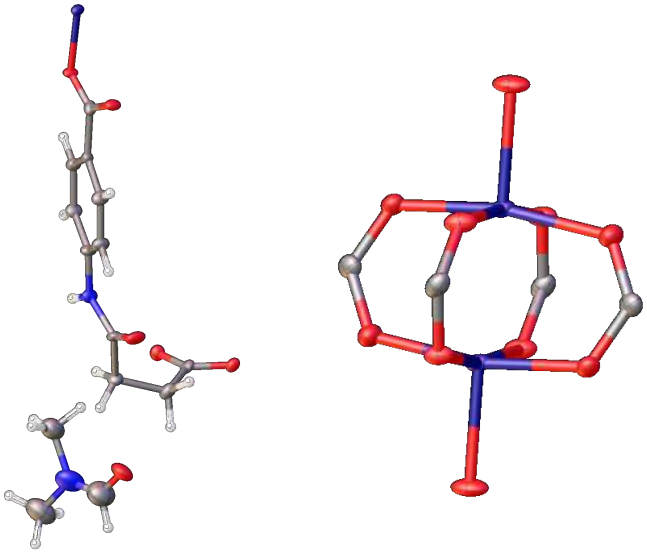

Figure 5.26. Asymmetric unit (left) and paddlewheel IBU (right) of Cu: CSA. Copper (navy blue), carbon (grey), nitrogen (blue), oxygen (red), hydrogen (white).

The asymmetric unit (Figure 5.26) for Cu: CSA consists of a CSA linker co – ordinated to a single Cu^{2+}, with a DMF molecule and the IBU is a copper paddlewheel which is common in copper based MOFs with the generic formula $M_2(COO)_4(L)_2$ were L is an axial ligand usually a water. Here, the axial position of the copper cluster is occupied by a coordinated amide group of an adjacent CSA linker. The chemical composition of Cu: CSA was therefore determined to be $Cu(C_{11}H_9NO_5)\cdot DMF$ from the SCXRD data.

Cu: CSA crystallises in the monoclinic space group *C2/c* with lattice parameters *a* = 19.2168(12) Å, *b* = 9.5684(6) Å, *c* = 13.8559(10) Å, β = 92.637(7) °, V = 2545.0(3) Å^3. Data collection and refinement parameters can be found in Appendix II.

A copper paddlewheel IBU generally forms square shaped pores, with the axial oxygen atoms coming from co – ordinated water molecules. In this material, however, the shape of the channels seen are similar to those present in In:CSA.

Cu: CSA, unlike In: CSA is a 3-dimensional framework, which stems from the copper paddlewheel IBU being further co – ordinated by the amide oxygen atom of the CSA linker in addition to the carboxylate groups. This extra connectivity allows for the growth of the material into a 3–dimensional framework. This extra co – ordination also provides some rigidity to the aliphatic chain of the linker, reducing its ability to rotate about the amide carbon.

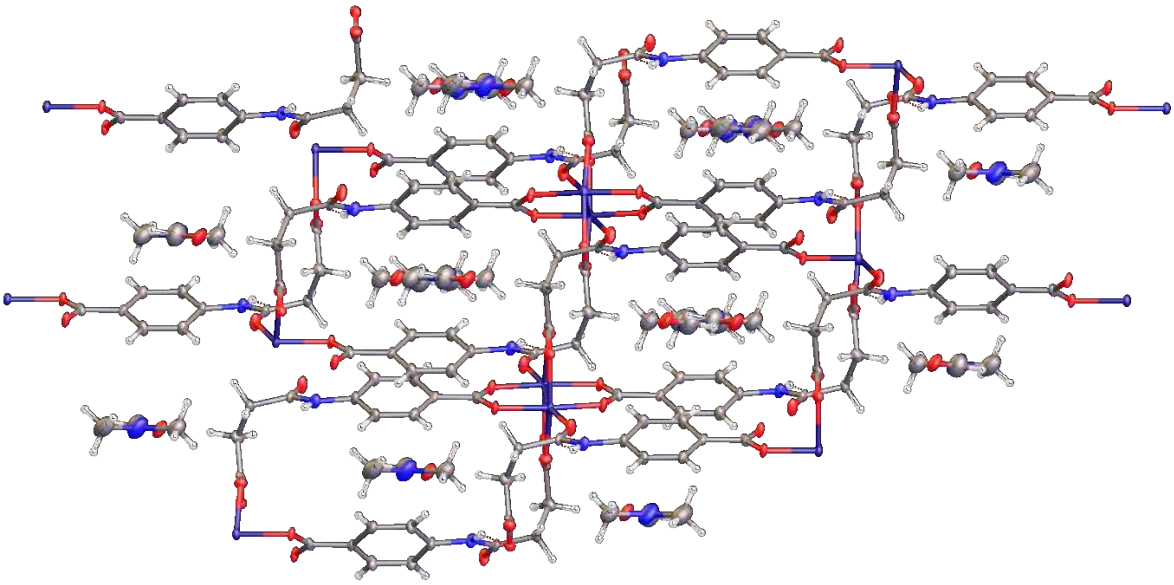

Figure 5.27. View along the crystallographic *b* – axis of Cu: CSA. Copper (navy), carbon (grey), nitrogen (blue), oxygen (red), and hydrogen (white).

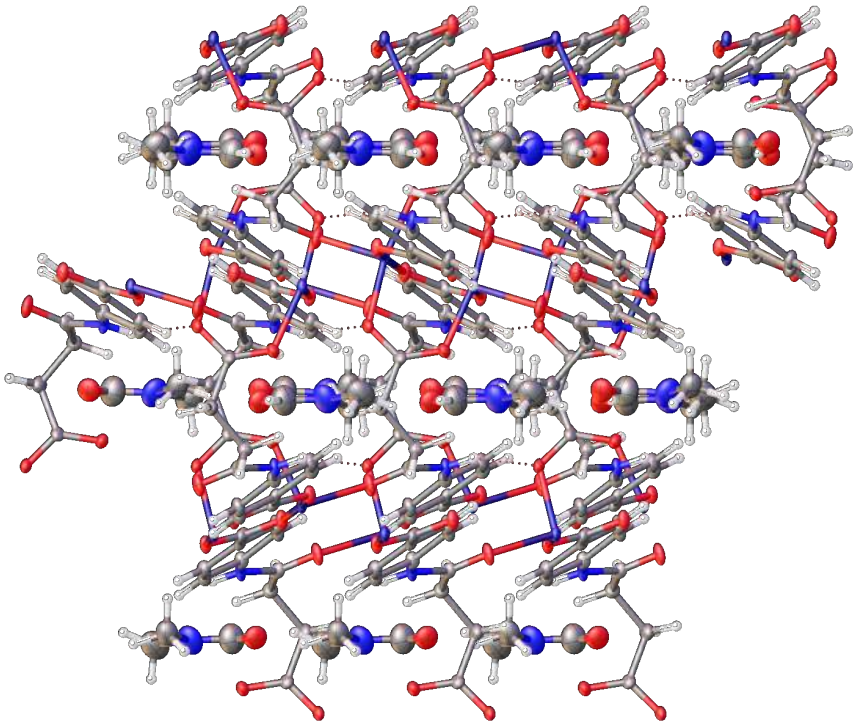

Figure 5.28. View along the crystallographic *a* – axis of Cu: CSA. Copper (navy), carbon (grey), nitrogen (blue), oxygen (red), and hydrogen (white).

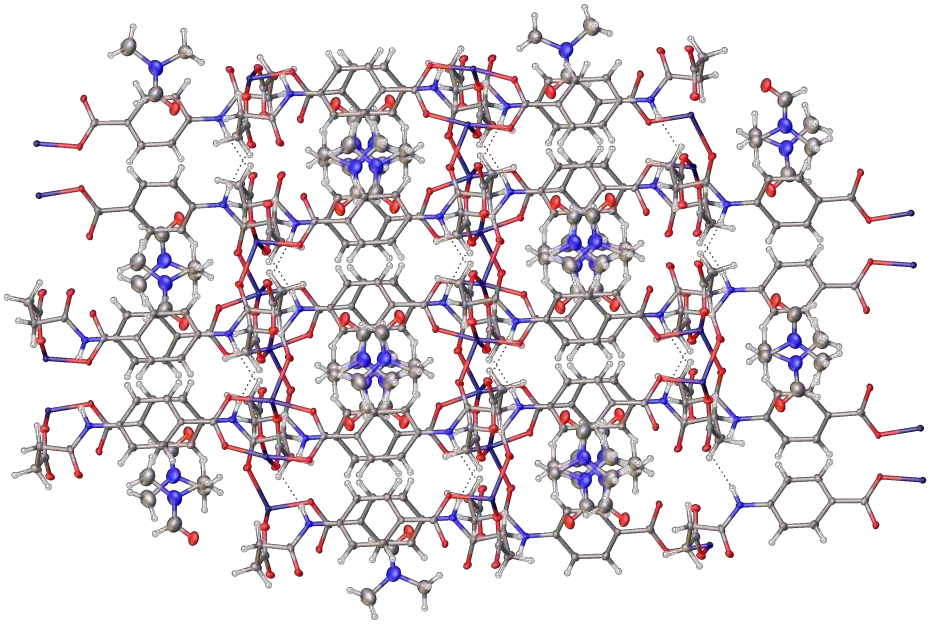

Figure 5.29. View along the crystallographic *c* – axis of Cu: CSA. Copper (navy), carbon (grey), nitrogen (blue), oxygen (red), and hydrogen (white).

The largest voids in this material are the cylindrical channels running along the crystallographic *b* – axis, in Figure 5.27, DMF molecules lie within these channels, which is confirmed for the bulk material using TGA (Figure 5.32). Figure 5.28 and Figure 5.29 show that along the crystallographic *a* and *c* – axes, there are no discernable voids.

These channels that run along the crystallographic *b* - axis have a largest penetrating sphere of 0.6 Å radius, however the largest overall spherical void has a radius of 2.2 Å, which is large enough to host a nitrogen molecule of 1.82 Å radius and are presented in Figure 5.30.

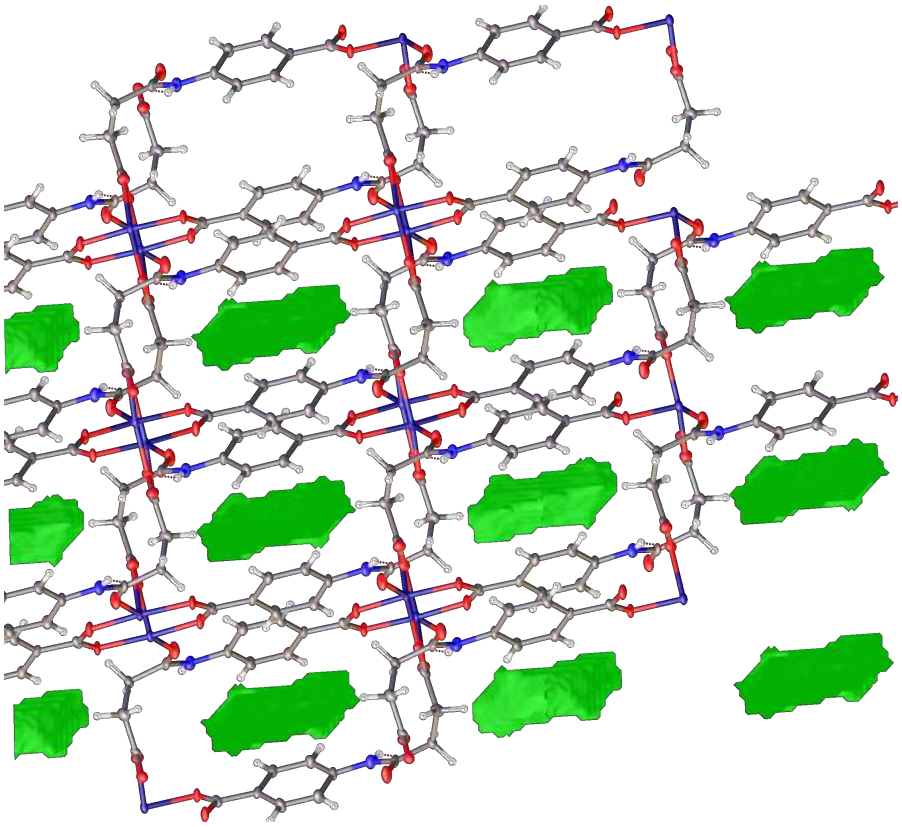

Figure 5.30. Voids (red masses) of Cu: CSA when viewed along the crystallographic *b* – axis.

These were calculated using a probe of the same size as nitrogen, after removing the guest DMF molecules manually. This implies that, if the

material has some flexibility to expand and contract upon adsorption of molecules, there is potential for some gas uptake onto Cu: CSA. The total solvent accessible volume of this material was calculated using a probe of 1.82 Å radius to be 504.6 $Å^3$ (19.8 %).

5.10.3.2 PXRD

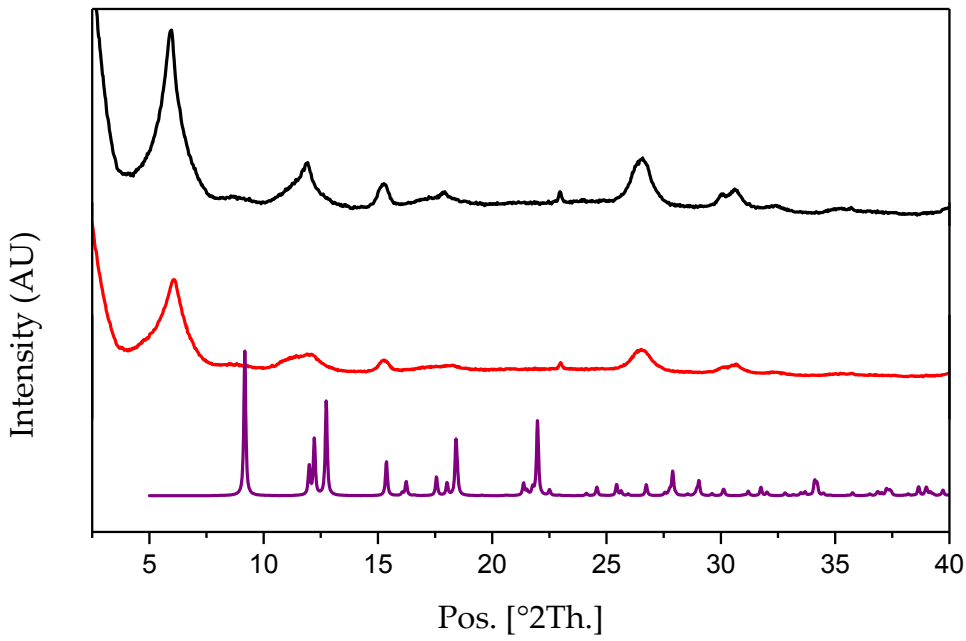

Figure 5.31. PXRD pattern of Cu: CSA, as-made (black), activated (red) and simulated from CIF (purple).

It is clear from the PXRD pattern that the bulk material is not very crystalline, and does not match the structure of the single crystal when the experimental patterns are compared to the simulated from the crystal structure. This shows that the bulk material has a different structure to that of the single crystal. The PXRD pattern remains the same after activation, which, according to the TGA data, was proven successful. So

far, there have been no successful attempts at improving upon this crystallinity or isolating a phase pure material.

5.10.3.3 TGA

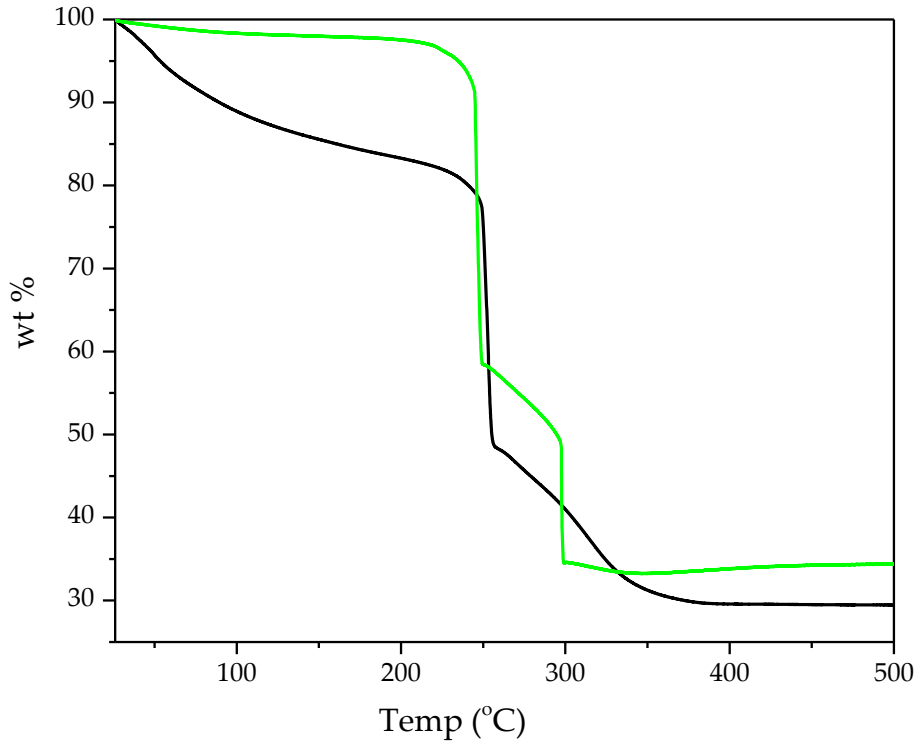

Figure 5.32. TGA trace of Cu: CSA as-made (black) and activated (green).

The TGA trace of the as – made material shows one, long mass loss step before the final decomposition step, due to the removal of guest solvent molecules within the pores of the MOF. From the SCXRD data, DMF is seen within the pores of the material, so this was expected. The activated material shows a much smaller initial mass loss up to 120 °C which is due to the removal of a small amount of atmospheric water that has been adsorbed onto the material. Although the building unit has the generic formula $Cu_2(L)_4$, the final overall formula for this material is

$Cu(C_{11}H_9NO_5)$, which has a theoretical copper content of 21.27 %, from the TGA, the copper content was calculated, using the activated material, to be 29.82 %.

This excess of copper in the final product implies that there is a large amount of copper oxide formed during the synthesis, or another compound is forming, the structure of which remains unknown. The latter explanation is more likely due to the lack of black powder in the final product, which would indicate copper oxide.

5.10.3.4 Elemental Analysis

$Cu(C_{11}H_9O_5N)$		
Element	Expected %	Measured %
C	44.23	35.95
H	3.04	3.04
N	4.69	4.05

Table 5.4. Elemental analysis of activated Cu: CSA.

The elemental analysis of the activated material does not agree with the theoretical values, confirming further that the product is not purely Cu: CSA. It does, however, back up the TGA data which implies an excess of inorganic material in the product. All attempts, during the exploratory synthesis phase, at isolating a phase pure Cu: CSA material were unsuccessful.

5.10.3.5 Surface Area Measurement

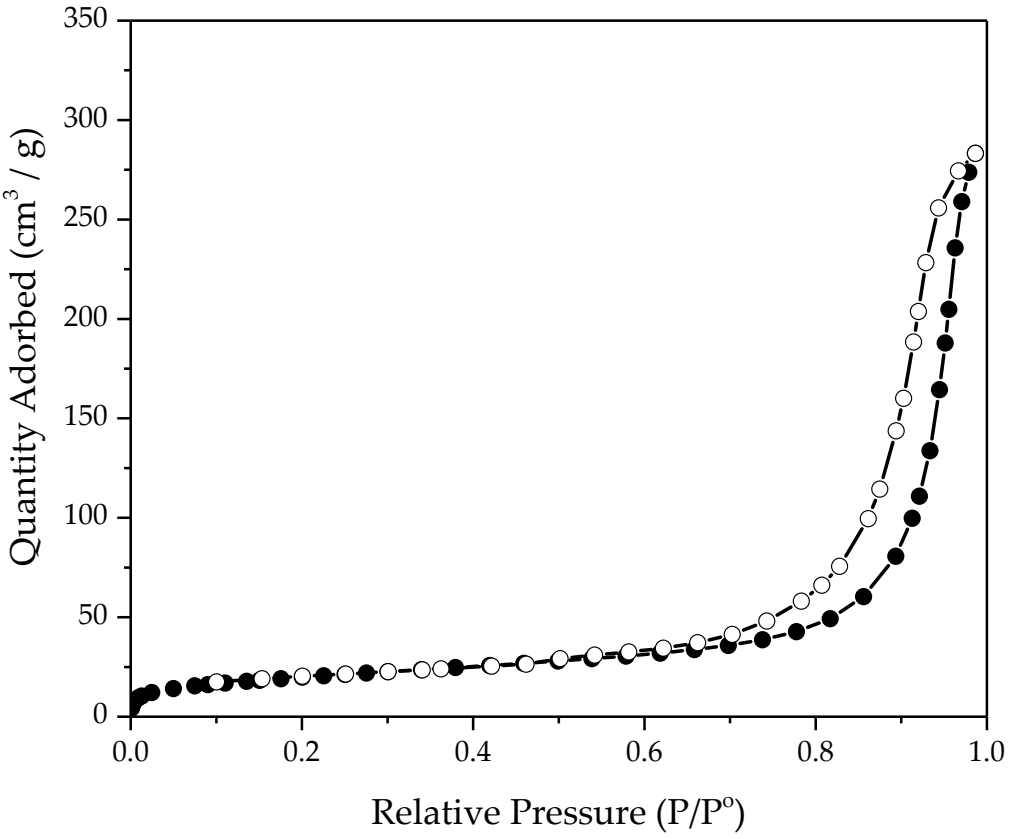

Figure 5.33. N_2 adsorption isotherm of Cu: CSA.

The N_2 adsorption isotherm, measured at 77.3 K shows a type II isotherm, which is representative of low porosity adsorbents. The BET area of this material was calculated to be 68 m^2 / g with a pore volume of 0.042 cm^3 / g calculated from the plateau of the isotherm (P/P_o = 0.5). The source of this slight porosity is unknown, due to the bulk material having a different structure to the single crystal. According to the crystal structure, there is some potential for nitrogen adsorption, if the material has the ability to swell in order to accommodate such a molecule.

5.10.3.6 SEM

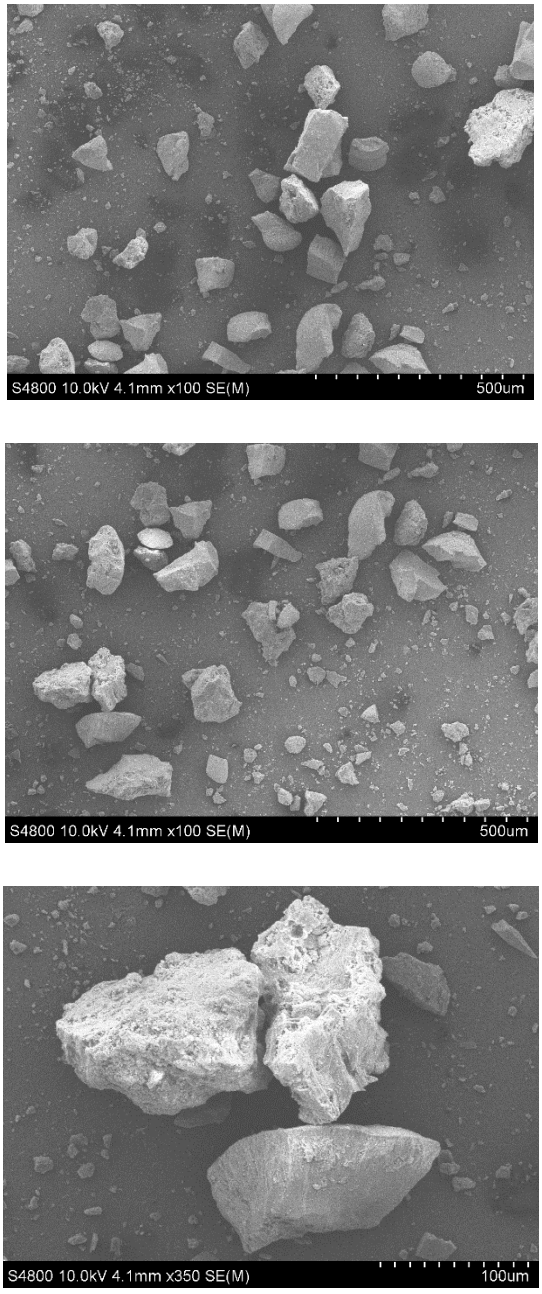

Figure 5.34. SEM images of activated Cu: CSA material.

SEM images of the activated material show two crystallite morphologies. One of which appears to be almost pebble like, with smooth external surfaces, while the second looks less smooth.

Due to the lack of a phase pure material and crystalline bulk material, all further testing and analysis was deemed unnecessary until these issues were resolved. Unfortunately, however, has not been managed thus far.

5.10.4 Analysis of Zn:CSA

5.10.4.1 PXRD

All attempts at growing a single crystal of Zn: CSA were unsuccessful, so in order to solve the crystal structure, it was heavily reliant on the material being isostructural to that of Cu: CSA. The PXRD patterns are presented in Figure 5.35.

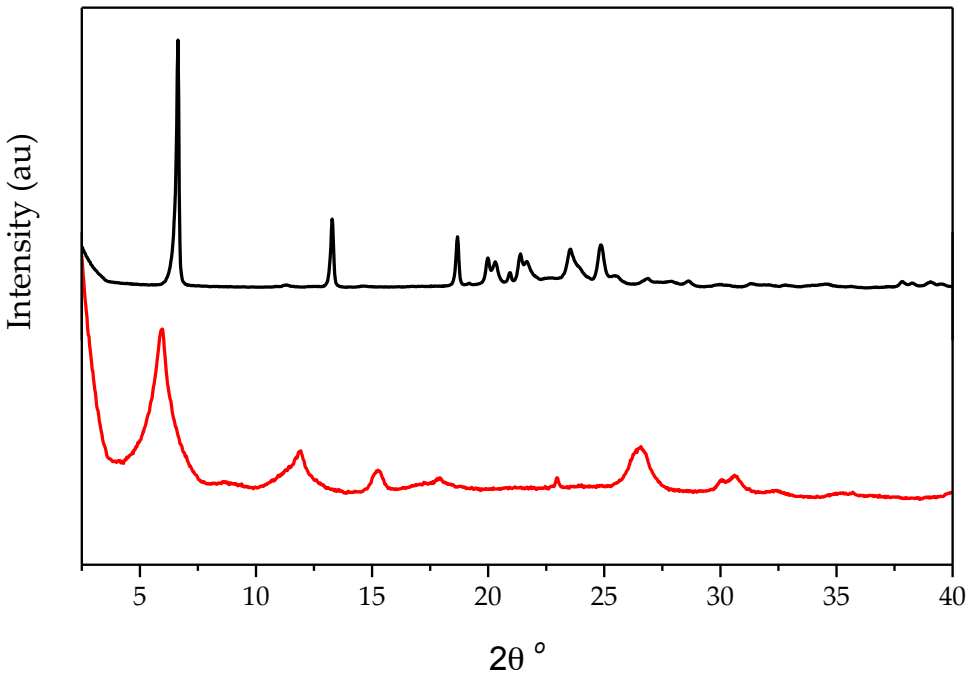

Figure 5.35. PXRD of Zn: CSA (black) and Cu: CSA (red).

The data shows that there is a crystalline material formed, however there is hardly any resemblance to the PXRD pattern of Cu: CSA. The Zn: CSA pattern was unsuccessfully indexed to the space group and lattice

parameters of Cu: CSA, which were obtained from the single crystal (Figure 5.36).

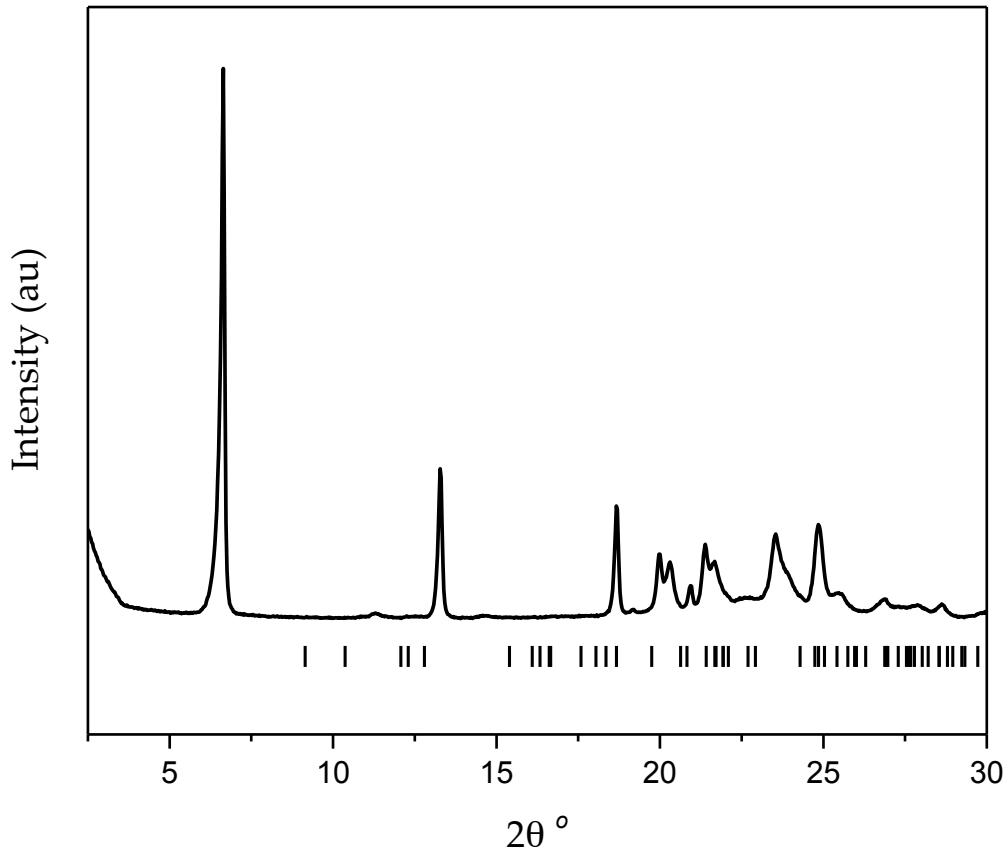

Figure 5.36. PXRD of Zn: CSA indexed against the unit cell of the Cu:CSA material discussed earlier. Calculated peaks indicated by black tick marks.

Due to the lack of crystal structure available for this material, it was not possible to determine the structure of the material, or to determine whether the product was phase pure.

Since no single crystal data was available for this material and the data collected on the bulk did not offer any further understanding into the nature or structure, it is clear that further research and exploratory

synthesis needs to be carried out. The complexity of this material lies in the ability of zinc based MOFs to form numerous different SBU's.

5.11 Conclusions

Using four different metals with the same linker has led to the formation of several different structures, however, due to the lack of single crystals for several systems, structure determination was not achieved.

In this chapter, first G13 (group 13) frameworks to be reported using amide containing linkers have been presented. The structures formed with aluminium and indium were characterised to be isostructural using PXRD, which indexed to the same unit cells and confirmed to be phase pure with the same formulae as each other using other characterisation techniques.

In: CSA undergoes a reversible structural change upon activation, which is not seen in its aluminium analogue. Although neither shows any porosity towards N_2, it is clear that this is not due to a collapse of the structure since the PXRD patterns remain the same before and after activation. Another notable discovery was that, regardless of reaction conditions used, no other materials with different linker conformations were obtained.

Carbon dioxide adsorption isotherms were measured and showed very small adsorption of CO_2 onto Al: CSA, whereas In: CSA showed none. This could stem from the structural change that In: CSA undergoes upon activation.

This shows that using a different metal with the same linker, allows the final material to behave in a different manner.

A single crystal of a 3-dimensional Cu: CSA framework was synthesised and the structure was successfully determined. The bulk material, however, was analysed using PXRD, TGA, elemental analysis and SEM to be impure. The initial adsorption isotherm shows that Cu: CSA shows some promise of porosity, which is in agreement with the crystal structure.

A fourth material has been synthesised, however, the structure of which could not be determined due to the lack of single crystal data. Based on PXRD data, the structure appears to be different to that of Cu: CSA. TGA and CHN data imply that the same IBU is formed in both materials, however, Zn: CSA is not pure, with a huge inorganic excess formed during the synthesis. Zn: CSA shows no initial signs of porosity, implying that the difference in structures between Cu and Zn: CSA stem from the lack of axial amide – metal bond in the zinc material, thereby reducing it to a 2-dimensional material.

5.12 Future Work

Working with this flexible linker has revealed some very interesting structures. Further investigations into In: CSA could reveal some further interesting compounds as it is known that indium can adopt many unique IBUs which change that overall topology of the final framework. Both Al and In: CSA show some uptake of atmospheric water and are both stable under aqueous conditions, therefore, water sorption measurements could give some interesting results.

Isolating a phase pure Cu: CSA material would be interesting as this is the first reported copper compound, to the best of our knowledge, where the axial co – ordinating groups come from the linker itself and not water molecules.

Looking at other metals with the CSA linker could provide some interesting information also, especially metals which have the potential to produce single crystals. This would enable us to see if the conformation of the linker itself can change from metal to metal.

5.13 References

1. M. Hong, Y. Zhao, W. Su, R. Cao, M. Fujita, Z. Zhou and A. S. C. Chan, *Angew. Chem. Int. Ed.*, 2000, **39,** 2468.
2. C. A. T. Fernandez, P.K.Motkuri, R.K.Nune, S.K.Sumrak, J.C.Tian, j.Liu, J., *Cryst. Growth Des.*, 2010, **10**, 1037.
3. A. M. Fracaroli, H. Furukawa, M. Suzuki, M. Dodd, S. Okajima, F. Gandara, J. A. Reimer and O. M. Yaghi, *J. Am. Chem. Soc.*, 2014, **136**, 8863.
4. H. Reinsch, M. Kruger, J. Wack, J. Senker, F. Salles, G. Maurin and N. Stock, *Microporous Mesoporous Mater.*, 2012, **157**, 50.
5. J. A. Mason, M. Veenstra and J. R. Long, *Chemical Science*, 2014, **5**, 32.
6. H. Li, M. Eddaoudi, M. O'Keeffe and O. M. Yaghi, *Nature*, 1999, **402**, 276.
7. T. Loiseau, C. Serre, C. Huguenard, G. Fink, F. Taulelle, M. Henry, B. T and G. Ferey, *Chem. Eur. J*, 2004, **10**, 1373.
8. Z. Zhang, Z. Yao, S. Xiang and B. Chen, *Energy Environ., Sci*, 2014, **7**, 2868.

Chapter 6 . PDG Systems

Due to the CSA linker, which was used in chapter 5, having a flexible alkyl chain, which allowed the linker to adopt an L – shaped conformation, prohibiting the formation of a porous, 3-dimensional framework with both aluminium and indium. N,N'-(1,4-Phenylenedicarbonyl) diglycine (PDG), shown in Figure 6.1, was selected due to the shorter alkyl chains, reducing its flexibility. Like CSA, PDG has the ability to form a 3-dimensional framework with M^{2+} as reported by Plakatouras *et al*,[1] but has never been used with G13 metals, which is what this section addresses.

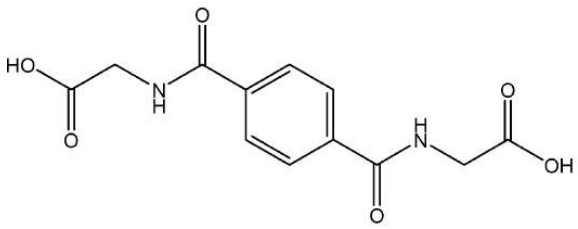

Figure 6.1. N,N'-(1,4-Phenylenedicarbonyl) diglycine (PDG).

6.1 Synthesis

N,N'-(1,4-Phenylenedicarbonyl) diglycine (PDG) was purchased from Manchester Organics in 95% purity and anhydrous $InCl_3$ was purchased from Alfa Aesar in 99.99 % purity. $Al(NO_3)_3.9H_2O$ was purchased from Sigma Aldrich in 97 % purity, DMF and THF were purchased from Fisher and all reagents were used without any further purification.

Again, since these two materials are new, exploratory synthesis was used in a high throughput approach, investigating a number of different reaction conditions in order to obtain single crystals of the product(s) and then further optimisation to make them phase pure. Adjusting molar

ratios, reaction temperature, time, metal source, solvent mixtures and introducing additives into the reaction mixture. Initially, molar ratios were altered to determine the optimum conditions, ranging from a 0.1:1 M:L ratio through to 1:0.1, alongside this, solvent mixtures were altered. Solvent mixtures such as DMF / H2O, changing the ratios from 0 : 10 through to 10 : 0 mL, inclusion of ethanol and the introduction of bases such as NaOH. Reaction temperature ranges were studied from 80 oC through to 150 ^{o}C with reaction time ranging from 12 hours to 3 days.

The synthesis conditions presented in this chapter represent those that give the best results in terms of product crystallinity and purity.

6.1.1 Synthesis of In: PDG

PDG (280 mg, 1 mmol) was weighed out into a 40 mL Teflon capped glass vial, to this, $InCl_3$ (110 mg, 0.5 mmol), DMF (2 mL) and H_2O (3 mL) were added. The reaction mixture was heated to 100 ^{o}C at 2.5 ^{o}C / min for 12 hours before cooling to room temperature at 0.2 ^{o}C / min. Small needle – shaped single crystals were obtained and a small aliquot of the product was removed for SCXRD. The resultant white powder was filtered and washed with DMF (4 x 20 mL), THF (3 x 20mL) and ethanol (3 x 20mL) and left to pump dry giving a yield of 186 mg. From TGA data, 11 % of this mass is due to adsorbed solvent, therefore the final, dry yield, which has the formula $In(OH)(C_{12}O_6N_2H_{12})$, was 165 mg.

6.1.2 Synthesis of Al: PDG

PDG (280 mg, 1 mmol) was weighed out into a 40 mL Teflon capped glass vial, to this, $Al(NO_3)_3.9H_2O$ (188 mg, 0.5 mmol), DMF (2 mL) and H_2O (3 mL) were added. The reaction mixture was heated to 100^{o}C at a

rate of 2.5°C per minute, and left for 12 hours before being cooled to room temperature at 0.2°C per minute. The resultant white powder was filtered and washed with DMF (4 x 20 mL), THF (3 x 20mL) and ethanol (3 x 20mL) and left to pump dry, this yielded 187 mg of a white powder. 98 mg of the material was activated according to the previous procedure, leaving a final yield of 72 mg (86% yield). The final composition was determined to be [Al(OH)($C_{11}H_9O_5N$)] by elemental analysis and TGA.

6.1.3 Activation Procedure

As-made material (70 – 90 mg) was activated at 155 °C, under dynamic vacuum (10^{-2} mbar) overnight.

6.1.4 Water Stability Tests

As-made material (30 – 40 mg) and H_2O (15 mL) were loaded into a 40 mL Teflon capped glass vial with a magnetic stirrer bar, which was placed on a stirrer plate at room temperature overnight.

6.2 Characterisation of In:PDG

6.2.1 Structure

The structure of this material was solved from SCXRD by Dr George Whitehead using OLEX2 and Shelx software.

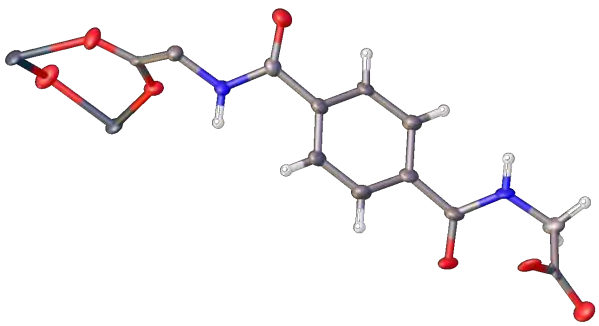

Figure 6.2. Asymmetric unit of In: PDG, Indium (dark grey), oxygen (red), carbon (grey), nitrogen (blue), hydrogen (white).

In: PDG crystallises in the space group triclinic space group $p-1$ with lattice parameters a = 7.2041(12), b = 10.1131(14), c = 11.757(2), α = 78.098(14) °, β = 79.138(15) °, γ = 85.697(13) ° and V = 822.6(2) A^3. Data collection and refinement parameters can be found in Appendix II. There was some disordered solvent in this structure, which could not be modelled. The asymmetric unit of In: PDG (Figure 6.2) shows the bridging mode of the carboxylate groups of the linker as well as the bridging hydroxyl groups. The flexibility of this linker at both ends gives rise to the adoption of a Z – shaped conformation (evident in Figure 6.5) as opposed to the CSA linker which adopts an L – shaped conformation.

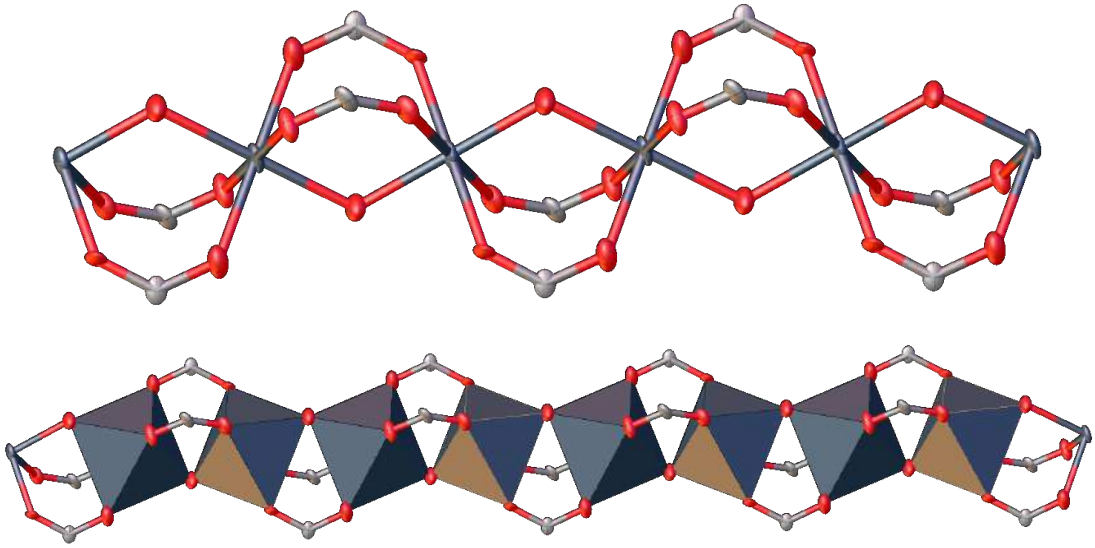

Figure 6.3 IBU of In: PDG (top), with polyhedra (bottom). Indium (dark grey), oxygen (red), carbon (grey), nitrogen (blue), hydrogen (white).

The IBU is consistent with those of other G13 MOFs as seen in In: CSA; infinite chains of *trans* – corner – sharing $In(OH)_2O_4$ octahedra. Here *trans* – refers to the relative positions of the co – ordinated hydroxy groups.

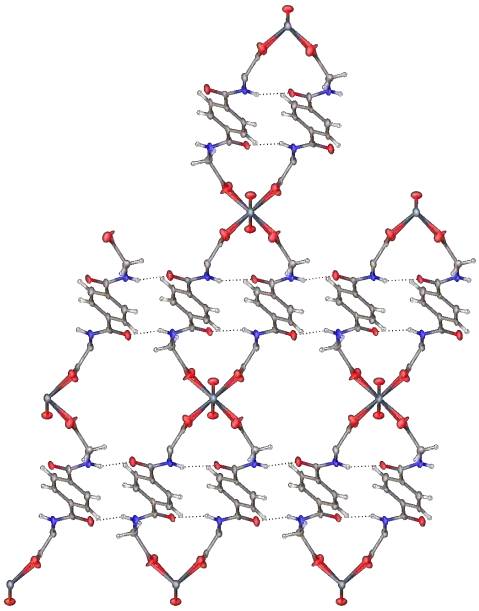

Figure 6.4. In: PDG viewed along the crystallographic *a* – axis. Indium (dark grey), oxygen (red), carbon (grey), nitrogen (blue), hydrogen (white).

In: PDG is made up of 2-dimensional sheets (shown in Figure 6.4), which are hydrogen bonded (dashed bond lines) to each other via the amide oxygen to an NH on an adjacent sheet. The In(OH) chains run along the crystallographic *a* – axis, with each chain only connecting to two adjacent chains as opposed to four. This stems from the ability of the linker to flex at each end, resulting in the prevention of the formation of a 3-dimensional framework.

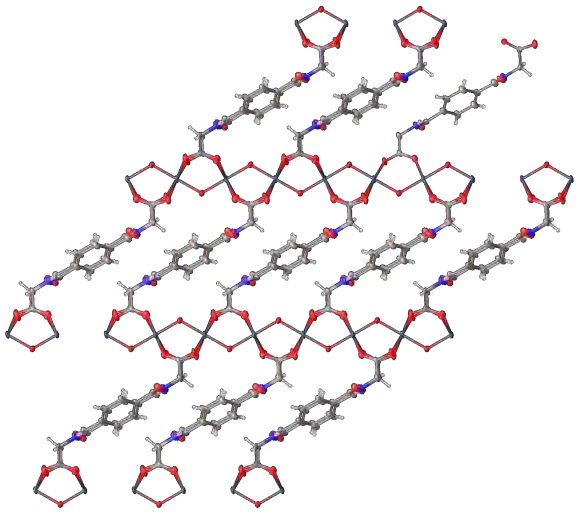

Figure 6.5. In: PDG when viewed along the crystallographic *b* – axis. Indium (dark grey), oxygen (red), carbon (grey), nitrogen (blue), hydrogen (white).

This is a similar structure to In: CSA whereby 2-dimensional sheets are packed together via intermolecular attractions.

The view along the crystallographic *b* – axis (Figure 6.5) shows the Z – shaped conformation adopted by the PDG linker opposed to the L – shaped linker in In: CSA. The overall structure of In: PDG is very similar to that of In:CSA, with the same infinite chains of $In(OH)_2O_4$ octahedra, and the same connectivity of the linker molecules. The flexibility of the PDG linker still prohibits the formation of an extended 3 – dimensional framework.

According to the crystal structure, In: PDG has the largest channel running along the crystallographic *a* – axis, with a penetrable sphere of 2.00 Å, with a largest spherical void of 2.40 Å. This is large enough to allow the uptake of N_2 and CO_2. The solvent accessible pore volume was calculated to be 162.9 $Å^3$ (19.8 %) and 171.0 $Å^3$ (20.8 %) when using N_2 and CO_2 probes respectively, showing some potential for porosity. The surface map calculated using a nitrogen probe (1.82 Å radius) is shown in Figure 6.6.

The voids that run along this axis, are found in between two sheets and not part of a 3-dimensional framework, and so permanent porosity might not be exhibited by this material.

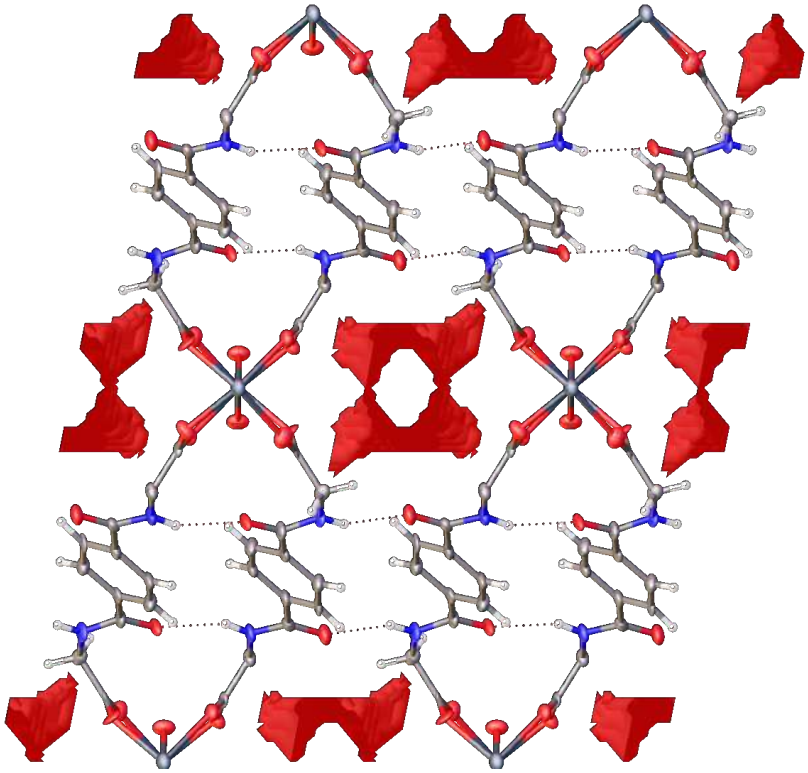

Figure 6.6. Surface map of In: PDG viewed along the crystallographic *a* – axis. Indium (dark grey), oxygen (red), carbon (grey), nitrogen (blue), hydrogen (white).

6.2.2 PXRD

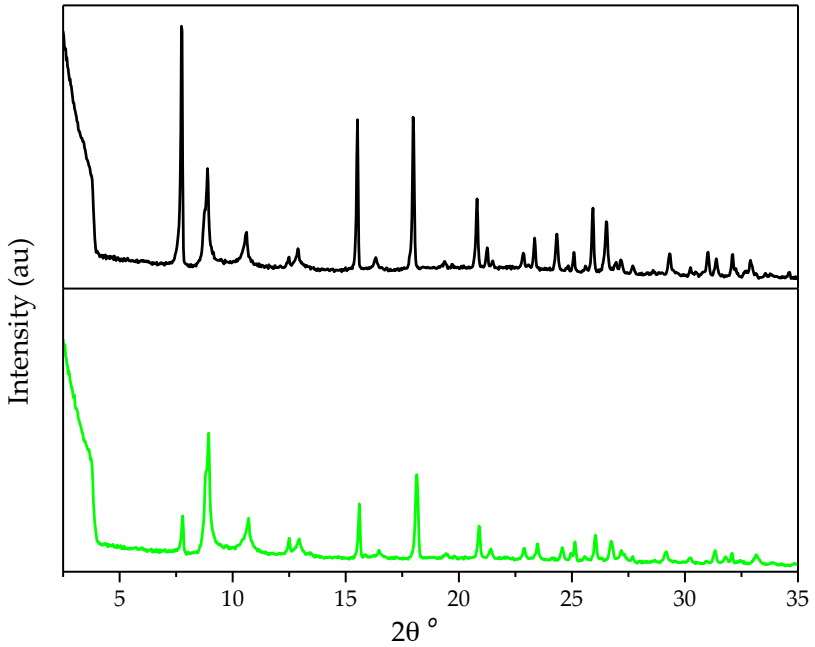

Figure 6.7. PXRD pattern of In: PDG, as-made (black) and activated (green).

After activation, there are some differences in the PXRD patterns, however, it is clear that the structure itself remains the same. The unit cell remains very similar after activation, with a slight reduction in parameters a = 7.061(1) Å, b = 10.327(1) Å, c = 11.746(1) Å, α = 78.098°, β = 79.138 °, γ = 85.697 °. The main difference in the patterns is the relative intensities of the peaks, which provide information with respect to the arrangement of atoms in the crystal structure. The change in relative intensity shows that the contents of the unit cell changes, from which, it can be said that the guest solvent molecules have been removed. This agrees with the TGA data (Figure 6.8) which shows that the activation procedure was successful.

6.2.3 TGA

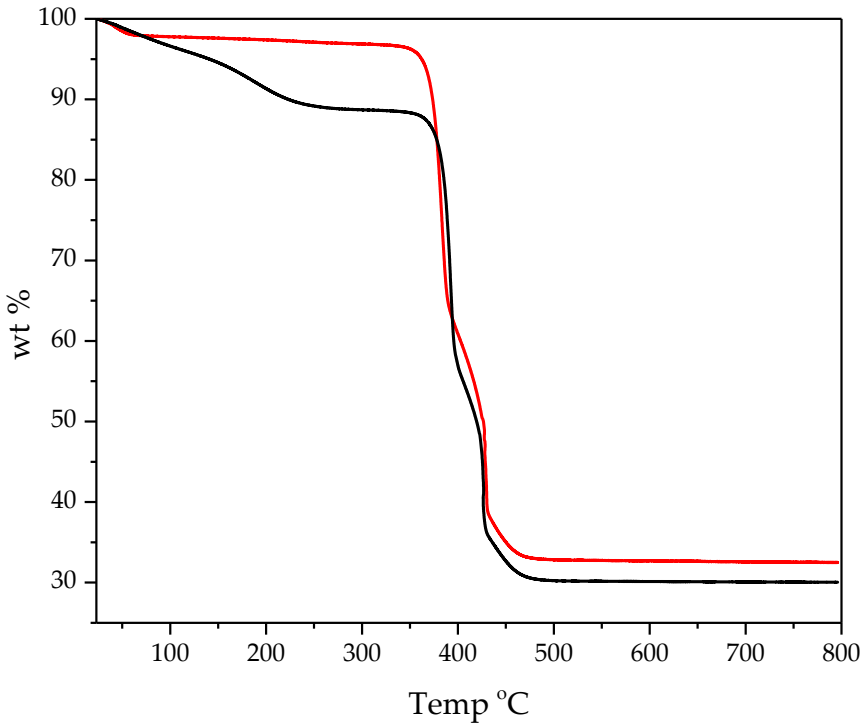

Figure 6.8. TGA of In: PDG, as-made (black), activated (red).

The TGA trace of the *as* – made material shows an initial mass loss before reaching a plateau at 250 °C, this 11 % mass loss is attributed to removal of all guest solvent molecules from the material. After activation, a much smaller initial mass loss is seen (c.a. 2.4 wt %) which is attributed to the removal of atmospheric water that has been adsorbed onto the material. The data shows that the material is thermally stable up to 340 °C before decomposing, leaving In_2O_3 residue which makes up 32.54 % of the dry measured sample. The indium content was calculated to be 27.65 % which agrees with the theoretical content of 28.00 % based on the dry formula [In(OH)(PDG)].

6.2.4 Elemental Analysis

$In(OH)(C_{12}H_{10}O_6N_2)(H_2O)_{0.5}$		
Element	Expected %	Measured %
C	34.39	34.34
H	2.89	2.68
N	6.69	7.01

Table 6.1. Elemental analysis of an activated sample of In: PDG.

According to the TGA trace, a small amount of water is adsorbed onto the material from the atmosphere. Taking this into account, when one water molecule is added per two linkers, equating to 2.15 % of the formula, which agrees with TGA data, there is also good agreement with the elemental data. This shows that the bulk material is pure, and supports the theory that the change in peak intensities after activation is due to the removal of DMF molecules from within the pores.

6.2.5 SEM

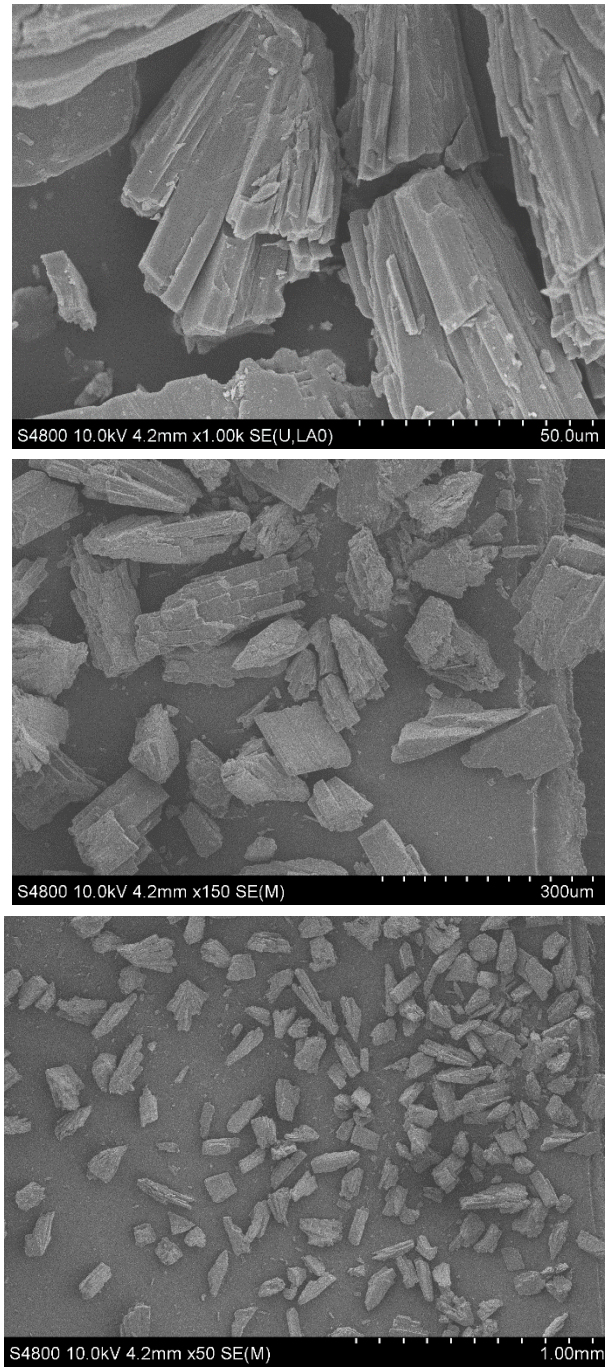

Figure 6.9. SEM images of an activated sample of In: PDG.

The SEM images show one crystal morphology, which supports all measured data showing that the material is phase pure and there is very little (if any) amorphous material made during the synthesis.

6.2.6 Surface Area Measurements

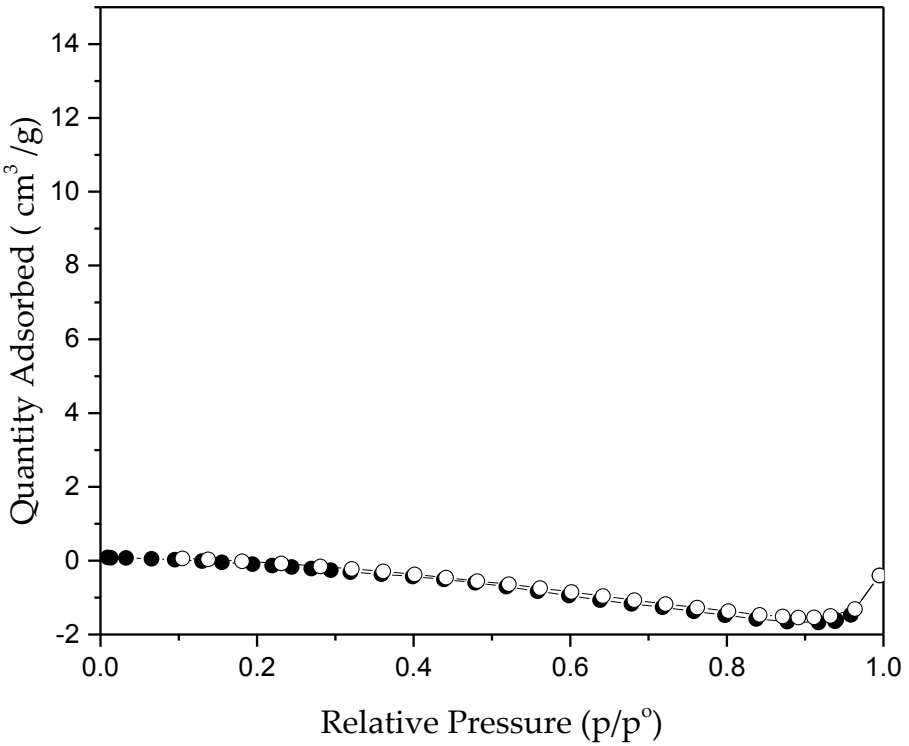

Figure 6.10. N_2 adsorption isotherm of In: PDG at 77.3 K.

The N_2 sorption isotherm at 77.3 K shows no porosity for this material towards nitrogen. This was expected due to the voids being found in interplanar spaces meaning that they are not part of a 3-dimensional framework, causing a lack of permanent porosity. It is known from the PXRD data that this material doesn't collapse after activation therefore, according to the crystal structure, there should still be some solvent accessible voids. It is for this reason that CO_2 sorption experiments were ran and the data is shown in Figure 6.11.

6.2.7 CO_2 Sorption Measurements

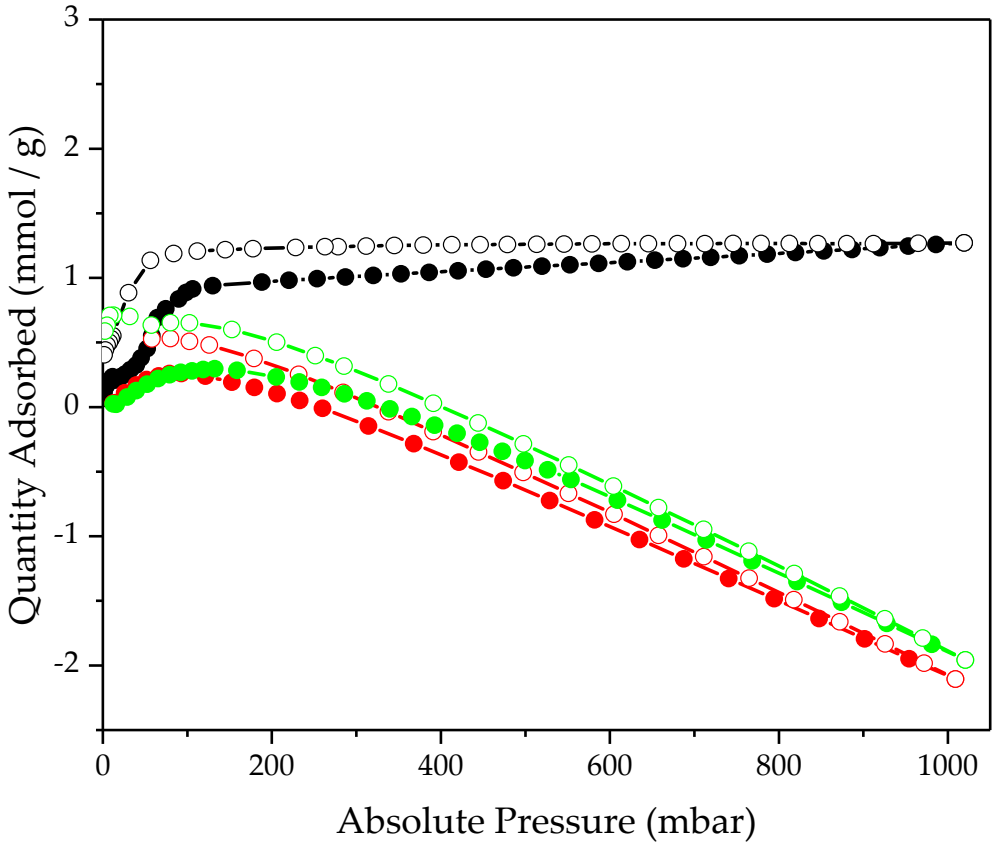

Figure 6.11. CO_2 isotherms of In: PDG measured at 298 K (green), 273 K (red) and 195 K (black).

The CO_2 sorption isotherms (Figure 6.11) show that In: PDG has very limited porosity towards CO_2, which is also observed for In: CSA. This evident lack of porosity could stem from the fact that the only appropriate solvent accessible voids lie between two 2-dimensional sheets (shown in Figure 6.6).

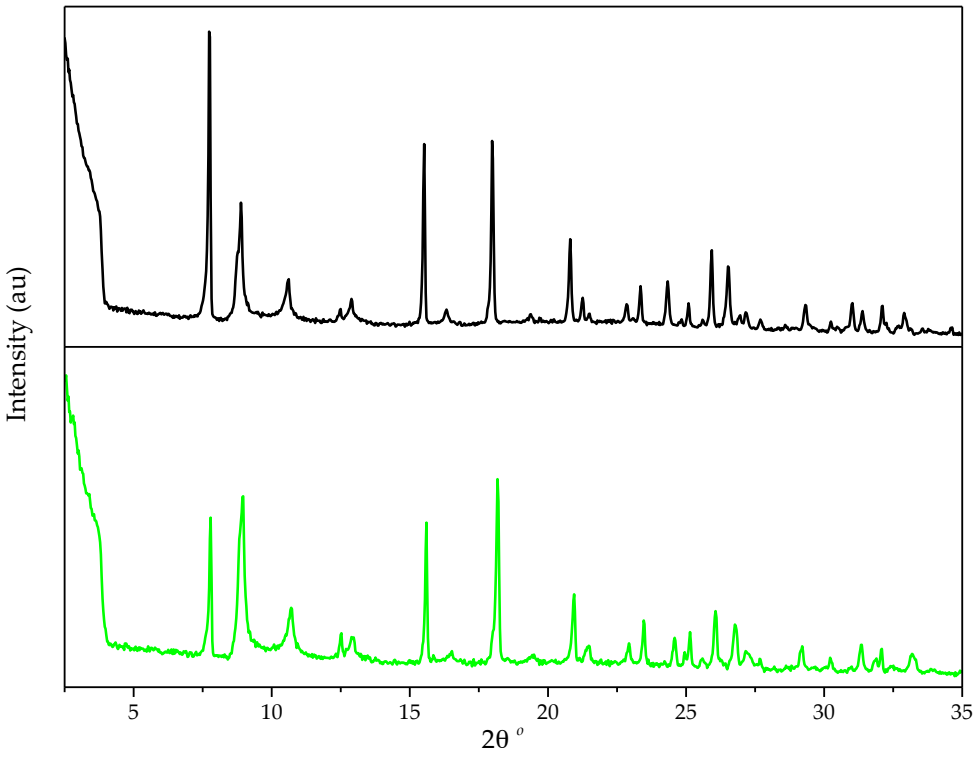

Figure 6.12. PXRD patterns of as-made (black) and after CO_2 adsorption measurements (green) In: PDG.

The PXRD patterns show that the material retains its crystal structure after measuring the CO_2 sorption isotherms, with the same change of relative peak intensities seen after the material is activated.

6.2.8 Water Stability

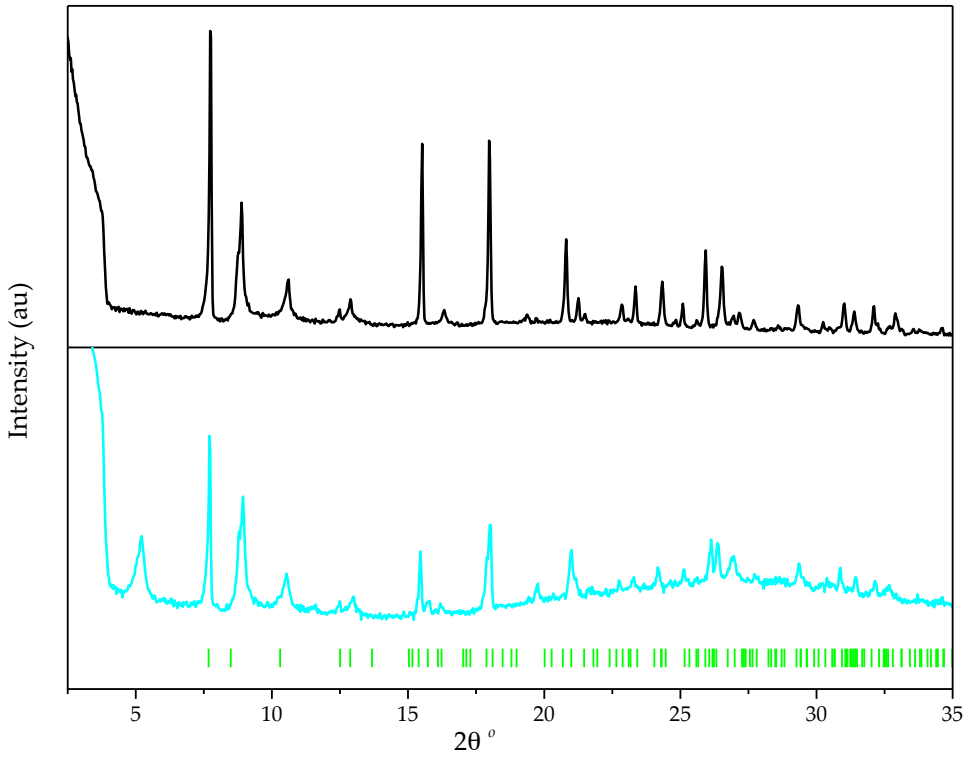

Figure 6.13. PXRD of as-made (black) and after stirring in water overnight (cyan) In: PDG, allowed peaks represented by green tick marks.

The material retains its crystallinity after stirring in water overnight which is testament to its stability. It is clear, however, from Figure 6.13, that the material undergoes some structural change, evidenced by the appearance of an extra peak at 5 ^{o} 2θ and others, which cannot be indexed to the unit cell of the *as*-made material. SCXRD was carried out on a crystal found in this sample, however, the phase change observed in the PXRD was not observed via SCXRD. It was for this reason that this phase change was not quantifiable, but poses some interesting future work in solvent soaking studies and how the framework reacts to these different chemical stimuli.

6.3 Characterisation of Al: PDG

6.3.1 PXRD

All attempts at growing a single crystal of Al: PDG were unsuccessful, so SCXRD was not possible here, however, as seen previously with the CSA systems, it is possible to produce isostructural materials of indium and aluminium.

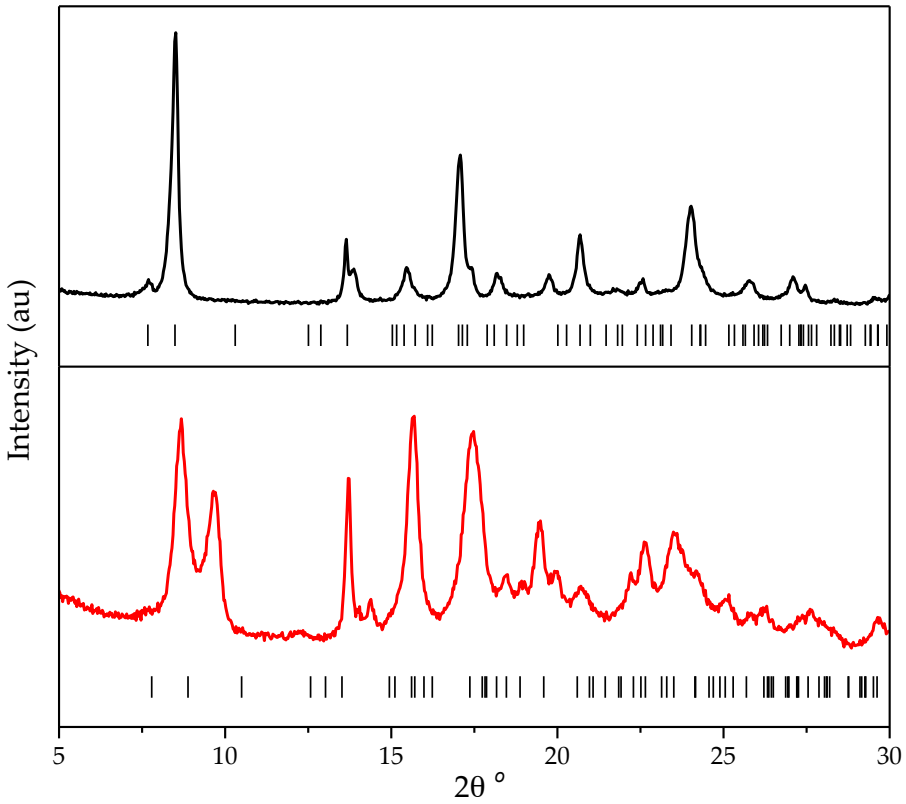

Figure 6.14. PXRD of as-made (black) and activated (red), indexed to the respective unit cells of In: PDG.

The PXRD data (Figure 6.14) shows that the material undergoes a significant structural change upon activation, but due to the lack of single crystal, it was not possible to quantify this change.

It is also clear from Figure 6.14 that not all peaks for both the as-made or the activated Al: PDG materials can be indexed to the unit cells of In: PDG, indicating that the crystal structures are not the same. The IBU of Al: PDG is expected to be the same for its indium analogue, so the difference in structure could stem from the linker adopting a different conformation with each metal. This is purely speculation and a thorough Rietveld refinement on this material would be required in order to confirm this theory.

6.3.2 TGA

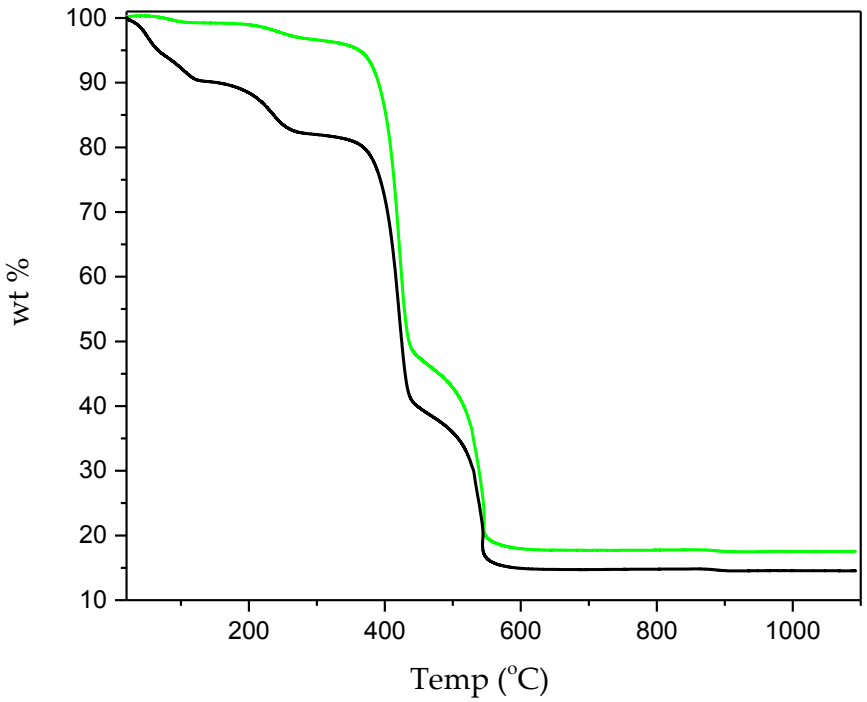

Figure 6.15. TGA trace of as-made (black) and activated (green) Al: PDG.

The TGA trace of the *as* – made material shows two mass loss steps up to 300 °C. The first of which (ca 10 % wt) can be attributed to the removal of

low boiling point solvent guests from the synthesis and washing procedure. The second mass loss of 8 % is due to the removal of DMF. The trace of the activated material shows that the activation was not fully successful since a slight mass loss of 3 % can be seen between 190 – 300 ^{o}C., indicating that DMF is still present. This is highly unusual after activation at 155^{o}C but was taken into account when analysing the elemental analysis shown in Table 6.2.

The final inorganic residue (Al_2O_3) makes up 17.50 % of the activated sample, which equates to 18.11 % of the dry material (reading taken at 300 ^{o}C), giving a final aluminium content of 9.59 %. Since the structure and composition of this material is unknown, there is no absolute value to compare this with. Based on a theoretical formula of [Al(OH)($C_{12}H_{10}O_6N_2$)], the aluminium content should be 8.37 % which is lower than the measured value, implying there is probably some alumina formed during the synthesis.

6.3.3 Elemental Analysis

Al(OH)($C_{12}H_{10}O_6N_2$)(C_3H_7NO)$_{0.1}$(H_2O)$_{0.2}$		
Element	Expected %	Measured %
C	44.35	43.99
H	3.66	3.77
N	8.83	8.71

Table 6.2. Elemental analysis of an activated sample of Al: PDG

From the TGA data, it was clear that not all guest solvent molecules were removed during the activation process, this had to be taken into account when analysing the elemental analysis data. When a sensible ratio of water and DMF guests were incorporated into the formula, the elemental data gives really good agreement. This is also supported by the TGA data which shows that a 1 % mass loss is due to water and a further 2.4 % mass loss due to DMF.

6.3.4 SEM

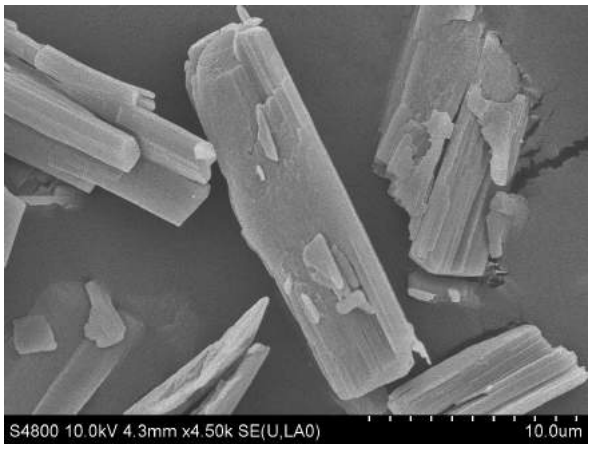

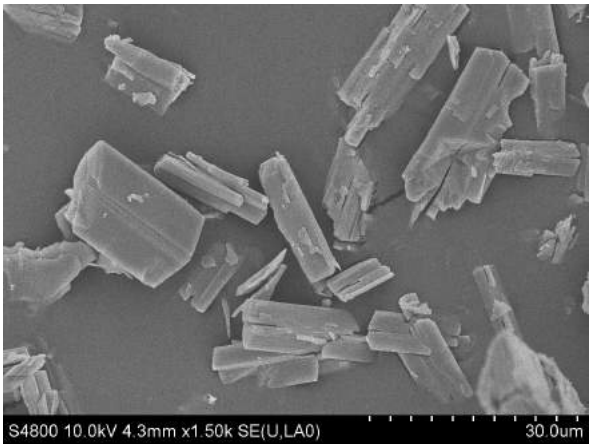

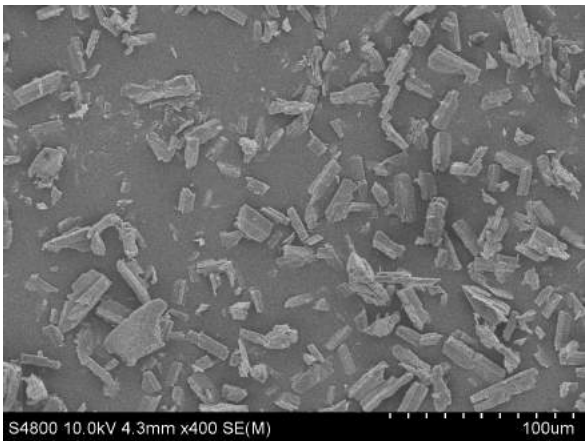

Figure 6.16. SEM images of activated Al: PDG

SEM images (Figure 6.16) show one crystallite morphology, with no clear evidence of any other product. According to the TGA there is an inorganic excess of ca 10 % wt, which is not apparent in the SEM data.

6.3.5 BET

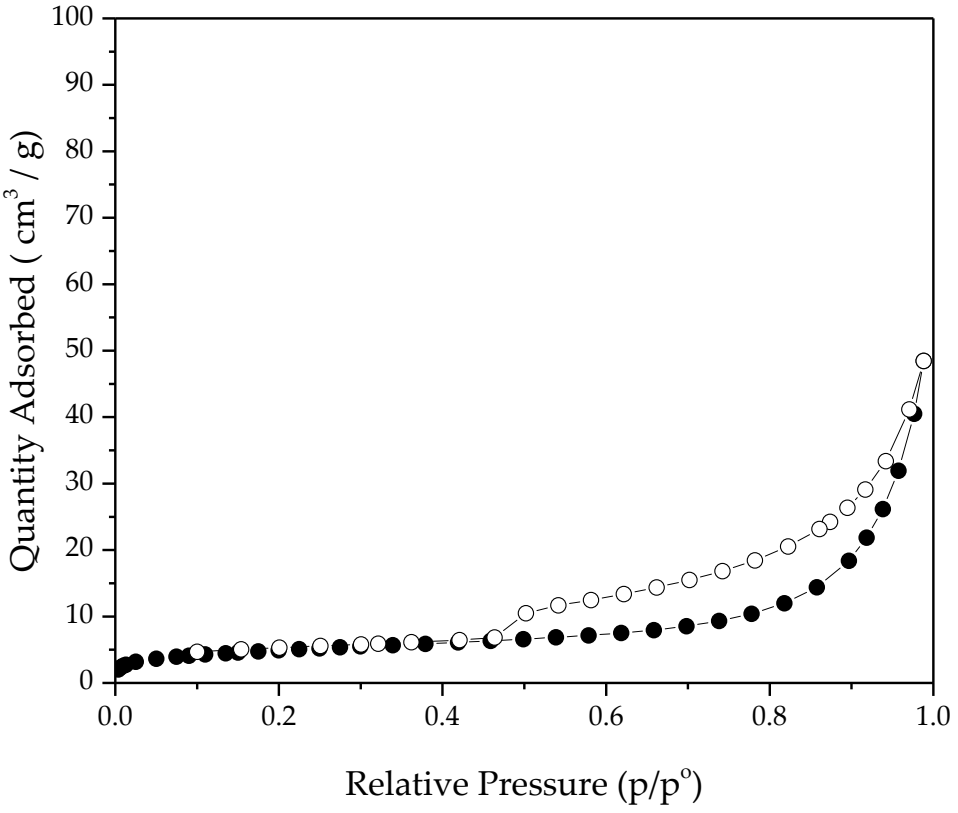

Figure 6.17. N_2 adsorption isotherm of Al: PDG at 77.3 K**.**

The N_2 adsorption isotherm of Al: PDG can be seen in Figure 6.17, and it is clear that the material has very little porosity. A type II isotherm is observed which indicates a non - porous material. Unfortunately, due to the lack of crystal structure available for this material, it is not possible to assess whether or not this agrees with the structure.

CO_2 sorption measurements were ran at various temperatures and the results are shown in Figure 6.18.

6.4 CO_2 Adsorption

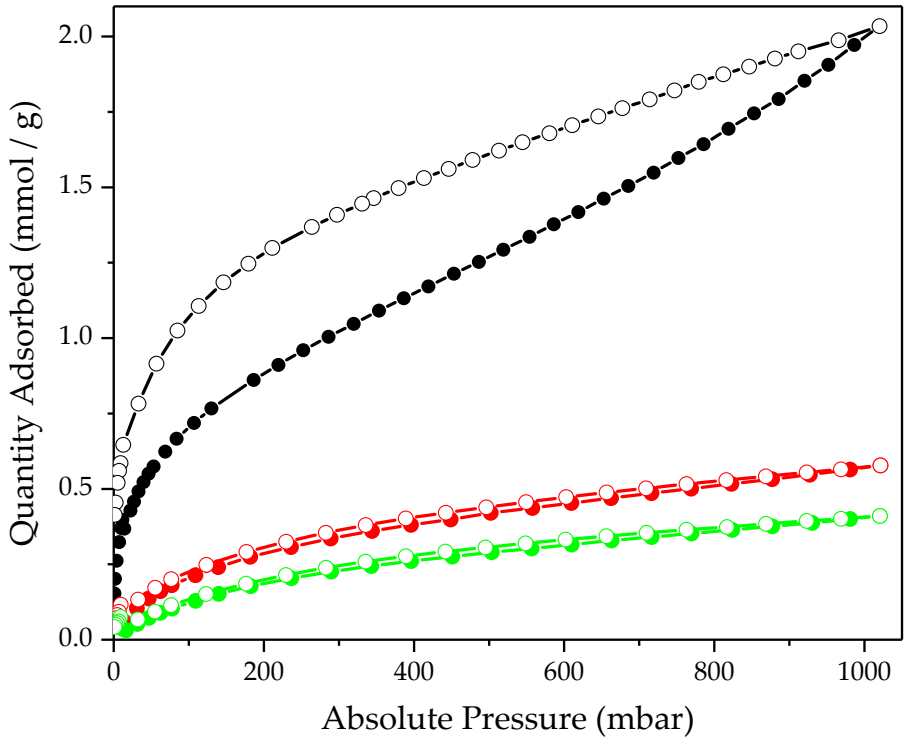

Figure 6.18. CO_2 adsorption isotherms of Al: PDG at 298 K (green), 273 K (red) and 195 K (black).

The CO_2 isotherms for Al: PDG show that the material, like Al: CSA, does have some porosity towards this guest, however, the nature of the pores is unclear. Although there is some porosity and some uptake of CO_2 onto

this material, at 150 mbar, the highest uptake of 0.80 mmol / g occurs at 195 K, with the worst performance of 0.16 mmol / g occurring at 298 K, which is the closest temperature to the desired working conditions for such an application. This data shows that although Al: PDG has some capacity for the uptake of CO_2, when compared with reported values, under the desired conditions (close to room temperature), as seen with Al: CSA, it falls on the lower end of the scale and only shows some reasonable uptake at 195 K., which is useless from a practical and industrial perspective.

To ensure the material remained intact after these measurements, the PXRD pattern was measured and the results are shown in Figure 6.19.

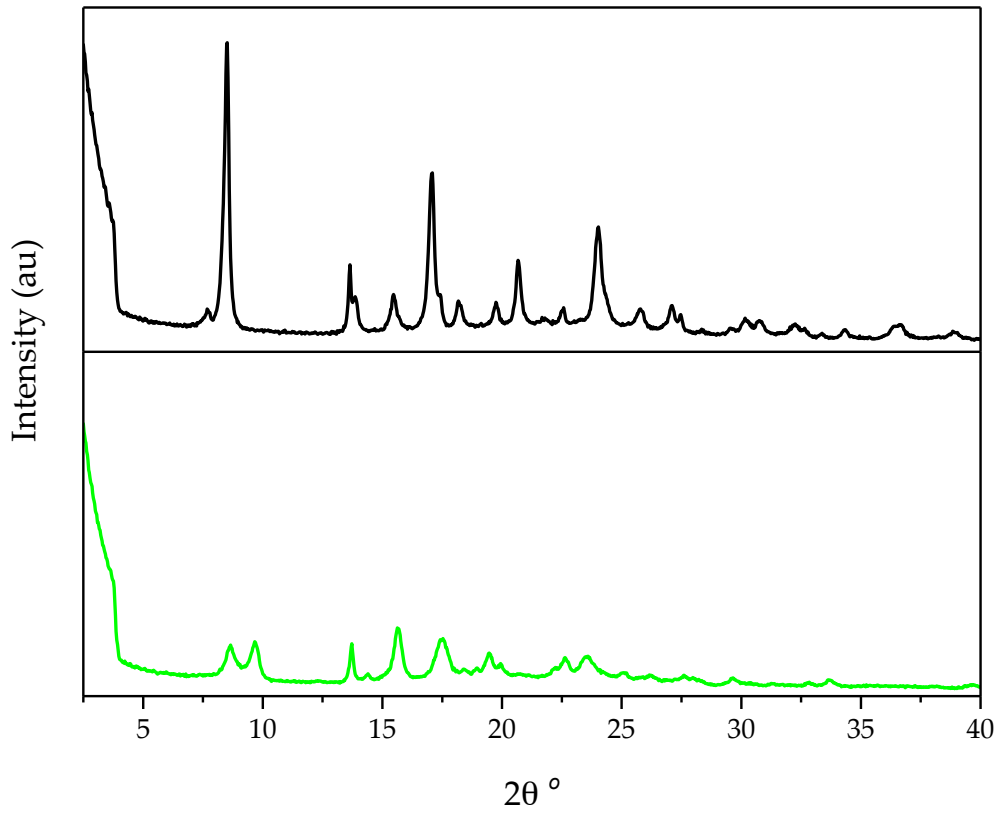

Figure 6.19. PXRD of as-made (black) and post CO_2 adsorption measurement (green) Al: PDG.

The change in PXRD pattern, and therefore the structure is the same seen after activation earlier and unfortunately, due to no knowledge of the structure of this material, these changes could not be quantified.

6.5 Water Stability

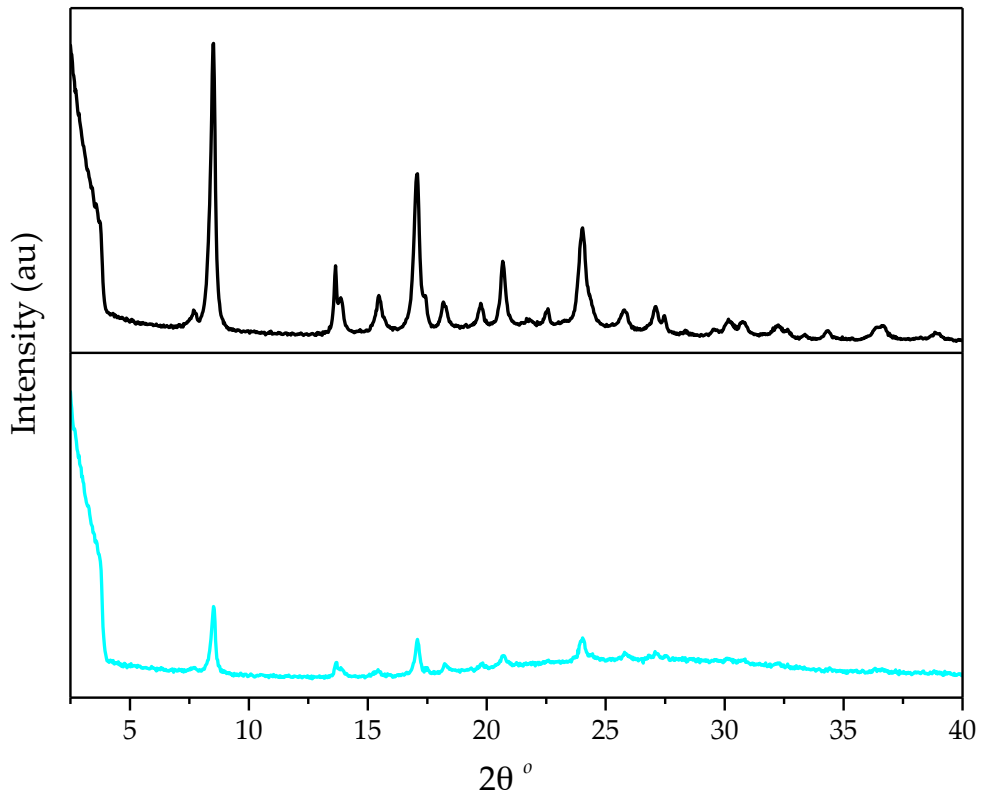

Figure 6.20. PXRD of as-made (black) and after stirring in water overnight (cyan) Al: PDG.

The loss of crystallinity observed after the water treatment is highly unusual since all previous G13 FL – MOFs reported in this thesis have proven to be stable under such conditions.

6.6 Conclusions

In this section, a linker containing two amide groups was used with aluminium and indium with the aim of synthesising two 3–dimensional porous frameworks. Unfortunately, this aim was not achieved.

This section reports the discovery of a new indium MOF with a flexible amide – containing linker, with the same connectivity seen in In: CSA,

Reactions with indium yielded single crystals, from which the structure of the material was determined and the bulk powder was fully characterised and analysed to be phase pure with the formula [In(OH)PDG]. The N_2 adsorption isotherm showed no porosity, even though there are sufficient voids within this material as shown in the crystal structure. A carbon dioxide adsorption isotherm was measured which also showed no porosity, contradicting the evidence of sufficient voids to accommodate CO_2 molecules. This lack of porosity was hypothesised to stem from these sufficient voids running between 2-dimensional sheets and not part of a 3-dimensional framework. The In: PDG material undergoes a structural change upon soaking in water, however, SCXRD of this post – soaked sample shows no structural change, indicating this is not a single crystal – single crystal transformation. This rendered the phase change unquantifiable.

Although the absolute formula and structure of Al: PDG remains unknown, what information can be deduced here is that using a different metal with similar chemistry, can have an impact on the final structure. This is evident as the data presented points towards Al: PDG having a different structure to that of its indium analogue. This phenomenon was discussed previously in this thesis and the results in this section highlight it well. All analytical data was compared with an assumed formula of

Al(OH)($C_{11}H_9NO_5$) and showed that an excess of alumina was formed during the synthesis. Having no crystal structure for a material is highly problematic when it comes to analysing and characterising it, especially trying to solve its crystal structure. As seen in this section, there are still a lot of unknowns surrounding Al: PDG, and further investigations into the system could provide some answers.

6.7 Future Work

Further investigations into the possible compounds between G13 metals and PDG could yield some fascinating structures, and even some 3–dimensional frameworks. Especially indium, which has the ability to adopt a number of different IBUs, causing a huge overall change in the final topology of the framework. Incorporating a template molecule into the synthesis or one that uses intermolecular interactions to prevent the linker from adopting a specific bent conformation could induce the formation of a 3–dimensional framework. Initial experiments into this investigation using trifluoroethanol showed no evidence of a structural change in the product.

Collecting SCXRD data at 500 K for both In: CSA and In: PDG would properly show how these structures change upon the removal of the guest solvents, which results in the change in PXRD patterns. This data could help explain the lack of porosity of these materials despite the calculations indicating that there should be some.

A Rietveld refinement on the Al: PDG could be used to refine the structure of this material, however, due to the number of variables, this would be very difficult.

6.8 References

1. G. E. Kostakis, L. Casella, A. K. Boudalis, E. Monzani and J. C. Plakatouras, *New J. Chem.*, 2011, **35**, 1060.

Chapter 7. Mg: Mucic Acid

7.1 Overview

Mucic acid (MA) (or galactaric acid), shown in **Figure 7.1**, is an aldaric acid which is synthesised by the oxidation of an aldose (galactose) with nitric acid.

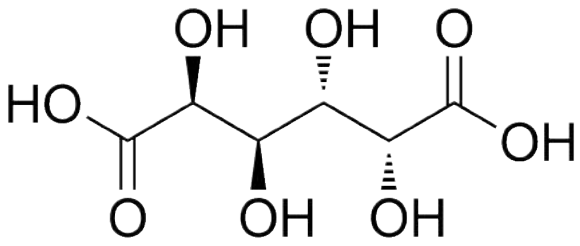

Figure 7.1. Mucic acid (MA).

An aldose is a simple sugar (or monosaccharide) that contains a single aldehyde group per molecule.[1] Due to their availability, sugar derivatives are appealing candidates as building blocks for potentially useful polymers and MOFs. Due to its high functionality with four hydroxy groups along the carbon chain, mucic acid could provide a MOF with some interesting and useful properties. Due to significant interest in introducing a "green" chemical industry of the future, molecules such as aldaric acids, which are derived from natural and renewable sources, have been studied for their use in industry.[2] An example is the use of mucic acid as a precursor for adipic acid which is used in the synthesis of nylon, the current process of obtaining adipic acid is from crude oil.[3]

Mucic acid is the meso compound of saccharic acid, meaning that although it contains four chiral carbons, it itself is not chiral. Saccharic

acid being chiral, has been used with zinc in the synthesis of a porous MOF with an interesting motif arising from the chirality of the linker as shown in **Figure 7.2**.[2]

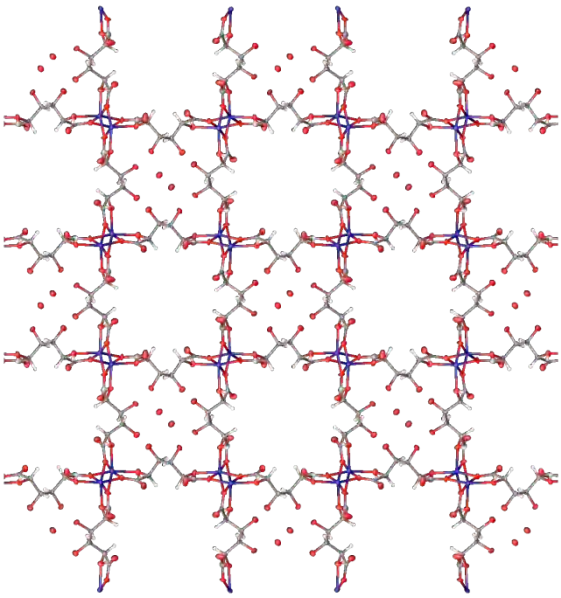

Figure 7.2 Pore motif of zinc saccharate. Figure from reference.[2]

A chess board like motif of hydrophilic and hydrophobic channels arise from the chirality of the saccharic acid linker. Using a non – chiral alternative to this linker could lead to the formation of a material of with uniform pores, either hydrophobic or hydrophilic depending on the orientation of the hydroxy groups of mucic acid.

In the past thirty years, there have been a few complexes reported using mucic acid with different metals including aluminium, magnesium and cobalt.[4, 5] As well, due to its highly appealing attributes, there have also been a number of reported lanthanide based materials with mucic acid, however, many of them are 2– dimensional.[6]

In 1989, Mackie *Et al.*, reported the structure of an Mg: MA complex whereby all hydroxy groups co – ordinated to the metal centre.[5]

Herein is the first reported porous 3–dimensional MOF using magnesium and mucic acid, its structure was solved from SCRXD data by Dr George Whitehead using Shelx and OLEX 2 software. The bulk powder was analysed and characterised to be phase pure and porosity was measured using N_2 and CO_2 adsorption isotherms.

7.2 Experimental

Mucic acid and $Mg(NO_3)_2.6H_2O$ were purchased from Sigma Aldrich in 97 % and 99.999 % purity respectively and were used without further purification. DMF, ethanol and THF were purchased from Fisher scientific and were used without any further purification.

A high throughput exploratory synthesis approach was adopted when investigating into this new material. Although an Mg: MA complex has been reported already, in order to obtain a fully 3–dimensional framework, a thorough investigation into reaction conditions was needed. Altering parameters such as reaction time and temperature, solvent mixtures and molar ratios of starting materials resulted in finding the optimum reaction conditions required to make a phase pure, 3–dimensional Mg: MA framework.

Initially, M : L molar ratios were adjusted from 0.1 : 1 to 1 : 0.1, alongside experimenting with reaction times and temperatures, ranging from 70 ^oC to 150 ^oC and from 8 hours to 48 hours. Adjusting the volume of the reaction mixture from 5 mL to 20 mL using various different solvent mixtures, pure water, pure DMF and adjusting the mixture ratios throughout. Introducing different volumes of ethanol into the mixture was also tried.

7.2.1 Synthesis of Mg: MA

A 0.5 M stock solution of $Mg(NO_3)_2.6H_2O$ in DMF was prepared. To a 40 mL Teflon capped glass vial, mucic acid (105.1 mg, 0.5 mmol), $Mg(NO_3)_2.6H_2O$ solution (1 mL, 0.5 mmol), DMF (8 mL), H_2O (0.6 mL) and ethanol (0.6 mL) were added. The reaction mixture was heated at 2.5 ^oC / min to 125 ^oC for 21 hours before cooling to room temperature at 0.2 ^oC / min. This yielded some small block like crystals and some plates, a small aliquot of the product was removed for SCXRD analysis. The remaining pale yellow powder was washed with DMF (3 x 20 mL), ethanol (3 x 20 mL) and THF (3 x 20 mL) and left to filter dry under vacuum. The final composition of this material was found to be $Mg(C_6H_8O_8)\cdot H_2O$.

7.3 Characterisation of Mg: MA

7.3.1 Structure

The synthesis of this material yielded two types of single crystal, which were used to determine the crystal structures of the products.

The block crystals were analysed to be a side product; magnesium formate MOF which was assumed to be washed out during the washing procedure.

The second lot of crystals which had plate – like shapes were analysed at I19 beamline at Diamond Light Source and the structure was solved by Dr George Whitehead. Data collection and refinement parameters are presented in Appendix II.

Mg: MA crystallises in the monoclinic space group *C2/c* with lattice parameters a = 12.111(3) Å, b = 16.598(2) Å, c = 5.889(3) Å, β = 116.564(11) ^{o}.

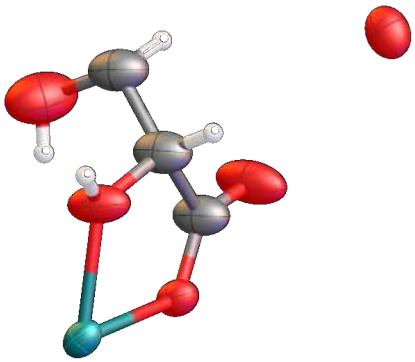

Figure 7.3. Asymmetric unit of Mg: MA. Magnesium (turquoise), carbon (grey), oxygen (red) and hydrogen (white).

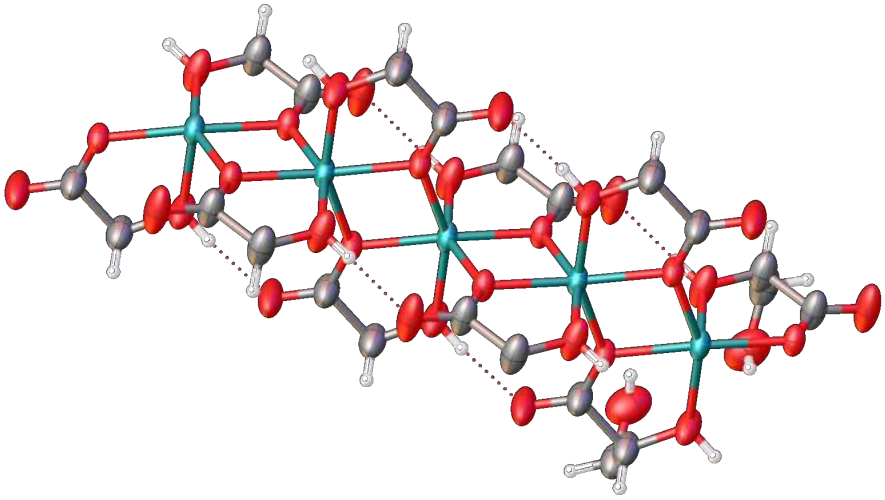

Figure 7.4. SBU of Mg: MA. Magnesium (turquoise), carbon (grey), oxygen (red) and hydrogen (white).

The binding mode of Mg: MA is displayed clearly in the asymmetric unit of the material (see Figure 7.3) and is commonly seen in MOFs that use linkers with hydroxyl groups on adjacent carbons to the carboxylic acid groups (MOF–74,[7] saccharate MOFs[2]). Also shown in this figure is the presence one water molecule per magnesium ion, which is in good agreement with TGA data collected on this material (see Figure 7.13).

One of the carboxylate oxygen atoms bridges between two different magnesium ions, leaving the second oxygen atom free, the hydroxyl group on the adjacent carbon then also binds to one of the two magnesium ions. This same hydroxyl group forms a hydrogen bond with the free carboxylate oxygen atom on an adjacent MA linker. This binding motif occurs at both ends of the linker molecule. The SBU seen in this material is made up of simple MgO_6 octahedra as shown in Figure 7.4, four of the oxygen atoms bridge two adjacent magnesium ions, while the final two come from the co – ordinated mucic acid hydroxy groups.

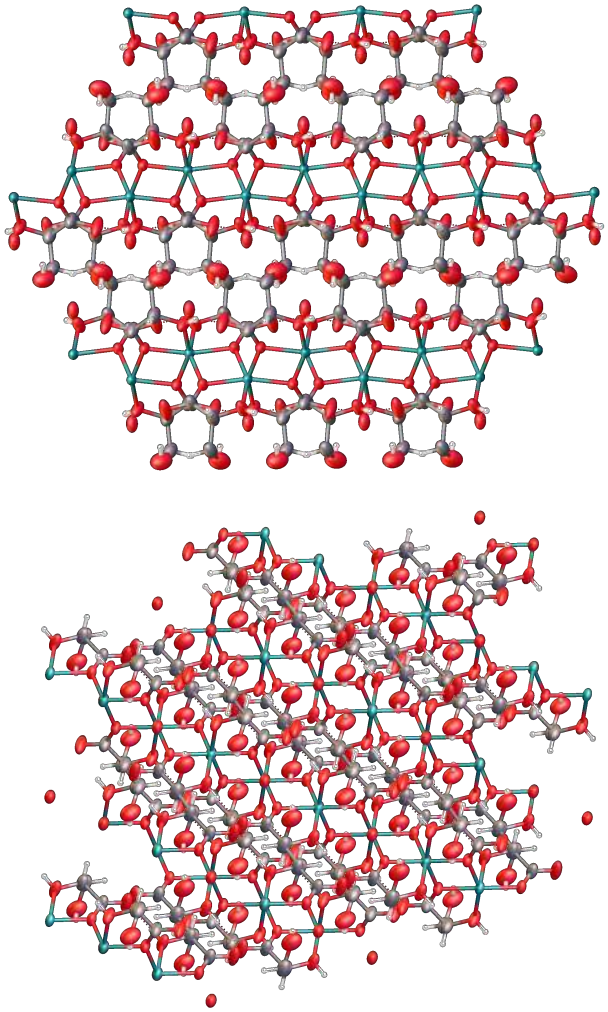

Figure 7.5. Mg: MA framework viewed along crystallographic *a* (top) and *b* (bottom) – axes. Magnesium (turquoise), carbon (grey), oxygen (red) and hydrogen (white).

Along the crystallographic *a* and *b* – axes shown in Figure 7.5, there are no solvent accessible voids, evidenced by the dense packing and the largest penetrable sphere of 0.2 Å radius. Figure 7.6 shows the material along the crystallographic *c* – axis, whereby there are clear channels, which are occupied by two water molecules. The largest penetrable sphere along this axis is 2.00 Å in radius which is large enough to potentially accommodate a number of gases from water to methane.

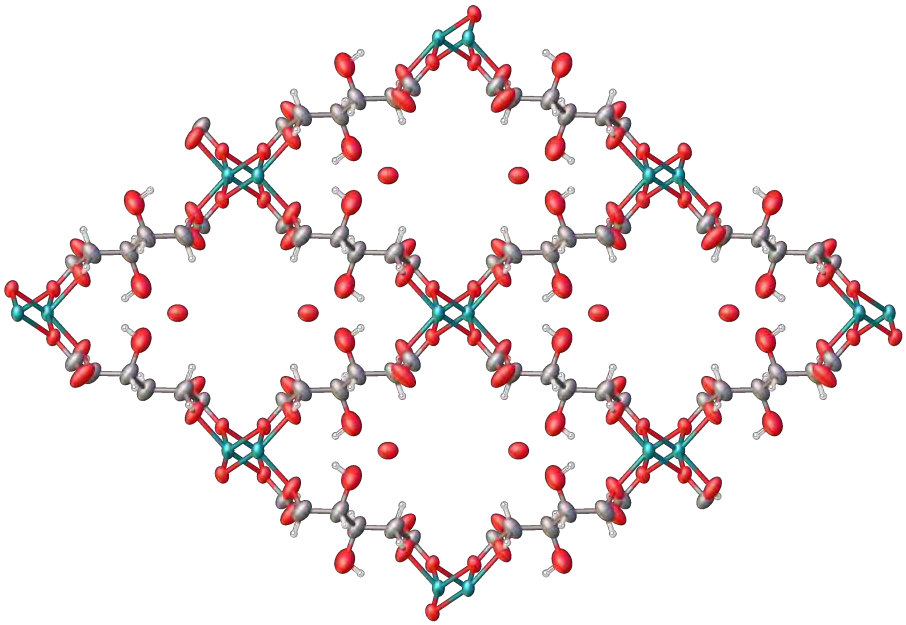

Figure 7.6. Mg: MA framework viewed along crystallographic *c* – axis. Magnesium (turquoise), carbon (grey), oxygen (red) and hydrogen (white).

The largest spherical void in the material has a 2.20 Å radius, which is large enough to host a number of guest molecules as mentioned earlier.

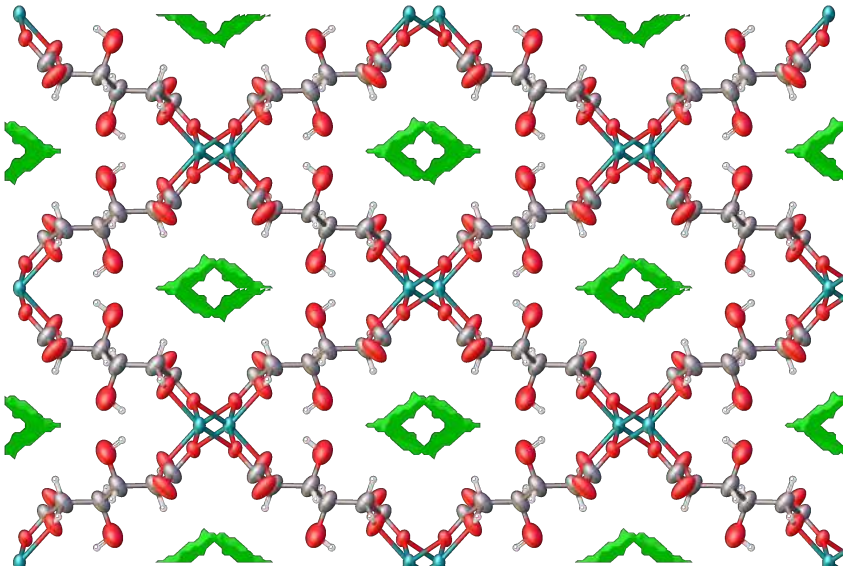

Figure 7.7. Surface map of Mg: MA viewed along crystallographic *c* – axis, modelled using a water – sized probe (1.32 Å radius). Magnesium (turquoise), carbon (grey), oxygen (red) and hydrogen (white).

The solvent accessible volume of Mg: MA was calculated for both N_2 and CO_2 to be 184.6 $Å^3$ (17.4 %) and 194.2 $Å^3$ (18.3 %) respectively, the voids for a nitrogen probe are shown in **Figure 7.8** and **Figure 7.9**.

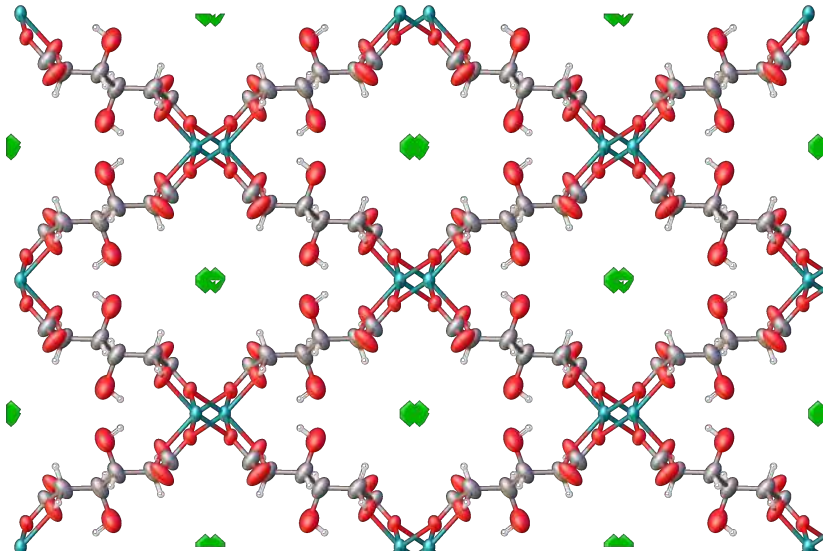

Figure 7.8. Surface map of Mg: MA viewed along crystallographic *c* – axis, modelled using a nitrogen – sized probe (1.8 Å radius). Magnesium (turquoise), carbon (grey), oxygen (red) and hydrogen (white).

The *c* – axis has a largest penetrable sphere of 2.00 Å, however, the surface map calculated using a nitrogen probe shows that although there are voids large enough to accommodate this molecule, the access window is too small. This is clear by the lack of white space in the centre of the voids, which, in general, represent the access window.

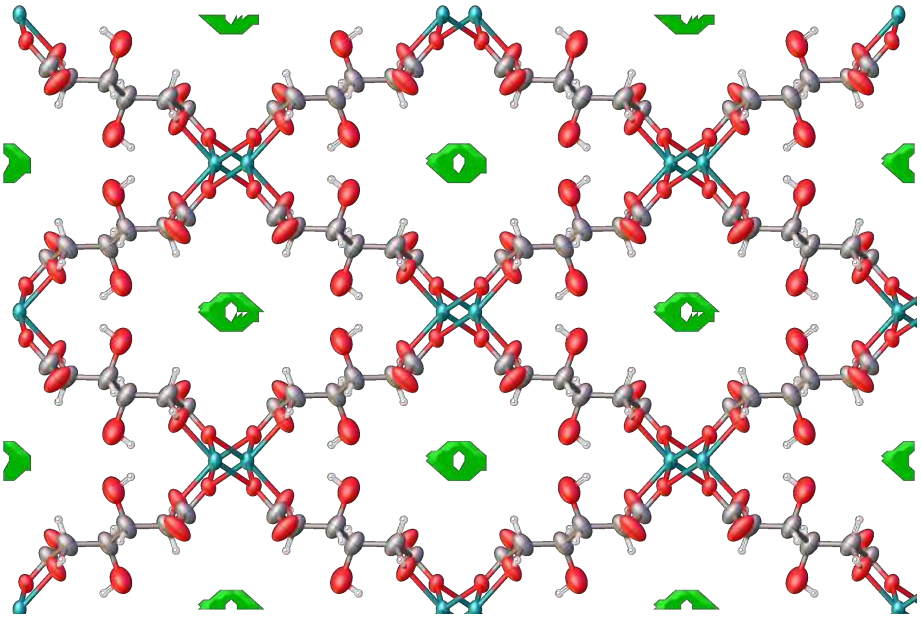

Figure 7.9. Surface map of Mg: MA viewed along crystallographic *c* – axis, modelled using a nitrogen – sized probe (1.65 Å radius). Magnesium (turquoise), carbon (grey), oxygen (red) and hydrogen (white).

From the crystal structure, it is therefore predicted that this material will show some porosity towards CO_2 with little / none towards N_2.

7.3.2 PXRD

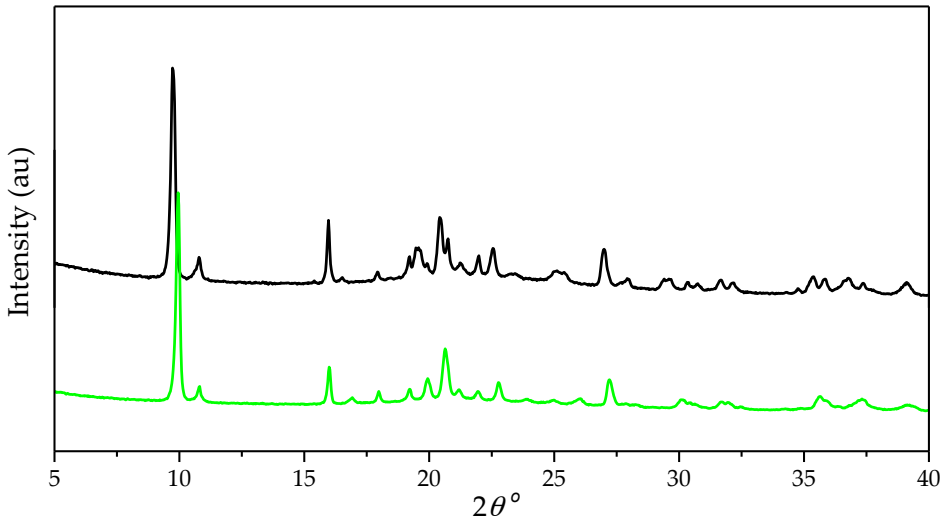

Figure 7.10. PXRD of Mg: MA, as–made (black), activated (green).

The PXRD patterns show that the material retains its crystallinity after activation which, according to the TGA data (Figure 7.13), was proven successful. All peaks were indexed to the space group of the single crystal as shown in Figure 7.11 with lattice parameters a = 12.111(3) Å, b = 16.598(2) Å, c = 5.889(3) Å, β = 116.564(11) °.

When comparing the collected patterns of the as–made and activated materials with the simulated pattern generated from the crystal structure, the patterns it is clear that the bulk of the material has the same structure as the single crystal.

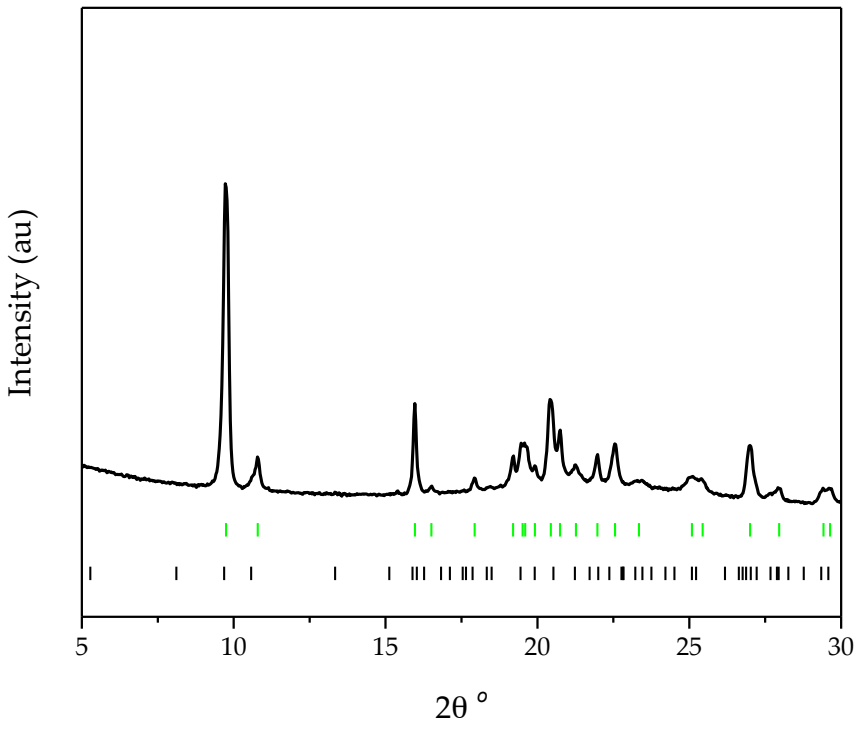

Figure 7.11. PXRD of as–made Mg: MA indexed to the unit cell from the crystal structure, calculated peaks indicated by black tick points.

There is a slight shift in peak positions from the calculated positions, which is attributed to a slight change in lattice parameters that occurs between the temperatures of SCXRD collection, 100 K and PXRD collection, 298K.

The lattice parameters obtained from PXRD data for the as–made material were a = 12.083(5) Å, b = 16.699(7) Å, c = 5.879(1) Å, β = 116.76(1) ° showing that there is a slight contraction along the crystallographic a and b axes and elongation along the c – axis.

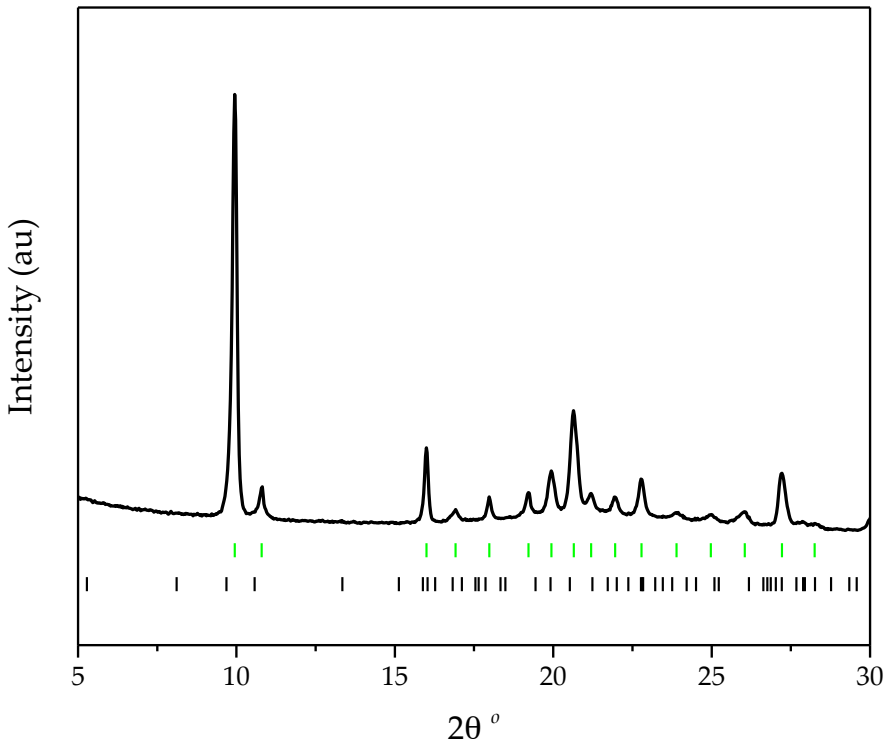

Figure 7.12. PXRD of activated Mg: MA indexed to the unit cell from the crystal structure. Calculated peaks shown by black tick marks.

The change in lattice parameters is more evident in the activated material (**Table 7.1**). This implies that the pores exhibit a similar "breathing" effect as seen with MIL–53 whereby pores expand and contract upon uptake and removal of guest solvents or gas molecules. The activated lattice parameters are shown in the table below. Here, there is evidence that the pores contract slightly upon activation. This could be further probed by in – situ gas loading with PXRD to examine the structural change seen upon gas uptake.

	a (Å)	*b* (Å)	*c* (Å)	B (°)
As–made	12.083(5)	16.699(7)	5.879(1)	116.76(1)
Activated	11.761(5)	16.751(7)	5.871(2)	116.91(2)

Table 7.1. Lattice parameters of both as–made and activated Mg: MA material

7.3.3 TGA

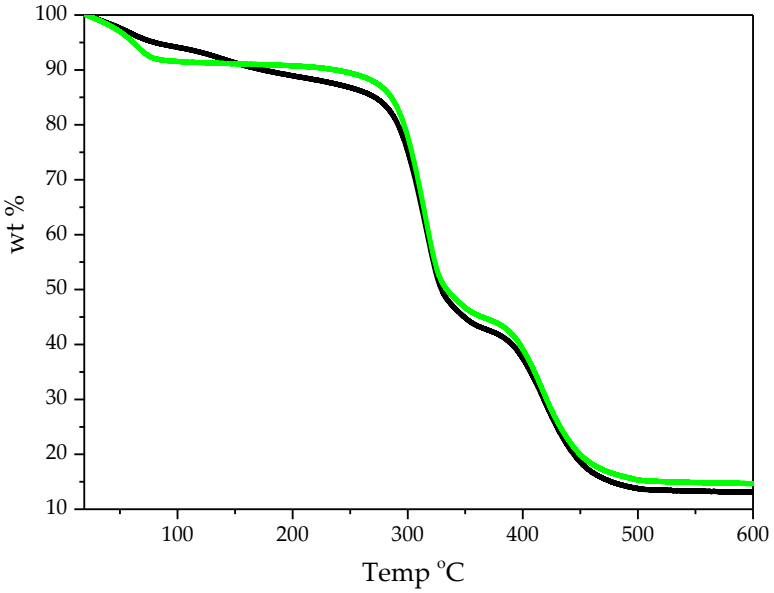

Figure 7.13. TGA trace of Mg: MA, as–made (black) and activated (green).

The TGA data shows that the activation process was a success and the removal of all the DMF was achieved. The data collected from the activated sample shows some mass loss of ca 9 % up to 100 °C attributed to the removal of adsorbed water from the atmosphere.

Thermal decomposition into its inorganic residue doesn't occur until above 200 °C, leaving behind 14.50 % MgO. The final magnesium content of the material was then calculated to be 9.59 %, compared to the

theoretical value based on the formula [$Mg(C_6H_8O_8)$] of 10.46 %, which is in decent agreement. However, there is some evidence of excess organic content.

7.3.4 Elemental Analysis

	$Mg(C_6H_8O_8)\cdot H_2O$	
Element	Expected %	Measured %
C	28.78	28.77
H	4.02	4.29
N	0.00	0.00

Table 7.2. CHN data of an activated sample of Mg: MA.

The elemental analysis gives good agreement with the expected formula, and the TGA data presented earlier, which showed that ca. 9 % of the material is water. The expected formula here, includes one water molecule, equating to ca. 7 % of the material. The lack of nitrogen measured in this analysis further proves that all DMF has been removed during the activation process.

7.3.5 Surface Area Measurement

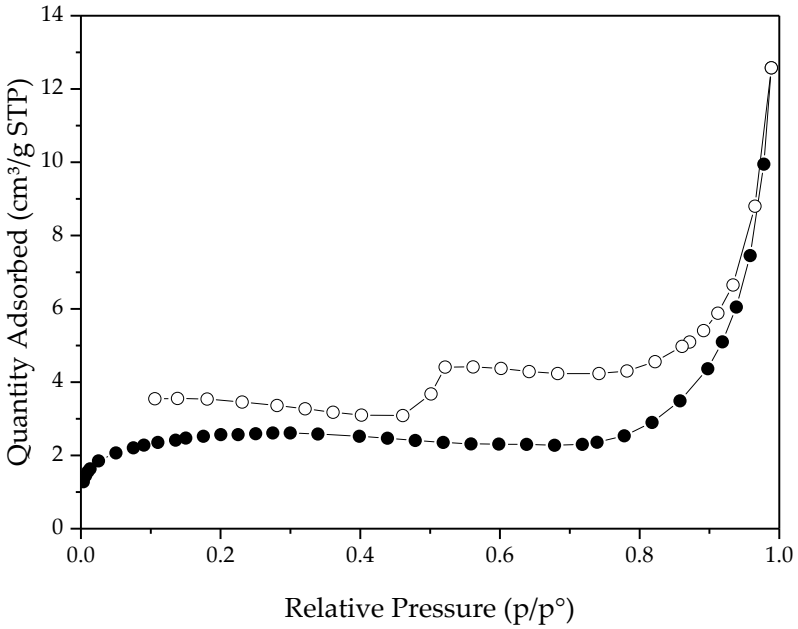

Figure 7.14. N_2 adsorption isotherm of Mg: MA at 77.3 K.

The N_2 adsorption isotherm shows that the material is essentially not porous towards nitrogen, which is in agreement with the crystal structure which shows the voids are too small to uptake a molecule as large as nitrogen. Although the largest penetrable sphere is 2.00 Å radius implies that the host – guest interactions play a more dominant role over size exclusion in adsorption for this material, therefore, CO_2 adsorption isotherms were ran at different temperatures and the data is presented in the next section.

7.4 CO_2 Sorption Measurements

The CO_2 adsorption isotherms were carried out at high pressure on the intelligent gravimetric analyser at 298 K (Figure 7.15) and 195 K (Figure 7.16).

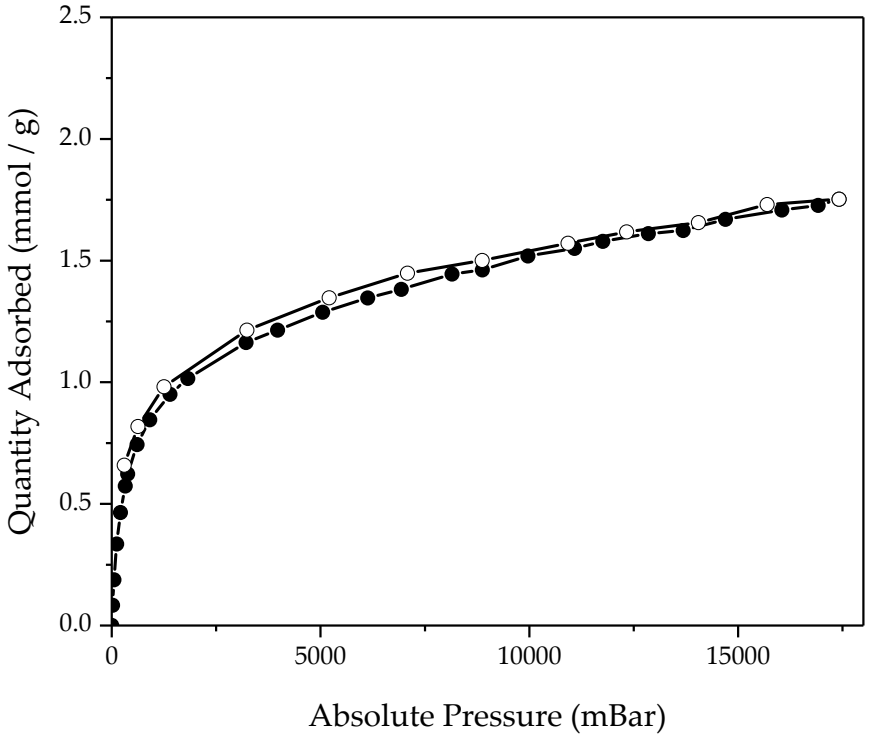

Figure 7.15. CO_2 sorption isotherm of Mg: MA at 298 K.

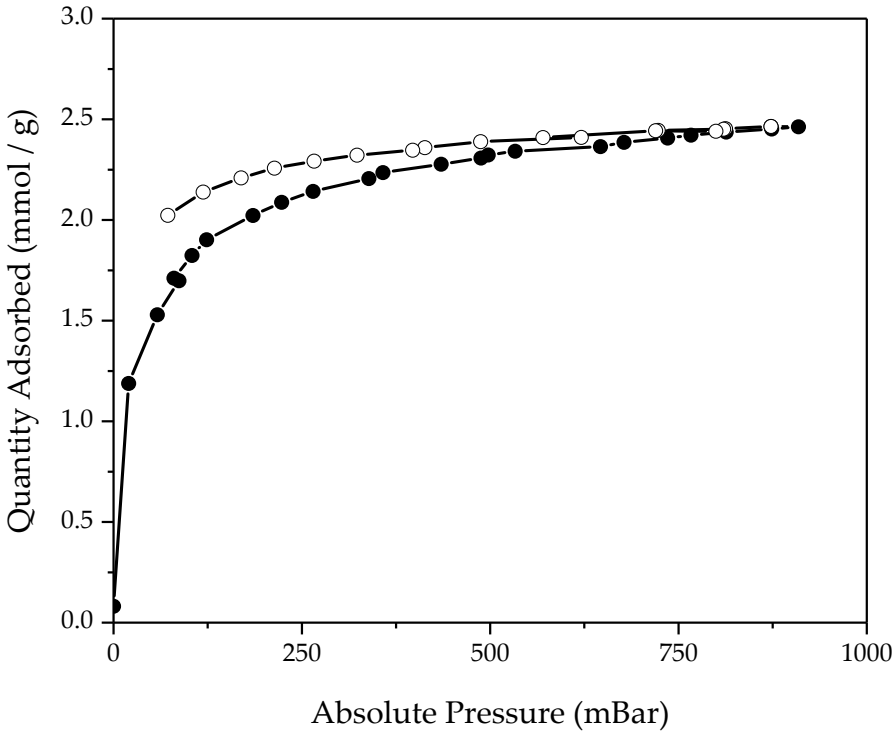

Figure 7.16. CO_2 sorption isotherm of Mg: MA at 195 K.

The measurements show that there is some adsorption of CO_2 onto the material at both temperatures. At the higher temperature, saturation of 1.75 mmol / g is achieved by 17.5 bar, meanwhile at 195 K, saturation is reached by 1 bar at a capacity of 2.45 mmol / g. The uptake of CO_2 at 150 mbar is 0.38 mmol / g and 1.90 mmol / g at 298 K and 195 K respectively. These values, when compared with reported values, fall at the lower end of the scale as seen with Al: CSA and Al: PDG.

7.5 Water stability

The purpose of this test was to see if the material undergoes any structural changes after stirring in water, it is well known that many M^{2+} MOFs have very little water stability.

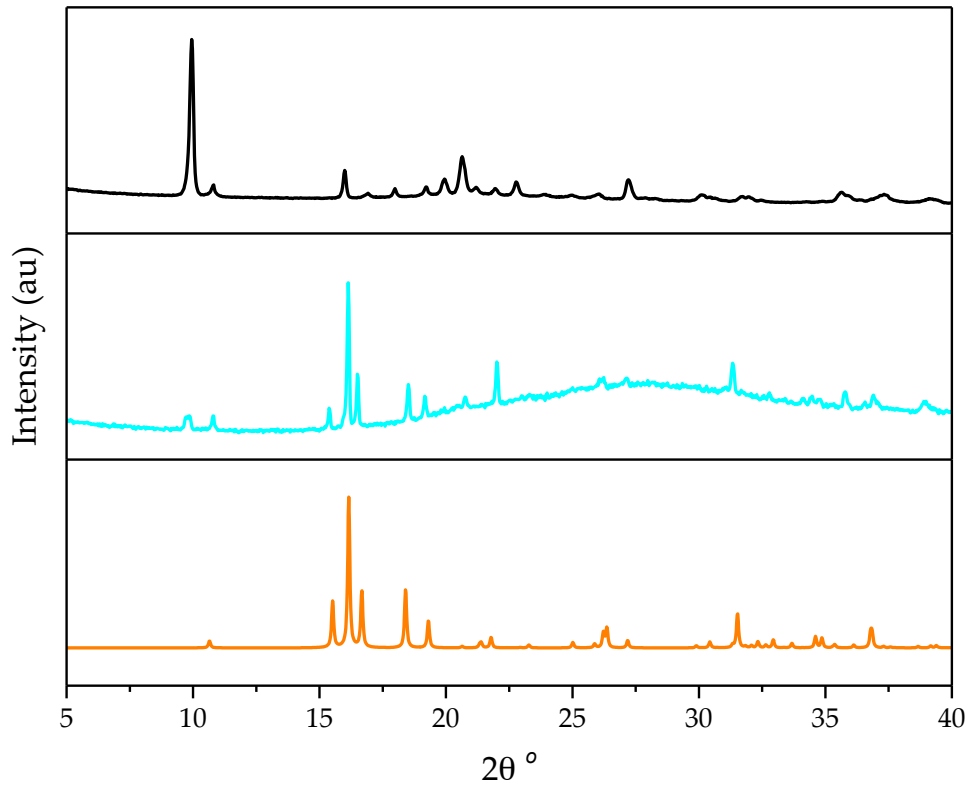

Figure 7.17. PXRD pattern of activated Mg: MA (black), Mg: MA after soaking in water (cyan) and simulated PXRD pattern of Co: MA *cis* – chains (orange).

After stirring for 1.5 hours in water, the material was loaded into a 1mm diameter borosilicate capillary while still in solution and the PXRD pattern was collected using the Bruker D8 instrument.

It is clear from the PXRD that there has been a significant change in the crystal structure. The amorphous hump between 20 and 40 degrees 2 theta is attributed to the presence of solution in the capillary. The PXRD pattern changes significantly, and after the stirring, resembles that of Co: MA *cis*–chains (Figure 7.18) which were synthesised while trying to produce a Co: MA framework. Here *cis* refers to the respective positions of the co – ordinated water molecules onto the magnesium ions.

This data shows that Mg: MA is unstable to stirring in water, but could still be stable to water vapour. This would be interesting to measure, as well as a water isotherms as it is know from the crystal structure that the material can accommodate water molecules.

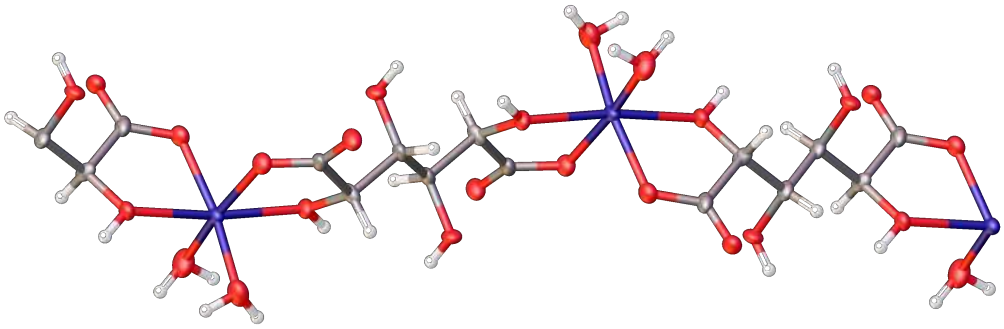

Figure 7.18. Co: MA chains formed when trying to synthesise a Co: MA framework. Cobalt (blue), carbon (grey), oxygen (red), hydrogen (white).

7.6 Conclusions

In this section, a new, 3–dimensional, porous material has been reported with the formula [Mg(MA)] and has the composition $MgC_6H_8O_8$. From a single crystal, the structure was fully determined and the bulk has been fully characterised and analysed using a variety of analytical techniques.

The outcome suggests the formula obtained from the crystal structure is correct, however, some inorganic impurities were formed during the synthesis. Although the material did not exhibit any porosity towards nitrogen, it did show some towards carbon dioxide, which was not comparable to reported materials with similar structures and co – ordination environments. Mg–MOF–74 for example, has the same co – ordination environment as Mg: MA and has one for the highest reported CO_2 uptake capacities. Mg: MA was tested for its water stability and after just 1.5 hours stirring in water at room temperature, the structure changed significantly, to resemble that of the *cis*–chains formed with cobalt and mucic acid.

These results show that, although a Mg: MA complex has been reported, it was not the only possible product of these two reagents. The material has what can be described as hydrophilic channels running along the crystallographic *c*–axis, which could be exploited for various applications including ammonia uptake.

7.7 Future Work

As mentioned earlier, testing the stability of this material towards water vapour and therefore running water isotherms could provide interesting information regarding the stability of this material. This could lead to the material being tested for other applications where molecules with similar chemistry to water are used, e.g. ammonia uptake. Although there have been no preliminary tests to prove that this could be a valid application so far, and the material has been proven to be unstable in liquid water, the fact that two water molecules can be found inside the pores of this material give a good indication that it could work.

7.8 References

1. L. M. Berg, *Biochemistry (sixth edition)*, W. H. Freeman and Company, New York, 2006.
2. B. F. Abrahams, M. Moylan, S. D. Orchard and R. Robson, *Angew. Chem. Int. Ed.*, 2003, **42**, 1848.
3. D. E. Kiely, *ACS Symp. Ser.*, 2001, **784**, 64.
4. A. Lakatos, R. Bertani, T. Kiss, A. Venzo, M. Casarin, F. Benetolo and D. Favretto, *Chem. Eur. J.*, 2004, **10**, 1281.
5. B. Sheldrick and W. Mackie, *Acta Crystallogr. Sect. C.*, 1989, **45**, 1072.
6. B. F. Abrahams, M. Moylan, S. D. Orchard and R. Robson, *CrystEngComm*, 2003, **5**, 313.
7. P. D. Dietzel, Y. Morita, R. Blom and H. Fjellvag, *Angew. Chem. Int. Ed.*, 2005, **44**, 6354.

Chapter 8 Summary

The overall aim of this study was to research into the synthesis of new, porous materials with functionalised and flexible linkers. Although only one MOF reported in this thesis reports any significant porosity (Al: FDC), other materials presented in this work provide further insight into MOF synthesis.

Using the same FDC linker but altering the metal from Al to In has a huge impact on the outcome of the reaction as evidenced by the formation of In: FDC compound 1 under very similar reaction conditions as those used for Al: FDC. Furthermore, by altering the reaction conditions further and introducing basic reagents into the reaction mixture gives rise to the formation of another set of unique structures such as In: FDC compounds 2 and 3.

The same phenomenon is seen throughout this work, another example comes from changing the metal from Zn to Cu using the same CSA linker and the same reaction conditions gives rise to the formation of a different structure. Unfortunately the structure of Zn: CSA could not be solved due to lack of single crystals for this system.

On the contrary, the same structure was obtained for both In and Al analogues. It is unknown why this system behaves the same for both metals, but even with apparently the same crystal structure, both analogues exhibit different adsorption behaviours towards CO_2 and CH_4.

With all systems for CSA and PDG, altering the reaction conditions during the exploratory synthesis stage, did not obtain any different structures. This was unexpected based on the different structures obtained from In: FDC materials, this could however, be due to the reaction conditions not been altered enough to find a new kinetically

stable material or even the thermodynamic product. This would need further probing to see if there are any other possible structures for any of these systems.

Finally, although the overall aim was not reached in this work, the number of structures reported using only four different linkers shows how diverse the field of MOF research is. It also shows how and why the number of reported structures has boomed over the past decade, and provides evidence that this field will continue to grow at an incredible rate over the coming years.

Appendix I

Reaction set 1 in 21 mL Teflon lined steel autoclave	
M:L molar ratios (mmol)	0.1:1, 0.5:1, 0.75:1, 1:1, 1.25:1, 1.5:1, 2:1, 3.5:1.7
Solvent	H_2O
Volume (mL)	5
Reaction Time (hrs)	72
Reaction Temperature (^oC)	220

Reaction set 2 in 40 mL screw–top glass vials (all future reactions carried out in these vessels)	
M:L molar ratios (mmol)	0.1:1, 0.5:1, 0.75:1, 1:1, 1.25:1, 1.5:1, 2:1, 3.5:1.7
Solvent	H_2O
Volume (mL)	5
Time (hrs)	72
Temperature (^oC)	220

Reaction set 3	
M:L molar ratios (mmol)	0.1:1, 0.5:1, 0.75:1, 1:1, 1.25:1, 1.5:1, 2:1, 3.5:1.7
Solvent	DMF
Volume (mL)	5
Time (hrs)	72
Temperature (^oC)	220

Reaction sets 4–7	
M:L molar ratios (mmol)	0.1:1, 0.2:1, 0.3:1, 0.4:1, 0.5:1, 0.6:1, 0.7:1, 0.8:1, 0.9:1, 1:1
Solvent	DMF
Volume (mL)	5
Time (hrs)	72
Temperature (^oC)	220
Additive	2–Furoic acid
Additive:Linker ratio (mmol)	(1:1, 2:1, 5:1, 10:1)

Reaction sets 8–12	
M:L molar ratios (mmol)	0.1:1, 0.2:1, 0.3:1, 0.4:1, 0.5:1, 0.6:1, 0.7:1, 0.8:1, 0.9:1, 1:1
Solvent	DMF
Volume (mL)	5
Time (hrs)	72
Temperature (°C)	220
Additive	HCl
Additive:Linker ratio (mmol)	(1:1, 2:1, 5:1, 10:1, 100:1)

Reaction sets 13–38	
M:L molar ratios (mmol)	0.1:1, 0.2:1, 0.3:1, 0.4:1, 0.5:1, 0.6:1, 0.7:1, 0.8:1, 0.9:1, 1:1
Solvent (ratios)	DMF:H_2O (1:4, 2:3, 2.5:2.5, 3:2, 4:1)
Volume (mL)	5
Time (hrs)	72
Temperature (°C)	220, 170, 150, 120, 100

Reaction sets 39 – 42	
M:L molar ratios (mmol)	0.1:1, 0.2:1, 0.3:1, 0.4:1, 0.5:1, 0.6:1, 0.7:1, 0.8:1, 0.9:1, 1:1
Solvent (ratio)	DMF:H_2O (2:3)
Volume (mL)	5
Time (hrs)	72, 36, 24, 12
Temperature (°C)	100

Reaction sets 43 – 51	
M:L molar ratios (mmol)	0.1:1, 0.2:1, 0.3:1, 0.4:1, 0.5:1, 0.6:1, 0.7:1, 0.8:1, 0.9:1, 1:1
Solvent (ratios)	DMF:H_2O (9:1, 8:2, 7:3, 6:4, 5:5, 4:6, 3:7, 2:8, 1:9)
Volume (mL)	10
Time (hrs)	12
Temperature (°C)	100

Appendix II

Table AII.1 Data collection and structure refinement for Al:FDC

Identification code	Al:FDC
Empirical formula	$C_6H_3AlO_6$
Formula weight	198.06
Temperature/K	293
Crystal system	Tetragonal
Space group	*I* 4_1/ *amd*
a/Å	21.0627(12)
b/Å	21.0627(12)
c/Å	10.5018(16)
α/°	90
β/°	90
γ/°	90
Volume/Å^3	4659.0(8)
Z	16
Radiation	Synchrotron (λ = 0.82596)
2Θ range for data collection/°	0 to 149
R_p, R_{wp}, GOF,	1.93, 2.44, 1.39

Table AII.2 Crystal data and structure refinement for In:FDC 1

Identification code	In:FDC 1
Empirical formula	$C_{31}H_{35}In_3N_3O_{24}$
Formula weight	1178.08
Temperature/K	100
Crystal system	orthorhombic
Space group	*Pbca*
a/Å	17.7313(2)
b/Å	20.5132(4)
c/Å	21.2291(3)
α/°	90
β/°	90
γ/°	90
Volume/Å^3	7721.6(2)
Z	8
ϱ_{calc}g/cm^3	2.027
μ/mm^{-1}	1.876
F(000)	4648.0
Crystal size/mm^3	0.2 × 0.1 × 0.05
Radiation	MoKα (λ = 0.71073)
2Θ range for data collection/°	3.592 to 52.744
Index ranges	-22 ≤ h ≤ 22, -25 ≤ k ≤ 25, -20 ≤ l ≤ 26
Reflections collected	85541
Independent reflections	7887 [R_{int} = 0.0670, R_{sigma} = 0.0307]
Data/restraints/parameters	7887/12/532
Goodness-of-fit on F^2	1.070
Final R indexes [I>=2σ (I)]	R_1 = 0.0416, wR_2 = 0.0875
Final R indexes [all data]	R_1 = 0.0597, wR_2 = 0.0943
Largest diff. peak/hole / e Å^{-3}	1.47/-1.26

.

Table AII.3 Crystal data and structure refinement for activated In:FDC 1

Identification code	In:FDC Activated
Empirical formula	$C_{28}H_{25}In_3N_2O_{23}$
Formula weight	1101.96
Temperature/K	100
Crystal system	orthorhombic
Space group	*Pbca*
a/Å	17.7886(9)
b/Å	20.9976(17)
c/Å	21.4309(12)
α/°	90
β/°	90
γ/°	90
Volume/Å^3	8004.8(9)
Z	8
ϱ_{calc}g/cm^3	1.829
μ/mm^{-1}	1.800
F(000)	4304.0
Crystal size/mm^3	0.2 × 0.1 × 0.05
Radiation	MoKα (λ = 0.71073)
2Θ range for data collection/°	3.552 to 37.694
Index ranges	-16 ≤ h ≤ 15, -19 ≤ k ≤ 15, -19 ≤ l ≤ 18
Reflections collected	18115
Independent reflections	3149 [R_{int} = 0.1407, R_{sigma} = 0.0915]
Data/restraints/parameters	3149/0/343
Goodness-of-fit on F^2	1.072
Final R indexes [I>=2σ (I)]	R_1 = 0.0736, wR_2 = 0.1692
Final R indexes [all data]	R_1 = 0.1201, wR_2 = 0.2036
Largest diff. peak/hole / e Å^{-3}	1.21/-1.16

Table AII.4 Crystal data and structure refinement for In:FDC 2

Identification code	In:FDC 2
Empirical formula	$C_{5.33}In_{0.78}O_{5.56}$
Formula weight	273.01
Temperature/K	293(2)
Crystal system	triclinic
Space group	$P\bar{1}$
a/Å	9.6981(2)
b/Å	14.1055(5)
c/Å	16.5294(6)
α/°	69.109(3)
β/°	87.572(3)
γ/°	81.457(3)
Volume/Å^3	2088.94(12)
Z	9
ϱ_{calc}g/cm^3	1.953
μ/mm^{-1}	2.497
F(000)	1197.0
Radiation	MoKα (λ = 0.71073)
2Θ range for data collection/°	3.122 to 58.26
Index ranges	$-9 \le h \le 13$, $-19 \le k \le 19$, $-22 \le l \le 22$
Reflections collected	28990
Independent reflections	11240 [R_{int} = 0.0477, R_{sigma} = 0.0729]
Data/restraints/parameters	11240/0/523
Goodness-of-fit on F^2	1.195
Final R indexes [I>=2σ (I)]	R_1 = 0.0630, wR_2 = 0.1708
Final R indexes [all data]	R_1 = 0.0974, wR_2 = 0.1928
Largest diff. peak/hole / e Å^{-3}	2.27/-3.56

Table AII.5 Crystal data and structure refinement for In:FDC 3

Identification code	In:FDC 3
Empirical formula	$C_{18}H_{16}In_3NNa_{0.5}O_{25.96}$
Formula weight	1139.63
Temperature/K	293(2)
Crystal system	triclinic
Space group	$P\bar{1}$
a/Å	10.0982(6)
b/Å	13.3547(8)
c/Å	15.3753(6)
α/°	99.278(4)
β/°	95.128(4)
γ/°	110.047(5)
Volume/Å^3	1898.84(18)
Z	2
ϱ_{calc}g/cm^3	1.993
μ/mm^{-1}	1.925
F(000)	1104.0
Radiation	MoKα (λ = 0.71073)
2Θ range for data collection/°	3.316 to 52.74
Index ranges	-12 ≤ h ≤ 12, -16 ≤ k ≤ 16, -19 ≤ l ≤ 18
Reflections collected	21938
Independent reflections	7768 [R_{int} = 0.0530, R_{sigma} = 0.0634]
Data/restraints/parameters	7768/915/796
Goodness-of-fit on F^2	1.054
Final R indexes [I>=2σ (I)]	R_1 = 0.0508, wR_2 = 0.1189
Final R indexes [all data]	R_1 = 0.0800, wR_2 = 0.1358
Largest diff. peak/hole / e Å^{-3}	0.78/-0.81

Table AII.6 Crystal data and structure refinement for In:CSA

Identification code	In:CSA
Empirical formula	$C_{11}H_{10}InNO_6$
Formula weight	385.04
Temperature/K	100
Crystal system	monoclinic
Space group	$P2_1/c$
a/Å	8.0483(3)
b/Å	7.2282(3)
c/Å	24.2472(18)
α/°	90.0
β/°	93.708(8)
γ/°	90.0
Volume/Å^3	1407.62(18)
Z	4
ρ_{calc}g/cm^3	1.817
μ/mm^{-1}	1.708
F(000)	760.0
Radiation	MoKα (λ = 0.71073)
2Θ range for data collection/°	5.072 to 53.02
Index ranges	$-10 \le h \le 10$, $-9 \le k \le 9$, $-30 \le l \le 30$
Reflections collected	3669
Independent reflections	3669 [R_{int} = 0.0929, R_{sigma} = 0.0520]
Data/restraints/parameters	3669/213/182
Goodness-of-fit on F^2	1.089
Final R indexes [I>=2σ (I)]	R_1 = 0.0867, wR_2 = 0.1869
Final R indexes [all data]	R_1 = 0.1138, wR_2 = 0.1993
Largest diff. peak/hole / e Å^{-3}	1.69/-2.05

Table AII.7 Crystal data and structure refinement for activated In:CSA

Identification code	In:CSA activated
Empirical formula	$C_{7.33}H_{7.33}In_{0.67}N_{0.67}O_{4.67}$
Formula weight	287.02
Temperature/K	293(2)
Crystal system	monoclinic
Space group	$P2_1/c$
a/Å	7.9601(7)
b/Å	7.2502(6)
c/Å	23.809(3)
α/°	90
β/°	90.729(9)
γ/°	90
Volume/Å^3	1374.0(2)
Z	6
ϱ_{calc}g/cm^3	2.081
μ/mm^{-1}	2.539
F(000)	840.0
Radiation	MoKα (λ = 0.71073)
2Θ range for data collection/°	5.118 to 52.746
Index ranges	$-9 \le h \le 9$, $-9 \le k \le 8$, $-29 \le l \le 28$
Reflections collected	14467
Independent reflections	2799 [R_{int} = 0.0922, R_{sigma} = 0.0662]
Data/restraints/parameters	2799/0/184
Goodness-of-fit on F^2	1.149
Final R indexes [I>=2σ (I)]	R_1 = 0.0893, wR_2 = 0.1767
Final R indexes [all data]	R_1 = 0.1282, wR_2 = 0.1935
Largest diff. peak/hole / e Å^{-3}	2.98/-2.95

Table AII.8 Crystal data and structure refinement for Cu:CSA

Identification code	Cu: CSA
Empirical formula	$C_{22}H_{18}Cu_2N_2O_{10}$
Formula weight	670.56
Temperature/K	100
Crystal system	monoclinic
Space group	*C2/c*
a/Å	19.2168(12)
b/Å	9.5684(6)
c/Å	13.8559(10)
α/°	90
β/°	92.637(7)
γ/°	90
Volume/Å^3	2545.0(3)
Z	4
ϱ_{calc}g/cm^3	1.750
μ/mm^{-1}	1.741
F(000)	1368.0
Radiation	MoKα (λ = 0.71073)
2Θ range for data collection/°	4.244 to 52.736
Index ranges	-24 ≤ h ≤ 17, -11 ≤ k ≤ 11, -17 ≤ l ≤ 17
Reflections collected	10530
Independent reflections	2607 [R_{int} = 0.0946, R_{sigma} = 0.0938]
Data/restraints/parameters	2607/30/210
Goodness-of-fit on F^2	1.082
Final R indexes [I>=2σ (I)]	R_1 = 0.0675, wR_2 = 0.1304
Final R indexes [all data]	R_1 = 0.1009, wR_2 = 0.1438
Largest diff. peak/hole / e Å^{-3}	0.83/-0.69

Table AII.9 Crystal data and structure refinement for In:PDG

Identification code	In: PDG
Empirical formula	$C_6H_4In_{0.5}NO_{3.5}$
Formula weight	287.02
Temperature/K	293(2)
Crystal system	triclinic
Space group	$P\bar{1}$
a/Å	7.2041(12)
b/Å	10.1131(14)
c/Å	11.757(2)
α/°	78.098(14)
β/°	79.138(15)
γ/°	85.697(13)
Volume/Å^3	822.6(2)
Z	4
ϱ_{calc}g/cm^3	2.318
μ/mm^{-1}	2.828
F(000)	560.0
Radiation	MoKα (λ = 0.71073)
2Θ range for data collection/°	3.598 to 42.996
Index ranges	$-6 \le h \le 7$, $-10 \le k \le 10$, $-12 \le l \le 12$
Reflections collected	5520
Independent reflections	1887 [R_{int} = 0.1031, R_{sigma} = 0.1234]
Data/restraints/parameters	1887/165/202
Goodness-of-fit on F^2	1.036
Final R indexes [I>=2σ (I)]	R_1 = 0.0733, wR_2 = 0.1830
Final R indexes [all data]	R_1 = 0.1060, wR_2 = 0.2117
Largest diff. peak/hole / e Å^{-3}	2.04/-1.26

Table AII.10 Crystal data and structure refinement for Mg:MA

Identification code	Mg:MA
Empirical formula	$C_6H_8MgO_8$
Formula weight	140.38
Temperature/K	273.15
Crystal system	monoclinic
Space group	*C2/c*
a/Å	12.111(3)
b/Å	16.598(2)
c/Å	5.889(3)
α/°	90
β/°	116.564(11)
γ/°	90
Volume/Å^3	1058.8(6)
Z	4
ϱ_{calc}g/cm^3	0.881
μ/mm^{-1}	0.130
F(000)	288.0
Radiation	MoKα (λ = 0.71073)
2Θ range for data collection/°	4.49 to 52.728
Index ranges	$-15 \le h \le 15$, $-20 \le k \le 20$, $-7 \le l \le 7$
Reflections collected	6863
Independent reflections	1082 [R_{int} = 0.0334, R_{sigma} = 0.0235]
Data/restraints/parameters	1082/4/94
Goodness-of-fit on F^2	1.050
Final R indexes [I>=2σ (I)]	R_1 = 0.0810, wR_2 = 0.2447
Final R indexes [all data]	R_1 = 0.0880, wR_2 = 0.2517
Largest diff. peak/hole / e Å^{-3}	0.84/-0.43

Appendix III

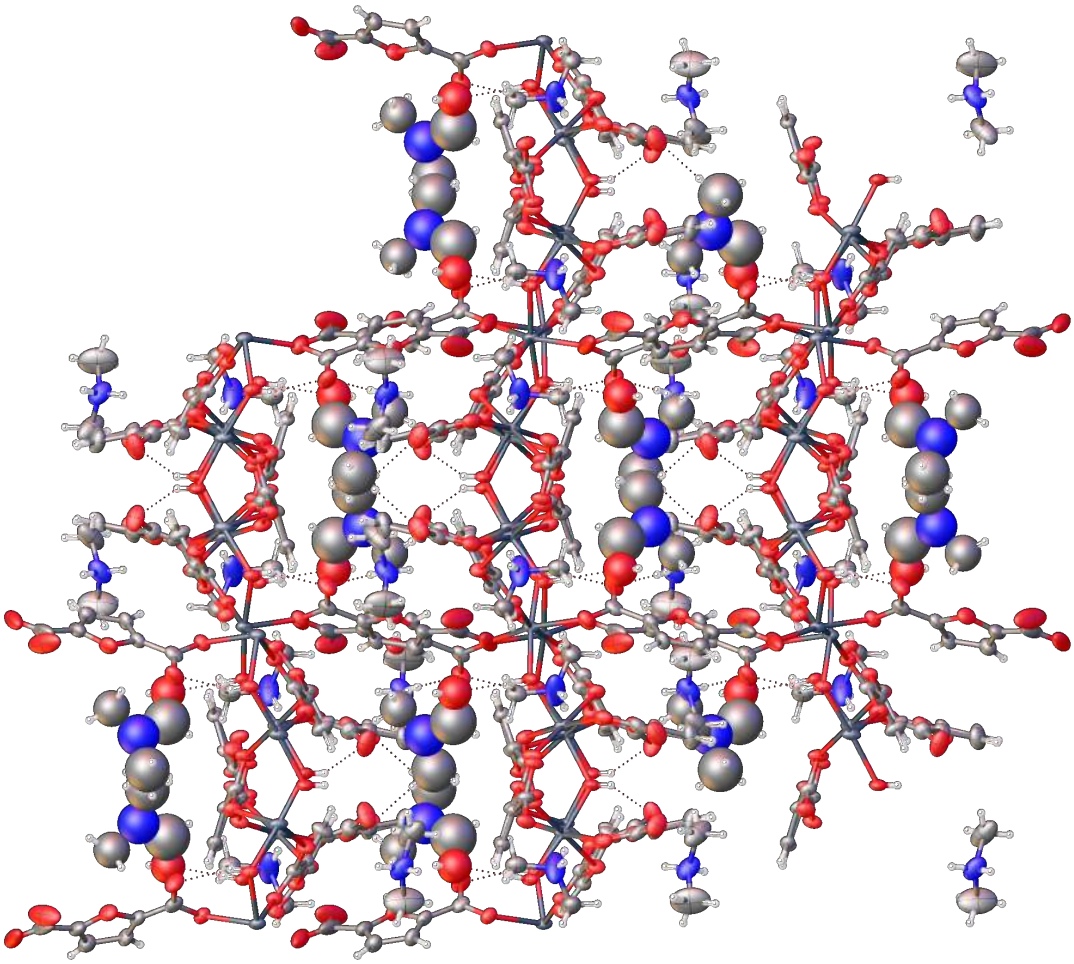

Figure AIII.1 Structure of as–made In:FDC compound 1, view along crystallographic *a*–axis. Indium (dark grey), carbon (pale grey), oxygen (red), hydrogen(white).

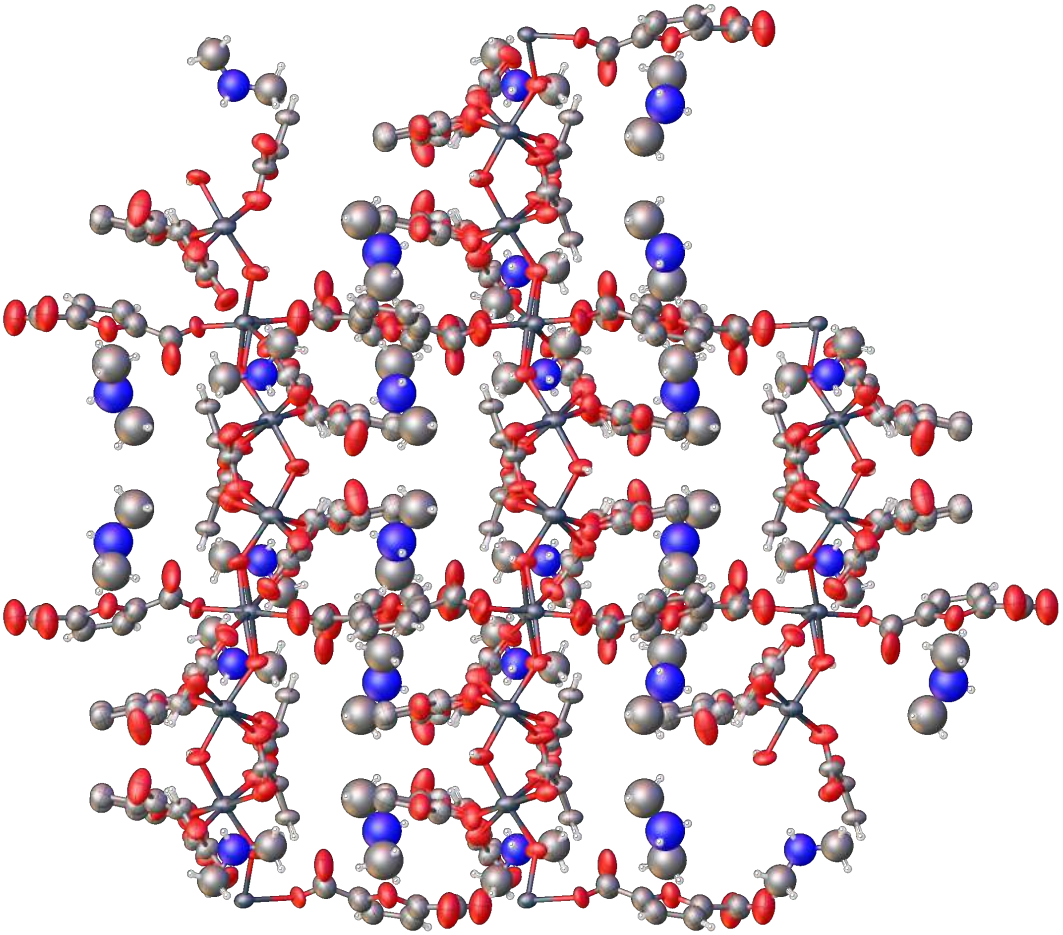

Figure AIII.2 Structure of activated In:FDC compound 1, view along crystallographic *a*–axis. Indium (dark grey), carbon (pale grey), oxygen (red), hydrogen(white).